Turbulence and planetesimal formation induced by the streaming instability

Dissertation zur Erlangung des Doktorgrades
an der Fakultät für Mathematik, Informatik und Naturwissenschaften
Fachbereich Physik
der Universität Hamburg

vorgelegt von

Urs Schäfer

Hamburg

2020

Gutachter der Dissertation:	Prof. Dr. Robi Banerjee Prof. Dr. Anders Johansen
Zusammensetzung der Prüfungskommission:	Prof. Dr. Robi Banerjee Prof. Dr. Anders Johansen Prof. Dr. Wilhelm Kley Prof. Dr. Jochen Liske PD Dr. Wolfram Schmidt
Vorsitzende/r der Prüfungskommission:	Prof. Dr. Jochen Liske
Datum der Disputation:	30.09.2020
Vorsitzender des Fach-Promotionsausschusses PHYSIK:	Prof. Dr. Günter Hans Walter Sigl
Leiter des Fachbereichs PHYSIK:	Prof. Dr. Wolfgang Hansen
Dekan der Fakultät MIN:	Prof. Dr. Heinrich Graener

Für Katharina.

Abstract

In the protoplanetary disks surrounding young stars, micron-sized dust grains grow over more than ten orders of magnitude in size until they form planets. The streaming instability plays an important role in this process in two regards: On the one hand, it drives turbulence in the dust layer around the mid-plane of protoplanetary disks. Turbulence influences the process of planet formation at all stages. On the other hand, the instability can induce concentration of millimetre- and centimetre-sized dust aggregates in gravitationally unstable overdensities. From the collapse of these overdensities, planetesimals with sizes of tens or hundreds of kilometres emerge – a crucial step on the path to ten-thousand-kilometre-sized planets.

Both aspects of the instability are investigated in this thesis. In a first publication, it is shown that the initial mass function of the planetesimals is better represented by a power law with an exponential tapering at its high-mass end than by a power law only. In a second publication, the first simulations of protoplanetary disks on global scales are presented that include the streaming instability as well as Lagrangian particles to model the dust. In this study, the streaming instability is considered as a source of turbulence and as such compared to another hydrodynamical instability, the vertical shear instability. In particular, it is shown that the streaming instability is the dominant source of turbulence in the dust layer if both instabilities begin to grow simultaneously, while the vertical shear instability remains dominant if it has already saturated before the streaming instability starts to operate. The streaming instability causes weaker turbulence and dust diffusion than the vertical shear instability. Nonetheless, the two instabilities in combination give rise to denser dust accumulations than the streaming instability alone. This indicates that the vertical shear instability is conducive to planetesimal formation owing to the streaming instability.

Zusammenfassung

In den protoplanetaren Scheiben um junge Sterne wachsen mikrometergroße Staubkörner um mehr als zehn Größenordnungen, bis sie Planeten bilden. Die Streaming Instability spielt in diesem Prozess in zweierlei Hinsicht eine wichtige Rolle: Einerseits verursacht sie Turbulenz in der staubreichen Schicht um die Mittelebene protoplanetarer Scheiben. Turbulenz beeinflusst den Prozess der Planetenentstehung in allen Stadien. Andererseits kann die Instabilität eine Konzentration von millimeter- und zentimetergroßen Staubaggregaten in gravitativ instabilen Überdichten bewirken. Aus dem Kollaps dieser Überdichten gehen Planetesimale hervor, die mehrere zehn oder hunderte Kilometer groß sind – ein entscheidender Schritt auf dem Weg zu zehntausend Kilometer großen Planeten.

Beide Aspekte der Instabilität werden in dieser Arbeit untersucht. In einer ersten Veröffentlichung wird gezeigt, dass die ursprüngliche Massenfunktion der Planetesimale besser durch ein Potenzgesetz beschrieben wird, das für hohe Massen exponentiell abfällt, als durch ein reines Potenzgesetz. In einer zweiten Veröffentlichung werden die ersten Simulationen protoplanetarer Scheiben auf globalen Skalen präsentiert, die sowohl die Streaming Instability als auch Lagrange-Teilchen zur Modellierung des Staubs umfassen. In dieser Studie wird die Streaming Instability als Quelle von Turbulenz betrachtet und als solche mit der Vertical Shear Instability, einer weiteren hydrodynamischen Instabilität, verglichen. Insbesondere wird gezeigt, dass die Streaming Instability vorherrschend als Quelle von Turbulenz ist, wenn beide Instabilitäten zeitgleich anfangen zu wachsen. Hingegen bleibt die Vertical Shear Instability dominant, falls sie bereits saturiert ist, wenn die Streaming Instability zu agieren beginnt. Die Streaming Instability verursacht schwächere Turbulenz und Staubdiffusion als die Vertical Shear Instability. Nichtsdestotrotz führt eine Kombination der beiden Instabilitäten zu dichteren Staubansammlungen als die Streaming Instability alleine. Dies impliziert, dass die Vertical Shear Instability förderlich für die Entstehung von Planetesimalen aufgrund der Streaming Instability ist.

List of publications

This thesis includes the following two publications. Both have been published as peer-reviewed articles in the journal *Astronomy & Astrophysics*.

1. **Schäfer, U.**, Yang, C.-C., and Johansen, A. Initial mass function of planetesimals formed by the streaming instability. *A&A*, 597:A69, 2017.

2. **Schäfer, U.**, Johansen, A., and Banerjee, R. The coexistence of the streaming instability and the vertical shear instability in protoplanetary disks. *A&A*, 635:A190, 2020.

In what follows, these publications are referred to as SYJ17 and SJB20. They are reproduced in Chapters 5 and 6 with permission ©ESO.

Contents

1 Introduction

Planets form in the protoplanetary disks around young stars. Stars and disks, in turn, emerge from the gravitational collapse of the cores of molecular clouds, the densest and coldest regions in the interstellar medium. Collapse ensues when the self-gravity of a molecular cloud core overcomes the stabilising effects of thermal pressure, magnetic fields, and turbulence (e.g., Mac Low and Klessen 2004; McKee and Ostriker 2007). Owing to the random turbulent motions in them, cores possess a non-zero net angular momentum. As a consequence of the conservation of this angular momentum, the collapse of a core leads to the formation of a rotating protoplanetary disk surrounding the (likewise rotating) star (e.g., Li et al. 2014) – and perhaps of one or multiple stellar companions since about half of all stellar systems are multiple systems (Duquennoy and Mayor 1991; Raghavan et al. 2010).

Figure 1.1 shows images of the protoplanetary disks around the stars HL Tauri (left) and IM Lupi (right). These images are obtained from observations of dust in the disks. Like the interstellar medium they form in, pristine disks by mass consist of 99% gas and 1% solid dust. Initially, a young star and the disk surrounding it are embedded in an envelope from which both accrete (e.g., Li et al. 2014). In this thesis, I investigate disks at a later time when accretion and outflows have caused this envelope to disperse. The disk also slowly dissolves because of accretion by the star, magnetically launched jets and disk winds, as well as photoevaporation[1] (e.g., Alexander et al. 2014). After a typical lifetime of a few million years (Haisch et al. 2001; Mamajek 2009), all the gas in the disk has dissipated and only solids and planets remain.

Two scenarios exist for the formation of a planet in a protoplanetary disk: top-down formation by collapse of a gravitationally unstable region in the disk and bottom-up formation from dust. In the former scenario, giant planets may form in about 1000 yr, but only in comparably massive disks with a sufficiently short cooling timescale (e.g., Boss 2002, 2010; Helled et al. 2014; Kratter and Lodato 2016, see also Sect. 4.2). Furthermore, the formation of brown dwarfs or stellar companions is more likely than that of giant planets, and it is difficult to explain the formation of terrestrial planets and minor bodies like asteroids and trans-Neptunian objects which are predominantly solid rather than gaseous.

[1] Photoevaporation denotes the heating by ionising radiation emitted by the central or nearby stars, and the resulting escape of the gas from the disk if its sound speed exceeds its orbital speed.

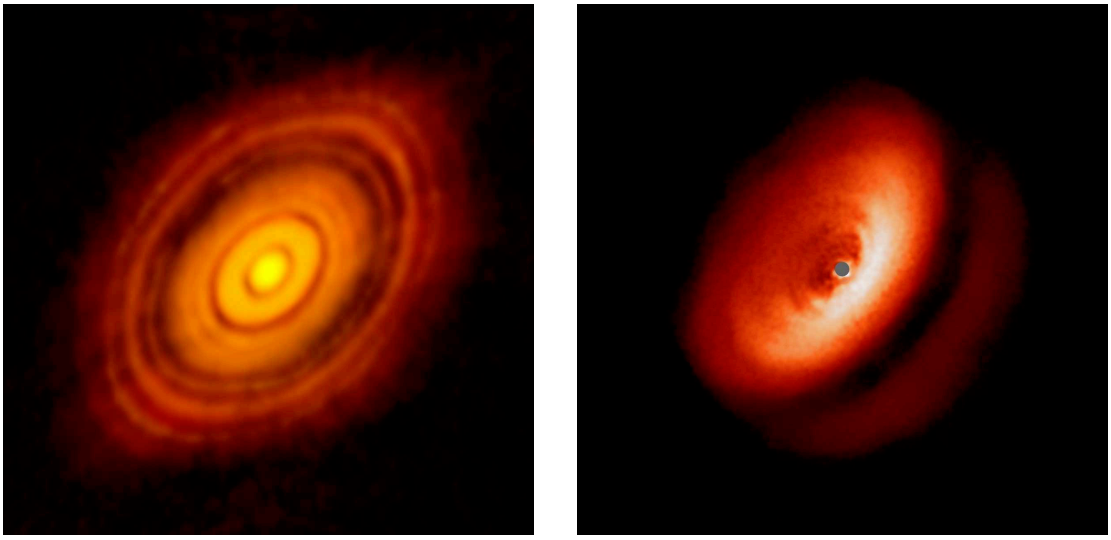

Figure 1.1: Images of the dust in the protoplanetary disks surrounding the stars HL Tauri (left) and IM Lupi (right). It is interesting to note the structure of concentric rings in the former disk and the thickness of the latter disk increasing with the radial distance to the star. Image credits: ALMA (ESO/NAOJ/NRAO) (left); ESO/H. Avenhaus et al./DARTT-S collaboration (right).

The bottom-up scenario (Safronov 1969) is studied in this thesis. In it, micron-sized dust grains must grow over 13 orders of magnitude in size – 39 orders of magnitude in mass – to 10 000 km-sized planets. The time scale of planet formation in this scenario is constrained by the lifetime of protoplanetary disks as the last step in the formation of a gas giant planet, the accretion of its gaseous envelope (e.g., Helled et al. 2014; Johansen and Lambrechts 2017), must occur before the gas in the disks has completely dispersed. The stages of bottom-up planet formation are illustrated in Fig. 1.2: Initially, dust grains form larger and larger aggregates owing to coagulation, that is to say they stick under mutual collisions (see Chapter 2). It takes about 10^3 to 10^4 orbital periods for aggregates to grow to sizes of millimetres (Zsom et al. 2010; Lorek et al. 2018). However, once they have reached these sizes, they are prone to bounce or even fragment when they collide (see Sect. 2.3). Furthermore, the drag exerted by the gas on the dust leads to the dust drifting towards the star in the radial direction, which poses a time constraint for dust growth (see Sect. 2.4; Whipple 1972; Adachi et al. 1976; Weidenschilling 1977a; Brauer et al. 2007).

Arguably the most promising mechanism to overcome these barriers is the streaming instability. It can induce the local concentration of centimetre-sized dust aggregates in gravitationally unstable clumps within some tens of orbital periods (see Chapter 3; e.g., Youdin and Goodman 2005; Youdin and Johansen 2007; Johansen and Youdin 2007; Johansen et al. 2007, 2009; Bai and Stone 2010a,b,c). As we show in SJB20, this dust accumulation is stronger if it is caused not by the streaming instability alone, but by a combination of the streaming instability and the vertical shear instability. The collapse of the dust clumps results in the formation of planetesimals (Goldreich and Ward 1973) – similar to the formation of stars in molecular cloud cores. Planetesimals are bodies with typical sizes of tens or hundreds of kilometres which are

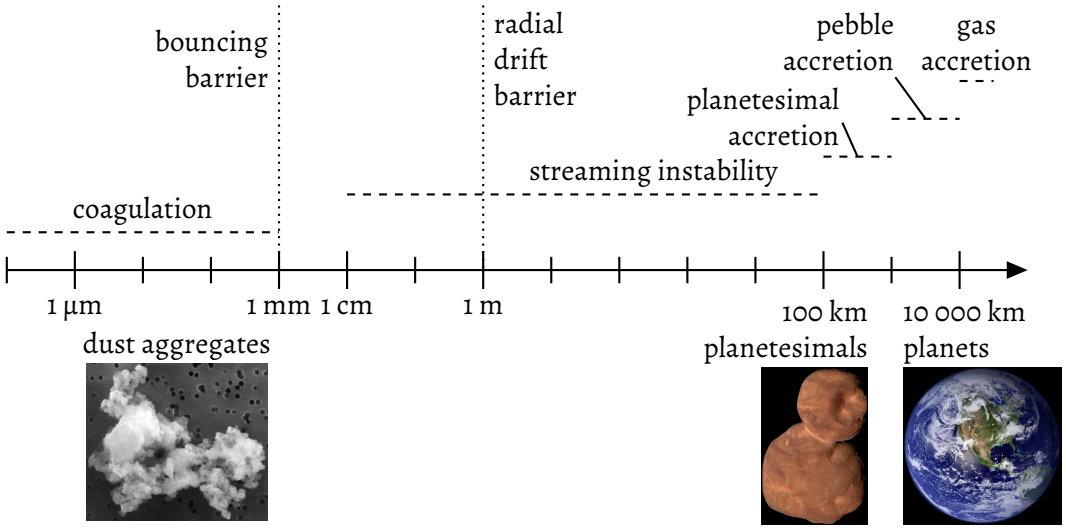

Figure 1.2: Size scales of bottom-up planet formation, from micron-sized dust to $10\,000$ km-sized planets. The dashed lines indicate the dominant growth processes at different sizes, while the dotted lines represent growth barriers. The images show, from left to right: an interplanetary dust aggregate from the Solar System, the Kuiper belt object 486958 Arrokoth, and the Earth. Image credits: NASA (left); NASA, Johns Hopkins University APL, Southwest Research Institute, and Roman Tkachenko (middle); NASA's Earth Observatory (right).

bound by self-gravity rather than material strength and are negligibly affected by the drag exerted by the gas (e.g., Johansen et al. 2014). The initial mass function of the planetesimals forming via the streaming instability has been subject of a number of numerical studies (Johansen et al. 2015; Simon et al. 2016, 2017; Abod et al. 2019; Li et al. 2019; Gole et al. submitted; SYJ17) as it crucially influences the following stages of planet formation. In SYJ17, we find that the mass distribution is represented better by a power law with an exponential tapering than by a power law only.

The formation of planets proceeds with what is called core accretion (e.g., Helled et al. 2014; Johansen and Lambrechts 2017). In the early stages, planetesimals grow by collisions. Once they attain sizes of thousands of kilometres, the accretion of large dust aggregates becomes the most efficient growth mechanism, a process that is referred to as pebble accretion. When planetary cores reach the so-called pebble isolation mass of several tens to some hundred Earth masses, they carve a gap in the gas disk which inhibits further pebble accretion. Consequently, the gaseous envelope around the core is no longer heated by pebble accretion and contracts. As soon as the envelope mass is comparable to the core mass, a stage of runaway gas accretion begins, which ends with the dissipation of the protoplanetary disk. The final architecture of a planetary system is shaped by interactions between planets and the gaseous disk (e.g., Baruteau et al. 2014) as well as mutually between planets (e.g., Davies et al. 2014).

As of August 2020, over 4300 exoplanets have been found in close to 3200 exoplanetary systems, of which more than 700 are multiple systems[2]. Observational bias favours the detection of large planets close to their host star. In particular, the planets in the Solar System would by

[2] `http://exoplanet.eu/catalog/`

tendency be either too small – the terrestrial planets – or too far away from the star – the giant planets – to be detected (e.g., Winn 2018). Nonetheless, it is interesting to consider the frequency of those types of planets for which statistics are comparatively complete. Giant planets with an orbital period of at most a few years are hosted by $\sim 10\%$ of Sun-like stars, and so-called hot Jupiters with orbital periods of ten days or less by $\sim 1\%$ of them (e.g., Winn 2018). Smaller planets with orbital periods shorter than a hundred days and sizes in the range between those of Earth and Neptune, which are referred to as super-Earths or sub-Neptunes, are more common. They can be found around about half of all Sun-like stars.

Turbulence affects all stages of planet formation: from the formation of a dust layer in the mid-plane of protoplanetary disks whose thickness is determined by the balance between vertical sedimentation and turbulent diffusion (Dubrulle et al. 1995; Fromang and Papaloizou 2006; Carballido et al. 2006; Youdin and Lithwick 2007); to dust growth by turbulent collisions (see Chapter 2); to planetesimal formation owing to the streaming instability (see Chapters 3 and 4); to planet-disk interactions (e.g., Baruteau et al. 2014). A number of instabilities have been theoretically established as sources of turbulence in protoplanetary disks (see Chapter 4), among which the vertical shear instability is one of the most promising (see Sect. 4.4.1). In SJB20, we present the first detailed study of the turbulence caused by the streaming instability, both in isolation as well as in interaction with the vertical shear instability. If both instabilities start to grow at the same time, we find the streaming instability to drive the turbulence in the disk mid-plane . On the other hand, the vertical shear instability remains the main source of turbulence in this plane if it has attained a saturated state before the streaming instability begins to be operate.

This thesis is structured as follows: In Chapter 2, I present observational and theoretical constraints on the maximum size to which dust in protoplanetary disks can grow by coagulation. These constraints establish the necessity of a mechanism to cause local dust overdensities that undergo gravitational collapse and form planetesimals. The streaming instability is introduced as such a mechanism in Chapter 3. Observational evidence for planetesimal formation via the streaming instability and the birth mass distribution of these planetesimals are also covered in this chapter, as are other mechanisms facilitating planetesimal formation. I discuss the streaming instability as a source of turbulence in Chapter 4, along with a number of other instabilities that drive turbulence and dust dynamics in protoplanetary disks. This chapter further includes a review of the turbulent strengths obtained from disk observations. In Chapters 5 and 6, the publications SYJ17 and SJB20 are reproduced. The model of the gas in protoplanetary disks that is employed throughout this thesis, with the exception of SYJ17, as well as tables containing all symbols used in the thesis can be found in Appendices A and B, respectively.

2
Barriers for collisional dust growth

In the first stage of their growth to planetary sizes, dust grains with sizes of up to microns, as are observed in the interstellar medium (Mathis et al. 1977), form aggregates via coagulation. That is, they stick together when they collide owing to intermolecular forces like the van der Waals force and hydrogen bonding. The focus of this chapter is to discuss to which maximum size aggregates can grow in this manner. On the one hand, the fact that these maximum sizes are smaller than planetesimal sizes demonstrates the necessity of a mechanism like the streaming instability to induce planetesimal formation by accumulating dust in gravitationally unstable overdensities. On the other hand, the strength of dust concentration and turbulence caused by the streaming instability depend on the dust size. The instability can induce planetesimal formation only if the aggregates are sufficiently large (see Sect. 3.2).

2.1 Observations

Observational estimates of dust sizes in the interior of protoplanetary disks can be obtained from thermal dust emission at wavelengths of millimetres and centimetres (e.g., Draine 2006; Testi et al. 2014). The presence of a disk around a young star is reflected in an excess in the stellar spectral energy distribution at infrared and longer wavelengths which is caused by dust emission[1]. The emission is usually assumed to be optically thin at millimetre- to centimetre-wavelengths for two reasons: Firstly, colder disk regions close to mid-plane are probed at these wavelengths. This is because, according to Wien's displacement law, the wavelength at which the spectrum of a black body peaks is inversely proportional to the temperature. Secondly, dust can not efficiently absorb radiation with wavelengths much greater than its size. If the

[1]The product of wavelength and flux density as a function of the wavelength is commonly referred to as the spectral energy distribution. The shape of the infrared excess in the spectral energy distribution of young stars gives rise to a categorisation in Classes I to III, which reflects a chronological order (Lada and Wilking 1984; Adams et al. 1987; Lada 1987). While Class I young stellar objects (YSOs) are still embedded in an envelope, stars whose envelope has dissolved are referred to as Class II YSOs or (classical) T Tauri stars. Both Class I and Class II stars are surrounded by a protoplanetary disk. After this disk has dispersed, a Class III YSOs or weak-line T Tauri star remains. The transitions between these classes are fluent, though, and an additional Class 0 (Andre et al. 1993) and a class with flat spectral energy distributions (Greene et al. 1994) have been identified.

emission is indeed optically thin, the opacity of the dust can be approximated as $\kappa_\lambda \propto \lambda^{-\beta}$, where λ is the wavelength and the spectral index β depends on the maximum dust size. While for grains in the interstellar medium $\beta \approx 1.7$, the spectral index approaches zero for larger aggregates.

Deriving the maximum dust size from the spectral index of the opacity requires a number of assumptions, including about the composition and porosity of the dust as well as the dust size distribution. This distribution is usually assumed to be a power law, $\mathrm{d}n_\mathrm{d}/\mathrm{d}a \propto a^{-q}$, where n_d is the dust number density and a the dust size. The exponent $q = 3.5$ in a steady-state collisional cascade model, in which mass is transferred from larger to smaller bodies by fragmentation (Dohnanyi 1969; Williams and Wetherill 1994), and ranges between 3 and 4 in models and observations of debris disks[2] (e.g., Hughes et al. 2018) as well as in the interstellar medium (Mathis et al. 1977).

From the opacity spectral index, dust sizes of up to centimetres in the inner regions of protoplanetary disks and millimetres in the outer regions are inferred (e.g., Pérez et al. 2012, 2015; Testi et al. 2014; Tazzari et al. 2016; Macías et al. 2019). However, doubt has recently been cast on the assumption of optically thin emission because scattering by dust grains might lead to optically thick disks being mistaken as optically thin (Liu 2019; Zhu et al. 2019). If disks were indeed optically thick, maximum dust sizes would amount to not more than millimetres. This would also explain the fact that the observed total dust masses in disks, particularly around low-mass stars, are insufficient to account for the observed total planet masses in exoplanetary systems (Najita and Kenyon 2014; Mulders et al. 2015; Manara et al. 2018) since dust would be hidden from observations in the optically thick regions.

Observations with the Atacama Large Millimeter/submillimeter Array (ALMA) reveal a structure of concentric rings in many protoplanetary disks (see Fig. 1.1). By employing models of this structure that include scattering and do not presuppose optically thin or thick emission, Carrasco-González et al. (2019) infer dust sizes of a few millimetres in the outer regions and less than one millimetre in the inner regions of the disk around HL Tauri, while Tapia et al. (2019) find that the dust has grown as large as a centimetre in the mid-plane of this disk.

Another approach to obtain maximum dust sizes is studying the polarisation of the emission of dust grains resulting from scattering by other dust grains. The emission is most strongly polarised if the maximum size is comparable to $\lambda/(2\pi)$ (Kataoka et al. 2015). This approach yields sizes of at most a few hundred microns in disks observed with ALMA (Kataoka et al. 2017; Bacciotti et al. 2018; Ohashi and Kataoka 2019). On the one hand, these maximum sizes are consistent with the ones inferred from the opacity spectral index if the dust emission is optically thick (Lin et al. 2020; Ohashi et al. 2020). On the other hand, Yang and Li (2020) and Kirchschlager and Bertrang (2020), respectively, propose that the discrepancy arising if the emission is optically thin can be alleviated when considering the chemical composition and the shape of the dust grains.

Further indications of how large dust aggregates can grow by coagulation can be found in the Solar System. Chondrites, stony meteorites that never melted, contain small spherical grains called chondrules. The sizes of these chondrules amount to up to a few millimetres (e.g.,

[2] A debris disk is the disk of dust and solid debris that remains after the gas in its progenitor protoplanetary disk has completely dispersed.

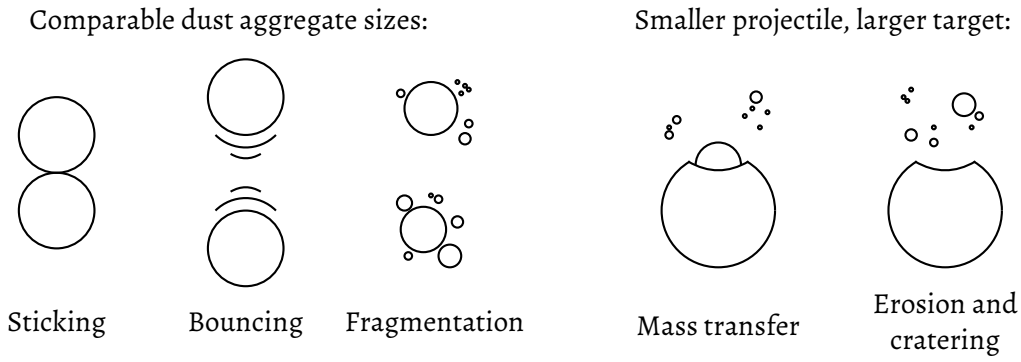

Figure 2.1: Sketches of the possible outcomes of collisions between two dust aggregates. Of these, only sticking of similarly sized aggregates and mass transfer from a smaller to a larger aggregate result in growth, while bouncing is neutral in this respect. In contrast, fragmentation as well as erosion and cratering lead to a reduction in the aggregate masses.

Friedrich et al. 2015), with evidence suggesting that they form centimetre-sized aggregates (Simon et al. 2018a,b). Measurements of the comet 67P/Churyumov-Gerasimenko by the Rosetta mission indicate that it consists of millimetre-sized aggregates (Blum et al. 2017).

Observations provide insights not only into how large, but also when during the evolution of protoplanetary disks dust aggregates grow. Observational evidence shows that dust of $100\,\mu$m- or millimetre-sizes is present already at an early stage, when a young star and the disk surrounding it are still embedded in an envelope (Miotello et al. 2014; Harsono et al. 2018; Agurto-Gangas et al. 2019). Dust having already grown too large to be observable would provide another explanation for the discrepancy between the total mass of the dust in disks observed after the dissipation of their envelope and the total mass of exoplanetary systems (Najita and Kenyon 2014; Manara et al. 2018).

2.2 Collisional outcomes and relative velocities

Whether the collision of two dust aggregates leads to growth depends on a number of parameters, including the relative velocity, size, composition, and porosity of the aggregates. The outcomes of collisions fall into five categories, as depicted in Fig. 2.1 (e.g., Güttler et al. 2010; Birnstiel et al. 2016; Blum 2018). Three of these categories pertain to collisions between two aggregates of similar sizes:

- Sticking
- Bouncing: Bouncing leads to neither an increase nor a decrease in the aggregate masses, but possibly to compaction of porous aggregates.
- Fragmentation: The resulting fragments are less massive than the colliding aggregates.

The other two categories cover outcomes of a smaller projectile hitting a larger target, with the projectile fragmenting as a result of the collision:

- Mass transfer: More mass is transferred from the projectile to the target than is lost by the target during the collision.
- Erosion and cratering: Both erosion by smaller projectiles and cratering by larger ones cause a mass loss of the target.

This categorisation is not exhaustive. For instance, the electrostatic repulsion of dust with like charges is not considered, which can inhibit the growth at sizes of microns, but can be overcome by turbulence (Okuzumi 2009, 2014; Akimkin et al. 2020).

Relative velocities between equally sized aggregates can be caused by Brownian motion or by gas turbulence. In addition, collisions of aggregates with different sizes can occur because the radial and azimuthal drift speeds, which result from the mutual drag between gas and dust (see Sects. 2.4 and 3.1), as well as the vertical settling speed (see Sect. 4.1) vary with the aggregate size. The random velocities of Brownian motion at a temperature T are described by a Maxwell-Boltzmann distribution, with the mean relative speed of aggregates of the same size being equal to

$$\Delta v_{\mathrm{d,Bm}} = \sqrt{\frac{16 k_{\mathrm{B}} T}{\mu m_{\mathrm{d}}}}, \tag{2.1}$$

where k_{B} is the Boltzmann constant, $\mu = 2.33$ the mean molecular weight, and m_{d} the dust mass.

Whether and how strongly dust is stirred by gas turbulence depends on the stopping time of the dust, the time scale over which the dust attains the same velocity as the gas owing to their mutual drag[3]. The dust stopping time is given by

$$t_{\mathrm{d,stop}} = \frac{m_{\mathrm{d}} \Delta \boldsymbol{v}}{\boldsymbol{F}_{\mathrm{drag}}} = \begin{cases} \frac{\rho_{\mathrm{s}} a}{\rho_{\mathrm{g}} c_{\mathrm{s}}} & a \leq \frac{9}{4} \lambda_{\mathrm{g,mfp}} \text{ (Epstein regime) or} \\ \frac{4 \rho_{\mathrm{s}} a^2}{9 \rho_{\mathrm{g}} c_{\mathrm{s}} \lambda_{\mathrm{g,mfp}}} & a > \frac{9}{4} \lambda_{\mathrm{g,mfp}} \text{ (Stokes regime),} \end{cases} \tag{2.2}$$

where $\Delta \boldsymbol{v}$ is the relative velocity between dust and gas, $\boldsymbol{F}_{\mathrm{drag}}$ the drag force, ρ_{g} the gas density, and c_{s} the sound speed. In Chapter 2, I choose a generic solid density of $\rho_{\mathrm{s}} = 1 \text{ g cm}^{-3}$, which is comparable to that of water ice (1 g cm^{-3}) and silicates ($\sim 3 \text{ g cm}^{-3}$). (The solid density ρ_{s}, the mass per volume of dust material, is not to be confused with the dust density ρ_{d}, the mass per volume of space.) The gas mean free path length $\lambda_{\mathrm{g,mfp}} = 1/(\sigma_{\mathrm{g}} n_{\mathrm{g}})$, where n_{g} is the gas number density and $\sigma_{\mathrm{g}} = 2 \times 10^{-15} \text{ cm}^2$ the molecular collision cross section (Chapman and Cowling 1970). The dust size being approximately equal to the mean free path length marks the transition from the Epstein to the Stokes drag regime, in which $t_{\mathrm{d,stop}} \propto a$ and $t_{\mathrm{d,stop}} \propto a^2$, respectively.

The dimensionless Stokes number $\mathrm{St} = t_{\mathrm{d,stop}} \Omega_{\mathrm{K}}$ gives the ratio of the dust stopping time to the dynamical time scale in protoplanetary disks, the inverse of the Keplerian orbital frequency $\Omega_{\mathrm{K}} = v_{\mathrm{K}}/r$. Here, v_{K} is the Keplerian orbital speed and r the radial distance to the star. Dust with a Stokes number much smaller than one adapts to the gas motions on a much shorter time scale than the dynamical one, that is to say almost instantaneously. Gas and dust are thus

[3] The gas stopping time can be calculated as $t_{\mathrm{g,stop}} = \rho_{\mathrm{g}}/\rho_{\mathrm{d}}\, t_{\mathrm{d,stop}}$.

perfectly coupled via drag. On the other hand, if the Stokes number is much larger than one, gas and dust are effectively decoupled. The Stokes number is a convenient measure of the dust size when physical processes involving the drag between gas and dust are considered, and used as such in this thesis.

If the stopping time of a dust aggregate is greater than the turnover time scale of a turbulent eddy in the gas, the motion of the aggregate is not completely adjusted to the turbulent motion before the eddy decays. This results in a random velocity of the aggregate. These random velocities differ even for aggregates with the same size. To derive the Stokes number $\mathrm{St}_{\mathrm{turb}}$ of the smallest aggregates that are stirred by turbulence, I equate the dust stopping time with the eddy turnover time scale τ_η at the dissipation scale η (Markiewicz et al. 1991; Cuzzi and Hogan 2003; Ormel and Cuzzi 2007). I further assume that the turnover time scale τ_L at the injection scale L is equal to the dynamical time scale $1/\Omega_{\mathrm{K}}$. Thus,

$$\frac{\tau_\eta}{\tau_L} = t_{\mathrm{d,stop}}\Omega_{\mathrm{K}} = \mathrm{St}. \tag{2.3}$$

The left-hand side of this equation can be related to the Reynolds number Re, which expresses the ratio of the turbulent to the molecular viscosity. If this number is greater than unity the gas is turbulent, and laminar otherwise. The rate at which kinetic energy is injected at the scale L is equal to the rate at which it is dissipated because of the molecular viscosity of the gas at the scale η. Under this condition,

$$\frac{v_{\mathrm{g},L}^2}{\tau_L} = \frac{v_{\mathrm{g},\eta}^2}{\tau_\eta} \quad \Leftrightarrow \quad \frac{\nu_{\mathrm{g,turb}}}{\tau_L^2} = \frac{\nu_{\mathrm{g,mol}}}{\tau_\eta^2} \quad \Leftrightarrow \quad \mathrm{Re} = \frac{\nu_{\mathrm{g,turb}}}{\nu_{\mathrm{g,mol}}} = \frac{\tau_L^2}{\tau_\eta^2}, \tag{2.4}$$

where $v_{\mathrm{g},L}$ and $v_{\mathrm{g},\eta}$ are the gas velocities at the injection and the dissipation scale, respectively. The molecular viscosity

$$\nu_{\mathrm{g,mol}} = \frac{1}{2}\lambda_{\mathrm{g,mfp}} v_{\mathrm{g,therm}}, \tag{2.5}$$

where $v_{\mathrm{g,therm}} = \sqrt{8/\pi}\, c_{\mathrm{s}}$ is the mean thermal speed of the gas.

To calculate the turbulent viscosity $\nu_{\mathrm{g,turb}}$, the so-called α-model devised by Shakura and Sunyaev (1973) can be used[4]. They define $\nu_{\mathrm{g,turb}} = \alpha c_{\mathrm{s}} H_{\mathrm{g}}$, where the dimensionless parameter α is a measurement of the turbulent strength and H_{g} is the gas scale height. In the thin-disk approximation, that is assuming that the radius r is much greater than the height z above or below the mid-plane, the gas scale height $H_{\mathrm{g}} = c_{\mathrm{s}}/\Omega_{\mathrm{K}}$ and thus

$$\nu_{\mathrm{g,turb}} = \frac{\alpha c_{\mathrm{s}}^2}{\Omega_{\mathrm{K}}}. \tag{2.6}$$

On the other hand,

$$\nu_{\mathrm{g,turb}} \sim v_{\mathrm{g,turb}}^2 \tau_L = \frac{v_{\mathrm{g,turb}}^2}{\Omega_{\mathrm{K}}} = \frac{\mathcal{M}_{\mathrm{g}}^2 c_{\mathrm{s}}^2}{\Omega_{\mathrm{K}}}, \tag{2.7}$$

[4]The α-model was originally developed by Shakura and Sunyaev (1973) to describe the angular momentum transport by turbulence in the accretion disks surrounding black holes. It can be equivalently applied to angular momentum transport and turbulence in protoplanetary disks.

where $\mathcal{M}_\mathrm{g}$ is the Mach number of the gas motions. Comparing Eqs. 2.6 and 2.7 yields $\alpha \sim \mathcal{M}_\mathrm{g}^2$ and

$$\nu_\mathrm{g,turb} \sim \mathcal{M}_\mathrm{g}^2 c_\mathrm{s} H_\mathrm{g}, \tag{2.8}$$

which I treat as equalities rather than similarities in the following.

From Eqs. 2.3 and 2.4, it follows that the dust stopping time and the eddy turnover time at the dissipation scale being equal is equivalent to $\mathrm{St} = \mathrm{Re}^{-1/2}$. That is, gas turbulence induces random velocities of dust aggregates if the Stokes number of the aggregates exceeds

$$\mathrm{St}_\mathrm{turb} = \mathrm{Re}^{-1/2} = \sqrt{\frac{\nu_\mathrm{g,mol}}{\nu_\mathrm{g,turb}}} = \sqrt{\sqrt{\frac{2}{\pi}} \frac{\lambda_\mathrm{g,mfp}}{\mathcal{M}_\mathrm{g}^2 H_\mathrm{g}}}. \tag{2.9}$$

If the stopping time is not only greater than the turnover time at the dissipation scale, but also less than the one at the injection scale, the relative velocity of equally sized aggregates amounts to

$$\Delta v_\mathrm{d,turb} = \sqrt{2\mathrm{St}} \mathcal{M}_\mathrm{g} c_\mathrm{s} \tag{2.10}$$

(Ormel and Cuzzi 2007). The latter condition corresponds to the Stokes number being less than unity since I assume that the turnover time at the injection scale is equal to the dynamical time scale.

2.3 Bouncing and fragmentation barriers

Dust aggregates can grow by coagulation only to certain sizes. As soon as they reach these sizes, they start to bounce or fragment rather than sticking under mutual collisions. Growth beyond these sizes thus requires a mechanism that does not depend on collisions between aggregates. In what follows, I present estimates of the sizes that mark the transition from sticking to bouncing or fragmentation. In doing so, I focus on monodisperse growth. That is, I assume that all aggregates are of the same size. Therefore, I only take into account sticking, bouncing, and fragmentation as collisional outcomes. I further treat aggregates as perfectly compact spheres with a constant solid density of $1\ \mathrm{g\ cm^{-3}}$. I comment on the dependence of the estimates on the aggregate porosity below. The model of the gas in protoplanetary disks that is used in this thesis, with the exception of SYJ17, is detailed in Appendix A. For simplicity, when applying this model I only consider the disk mid-plane to which the dust sediments.

Employing laboratory experiments, Weidling et al. (2012) show that colliding aggregates bounce off of one another instead of sticking together if their relative velocity is greater than[5]

$$\Delta v_\mathrm{d,boun} = \left(\frac{m_\mathrm{d}}{3.3 \times 10^{-3}\ \mathrm{g}} \right)^{-5/18} \mathrm{cm\ s^{-1}} = 6.36 \left(\frac{a}{100\ \mu\mathrm{m}} \right)^{-5/6} \mathrm{cm\ s^{-1}}. \tag{2.11}$$

While Weidling et al. (2012) use silicate aggregates to obtain this threshold value, Gundlach et al. (2018) and Musiolik and Wurm (2019) find that water ice aggregates are not more prone to sticking than these.

[5]This is a conservative choice of the minimum relative velocity because collisions with this velocity always lead to bouncing, but bouncing is a possible outcome also for lower velocities (Weidling et al. 2012).

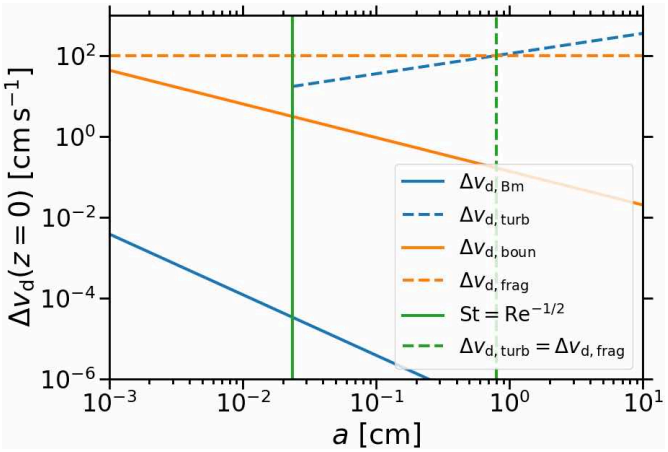

Figure 2.2: Relative velocity of dust aggregates Δv_d in the disk mid-plane as a function of the dust size a. Here, I exemplarily choose a radial distance to the star of 10 au and a Mach number of the gas velocity of 0.01, but the following conclusions are equally valid for a large range of radii and Mach numbers (see main text). The blue lines show the relative velocities that are induced by Brownian motion $\Delta v_\mathrm{d,Bm}$ (Eq. 2.11; solid line) and by gas turbulence $\Delta v_\mathrm{d,turb}$ (Eq. 2.10; dashed line), with the latter being much larger than the former. For the dust to be stirred by turbulence, its stopping time must be equal to or higher than the eddy turnover time at the dissipation scale. This condition yields a threshold Stokes number of $\mathrm{St} = \mathrm{Re}^{-1/2}$ (see Eq. 2.9) and the threshold aggregate size which is depicted as a solid green line. This size marks the transition from sticking to bouncing of colliding aggregates because turbulent relative velocities exceed the ones that lead to bouncing $\Delta v_\mathrm{d,boun}$ (Eq. 2.11; solid orange line) at all aggregate sizes. Fragmentation, on the other hand, requires turbulence to cause relative velocities in excess of $\Delta v_\mathrm{d,frag} = 100\,\mathrm{cm\,s^{-1}}$ (dashed orange line). This corresponds to aggregate sizes that are at least equal to the value marked with a dashed green line. That is, larger relative velocities and sizes of the dust are necessary for fragmentation than for bouncing.

Relative velocities that lead to the fragmentation of silicates in experiments are typically of the order of $1\,\mathrm{m\,s^{-1}}$ (e.g., Blum and Wurm 2008; Güttler et al. 2010). Higher relative velocities are necessary for water ice to fragment in the experiments by, for example, Gundlach and Blum (2015). However, as noted above, Gundlach et al. (2018) and Musiolik and Wurm (2019) find no such difference between the sticking properties of silicates and of water ice. The latter authors conduct experiments at temperatures that are lower and therefore more representative of the temperatures in protoplanetary disks than the ones in previous experiments, including the ones performed by Gundlach and Blum (2015). Therefore, I assume that aggregates fragment if their relative velocities exceed $\Delta v_\mathrm{d,frag} = 1\,\mathrm{m\,s^{-1}}$, regardless of the composition of the aggregates.

The relative dust velocities that are caused by Brownian motion (Eq. 2.1) and gas turbulence (Eq. 2.10) as well as the ones that result in bouncing and fragmentation are depicted in Fig. 2.2. From the figure, it can be seen that Brownian motion can be neglected if the dust is stirred by turbulence in the gas. This is the case if the dust stopping time exceeds the turnover time scale of the turbulent eddies at the dissipation scale, or equivalently if the Stokes number of the dust is at least equal to $\mathrm{St}_\mathrm{turb}$ (see Eq. 2.9).

In addition, the figure shows that even the lowest relative velocities induced by turbulence invariably lead to bouncing. That is, as soon as dust grows to a Stokes number of

$$\mathrm{St}_{\mathrm{boun}}(z=0) = \mathrm{St}_{\mathrm{turb}}(z=0) = 1.48 \times 10^{-4} \left(\frac{r}{1\,\mathrm{au}}\right)^{1/2} \left(\frac{\mathcal{M}_{\mathrm{g}}}{0.01}\right)^{-1}, \tag{2.12}$$

bouncing prevents further collisional growth. Assuming drag in the Epstein regime[6], Stokes numbers can be converted to dust sizes as

$$a(z=0) = \frac{\mathrm{St}(z=0)\rho_{\mathrm{g}}(z=0)c_{\mathrm{s}}}{\rho_{\mathrm{s}}\Omega_{\mathrm{K}}(z=0)} = 5.02 \left(\frac{\mathrm{St}}{0.01}\right) \left(\frac{r}{1\,\mathrm{au}}\right)^{-1} \mathrm{cm} \tag{2.13}$$

(see Eq. 2.2). It follows that aggregates bounce under mutual collisions if their size is at least

$$a_{\mathrm{boun}}(z=0) = 743 \left(\frac{r}{1\,\mathrm{au}}\right)^{-1/2} \left(\frac{\mathcal{M}_{\mathrm{g}}}{0.01}\right)^{-1} \mu\mathrm{m}. \tag{2.14}$$

I note that at very large radial distances to the star and high Mach numbers, it is possible that aggregates whose relative velocities are caused by turbulence stick together rather than bouncing off of each other when they collide. This is the case if the minimum relative velocity that leads to bouncing of the smallest such aggregates $\Delta v_{\mathrm{d,boun}}(\mathrm{St}_{\mathrm{turb}})$ (see Eq. 2.11) is greater than their turbulent relative velocity $\Delta v_{\mathrm{d,turb}}(\mathrm{St}_{\mathrm{turb}})$ (see Eq. 2.10). However, for a Mach number of 0.01, which is a typical value in the mid-plane of protoplanetary disks (see Chapter 4), this condition is met only at radii larger than 579 au. And even for a Mach number of 0.1, the threshold radius amounts to 93 au. I therefore neglect the possibility of sticking as a result of collisions induced by turbulence.

From the figure, it is further evident that fragmentation, like bouncing, is a possible collisional outcome only if turbulence gives rise to the relative velocities between aggregates. Nevertheless, fragmentation requires higher relative velocities than bouncing. Because the relative velocity induced by turbulence increases with the Stokes number, higher Stokes numbers are thus necessary. The requirement that the turbulent relative velocity $\Delta v_{\mathrm{d,turb}} = \sqrt{2\mathrm{St}}\mathcal{M}_{\mathrm{g}}c_{\mathrm{s}}$ is equal to or greater than the one resulting in fragmentation $\Delta v_{\mathrm{d,frag}}$ yields a minimum Stokes number of $\mathrm{St}_{\mathrm{frag}} = \Delta v_{\mathrm{d,frag}}^2/(2\mathcal{M}_{\mathrm{g}}^2 c_{\mathrm{s}}^2)$ or

$$\mathrm{St}_{\mathrm{frag}}(z=0) = 5.00 \times 10^{-3} \left(\frac{r}{1\,\mathrm{au}}\right)^{1/2} \left(\frac{\mathcal{M}_{\mathrm{g}}}{0.01}\right)^{-2}, \tag{2.15}$$

and a minimum aggregate size of

$$a_{\mathrm{frag}}(z=0) = 2.51 \left(\frac{r}{1\,\mathrm{au}}\right)^{-1/2} \left(\frac{\mathcal{M}_{\mathrm{g}}}{0.01}\right)^{-2} \mathrm{cm}. \tag{2.16}$$

[6]The transition from the Epstein to the Stokes drag regime occurs at a dust size of

$$a(z=0) = \frac{9}{4}\lambda_{\mathrm{g,mfp}}(z=0) = 4.388 \left(\frac{r}{1\,\mathrm{au}}\right)^{9/4} \mathrm{cm}$$

(see Eq. 2.2).

These simple estimates show that the so-called bouncing barrier – the term is coined by Zsom et al. (2010) – inhibits growth by coagulation beyond sizes of hundreds of microns or a few millimetres. As noted above, the derivation of the estimates involves the assumption of perfectly compact aggregates. For a given mass, aggregates are larger, but their Stokes number is smaller if they are not compact. The latter is because $\mathrm{St} \propto a\rho_\mathrm{s} \sim m_\mathrm{d}/\sigma_\mathrm{d}$, and the cross section of the dust σ_d increases with its size. Furthermore, bouncing can entail compaction of the colliding aggregates (e.g., Blum and Wurm 2008; Weidling et al. 2009; Güttler et al. 2009), which leads to a decline in size and cross section, but an increase in Stokes number.

Additionally, numerical simulations indicate that porous aggregates of comparable sizes stick together even if they collide with velocities exceeding $1\ \mathrm{m\,s^{-1}}$ (Wada et al. 2009, 2011; Seizinger and Kley 2013), i.e. with velocities that I assume to lead to fragmentation. However, in experiments collisions with such velocities are found to result in bouncing or fragmentation (Blum and Wurm 2008; Güttler et al. 2010; Weidling et al. 2012; Kothe et al. 2013; Weidling and Blum 2015).

It is interesting to note that the estimated maximum Stokes number of $\sim 10^{-4}$ to which aggregates can grow at a radius of 1 au is consistent with the value that Zsom et al. (2010) obtain using a distinctly more sophisticated model. Rather than assuming monodisperse growth of compact aggregates, these authors base their model on the experimental results of collisions between both porous and compact aggregates with either similar or different sizes. In their model, growth is as well limited by bouncing, not fragmentation or erosion. Yet, the transition from sticking to bouncing is not associated with the transition from Brownian motion to turbulent relative velocities – even aggregates that are stirred by turbulence can stick together. In addition, the authors find that the maximum Stokes number to which dust can grow is largely independent of the gas density and, in contrast to what can be gathered from Eq. 2.12, also of the turbulent strength.

Several pathways have been proposed for collisional growth to overcome the barriers posed by bouncing and fragmentation:

- If they are less affected by bouncing and fragmentation than more compact aggregates, highly porous aggregates with internal densities of orders of magnitude less than unity may grow to planetesimals (Okuzumi et al. 2012; Kataoka et al. 2013; Krijt et al. 2016b; Garcia and Gonzalez 2020a,b). They can overcome the radial drift barrier (see Sect. 2.4; Okuzumi et al. 2012; Garcia and Gonzalez 2020a,b) since for a given mass they are comparatively large, and their growth time scale $\tau_\mathrm{d,grow} \propto a\rho_\mathrm{s} \sim m_\mathrm{d}/\sigma_\mathrm{d}$ is thus short. In addition, porous aggregates reach sizes in excess of the gas mean free path length at smaller Stokes numbers $\mathrm{St} \propto a\rho_\mathrm{s}$ than compact ones. At these sizes, that is to say in the Stokes drag regime, $\mathrm{St}(z=0) \propto r^{-5/4}$, while in the Epstein regime $\mathrm{St}(z=0) \propto r$ (see Eq. 2.2). In the Stokes regime, the inwards radial drift of aggregates with a Stokes number greater than one therefore results in an incremental increase in their Stokes number and consequently a slowdown of their drift. Once aggregates have substantially grown in mass, compaction by the surrounding gas and self-gravity can increase their internal density to that expected for planetesimals (Kataoka et al. 2013). However, erosion inhibits the growth of porous aggregates beyond Stokes numbers of unity (Krijt et al. 2015, 2016b).

- The relative velocities caused by Brownian motion and turbulence are not always equal to, but distributed around the values given in Eqs. 2.1 and 2.10. Windmark et al. (2012b,c) and Garaud et al. (2013) therefore propose that "lucky" aggregates that are involved only in collisions with low relative velocities avoid bouncing and fragmentation and continue to grow. Their growth is aided by mass transfer in collisions with smaller aggregates (e.g., Blum and Wurm 2008; Windmark et al. 2012a). Nonetheless, just as there are "lucky" aggregates, there are "unlucky" ones which bounce or fragment although their sizes are smaller than the ones estimated above.

- Steinpilz et al. (2019) find in experiments and simulations that millimetre-sized aggregates with opposite charges stick and form centimetre-sized ones rather than bouncing off of one another. Collisions between dust grains can cause opposite charges even if the grains are identical and no external electric field is present (Yoshimatsu et al. 2017).

- Dust growth to centimetre sizes is as well possible outside of ice lines (Ros and Johansen 2013; Ros et al. 2019). As icy aggregates move radially inwards and cross an ice line, for instance owing to their radial drift (see Sect. 2.4), they sublimate. The forming vapour diffuses back outwards over the ice line and condensates on the aggregates outside.

2.4 Radial drift barrier

The drag exerted by the gas on the dust causes a radial dust drift towards the star, which poses a time constraint and thus constitutes another barrier for the growth from dust to planets (Whipple 1972; Adachi et al. 1976; Weidenschilling 1977a; Brauer et al. 2007). This is since the gas density and temperature decrease with increasing radial distance to the star, and the gas is thus supported against the stellar gravity both by the centrifugal force and by a pressure gradient. Therefore, its orbital speed is slightly less than Keplerian. The dust, on the other hand, is not pressure-supported. It would orbit with the Keplerian speed if it were not coupled to the gas via drag. Because of the drag, however, the dust loses angular momentum to the slower-rotating gas. This leads to the stellar gravity acting on the dust not being balanced by the centrifugal force, and the dust thus spiralling towards the star.

The speed of this radial drift of the dust can be derived as follows (Takeuchi and Lin 2002; Armitage 2010): The equations of motion of the dust in the radial and azimuthal dimension read

$$\frac{\partial v_{\mathrm{d},r}}{\partial t} = \frac{v_{\mathrm{d},\phi}^2}{r} - \frac{v_{\mathrm{K}}^2}{r} - \frac{v_{\mathrm{d},r} - v_{\mathrm{g},r}}{t_{\mathrm{d,stop}}} \text{ and} \tag{2.17}$$

$$\frac{\partial \left(r v_{\mathrm{d},\phi}\right)}{\partial t} = -\frac{r \left(v_{\mathrm{d},\phi} - v_{\mathrm{g},\phi}\right)}{t_{\mathrm{d,stop}}}, \tag{2.18}$$

where $\boldsymbol{v}$ is the velocity and t is the time. The subscripts d and g refer to dust and gas, while ϕ denotes the azimuth. The first term on the right-hand side of the former equation represents

the centrifugal force and the second term the stellar gravity, while the last term on the right-hand side of both equations describes the drag by the gas onto the dust.

The sub-Keplerian orbital velocity of the gas can be expressed as $v_{\mathrm{g},\phi} = v_{\mathrm{K}} - \Pi c_{\mathrm{s}}$. The dimensionless parameter Π, which is introduced by Bai and Stone (2010b), indicates the strength of the radial pressure gradient,

$$\Pi = -\frac{1}{2c_{\mathrm{s}}\rho_{\mathrm{g}}\Omega_{\mathrm{K}}}\frac{\partial P}{\partial r}. \tag{2.19}$$

In the mid-plane of the disk model described in Appendix A, it amounts to

$$\Pi(z=0) = 0.046\left(\frac{r}{1\,\mathrm{au}}\right)^{1/4}. \tag{2.20}$$

It follows that

$$v_{\mathrm{K}}^2 = v_{\mathrm{g},\phi}^2 + 2v_{\mathrm{g},\phi}\Pi c_{\mathrm{s}} + \Pi^2 c_{\mathrm{s}}^2. \tag{2.21}$$

Since the deviation of the orbital gas velocity from the Keplerian velocity is small, I neglect the last term on the right-hand side and approximate the second term as $2v_{\mathrm{K}}\Pi c_{\mathrm{s}}$. In addition, $v_{\mathrm{g},\phi}^2$, and analogously $v_{\mathrm{d},\phi}^2$, can be expanded in a Taylor series around v_{K}^2,

$$\begin{aligned} v_{\mathrm{g},\phi}^2 &= v_{\mathrm{K}}^2 + \frac{\partial v_{\mathrm{g},\phi}^2}{\partial v_{\mathrm{g},\phi}}\left(v_{\mathrm{g},\phi} - v_{\mathrm{K}}\right) + \mathcal{O}\left[\left(v_{\mathrm{g},\phi} - v_{\mathrm{K}}\right)^2\right] \\ &\approx v_{\mathrm{K}}^2 + 2v_{\mathrm{g},\phi}^2 - 2v_{\mathrm{g},\phi}v_{\mathrm{K}} \\ \Leftrightarrow v_{\mathrm{g},\phi}^2 &\approx 2v_{\mathrm{g},\phi}v_{\mathrm{K}} - v_{\mathrm{K}}^2. \end{aligned} \tag{2.22}$$

Substituting Eqs. 2.21 and 2.22 into Eq. 2.17 results in

$$\begin{aligned} \frac{\partial v_{\mathrm{d},r}}{\partial t} &= \frac{2v_{\mathrm{d},\phi}v_{\mathrm{K}} - v_{\mathrm{K}}^2}{r} - \frac{2v_{\mathrm{g},\phi}v_{\mathrm{K}} - v_{\mathrm{K}}^2 + 2v_{\mathrm{K}}\Pi c_{\mathrm{s}}}{r} - \frac{v_{\mathrm{d},r} - v_{\mathrm{g},r}}{t_{\mathrm{d,stop}}} \\ &= -\frac{2v_{\mathrm{K}}\Pi c_{\mathrm{s}}}{r} + \frac{2v_{\mathrm{K}}\left(v_{\mathrm{d},\phi} - v_{\mathrm{g},\phi}\right)}{r} - \frac{v_{\mathrm{d},r} - v_{\mathrm{g},r}}{t_{\mathrm{d,stop}}}. \end{aligned} \tag{2.23}$$

I assume that the radial dust drift is much faster than the gas drift, $v_{\mathrm{d},r} \gg v_{\mathrm{g},r}$, and that the drift speed of the dust is constant in time, $\partial v_{\mathrm{d},r}/\partial t = 0$.

If the dust has sufficiently settled towards the mid-plane, its Keplerian orbital velocity can be approximated as

$$v_{\mathrm{K}} = \sqrt{\frac{GM_{\mathrm{S}}r^2}{\left(r^2+z^2\right)^{3/2}}} \approx \sqrt{\frac{GM_{\mathrm{S}}}{r}}, \tag{2.24}$$

where G is the gravitational constant and M_{S} the stellar mass. Further assuming that the specific angular momentum of the dust remains close to Keplerian, $v_{\mathrm{d},\phi}r \approx v_{\mathrm{K}}r$, Eq. 2.18 yields

$$\frac{\partial\left(rv_{\mathrm{d},\phi}\right)}{\partial t} \approx \frac{\partial r}{\partial t}\frac{\partial\left(rv_K\right)}{\partial r} = v_{\mathrm{d},r}\left(v_{\mathrm{K}} + r\frac{\partial v_{\mathrm{K}}}{\partial r}\right) = v_{\mathrm{d},r}\left(v_{\mathrm{K}} - \frac{1}{2}v_{\mathrm{K}}\right) = \frac{1}{2}v_{\mathrm{d},r}v_{\mathrm{K}} \text{ and} \tag{2.25}$$

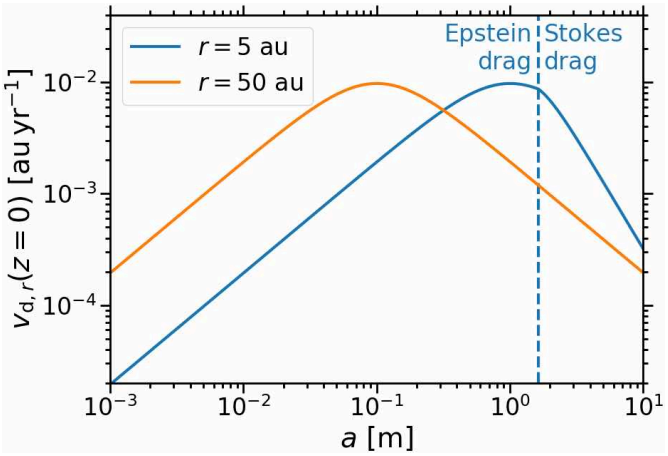

Figure 2.3: Radial drift velocity $v_{\mathrm{d},r}$ in the disk mid-plane as a function of the dust size a. Solid lines of different colours depict the velocity at different radial distances r from the star. The dashed line marks the transition from the Epstein to the Stokes drag regime. The maximum drift speed, about 0.01 au yr^{-1}, is reached for dust sizes of decimetres to metres.

$$v_{\mathrm{d},\phi} - v_{\mathrm{g},\phi} = -\frac{1}{2}\frac{t_{\mathrm{d,stop}} v_{\mathrm{d},r} v_{\mathrm{K}}}{r}. \tag{2.26}$$

By substituting this equation into Eq. 2.23, I obtain

$$\begin{aligned} 0 &= -\frac{2v_{\mathrm{K}}\Pi c_{\mathrm{s}}}{r} + \frac{2v_{\mathrm{K}}}{r}\left(-\frac{1}{2}\frac{t_{\mathrm{d,stop}} v_{\mathrm{d},r} v_{\mathrm{K}}}{r}\right) - \frac{v_{\mathrm{d},r}}{t_{\mathrm{d,stop}}} \\ &= -\frac{2v_{\mathrm{K}}\Pi c_{\mathrm{s}}}{r} - v_{\mathrm{d},r}\left(\frac{t_{\mathrm{d,stop}} v_{\mathrm{K}}^2}{r^2} + \frac{1}{t_{\mathrm{d,stop}}}\right) \end{aligned} \tag{2.27}$$

$$\Leftrightarrow v_{\mathrm{d},r} = \frac{2\Pi c_{\mathrm{s}}}{t_{\mathrm{d,stop}}\Omega_{\mathrm{K}} + (t_{\mathrm{d,stop}}\Omega_{\mathrm{K}})^{-1}} = \frac{2\Pi c_{\mathrm{s}}}{\mathrm{St} + \mathrm{St}^{-1}}. \tag{2.28}$$

Dust aggregates with a Stokes number of one, i.e. a stopping time that is equal to the dynamical time scale, drift with the speed $v_{\mathrm{d},r} = \Pi c_{\mathrm{s}}$. This speed is equal to the difference between the Keplerian velocity and the orbital velocity of the gas. The drift speed is less by a factor of St if the Stokes number of the dust $\mathrm{St} \ll 1$, and by a factor of $1/\mathrm{St}$ if $\mathrm{St} \gg 1$. In the former case, dust and the gas are well coupled and the orbital speed of the dust is close to the sub-Keplerian speed of the gas. In the latter case, on the other hand, gas and dust are effectively decoupled, and the dust orbits with the Keplerian speed.

I show the drift velocity as a function of the dust size in Fig. 2.3. It can be seen that, depending on their radial location, decimetre- to metre-sized aggregates can drift 1 au in as little as a hundred years, while millimetre-sized aggregates take ten thousand years or more to drift the same distance.

To estimate a dust size at which the radial drift of the dust constitutes a barrier[7] for its growth by coagulation, I compare the radial drift time scale $\tau_{\mathrm{d,drift}} = r/v_{\mathrm{d},r}$, i.e. the time scale

[7] Because the radial drift is fastest for dust aggregates with sizes of about metres, the radial drift barrier is also referred to as metre-size barrier.

over which a dust aggregate drifts into the star, to the growth time scale $t_{\mathrm{d,grow}} = a/\dot{a}$, where the dot symbolises the time derivative (e.g., Klahr and Bodenheimer 2006; Birnstiel et al. 2012, 2016). If the former time scale is less than the latter, drift is faster than growth.

A simple estimate of the growth rate $\dot{a}$ can be obtained by considering monodisperse growth and perfect sticking of colliding dust aggregates (Kornet et al. 2001). That is, each collision leads to a doubling in aggregate mass. I further assume spherical aggregates with a constant solid density. Under these assumptions,

$$\dot{a} = \frac{\partial a}{\partial m_{\mathrm{d}}} \frac{\partial m_{\mathrm{d}}}{\partial t} = \frac{1}{4\pi a^2 \rho_{\mathrm{s}}} \frac{m_{\mathrm{d}}}{\tau_{\mathrm{d,coll}}}. \tag{2.29}$$

The collision time scale, that is to say the average time that passes between two collisions, amounts to $\tau_{\mathrm{d,coll}} = 1/(n_{\mathrm{d}} \sigma_{\mathrm{d,coll}} \Delta v_{\mathrm{d,Bm}})$. Here, only relative velocities between colliding aggregates that are induced by Brownian motion are taken into account because I – in contrast to previous authors like Birnstiel et al. (2012, 2016) – neglect sticking as a possible outcome of collisions that are induced by gas turbulence (see Sect. 2.3). The cross section for the collision of two aggregates is equal to $\sigma_{\mathrm{d,coll}} = 4\pi a^2$.

The radial drift time scale can be approximated as $\tau_{\mathrm{d,drift}} \approx r/(2\Pi c_{\mathrm{s}} \mathrm{St})$ (see Eq. 2.28) if aggregates do not grow to a Stokes number of one and thus do not reach the maximum drift speed. By equating this time scale with the growth time scale $\tau_{\mathrm{d,grow}} = a\rho_{\mathrm{s}}/(\rho_{\mathrm{d}} \Delta v_{\mathrm{d,Bm}})$ and assuming drag in the Epstein regime (see Eq. 2.2)[6], I derive the threshold dust size for which further collisional growth is inhibited by the radial drift,

$$a_{\mathrm{drift}} = \left(\frac{3 k_{\mathrm{B}} T r^2 \epsilon^2 \rho_{\mathrm{d}}^2 \rho_{\mathrm{g}}^2}{\pi \mu \rho_{\mathrm{s}}^5 \Pi^2 \Omega_{\mathrm{K}}^2} \right)^{1/7} \tag{2.30}$$

(see also Eq. 2.1). In the mid-plane of the disk model I present in Appendix A, this corresponds to

$$a_{\mathrm{drift}}(z=0) = 883 \left(\frac{r}{1\,\mathrm{au}} \right)^{-5/7} \left(\frac{\rho_{\mathrm{d}}}{\rho_{\mathrm{g}}} \right)^{2/7} \mu\mathrm{m}. \tag{2.31}$$

Using the inverted Eq. 2.13,

$$\mathrm{St}(z=0) = 1.99 \times 10^{-3} \left(\frac{a}{1\,\mathrm{cm}} \right) \left(\frac{r}{1\,\mathrm{au}} \right), \tag{2.32}$$

this threshold size can be converted to a threshold Stokes number of

$$\mathrm{St}_{\mathrm{drift}}(z=0) = 1.76 \times 10^{-4} \left(\frac{r}{1\,\mathrm{au}} \right)^{2/7} \left(\frac{\rho_{\mathrm{d}}}{\rho_{\mathrm{g}}} \right)^{2/7}. \tag{2.33}$$

Figure 2.4 depicts the estimated maximum sizes and Stokes numbers to which dust aggregates can grow by coagulation before they bounce (Eqs. 2.12 and 2.14) or fragment (Eqs. 2.15 and 2.16) if they collide or before their radial drift is faster than their growth (Eqs. 2.31 and 2.33). The figure shows that dust sizes are limited to millimetres at small radial distances to the star owing to bouncing, and to tens or hundreds of microns at large radii because of the drift. Nonetheless, as discussed in more detail in Sect. 2.3, the depicted estimates are based on the simplifying assumption of monodisperse growth of perfectly compact spherical aggregates.

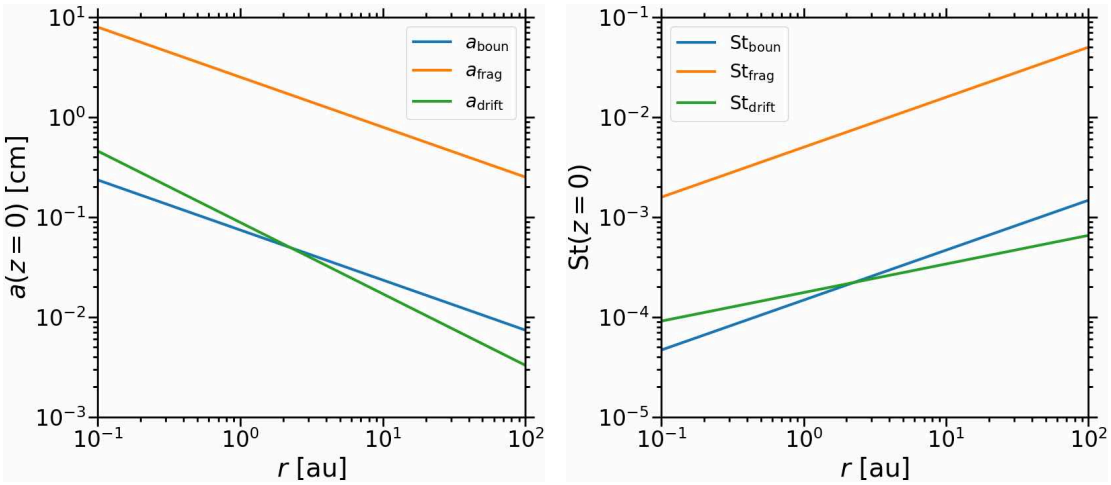

Figure 2.4: Dust size a and Stokes number St in the mid-plane as a function of the radial distance to the star r. The blue and orange lines show the threshold size and Stokes number for bouncing (Eqs. 2.12 and 2.14) and for fragmentation (Eqs. 2.15 and 2.16), respectively, under mutual dust collisions. The threshold values at which the radial drift of the dust is equally fast as its collisional growth (Eqs. 2.31 and 2.33) are marked with green lines. Here, I assume a Mach number of 0.01 and a dust-to-gas density ratio of one, which are typical values in the mid-plane of protoplanetary disks (see Chapters 3 and 4). It is evident that dust is prevented by bouncing from growing larger than millimetres at small radii, and by the drift from growing larger than tens or hundreds of microns at large radii.

3
Streaming instability

As discussed in the previous chapter, dust aggregates can grow to sizes between hundreds of microns and centimetres via coagulation, i.e. aggregates sticking together when they collide. Collisional growth beyond these sizes is prevented by bouncing or fragmentation under mutual collisions (see Sect. 2.3) as well as by the radial drift of the dust towards the star that is caused by the drag of the gas onto the dust (see Sect. 2.4). A number of mechanisms have been proposed to overcome theses barriers and induce the formation of planetesimals, the next stage in the growth from dust to planets (Goldreich and Ward 1973). Planetesimals are typically tens or hundreds of kilometres in size, large enough to be bound by self-gravity and to be effectively decoupled from the gas (e.g., Johansen et al. 2014). That is, they are not affected by either bouncing and fragmentation or by radial drift. While I introduce other mechanisms for planetesimal formation in Sect. 3.5, the focus of this thesis in general and this chapter in particular lies on the streaming instability as arguably the leading candidate mechanism.

3.1 Linear instability

The streaming instability was discovered analytically by Youdin and Goodman (2005) as a linear instability. The numerical studies conducted by Youdin and Johansen (2007), Johansen and Youdin (2007), and Bai and Stone (2010a) confirmed the presence of the linear instability and showed that it evolves into a non-linear regime. The instability operates when rotating gas and dust are mutually coupled via drag and there is a radial gradient in the gas pressure. It taps into the free energy provided by this pressure gradient. In general, density and temperature decrease with increasing radial distance to the star in protoplanetary disks, and the instability is thus active in all disk regions in which dust is present. In the following, I sketch the derivation of the linear instability as presented by Youdin and Goodman (2005) and Jacquet et al. (2011).

Linear instabilities arise from linear perturbations to an equilibrium state, that is to say to solutions of the equation of motions that are constant in time. Youdin and Goodman (2005) and Jacquet et al. (2011) obtain the equations of motion of the dust by approximating it as a pressureless fluid. This approximation is valid if the dust adopts the fluid behaviour of the

gas because gas and dust are strongly coupled via drag, i.e. the dust stopping time is shorter than the dynamical time scale $1/\Omega_\mathrm{K}$ and the Stokes number of the dust thus smaller than one (Youdin and Goodman 2005; Youdin and Johansen 2007; Jacquet et al. 2011). If gas and dust are only loosely coupled, though, the trajectories of adjacent dust aggregates can not be assumed to be similar as the ones of gas molecules, but can even cross. In addition, the description of the dust as a fluid with zero pressure allows for unphysical discontinuities in the dust density. Artificial dust viscosity can be employed to prevent these discontinuities in numerical simulations, but this in turn alters the dust dynamics, including suppressing dust concentrations.

The equations of motion of gas and dust as a fluid are given by

$$\frac{\partial \rho_\mathrm{g}}{\partial t} + \nabla \cdot (\rho_\mathrm{g} \boldsymbol{v}_\mathrm{g}) = 0, \tag{3.1}$$

$$\frac{\partial \rho_\mathrm{d}}{\partial t} + \nabla \cdot (\rho_\mathrm{d} \boldsymbol{v}_\mathrm{d}) = 0, \tag{3.2}$$

$$\frac{\partial \boldsymbol{v}_\mathrm{g}}{\partial t} + (\boldsymbol{v}_\mathrm{g} \cdot \nabla)\, \boldsymbol{v}_\mathrm{g} = -\Omega_\mathrm{K}^2 r \hat{r} - \frac{1}{\rho_\mathrm{g}} \nabla P + \frac{\rho_\mathrm{d}}{\rho_\mathrm{g}} \frac{\boldsymbol{v}_\mathrm{d} - \boldsymbol{v}_\mathrm{g}}{t_\mathrm{d,stop}}, \text{ and} \tag{3.3}$$

$$\frac{\partial \boldsymbol{v}_\mathrm{d}}{\partial t} + (\boldsymbol{v}_\mathrm{d} \cdot \nabla)\, \boldsymbol{v}_\mathrm{d} = -\Omega_\mathrm{K}^2 r \hat{r} - \frac{\boldsymbol{v}_\mathrm{d} - \boldsymbol{v}_\mathrm{g}}{t_\mathrm{d,stop}}, \tag{3.4}$$

where $\hat{r}$ is the unit vector in the radial direction and P the gas pressure. The first term on the right-hand side of the momentum equations of gas (Eq. 3.3) and dust (Eq. 3.4) reflects the radial stellar gravity, while the last term gives the acceleration caused by the mutual drag between gas and dust (see Eq. 2.2). For simplicity, both vertical stellar gravity and self-gravity of gas and dust are neglected.

To close the system of equations, both Youdin and Goodman (2005) and Jacquet et al. (2011) assume that the gas is incompressible. That is, the density of every gas parcel is considered to remain constant in time. This assumption is justified if turbulent velocities in the gas are slower than the sound speed, i.e. the turbulence is subsonic. Under this condition, thermal motions transport information about changes in the gas density faster than the changes are induced by turbulent motions. The turbulence driven by the streaming instability is indeed subsonic (see Sect. 4.5.1). If it is incompressible, that is to say $\partial \rho_\mathrm{g}/\partial t = \nabla \rho_\mathrm{g} = 0$, the continuity equation of the gas (Eq. 3.1) reduces to

$$\nabla \cdot \boldsymbol{v}_\mathrm{g} = 0. \tag{3.5}$$

Nakagawa et al. (1986) obtain solutions to the momentum equations of gas and dust (Eqs. 3.3 and 3.4) that are steady in time. The derivation of these equilibrium solutions involves the assumption of axisymmetry, i.e. independence of the azimuth. If the vertical stellar gravity is neglected, the solutions can be expressed as

$$v_{\mathrm{g},r} = \frac{2\mathrm{St} f_\mathrm{g} f_\mathrm{d}}{1 + \mathrm{St}^2 f_\mathrm{g}^2} \Pi c_\mathrm{s}, \tag{3.6}$$

$$v_{\mathrm{d},r} = -\frac{2\mathrm{St}f_\mathrm{g}^2}{1+\mathrm{St}^2 f_\mathrm{g}^2}\Pi c_\mathrm{s}, \tag{3.7}$$

$$v_{\mathrm{g},\phi} = v_\mathrm{K} + \left(\frac{f_\mathrm{d}}{1+\mathrm{St}^2 f_\mathrm{g}^2} - 1\right)\Pi c_\mathrm{s}, \tag{3.8}$$

$$v_{\mathrm{d},\phi} = v_\mathrm{K} - \frac{f_\mathrm{g}}{1+\mathrm{St}^2 f_\mathrm{g}^2}\Pi c_\mathrm{s}, \text{ and} \tag{3.9}$$

$$v_{\mathrm{g},z} = v_{\mathrm{d},z} = 0, \tag{3.10}$$

where $f_\mathrm{g} = \rho_\mathrm{g}/\rho_\mathrm{tot}$ and $f_\mathrm{d} = \rho_\mathrm{d}/\rho_\mathrm{tot}$ are the ratios of gas and dust density, respectively, to the total density $\rho_\mathrm{tot} = \rho_\mathrm{g} + \rho_\mathrm{d}$. I refer to Sect. 2.4, in which I explain that a gas pressure gradient directed radially away from the star causes the orbital velocities of gas and dust to be slightly less than the Keplerian velocity and the dust to drift radially towards the star. The dimensionless parameter Π, as introduced by (Bai and Stone 2010b), gives the strength of this radial pressure gradient. If they were not coupled via their mutual drag, the dust and the gas would orbit with the Keplerian velocity v_K and the sub-Keplerian velocity $v_\mathrm{K} - \Pi c_\mathrm{s}$, respectively.

It is interesting to consider the equilibrium values of the gas and dust velocities in the limits of very low and very high ratios of dust to gas density, corresponding to $f_\mathrm{g} \to 1$ ($f_\mathrm{d} \to 0$) and $f_\mathrm{d} \to 1$ ($f_\mathrm{g} \to 0$), respectively. The former case reflects that the dust-to-gas density ratio in the interstellar medium and consequently in protoplanetary disks is generally much less than one. In this case, the gas does not move radially, while Eq. 3.7 is equivalent to Eq. 2.28 giving the radial drift velocity of the dust. The radial dust drift is discussed in detail in Sect. 2.4. Both gas and dust orbit with a velocity that is close to the sub-Keplerian one of the gas because the drag exerted by the gas on the dust is much stronger than the drag of the dust onto the gas.

With increasing dust-to-gas density ratio, however, the orbital velocity of gas and dust increases towards the Keplerian velocity of the dust. Additionally, the inwards radial drift of the dust slows down, while the gas begins to drift radially outwards. The latter is since the centrifugal force acting on the gas and its pressure gradient, which are both directed radially outwards, are no longer balanced by the inwards-directed stellar gravity. In the layer around the disk mid-plane to which the dust sediments, the dust density approaches the gas density. If they are equal, gas and dust drift radially with the same speed. Locally in dust overdensities, for instance in those caused by the non-linear streaming instability (see Sect. 3.2), the dust density can even exceed the gas density by orders of magnitude. In the limit of very large dust-to-gas density ratios, the radial velocities of both gas and dust vanish. This is because the drag exerted by the dust on the gas dominates over the effect of the gas pressure gradient.

The dependence of the equilibrium gas and dust velocities on the Stokes number of the dust also merits a brief discussion. Neither the dust nor the gas drift radially if the Stokes number is either very small or very large. In the former case, the gas and dust are tightly coupled, and either the dust is dragged along by the gas or vice versa, depending on the dust-to-gas density ratio. In the latter case, on the other hand, gas and dust are effectively decoupled. Thus, the gas orbits with the sub-Keplerian velocity, while the orbital velocity of the dust is Keplerian.

To examine whether they lead to instability, Youdin and Goodman (2005) and Jacquet et al. (2011) analyse perturbations to the equilibrium state – the velocities of gas and dust in this state are given by Eqs. 3.6 to 3.10 – whose size scales are much less than the distance to the star. Therefore, they adopt the shearing box approximation (Goldreich and Lynden-Bell 1965). In this approximation, a disk region is considered that is small enough compared to the size of the disk for the disk curvature to be negligible.

Locations can therefore be indicated using a Cartesian coordinate system whose origin is located at the centre r_0 of the disk region (Goldreich and Lynden-Bell 1965; Youdin and Goodman 2005). The cylindrical radial coordinate r can be converted to the Cartesian radial coordinate x as

$$x = r - r_0 \tag{3.11}$$

and the cylindrical azimuthal coordinate ϕ to the Cartesian azimuthal coordinate y as

$$y = r_0 \sin(\phi - \Omega(r_0)t) \approx r_0(\phi - \Omega(r_0)t), \tag{3.12}$$

where Ω is the orbital frequency. The vertical coordinate z remains the same. Similar to locations, velocities are linearised with respect to the orbital velocity at the centre of the region. In particular, expanding the Keplerian orbital frequency $\Omega_\mathrm{K} \propto x^{-3/2}$ (see also Eq. 2.24) in a Taylor series around $x = 0$,

$$\begin{aligned} \Omega_\mathrm{K}(x) &= \Omega_\mathrm{K}(x=0) + \left.\frac{\partial \Omega_\mathrm{K}(x)}{\partial x}\right|_{x=0} x + \mathcal{O}(x^2) \\ &\approx \Omega_\mathrm{K}(x=0) - \frac{3}{2} \left.\frac{\Omega_\mathrm{K}(x)}{x}\right|_{x=0} x, \end{aligned} \tag{3.13}$$

yields the Keplerian orbital velocity

$$v_\mathrm{K}(x) = v_\mathrm{K}(x=0) - \frac{3}{2}\Omega_\mathrm{K}(x=0)x. \tag{3.14}$$

The equilibrium gas and dust densities are assumed to be homogeneous within the region, and the equilibrium gas pressure to decrease linearly with increasing radial coordinate (Youdin and Goodman 2005; Jacquet et al. 2011). That is, the pressure gradient is constant. Therefore, the equilibrium values of the radial velocities of gas (Eq. 3.6) and dust (Eq. 3.7) are also constant, while the azimuthal gas (Eq. 3.8) and dust velocities (Eq. 3.9) vary only with the Keplerian velocity.

The perturbations to the equilibrium state are considered to possess the form of axisymmetric waves (Youdin and Goodman 2005; Jacquet et al. 2011). That is, they are proportional to $\exp[i(k_x x + k_z z - \omega t)]$, where k_x and k_z are the wave numbers in the radial and vertical dimension and ω is the wave frequency. Each of the gas and dust densities and velocities as well as the gas pressure are expressed as the sum of the equilibrium value and a perturbation, with the perturbation being very small compared to the equilibrium value. Substituting these expressions into the equations of motion (Eqs. 3.1 to 3.5), linearising the result with respect to the perturbations, and solving for the wave frequency yields a polynomial dispersion relation $\omega(k_x, k_z)$. Every root of this polynomial represents a mode, a set of coherent oscillations of the densities and velocities of gas and dust as well as of the gas pressure.

The oscillations of a mode grow and thus cause instability if real values of radial and vertical wave number exist for which the imaginary part of the wave frequency is positive[1]. If the imaginary part is negative, the oscillations of the mode are damped. As gas and dust are described by eight equations of motion, three each for the three velocity components and one each for the density, the dispersion relation is of degree eight. The assumption of gas incompressibility reduces its degree to six. Of these six modes, three are strongly damped, while the other three are either weakly damped or growing (Youdin and Goodman 2005; Jacquet et al. 2011; Jaupart and Laibe 2020).

The latter three modes can be isolated from the former three by means of the so-called terminal velocity approximation (Youdin and Goodman 2005; Jacquet et al. 2011). This approximation is based on the assumption that forces resulting from gas pressure gradients are always balanced by mutual drag forces between gas and dust – the terminal relative velocity of gas and dust is attained instantaneously. That is,

$$\frac{1}{\rho_\mathrm{g}}\nabla P = \frac{\rho_\mathrm{d}}{\rho_\mathrm{g}}\frac{\boldsymbol{v}_\mathrm{d}-\boldsymbol{v}_\mathrm{g}}{t_\mathrm{d,stop}} - \left(-\frac{\boldsymbol{v}_\mathrm{d}-\boldsymbol{v}_\mathrm{g}}{t_\mathrm{d,stop}}\right) \tag{3.15}$$

(see Eqs. 3.3 and 3.4). The left-hand side of this equation gives the acceleration of the gas induced by pressure gradients, and the first and second term on the right-hand side the acceleration of gas and dust, respectively, owing to drag. The relative velocity of dust and gas can thus be expressed as

$$\boldsymbol{v}_\mathrm{d} - \boldsymbol{v}_\mathrm{g} = \frac{t_\mathrm{d,stop}}{\rho_\mathrm{tot}}\nabla P. \tag{3.16}$$

The terminal velocity approximation is valid under two conditions (Jacquet et al. 2011): Similar to the approximation of dust as a pressureless fluid, it requires that $f_\mathrm{g}\mathrm{St}$ is much smaller than one, that is to say that gas and dust are tightly coupled. In addition, it is necessary that

$$\frac{f_\mathrm{g}k_x t_\mathrm{d,stop}^2}{\rho_\mathrm{tot}}\frac{\partial P}{\partial r} \ll 1. \tag{3.17}$$

By applying the terminal velocity approximation, the degree of the dispersion relation can be reduced from six to three. This cubic relation is given by

$$\omega^3 + t_\mathrm{d,stop}\left(i\Omega_\mathrm{K}^2\frac{\rho_\mathrm{d}}{\rho_\mathrm{tot}} + \frac{\rho_\mathrm{g}}{\rho_\mathrm{tot}^2}\frac{\partial P}{\partial r}k_x\right)\omega^2 - \left(\Omega_\mathrm{K}\frac{k_z}{k}\right)^2\omega + t_\mathrm{d,stop}\Omega_\mathrm{K}^2\frac{\rho_\mathrm{d}-\rho_\mathrm{g}}{\rho_\mathrm{tot}^2}\frac{\partial P}{\partial r}\frac{k_x k_z^2}{k^2} = 0, \tag{3.18}$$

where i is the imaginary unit and the wave number $k = \sqrt{k_x^2 + k_z^2}$ (Jacquet et al. 2011). I note that Youdin and Goodman (2005) obtain a slightly different relation in which the first addend of the term that is quadratic in the wave frequency is greater by a factor of k_x^2/k^2. Jacquet et al. (2011) attribute this discrepancy to a typographical error in the relation inferred by Youdin and Goodman (2005).

[1] Instabilities like the streaming instability that arise from growing oscillations, that is to say from modes with non-zero real part of the wave frequency, are often referred to as "overstabilities". This is to distinguish from "instabilities" which are caused not by oscillations, but by modes with a purely imaginary wave frequency.

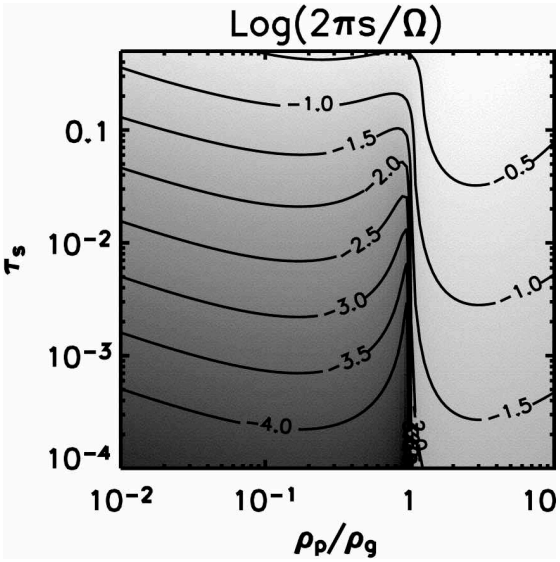

Figure 3.1: Figure adopted from Youdin and Goodman (2005, their Fig. 1, reproduced with permission ©AAS). Logarithm of the growth rate s of the secular mode of the linear streaming instability as a function of the Stokes number of the dust τ_s and the ratio of dust ρ_d to gas density ρ_g. The growth rate is given relative to the Keplerian orbital frequency Ω divided by 2π. It is depicted in grey tones and as contour lines. The growth rate is higher if the Stokes number is closer to one. In addition, growth is fastest if the dust-to-gas density ratio is nearly equal to one, but suppressed if the densities of dust and gas are too similar.

Two of the three modes defined by this reduced dispersion relation are damped epicyclic oscillations. These can grow if the full dispersion relation is considered (Youdin and Goodman 2005; Jaupart and Laibe 2020). Nevertheless, the growth rate of the third secular mode, that is to say the imaginary part of its wave frequency, is always larger than the ones of the epicyclic oscillations (Youdin and Goodman 2005). To leading order in the stopping time of the dust, the real part of the wave frequency of this secular mode is equal to

$$\mathrm{Re}(\omega) = -t_{\mathrm{d,stop}} \frac{\rho_\mathrm{d} - \rho_\mathrm{g}}{\rho_\mathrm{tot}^2} \frac{\partial P}{\partial r} k_x \tag{3.19}$$

and the imaginary part to

$$\mathrm{Im}(\omega) = t_{\mathrm{d,stop}}^3 \frac{\rho_\mathrm{d} \left(\rho_\mathrm{d} - \rho_\mathrm{g}\right)^2}{\rho_\mathrm{tot}^5} \left(\frac{\partial P}{\partial r} \frac{k k_x}{k_z} \right)^2 \tag{3.20}$$

(Jacquet et al. 2011). As with the dispersion relation, Youdin and Goodman (2005) find a growth rate that is larger by a factor of k_x^2/k^2.

Figure 3.1 depicts the growth rate of the secular mode as computed from the dispersion relation of degree six. From the figure and Eq. 3.20, it is evident that the growth rate increases with the velocity of the radial dust drift (see Eqs. 2.28 and 3.7), i.e. with the steepness of the gas pressure gradient as well as the Stokes number of the dust or equivalently its stopping time. Equation 3.20 indicates that the growth rate nominally depends on the cube of the stopping time.

Nonetheless, Youdin and Goodman (2005) find that growth is fastest when $k_z \propto t_{\mathrm{d,stop}} k_x^2$ and the growth rate therefore proportional to the stopping time (see also Fig. 3.1). When Stokes numbers exceeding one are considered, the growth rate decreases with increasing Stokes number. However, neither the fluid approximation of the dust nor the terminal velocity approximation are applicable for these Stokes numbers.

As can be seen from the figure, the maximum growth rate with respect to the ratio of dust to gas density is reached when the ratio amounts to a few. The growth rate declines as the dust-to-gas density ratio approaches values much smaller or much larger than unity. This is because the effect of the drag by the gas onto the dust is negligible in the former case and by the dust onto the gas in the latter case. Interestingly, the growth rate is also reduced if the dust-to-gas density ratio is too close to one. If the densities of gas and dust are equal, the growth rate given by Eq. 3.20 vanishes. While growth is suppressed, the growth rate is non-zero when the dispersion relation of degree six is considered (Youdin and Goodman 2005).

The cubic dispersion relation shows that only modes with oscillations both in the radial and in the vertical dimension are unstable. If $k_z = 0$, Eq. 3.18 reduces to a linear dispersion relation,

$$\omega = t_{\mathrm{d,stop}} \frac{\rho_{\mathrm{g}}}{\rho_{\mathrm{tot}}^2} \frac{\partial P}{\partial r} k_x - i t_{\mathrm{d,stop}} \Omega_{\mathrm{K}}^2 \frac{\rho_{\mathrm{d}}}{\rho_{\mathrm{tot}}}. \tag{3.21}$$

That is, only one mode with purely radial oscillations exists, with the oscillations being damped since the imaginary part of the wave frequency is negative. I note that Raettig et al. (2015), Schreiber and Klahr (2018), and Klahr and Schreiber (2020) report that they find the (non-linear) streaming instability, or at least a very similar instability, to operate in simulations of the radial-azimuthal plane. However, this is in contrast to the linear instability as originally discovered by Youdin and Goodman (2005) and discussed in this section growing only when the vertical dimension is taken into account.

In the above derivation of the linear instability, dust is treated as a single species with a uniform Stokes number. Krapp et al. (2019) and Zhu and Yang (submitted) find that the growth rate can significantly decline if multiple dust species with different Stokes numbers are taken into account instead. If and how strongly the growth rate decreases with the number of species depends on the minimum and maximum Stokes numbers and on the ratio of the dust to the gas density (Krapp et al. 2019; Zhu and Yang submitted) as well as on the slope of the power-law distribution of Stokes numbers (Zhu and Yang submitted). While the dependence on the minimum Stokes number and the steepness of the Stokes number distribution is comparatively weak, the growth rate decreases by several orders of magnitude – and does not converge for up to 2048 (Krapp et al. 2019) or 4096 species (Zhu and Yang submitted) – if both the maximum Stokes number and the dust-to-gas density ratio are less than unity (Krapp et al. 2019; Zhu and Yang submitted). I note that the numerical studies of the non-linear instability presented by Bai and Stone (2010b) and Schaffer et al. (2018) do not indicate such a decline in the growth if multiple dust species are simulated. This might be because the different species in these simulations are not well-mixed. Rather, dust with a smaller Stokes number is lifted to greater heights by the turbulence driven by the instability than dust with a larger Stokes number (see Sect. 4.5.1).

Physical interpretations of the linear instability have been devised by Jacquet et al. (2011), Lin and Youdin (2017), and Squire and Hopkins (2018a,b). Lin and Youdin (2017) show that the streaming instability, and in fact any instability which is induced by the mutual drag between gas and dust, arises because changes in gas pressure lag behind changes in dust density when the stopping time of the dust is finite. If they are tightly coupled, gas and dust can be approximated as a single fluid. The density of this fluid is equal to the total density of gas and dust, while only the gas contributes to the pressure of the fluid. A perturbation to its equilibrium pressure leads to the fluid expanding (contracting) to return to the equilibrium state. However, the fluid overshoots this state because the dust density still increases (decreases) when the equilibrium pressure is reached if the dust stopping time is non-zero. To compensate for this, the fluid contracts (expands), but overshoots again. These oscillations around the equilibrium state grow and instability ensues.

Squire and Hopkins (2018a,b) classify the streaming instability as a resonant drag instability (see also Squire and Hopkins 2020). Resonant drag instabilities occur when gas and dust are coupled via their mutual drag and a systematic motion of the dust is in resonance with a wave in the gas, for example epicyclic or buoyant oscillations (see also Sects. 4.4.1 and 4.4.2). To illustrate this, I employ a toy model that was first used by Jacquet et al. (2011) to elucidate the streaming instability only and later applied by Squire and Hopkins (2018b) to resonant drag instabilities in general. I consider an oscillation in the gas which entails local maxima in the gas pressure. Similar to the dust radially drifting towards the star, i.e. towards the global gas pressure maximum, the dust moves towards local pressure maxima (see Sect. 3.5). The drag by the dust onto the gas leads to the gas following this motion. This results in an enhancement of the gas pressure maxima and the amplitude of the wave, and thus instability. I note that this toy model is only applicable in the terminal velocity approximation, that is when the drag between gas and dust adjusts instantaneously to gradients in the gas pressure. In addition, neither rotation nor the global radial pressure gradient are taken into account, though these are necessary for the streaming instability to operate.

According to the interpretation by Squire and Hopkins (2018a,b), the streaming instability is actually two different instabilities: One of them occurs for dust-to-gas density ratios less than unity. This instability is a resonant drag instability which results from the radial drift of the dust being in resonance with epicyclic oscillations of the gas in the radial-vertical plane. The other instability, which is active if the dust density is greater than the gas density, is not a resonant drag instability. This distinction is reflected in the linear growth rate of the streaming instability being substantially reduced if dust and gas density are too similar.

3.2 Non-linear instability, dust concentration, and planetesimal formation

The linear streaming instability arises from growing oscillations in the gas and dust velocities and densities as well as the gas pressure, with the oscillations in the dust density entailing dust overdensities. However, the amplitude of these oscillations is not relevant for and thus not constrained by the analysis of the linear instability. Simulations by, for example, Johansen et al. (2009, 2012, 2015), Bai and Stone (2010b,c), and Yang and Johansen (2014) show that, after it has transitioned from its linear to its non-linear regime, the instability induces dust overdensities

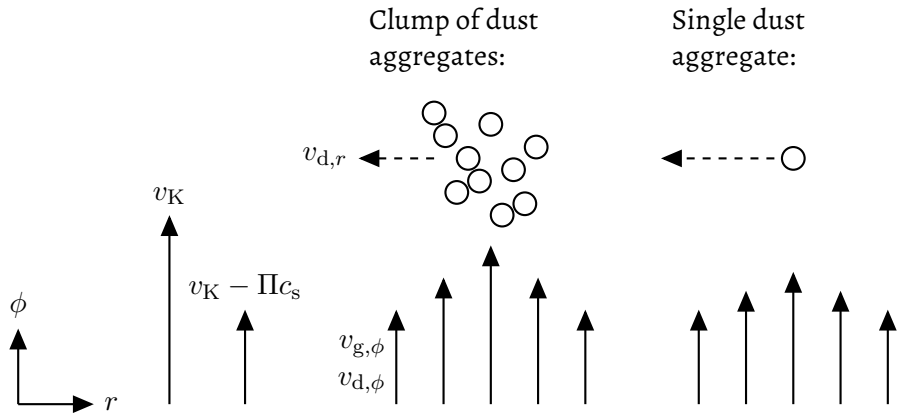

Figure 3.2: Toy model of the non-linear streaming instability. The illustration shows the radial-azimuthal plane. Solid arrows depict the orbital velocities of gas $v_{\mathrm{g},\phi}$ and dust $v_{\mathrm{d},\phi}$ that are coupled via their mutual drag, while dashed arrows represent the radial dust velocity $v_{\mathrm{d},r}$. Where no dust aggregates are present, the gas orbits with the sub-Keplerian velocity $v_{\mathrm{K}} - \Pi c_{\mathrm{s}}$, with Π expressing the strength of the radial pressure gradient in the gas (see Sect. 2.4). On the other hand, the orbital speed of the aggregates in isolation would be equal to the Keplerian speed v_{K}. Owing to their mutual drag, the orbital velocity of the coupled gas and dust lies in between. In the vicinity of a clump of dust aggregates (left) it is closer to the Keplerian velocity than near a single aggregate (right) because the local ratio of dust to gas density is higher (see Eqs. 3.8 and 3.9). Therefore, the speed of the radial drift of the clump is less than that of the single aggregate (see Eq. 3.7). The clump can thus accrete single aggregates that are moving slower azimuthally but faster radially. A feedback loop ensues: The accretion of aggregates causes the clump to drift more slowly in the radial direction and to orbit more rapidly, which in turn leads to it accreting even more aggregates.

that exceed the gas density by up to four orders of magnitude. This is sufficient for the dust to collapse under its self-gravity, leading to the formation of planetesimals. The simulations presented by these authors include the vertical stellar gravity, which is neglected in the analysis of the linear instability. The gravity leads to the dust settling towards the disk mid-plane and and forming a dense layer around this plane.

How dust is concentrated by the non-linear instability can be elucidated with the aid of the toy model illustrated in Fig. 3.2 (Johansen and Youdin 2007). I assume that gas and dust are well-coupled via drag and begin by considering a single dust aggregate (right). The gas away from this aggregate orbits with the sub-Keplerian velocity $v_{\mathrm{K}} - \Pi c_{\mathrm{s}}$, where Π indicates the steepness of the radial gradient in the gas pressure (see Sect. 2.4). The orbital velocity of the aggregate would be Keplerian if it were isolated, but is reduced by the drag of the slower-orbiting gas onto the aggregate. Nevertheless, the aggregate also exerts a drag on the gas. Therefore, the orbital velocity of the coupled gas and aggregate is marginally greater than the sub-Keplerian velocity of the gas in isolation.

Compared to the one exerted by a single aggregate, the drag of a clump of dust aggregates onto the gas is stronger (left). The orbital speed of the coupled gas and clump is therefore closer to Keplerian than that of gas and single aggregate. Consequently, the radial drift resulting from the stellar gravity not being balanced by the centrifugal force when the dust orbits with a sub-Keplerian speed is more rapid in the case of a single aggregate than in that of the clump. This follows also from Eqs. 3.7 to 3.9: Comparing the clump with a single aggregate cor-

responds to considering a higher ratio of the dust density to the total density of gas and dust. For higher f_d and lower f_g, the radial velocity of the dust $v_{\mathrm{d},r}$ is smaller, while the azimuthal velocities of gas $v_{\mathrm{g},\phi}$ and dust $v_{\mathrm{d},\phi}$ approach the Keplerian velocity v_K.

Thus, a large clump of aggregates can grow by accumulating smaller clumps and single aggregates that drift onto it radially or it drifts onto azimuthally. Growth of the large clump leads to deceleration of its radial drift and acceleration of its orbital motion, which in turn results in the clump accreting even more smaller clumps and aggregates. This effect can be likened to traffic jams (Johansen and Youdin 2007). It is also related to groups of cyclists or flocks of birds moving faster and catching up to isolated cyclists or birds, respectively, since the individual members of group or flock are less affected by air resistance – dust experiences a headwind of slower-orbiting gas – than the isolated cyclist or bird. Youdin and Johansen (2007) note that while this toy model illustrates how the instability induces growth of non-linear perturbations in the dust density, the same effect does not lead to growth of linear perturbations.

Taking into account a number of dust species with different Stokes numbers rather than only one species, as I implicitly assume in the toy model discussion above, has further implications for the radial and azimuthal velocities of gas and dust (Bai and Stone 2010b; Schaffer et al. 2018): The streaming instability arises from the interaction between the gas and the species with the greatest Stokes numbers, i.e. the species with the weakest coupling to the gas. Because of the inwards radial drift of the dust and the conservation of angular momentum, the gas drifts radially outwards. This can be gathered from considering Eq. 3.6 for a finite dust-to-gas density ratio, i.e. non-zero f_g and f_d. While the species with the largest Stokes numbers drift inwards, the species with smaller Stokes numbers are more tightly coupled to the gas and drift outwards with it. Nevertheless, the orbital velocity of the gas is closer to the Keplerian velocity owing to the drag exerted by the smaller species than if these species were not present. Thus, the inwards radial drift of the largest species and the outwards drift of the gas are slower than they would be in the absence of the smaller species.

Owing to the effect that I describe employing the toy model, the (non-linear) streaming instability concentrates dust in radially small but azimuthally elongated filaments (Johansen et al. 2007, 2009; Bai and Stone 2010b; Kowalik et al. 2013; Yang and Johansen 2014; Li et al. 2018; Abod et al. 2019; SYJ17). These filaments form within no more than some tens of orbital periods for dust with a Stokes number of ~ 0.1 (e.g., Johansen et al. 2007, 2009; Yang and Johansen 2014; Li et al. 2018; Abod et al. 2019), but their formation takes up to ~ 1000 orbital periods if Stokes numbers of 0.01 or 0.001 are considered (Yang et al. 2017). The formation time scale is nonetheless shorter than the radial drift time scale even for the latter Stokes numbers (see Sect. 2.4 Yang et al. 2017). In the left panel of Figure 3.3, I show the filaments that form in a simulation presented in SYJ17. The filaments are close to axisymmetric both in shearing box simulations, that is to say in simulations of disk regions on a local scale (e.g., Yang and Johansen 2014; Li et al. 2018; Abod et al. 2019; SYJ17), and in simulations of disks on a more global scale (Kowalik et al. 2013). Yang and Johansen (2014) and Li et al. (2018) obtain similar values of the average radial distance between these filaments of ~ 0.2 and ~ 0.15 gas scale heights. Abod et al. (2019) find that the radial extent of the filaments increases with the strength of the gas pressure gradient.

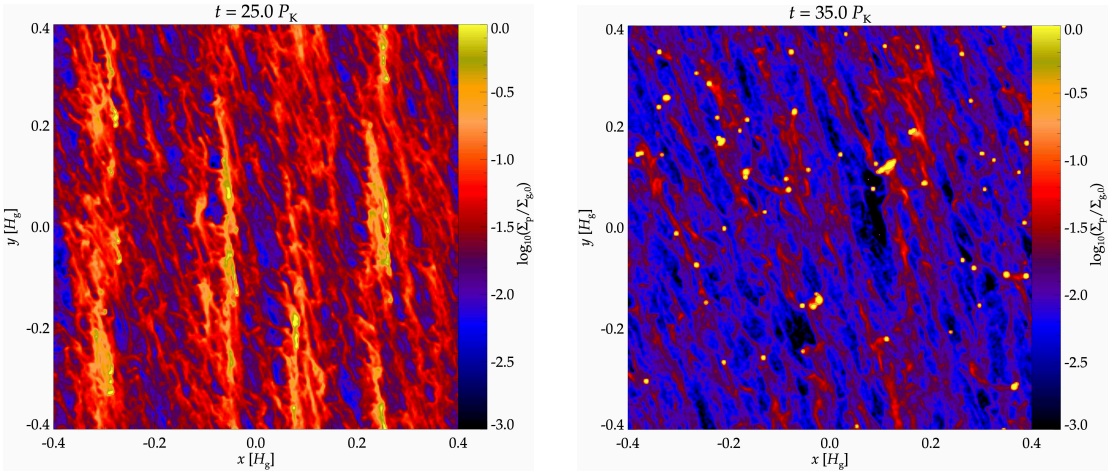

Figure 3.3: Figure adopted from SYJ17. Logarithm of the dust surface density Σ_p as a function of the radial coordinate x and the azimuthal coordinate y in a local shearing box simulation. The dust surface density is expressed as a fraction of the gas surface density at the centre of the simulation domain $\Sigma_{\mathrm{g},0}$, while the radial and azimuthal coordinates are given in units of gas scale heights H_g. The streaming instability causes the dust to accumulate in four filaments that are radially thin, but largely axisymmetric (left panel). Owing to their self-gravity, particularly dense dust clumps in these filaments undergo gravitational collapse, which leads to the formation of planetesimals (right panel).

Within these filaments, overdense clumps of dust can collapse under their self-gravity, contract, and form planetesimals (Johansen et al. 2007, 2009, 2011, 2015; Simon et al. 2016, 2017; SYJ17). The sizes of these planetesimals range from tens to hundreds of kilometres (Johansen et al. 2009, 2015; Simon et al. 2016; Abod et al. 2019; SYJ17). The planetesimals emerging from the filaments depicted in the left panel of Fig. 3.3 can be seen in the right panel. The collapse to 10 km- and 100 km-sized planetesimals, respectively, takes a few hundred years and $\sim$25 yr if the kinetic energy in clumps is dissipated solely via collisions between dust aggregates (Wahlberg Jansson and Johansen 2014). On the one hand, taking into account the drag of the dust onto the gas accelerates the collapse since it facilitates the dissipation of kinetic energy (Wahlberg Jansson and Johansen 2017). On the other hand, this drag leads to the collapse being retarded because the gas pressure in a clump increases with decreasing size of the clump (Shariff and Cuzzi 2015). We in SYJ17 and Abod et al. (2019) show that more numerous and more massive planetesimals emerge in larger filaments. The planetesimals typically migrate in the radial direction through and thus accrete dust from more than one filament, though (SYJ17).

A dust clump is commonly assumed to collapse when the self-gravity of the clump overcomes the tidal force of the star that acts to stretch it[2], that is when the density of the clump is higher than its Roche density (Johansen et al. 2011, 2015; Simon et al. 2016; SYJ17). The Roche density can be derived by considering an individual aggregate within a clump. I assume that the clump is located in the disk mid-plane and the aggregate on the side of the clump facing the star. If the radial distance between the aggregate and the centre of mass of the clump is equal to the so-called Hill radius r_H, the gravitational force exerted on the aggregate by the star is in

[2]The tidal force exerted by the star on a body is the force that results from parts of the body that are closer to the star being more strongly gravitationally attracted by the star than those that are further away.

equilibrium with the centrifugal force and the gravitational force by the clump acting on the aggregate. That is,

$$\frac{GM_{\rm S}m_{\rm d}}{\left(r_{\rm S}-r_{\rm H}\right)^2} = m_{\rm d}\Omega_{\rm K}^2\left(r_{\rm S}-r_{\rm H}\right) + \frac{Gm_{\rm c}m_{\rm d}}{r_{\rm H}^2}, \tag{3.22}$$

where $m_{\rm c}$ and $m_{\rm d}$ are the masses of clump and aggregate, and $r_{\rm S}$ is the radial distance between the centre of mass of the clump and the star. If the clump as a whole is orbiting with the Keplerian frequency $\Omega_{\rm K} = \left(GM_{\rm S}/r_{\rm S}^3\right)^{1/2}$ (see also Eq. 2.24), the above equation yields

$$\begin{aligned} \frac{M_{\rm S}}{\left(r_{\rm S}-r_{\rm H}\right)^2} &= \frac{M_{\rm S}\left(r_{\rm S}-r_{\rm H}\right)}{r_{\rm S}^3} + \frac{m_{\rm c}}{r_{\rm H}^2} \\ \Leftrightarrow M_{\rm S}\left(3r_{\rm S}^2r_{\rm H} - 3r_{\rm S}r_{\rm H}^2 + r_{\rm H}^3\right)r_{\rm H}^2 &= m_{\rm c}\left(r_{\rm S}-r_{\rm H}\right)^2 r_{\rm S}^3. \end{aligned} \tag{3.23}$$

Since the size of the clump is much less than its radial distance from the star, i.e. $r_{\rm H} \ll r_{\rm S}$, this equation reduces to

$$3M_{\rm S}r_{\rm S}^2r_{\rm H}^3 = m_{\rm c}r_{\rm S}^5 \tag{3.24}$$

$$\Leftrightarrow r_{\rm H} = r_{\rm S}\sqrt[3]{\frac{m_{\rm c}}{3M_{\rm S}}}. \tag{3.25}$$

If the clump consists only of aggregates that are located within its Hill radius, all of these aggregates are more strongly gravitationally attracted by the clump than by the star. That is, the self-gravity of the clump is stronger than the tidal force of the star acting on it. Assuming a spherical clump with a homogeneous density, this condition is equivalent to the density of the clump being greater than the Roche density

$$\rho_{\rm R} = \frac{3m_{\rm c}}{4\pi r_{\rm H}^3} = \frac{3m_{\rm c}}{4\pi}\frac{3M_{\rm S}}{r_{\rm S}^3m_{\rm c}} = \frac{9M_{\rm S}}{4\pi r_{\rm S}^3} = \frac{9\Omega_{\rm K}^2}{4\pi G}. \tag{3.26}$$

Gerbig et al. (2020) and Klahr and Schreiber (2020) extend this criterion for gravitational collapse of dust clumps by assuming that the collapse is inhibited not only by the stellar tidal force, but also by diffusion of the dust induced by gas turbulence. Specifically, Gerbig et al. (2020) show that turbulent diffusion prevents the collapse of a clump of radius $r_{\rm c}$ if

$$r_{\rm c} < \sqrt{\frac{\alpha c_{\rm s}H_{\rm g}\Omega_{\rm K}}{4\pi G{\rm St}\rho_{\rm c}}}, \tag{3.27}$$

where $\rho_{\rm c}$ is the density of the clump and the parameter α describes the strength of the turbulent gas viscosity $\nu_{\rm g,turb} = \alpha c_{\rm s}H_{\rm g}$ (see Sect. 2.2; Shakura and Sunyaev 1973). Klahr and Schreiber (2020), who consider the streaming instability as the source of turbulent diffusion, obtain a threshold diameter of $\sim$100 km of clumps that are both dense enough to overcome the tidal force and large enough to not be dispersed by turbulence.

The streaming instability always operates if dust and a radial gradient in the gas pressure are present. However, the formation of filaments, and planetesimals inside them, occurs only if the Stokes number of the dust and the ratio of dust to gas surface density – often referred to

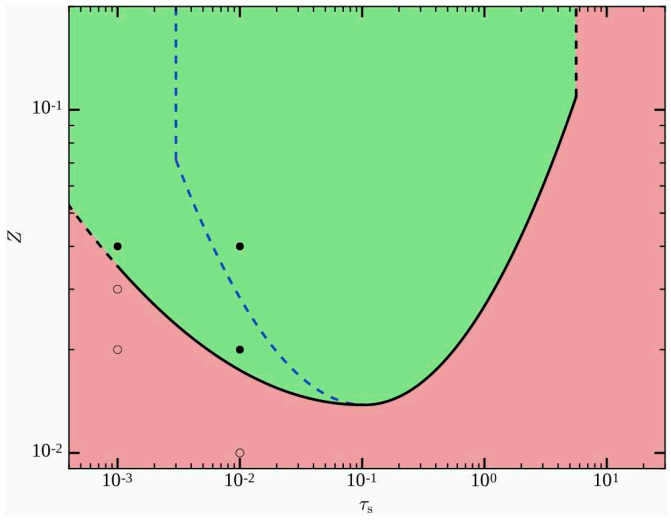

Figure 3.4: Figure adopted from Yang et al. (2017, their Fig. 9, reproduced with permission ©ESO). Ratio of dust to gas surface density Z and Stokes number of the dust τ_{s} plotted on the ordinate and abscissa, respectively. The green region encompasses all combinations of Stokes number and surface density ratio for which the streaming instability concentrates dust in filaments from which planetesimal emerge. The necessary surface density ratio is lowest if the Stokes number is equal to 0.1, but still exceeds the canonical interstellar medium value of 1%. Larger surface density ratios enable filament and planetesimal formation for Stokes numbers between 10^{-3} and a few.

as metallicity – (Johansen et al. 2009; Bai and Stone 2010b; Drążkowska and Dullemond 2014; Carrera et al. 2015; Yang et al. 2017) as well as the strength of the pressure gradient (Bai and Stone 2010c; Drążkowska and Dullemond 2014) exceed interdependent threshold values. The dependence on the surface density ratio is related to the growth rate of the linear instability being largest if the dust volume density is higher than the gas volume density (see Sect. 3.1; Youdin and Goodman 2005): For a given Stokes number and pressure gradient strength, only if the dust-to-gas surface density ratio is high enough does the mean volume density of the dust layer around the disk mid-plane exceed the gas volume density in this layer (Johansen et al. 2009). And only then does the (non-linear) instability give rise to strong dust concentration (Johansen and Youdin 2007; Johansen et al. 2009).

Sekiya and Onishi (2018) propose that the ability of the instability to cause dust accumulation in filaments is not dependent on the dust-to-gas surface density ratio Z and on the steepness of the gas pressure gradient – expressed in the parameter Π – individually, but on the dimensionless parameter $(2\pi)^{1/2}Z/\Pi$. To confirm this, they compare simulations with the same value of this parameter, but different surface density ratios and pressure gradient strengths. The instability indeed gives rise to similarly dense dust accumulations in these simulations.

Carrera et al. (2015) and Yang et al. (2017) conduct parameter studies to determine threshold Stokes numbers and dust-to-gas surface density ratios required for the instability to induce filament and subsequently planetesimal formation. The results of these studies are depicted in Fig. 3.4. In the studies, a fixed pressure gradient strength of $\Pi = 0.05$ is assumed. Yang et al. (2017) obtain equations expressing the threshold value Z_{thres} of the surface density ratio

as a function of the Stokes number,

$$\log_{10}\left(Z_{\mathrm{thres}}\right) = \begin{cases} 0.3\log_{10}\left(\mathrm{St}\right)^2 + 0.59\log_{10}\left(\mathrm{St}\right) - 1.57 & \mathrm{St} > 0.1 \text{ or} \\ 0.1\log_{10}\left(\mathrm{St}\right)^2 + 0.2\log_{10}\left(\mathrm{St}\right) - 1.76 & \mathrm{St} < 0.1. \end{cases} \tag{3.28}$$

Crucially, for all Stokes numbers the threshold ratio of dust to gas surface density exceeds the canonical value in the interstellar medium, and therefore in pristine protoplanetary disks, of 1% . At best, the threshold value amounts to 0.015 for a Stokes number of 0.1. Nevertheless, for larger surface density ratios strong dust accumulation occurs if the Stokes number is as small as 10^{-3} or as large as a few. Bai and Stone (2010c), on the other hand, find that if dust with a distribution of Stokes numbers ranging from 10^{-3} to 1 is taken into account, the threshold surface density ratio amounts to 2% and 6% if the parameter giving the strength of the pressure gradient $\Pi = 0.025$ and $\Pi = 0.1$, respectively. This is contrast to the growth rate of the linear instability increasing with the pressure gradient strength (see Eq. 3.20).

It is evident that the streaming instability alone can not induce planetesimal formation under conditions typical for protoplanetary disks. Figure 2.4 shows that bouncing under mutual collisions and radial drift prevent collisional growth of compact dust aggregates beyond sizes of millimetres in the inner disk regions and tens or hundred of microns in the outer ones. This is equivalent to Stokes numbers of 10^{-4} and of 10^{-3}, respectively. For these Stokes numbers, Yang et al. (2017) find that the dust-to-gas surface density ratio needs to be enhanced by a factor of four or more compared to the interstellar medium value. Conversely, the threshold surface density ratio is lowest – but still marginally higher than in the interstellar medium – for dust with a Stokes number of 0.1, which corresponds to a dust size of 10 cm at a radial distance to the star of 5 au and to 1 cm at a radius of 50 au if compact aggregates are considered (see Eq. 2.13).

However, a variety of processes can cause either an enhancement of the dust-to-gas density ratio that is conducive to the streaming instability or dust growth despite the bouncing and radial drift barriers. I discuss the former kind of processes in Sect. 3.5, and the latter kind in Sect. 2.3. Dust aggregates can grow to centimetre-sizes at ice lines (Ros and Johansen 2013; Ros et al. 2019), if the aggregates are charged (Steinpilz et al. 2019), or if they are "lucky" in that they are not involved in collisions with high relative velocities (Windmark et al. 2012b,c; Garaud et al. 2013). Furthermore, Krijt et al. (2015, 2016b) find that porous aggregates with Stokes numbers between 10^{-2} and a few are present in large regions of protoplanetary disks.

3.3 Planetesimal initial mass function

Initial mass function denotes a distribution of birth masses, most commonly of stars but here of the planetesimals that emerge from filaments formed by the streaming instability. The mass distribution can be expressed in differential form, $\mathrm{d}N/\mathrm{d}M$, or in cumulative form,

$$N_{>}(M) = \int_{M}^{M_{\mathrm{max}}} \frac{\mathrm{d}N}{\mathrm{d}M'}\mathrm{d}M', \tag{3.29}$$

where N is the number of planetesimals, M their mass, and M_{max} their maximum mass. The number of planetesimals with masses ranging between M and $M + \mathrm{d}M$ can be calculated

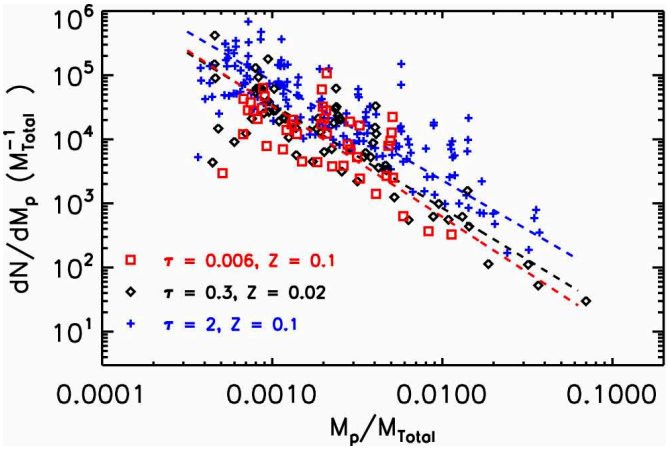

Figure 3.5: Figure adopted from Simon et al. (2017, their Fig. 2, reproduced with permission ©AAS). Differential mass distribution $\mathrm{d}N/\mathrm{d}M_\mathrm{p}$ as a function of the planetesimal mass M_p. The values plotted on the abscissa and the ordinate are normalised by the total dust mass M_Total and its inverse, respectively. The mass distributions in three simulations with different combinations of the Stokes number of the dust τ and the dust-to-gas surface density ratio Z are depicted using different symbols and colours, with the combinations being given in the legend. Despite the varying Stokes numbers and surface density ratios, each of the three distributions is described well by a power-law distribution $\mathrm{d}N/\mathrm{d}M_\mathrm{p} \propto M_\mathrm{p}^{-1.6}$ (dashed lines).

as $\mathrm{d}N/\mathrm{d}M\,\mathrm{d}M$, while $N_>(M)$ gives the total number with masses greater than M. In other words, the probability for the mass of a planetesimal to exceed M is equal to $N_>(M)/N_\mathrm{tot}$. Here, N_tot is the total number of planetesimals. In this section, I first discuss the shape of the initial mass function and then the characteristic mass of planetesimals.

All studies of the planetesimal birth mass distribution have been conducted numerically using the shearing box approximation (see Sect. 3.1; Johansen et al. 2015; Simon et al. 2016, 2017; Abod et al. 2019; Li et al. 2019; Gole et al. submitted; SYJ17). Consequently, in these studies the mass distribution does not only depend on physical parameters like the Stokes number of the dust and the ratio of dust to gas surface density, but also on numerical parameters like the simulation domain size and resolution. In shearing box simulations, a domain is considered that is much smaller than the size of protoplanetary disks. That is, local scale-free units can be employed. In simulations of the streaming instability, these typically are the gas scale height H_g, the dynamical time scale $1/\Omega_\mathrm{K}$, and the gas density at the centre of the domain $\rho_{\mathrm{g},0}$ as the units of length, time, and density. Consequently, arbitrary values of the dimensionless parameters Π (see Eq. 2.19) and

$$\gamma = \frac{4\pi G\rho_{\mathrm{g},0}}{\Omega_\mathrm{K}^2} = \frac{9\rho_{g,0}}{\rho_\mathrm{R}} \tag{3.30}$$

(see also Eq. 3.26) can be chosen. While Π expresses the steepness of the global gas pressure gradient, γ gives the relative strength of self-gravity – nominally of the gas, but also of the dust given a dust-to-gas density ratio – and tidal force exerted by the star. I note that, despite the domain dimensions being much less than those of protoplanetary disks, in all shearing box simulations of planetesimal formation via the streaming instability the resolution is too low to resolve the gravitational collapse of dust clumps down to planetesimal sizes.

The planetesimal initial mass function obtained in a majority of studies is represented well by a power law

$$\frac{\mathrm{d}N}{\mathrm{d}M} \propto M^{-1.6} \tag{3.31}$$

(Johansen et al. 2015; Simon et al. 2016, 2017; Abod et al. 2019). I show this mass distribution in Fig. 3.5. While Li et al. (2019) find a function composed of multiple power laws to yield a better fit to the differential mass distribution than a single power law, at least one of the fitted power-law exponents lies in the range between -1.35 and -1.87. The power-law distribution given in Eq. 3.31 is universal in that its exponent is largely independent of the Stokes number of the dust (see Fig. 3.5; Simon et al. 2017), the simulation resolution (Johansen et al. 2015; Simon et al. 2016), as well as the parameters Π (Abod et al. 2019) and γ (Simon et al. 2016). The mass distribution can be converted to a size distribution as

$$\frac{\mathrm{d}N}{\mathrm{d}R} = \frac{\mathrm{d}M}{\mathrm{d}R}\frac{\mathrm{d}N}{\mathrm{d}M} \propto R^2 \left(R^3\right)^{-1.6} = R^{-2.8}, \tag{3.32}$$

where R is the planetesimal size (Johansen et al. 2015; Simon et al. 2016; Abod et al. 2019).

It is interesting to compare the planetesimal initial mass function to that of stars. The stellar mass distribution can be expressed as $\mathrm{d}N/\mathrm{d}M \propto M^{-2.3}$ for stars with masses exceeding one Solar mass (Salpeter 1955; Kroupa 2001; Chabrier 2003). That is to say, it is the steeper than the mass distribution of planetesimals. The total mass of objects with masses in the interval between M and $M + \mathrm{d}M$ can be computed as $M\,\mathrm{d}N/\mathrm{d}M\,\mathrm{d}M$. In the case of stars, this total mass per mass interval is proportional to $M^{-1.3}$. Thus, the least massive stars contribute most mass to the total mass of all stars. In contrast, the planetesimal mass distribution expressed in Eq. 3.31 yields a total mass per mass interval proportional to $M^{-0.6}$. That is, the most massive planetesimals dominate the total planetesimal mass. Abod et al. (2019) find this to be true even if the formation of the planetesimals is not induced by the streaming instability.

We in SYJ17, Abod et al. (2019) and Johansen et al. (2015) show that the birth mass distribution of planetesimals that form owing to the streaming instability is exponentially tapered at the high-mass end. In Figure 3.6, the cumulative distribution in a simulation presented in SYJ17 is depicted. It is evident that a power law with an exponential cutoff $\exp[-(M/M_{\mathrm{exp}})^{0.38}]$ (red line) fits the distribution better than a power law without cutoff (green line). Our simulations with different domain sizes yield comparable values of the characteristic mass of the cutoff M_{exp} and its exponent, with the latter ranging from 0.3 to 0.4. Similar to us, Abod et al. (2019) find an exponentially tapered power law, $\mathrm{d}N/\mathrm{d}M \propto M^{-1.3}\exp(-M/M_{\mathrm{exp}})$, to represent the mass distribution better than a simple power law, $\mathrm{d}N/\mathrm{d}M \propto M^{-1.6}$. This is valid independent of the strength of the gas pressure gradient. Nevertheless, the exponential cutoff considered by Abod et al. (2019) is steeper than the one we infer in SYJ17. Johansen et al. (2015) determine an even higher exponent of the cutoff of $4/3$. I note, however, that significantly fewer planetesimal masses constitute the cutoff in the study by Johansen et al. (2015) than in the one by Abod et al. (2019) and in ours (compare Fig. 4 of Johansen et al. (2015) with Fig. 6 of Abod et al. (2019) and Fig. 4 of SYJ17).

In addition to for a cutoff at the high-mass end, evidence exists also for a turnover at the low-mass end of the initial mass function. The first authors to present such evidence were Li et al. (2019). They performed the simulation with the highest resolution to date, with higher

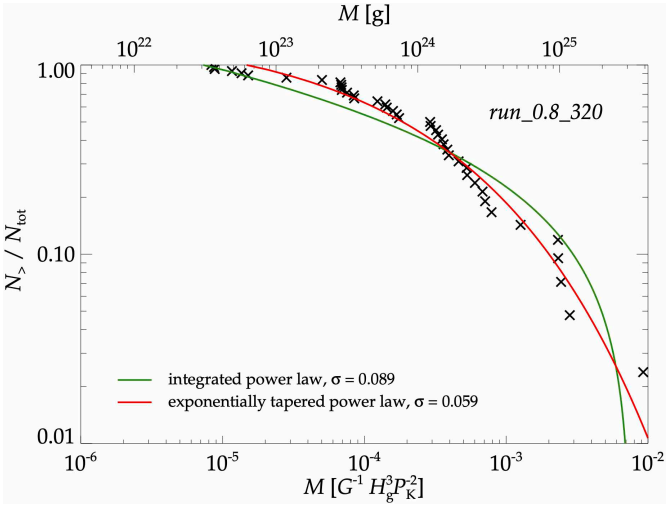

Figure 3.6: Figure adopted from SYJ17. Cumulative mass distribution $N_{>}$, relative to the total number of planetesimals $N_{\rm tot}$, as a function of the planetesimal mass M. As can be gathered from a comparison of the power-law distributions with (red line) and without exponential tapering (green line), the former represents the planetesimal mass distribution better.

resolutions enabling the formation of smaller, less massive planetesimals (Johansen et al. 2015; Simon et al. 2016; Li et al. 2019). Li et al. (2019) show that the differential mass distribution in this simulation, which can be seen in Fig. 3.7, is described well by a broken power law. Gole et al. (submitted) perform simulations with a lower resolution, but including driven turbulence. They as well find a turnover in the mass distribution, and the distribution therefore to be well-presented by a broken power law. Planetesimals only form in their simulations if the turbulence is not too strong (see Sect. 4.5.1). However, if planetesimals emerge, their initial mass function is largely independent of whether turbulence is present and of the turbulent strength. I note, though, that the exponent of the power law at the low-mass end that Gole et al. (submitted) obtain differs from the one determined by Li et al. (2019). Additionally, the power law that Gole et al. (submitted) fit to the high-mass end of the differential distribution is considerably steeper than in all previous studies, with the exponent ranging between -2.48 and -2.71.

While the shape of the initial mass function – specifically of the power-law distribution expressed in Eq. 3.31 – is more robust in this regard, the number and masses of the planetesimals emerging in shearing box simulations vary with both numerical and physical parameters: Firstly, with increasing resolution the minimum mass of planetesimals decreases. Their mean mass declines as well since their maximum mass remains roughly constant, while their number increases (Johansen et al. 2015; Simon et al. 2016; Li et al. 2019). Secondly, fewer and in total less massive planetesimals emerge if the gas pressure gradient is steeper (Abod et al. 2019). On the other hand, Abod et al. (2019) find the characteristic mass of the exponential tapering of the initial mass function to increase linearly with the strength of the pressure gradient. (They note that they can not exclude that the characteristic mass is independent of the strength.) This might be a consequence of radially larger filaments forming in simulations with stronger

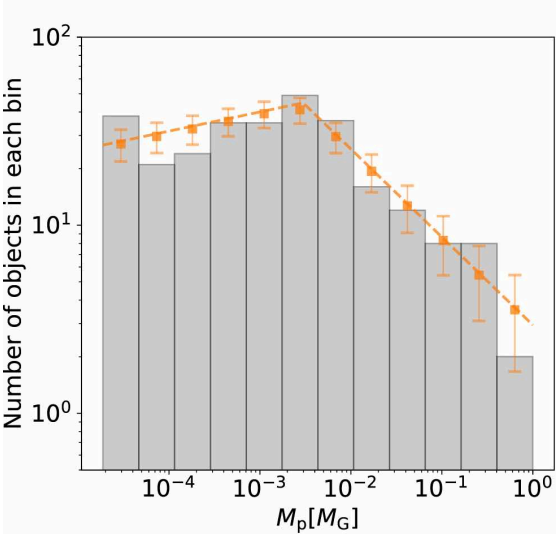

Figure 3.7: Figure adopted from Li et al. (2019, their Fig. 4, reproduced with permission ©AAS). Number of planetesimals per mass bin as a function of the planetesimal mass M_p. The latter is given in units of gravitational masses $M_\mathrm{G} = 4\pi^5 G^2 \Sigma_\mathrm{d}^3 / \Omega_\mathrm{K}^4$, where Σ_d is the dust surface density (Abod et al. 2019). It is evident that there is a turnover in the mass distribution. Thus, the distribution is fitted well with a broken power law (orange line).

pressure gradients since the budget of dust mass available for every planetesimal to accrete increases with the filament size. In SYJ17, we indeed obtain an analogous result from comparing simulations with different domain sizes: the mean planetesimal mass and characteristic mass of the exponential cutoff increase with the radial filament extent.

Thirdly, the total planetesimal mass increases with the Stokes numbers of the dust, while minimum and maximum mass remain largely constant (Simon et al. 2017). Furthermore, the maximum mass is larger if the dust-to-gas surface density ratio Z is higher (Johansen et al. 2015), and both the maximum and total mass are enhanced for greater values of the parameter γ (Simon et al. 2016). This is because the strength of the dust self-gravity increases with $Z\gamma \propto GZ\rho_{\mathrm{g},0} \sim G\rho_\mathrm{d}$ (see Eq. 3.30). In other words, if $Z\gamma \propto \rho_\mathrm{d}/\rho_\mathrm{R}$ is greater, weaker dust overdensities exceed the Roche density, can undergo gravitational collapse and form planetesimals. Finally, the number and total mass of planetesimals decreases with the strength of the gas turbulence (Gole et al. submitted). Nonetheless, the turnover masses of the broken power laws that Gole et al. (submitted) fit to the mass distributions in simulations with varying turbulent strengths differ only marginally.

In what follows, I adopt the approach devised by Liu et al. (2020) to derive a characteristic planetesimal mass M_char based on the findings discussed above. Like Liu et al. (2020), I assume the characteristic mass of the exponential cutoff of the initial mass function inferred in SYJ17 to be the fiducial characteristic mass. This is justified by the most massive planetesimals adding more mass per mass interval to the total planetesimal mass than less massive planetesimals. As the characteristic mass of the cutoff varies between $1.82 \times 10^{-5}\ \rho_{g,0} H_\mathrm{g}^3$ and $1.85 \times 10^{-4}\ \rho_{g,0} H_\mathrm{g}^3$ in the simulations we present in SYJ17, a value of $5 \times 10^{-5}\ \rho_{g,0} H_\mathrm{g}^3$ is used in the following. Because $\rho_{\mathrm{g},0}$ and H_g are typically used as the units of density and length

in shearing box simulations of the streaming instability, the unit of mass in these simulations is $[M] = 1\ \rho_{g,0} H_\mathrm{g}^3$.

In SYJ17, we choose a Stokes number of the dust of $\pi/10$, a ratio of dust to gas surface density of 2%, and the parameter values $\gamma = 1/\pi$ and $\Pi = 0.05$. Since neither the minimum nor the maximum planetesimal mass varies significantly with the Stokes number (Simon et al. 2017), the characteristic mass is considered to also be independent of the Stokes number. In addition, it can be seen from the right panel of Fig. 9 of Simon et al. (2016) that the maximum mass approximately scales with $\gamma^{3/5}$. I adopt this scaling for the characteristic mass. I further follow Liu et al. (2020) in assuming the scaling with the dust-to-gas density ratio to be the same as that with γ. The justification for this is that $Z\gamma$ expresses the strength of the dust self-gravity. Furthermore, Abod et al. (2019) find the characteristic mass of the exponential tapering to be proportional to Π. Lastly, because the mass at which Gole et al. (submitted) find the initial mass function to turn over is independent of the strength of turbulence, I assume this to be true for the characteristic mass as well.

Combining its fiducial value with its dependence on the dust-to-gas surface density ratio as well as on the parameters Π and γ yields the characteristic planetesimal mass

$$M_\mathrm{char} = 1.70 \times 10^{-5} \left(\frac{Z}{0.02}\right)^{3/5} \left(\frac{\gamma}{0.1}\right)^{3/5} \left(\frac{\Pi}{0.05}\right) \rho_{\mathrm{g},0} H_\mathrm{g}^3. \tag{3.33}$$

To convert the characteristic mass from local to global units, I apply the model of the gas in protoplanetary disks presented in Appendix A. In the disk mid-plane of this model, the mass unit $[M] = 1\ \rho_{\mathrm{g},0} H_\mathrm{g}^3$ is equivalent to

$$[M](z=0) = 3.48 \times 10^{26} \left(\frac{r}{1\ \mathrm{au}}\right)^{-1} \mathrm{g} = 374 \left(\frac{r}{1\ \mathrm{au}}\right)^{-1} M_\mathrm{Ceres}, \tag{3.34}$$

where M_Ceres is the mass of the dwarf planet Ceres, the most massive object in the asteroid belt. Similarly, the parameter γ can be converted as

$$\gamma(z=0) = 0.021 \left(\frac{r}{1\ \mathrm{au}}\right)^{3/4} \tag{3.35}$$

and the parameter Π using Eq. 2.20. That is, the characteristic mass can be expressed as

$$\begin{aligned} M_\mathrm{char}(z=0) &= 2.47 \times 10^{27} \left(\frac{Z}{0.02}\right)^{3/5} \left(\frac{r}{1\ \mathrm{au}}\right)^{-3/10} g \\ &= 2.29 \times 10^{-3} \left(\frac{Z}{0.02}\right)^{3/5} \left(\frac{r}{1\ \mathrm{au}}\right)^{-3/10} M_\mathrm{Ceres}. \end{aligned} \tag{3.36}$$

As an example, assuming a dust-to-gas surface density ratio of 2% – about the lowest value for which the streaming instability can induce planetesimal formation (see Fig. 3.4 and Eq. 3.28) – the characteristic mass is equal to $1.75 \times 10^{-3}\ M_\mathrm{Ceres}$ at the perihelion of Ceres, which is located at a radial distance to the Sun of 2.5 au.

Abod et al. (2019) are the only authors to propose a physical explanation for the value of a parameter of the planetesimal initial mass function. They find the characteristic mass of its exponential cutoff to be similar to the gravitational mass

$$M_{\rm G} = \pi \left(\frac{\lambda_{\rm G}}{2} \right)^2 \Sigma_{\rm d} = 4\pi^5 \frac{G^2 \Sigma_{\rm d}^3}{\Omega_{\rm K}^4} = \frac{81\pi^3}{4} \frac{\Sigma_{\rm d}^3}{\rho_{\rm R}^2} \tag{3.37}$$

(see also Eq. 3.26), where $\Sigma_{\rm d}$ is the dust surface density and the wavelength

$$\lambda_{\rm G} = 4\pi^2 \frac{G\Sigma_{\rm d}}{\Omega_{\rm K}^2} = \frac{9}{\pi} \frac{\Sigma_{\rm d}}{\rho_{\rm R}} \tag{3.38}$$

results from an analysis of the linear gravitational instability. At wavelengths less than $\lambda_{\rm G}$, self-gravity is stronger than the stellar tidal force. The finding that the characteristic mass of the cutoff and the gravitational mass are comparable implies that the former does not depend on whether it is the streaming instability or a different mechanism that enhances the dust density sufficiently for gravitational collapse to lead to planetesimal formation.

It can be shown that the characteristic mass of the cutoff that we infer in SYJ17 is indeed also of the order of the gravitational mass. As discussed above, this characteristic mass is similar to $M_{\rm exp} = 5 \times 10^{-5}\, \rho_{\rm g,0} H_{\rm g}^3$. The gravitational mass

$$M_{\rm G} = \frac{\sqrt{2}}{2} \pi^{9/2} Z^3 \gamma^2\, \rho_{\rm g,0} H_{\rm g}^3 \tag{3.39}$$

(Abod et al. 2019). Thus, given that a dust-to-gas surface density ratio $Z = 0.02$ and a parameter $\gamma = 1/\pi$ are chosen in SYJ17, the characteristic mass $M_{\rm exp} = 0.505\, M_{\rm G}$.

3.4 Observational evidence

ALMA observations of protoplanetary disks provide indications of the streaming instability inducing the formation of planetesimals. Dullemond et al. (2018) associate the largely concentric dust rings in five disks observed as part of the Disk Substructures at High Angular Resolution Project (DSHARP) with pressure bumps (see Sect. 3.5). These authors find the ratio of dust to gas surface density in these rings to be potentially high enough for planetesimal formation owing to the streaming instability. All eight rings in these five disks are marginally optically thin, with their optical depths lying in the range between 0.2 and 0.5. Based on a model of one of the rings, Stammler et al. (2019) interpret the fact that the optical depths are not higher as evidence for the streaming instability. In their model, an optical depth of ~ 0.5 is equivalent to the densities of gas and dust being equal. Dust-to-gas density ratios exceeding unity are not observable because stronger dust overdensities are enhanced by the streaming instability until they collapse and form planetesimals.

Macías et al. (2019) also measure optical depths of 0.7 or less in the four rings in the disk surrounding HD 169142. Specifically in the innermost ring, they further infer a dust surface density that is comparable to the gas surface density obtained by Fedele et al. (2017) and a maximum dust size of 5 mm. These are ideal conditions for the streaming instability to lead to

planetesimal formation. (I note that these authors derive the dust size from the spectral index of the dust opacity, but do not take the effect of scattering by dust grains on the opacity into account; see Sect. 2.1.)

Asteroids, Kuiper belt objects, and comets are remnants of the formation and evolution of planetesimals in the Solar System (e.g., Johansen et al. 2014). Blum et al. (2017) find that the comet 67P/Churyumov-Gerasimenko, which was investigated by the Rosetta mission, probably formed from the gravitational collapse of an accumulation of dust aggregates. In particular, the sizes of the aggregates it is composed of lie in a range for which the streaming instability causes dust concentration in gravitationally unstable clumps if the dust-to-gas surface density ratio is twice the canonical value in the interstellar medium. In addition, the comet is homogeneous on scales larger than tens to hundreds of meters, consistent with a formation via gravitational collapse (Kofman et al. 2015; Pätzold et al. 2016).

Observations of binaries in the cold classical Kuiper belt yield compelling evidence for their progenitor planetesimals forming by gravitational collapse, possibly induced by the streaming instability. The (main) classical Kuiper belt is located between radial distance to the Sun of 40 au and 48 au, with the eccentricities of the objects in it being low enough for their orbits not to cross that of Neptune at a radius of 30 au (e.g., Elliot et al. 2005; Delsanti and Jewitt 2006; Gladman et al. 2008). In particular, the cold classical Kuiper belt objects are characterised by low eccentricities and inclinations, which indicates that their orbits are largely unperturbed – they are "dynamically cold", analogous to the velocities of Brownian motion being less at lower temperatures – and are thus relatively pristine. Among these cold classical Kuiper belt objects, according to estimations at least $\sim 30\%$ are binaries (Noll et al. 2008; Fraser et al. 2017a,b) and 10–25 % contact binaries whose two components are of comparable size (Sheppard and Jewitt 2004; Thirouin and Sheppard 2019).

Since the angular momentum of gravitationally unstable dust clumps formed by the streaming instability is typically too high for their self-gravity to overcome their rotation, binaries rather than single planetesimals emerge from them (Johansen et al. 2015; Nesvorný et al. 2019). Generally, the binary components are similar in size and their separation comparatively large, i.e. they are not contact binaries (Nesvorný et al. 2010, 2019; Robinson et al. accepted). In 80% of cases, gravitational collapse leads to the inclination of the mutual orbit of the components being prograde with respect to their joint orbit around the star (Nesvorný et al. 2019). In other words, the majority of binary components rotate counterclockwise both around the star and around one another. This is indeed true also for seven out of ten Kuiper belt binaries studied by Grundy et al. (2011) and 28 out of 35 observed by Grundy et al. (2019). In contrast, if the binary components become gravitationally bound during a chance encounter (Goldreich et al. 2002), their orbital inclinations are either predominantly retrograde or equally often prograde and retrograde (Schlichting and Sari 2008).

The components of Kuiper belt binaries forming together further naturally explains their similar composition, which is reflected in their colours in general being indistinguishable (Benecchi et al. 2009). In addition, observations of comets (Jutzi and Asphaug 2015) and particularly of the Kuiper belt object 486958 Arrokoth by the New Horizons mission (see Fig. 1.2; Stern et al. 2019; McKinnon et al. 2020) indicate that their components collided gently, not violently. Both this and the fact that they are similar in composition and colour (Grundy et al. 2020)

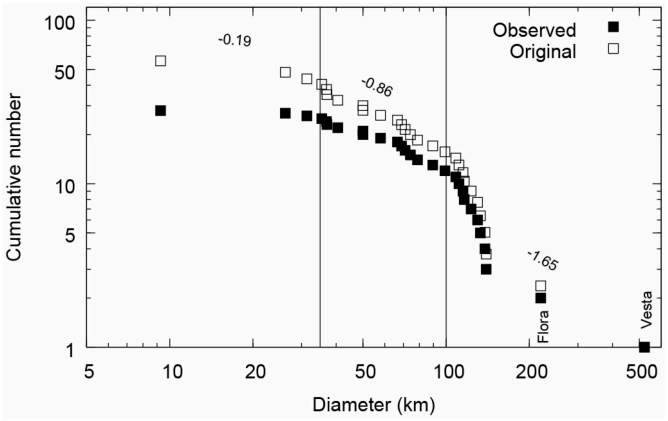

Figure 3.8: Figure adopted from Delbo' et al. (2019, their Fig. 6, reproduced with permission ©ESO). Cumulative diameter distribution of primordial asteroids. Filled squares represent the observed distribution. Correcting this distribution for 10 Gyr of dynamical and collisional evolution of the asteroids yields the distribution depicted as open squares. The latter distribution is fitted with three power laws, one each for diameters up to 35 km, between 35 km and 100 km, and more than 100 km. The exponents of the power laws are given in the figure.

suggest that the components of Arrokoth formed from the same dust accumulation and subsequently merged (Stern et al. 2019; McKinnon et al. 2020; Lyra et al. submitted; Robinson et al. accepted).

It is interesting to compare the birth size distribution of planetesimals that form via the streaming instability with the size distributions of asteroids and Kuiper belt objects. Bottke et al. (2005) and Morbidelli et al. (2009) construct models to reproduce the asteroid size distribution, which features a bump at a diameter of ~ 100 km. They find that the asteroids larger than this diameter are primordial, while most smaller asteroids are the result of collisions between larger bodies. This is consistent with constraints stemming from asteroid families, groups of asteroids with similar semi-major axes, eccentricities and inclinations that are interpreted as remnants of the same parent body (e.g., Nesvorný et al. 2015). The finding is further corroborated by the fact that not more than a single crater resulting from the impact of a body with a size of ~ 35 km or more is observed on the second-most massive asteroid Vesta (Thomas et al. 1997).

Bottke et al. (2005) fit the differential size distribution of asteroids larger than 120 km with a power law with an exponent of -4.5. In contrast, the exponent of the power-law size distribution that arises from planetesimal formation owing to the streaming instability amounts to -2.8 (see Eq. 3.32). Nevertheless, Johansen et al. (2015) show that the latter size distribution, which they consider to be exponentially tapered, can evolve into the asteroid size distribution obtained by Bottke et al. (2005) when the accretion of chondrules – millimetre-sized spherical dust grains that are found in chondrite meteorites (e.g., Friedrich et al. 2015) – by the planetesimals is taken into account.

The cumulative size distribution of primordial asteroids inferred by Delbo' et al. (2017, 2019) is shown in Fig. 3.8. This size distribution is well-represented by a broken power law with a turnover at a diameter of 100 km. It is similar to the planetesimal size distribution result-

ing from the streaming instability in multiple regards: For diameters larger than 100 km, the slope of the cumulative distribution measured by Delbo' et al. (2019) corresponds to an exponent of the differential distribution of -2.65. This exponent is considerably smaller than the one determined by Bottke et al. (2005), but close to that of the planetesimal size distribution of -2.8. Additionally, the studies of the streaming instability by Li et al. (2019) and Gole et al. (submitted) indicate the presence of a turnover as well in the planetesimal initial mass function. Furthermore, Klahr and Schreiber (2020) calculate a threshold diameter of 100 km of dust clumps whose self-gravity is stronger than both stellar tidal force and turbulent diffusion caused by the streaming instability. Nonetheless, I note that the size distribution inferred by Delbo' et al. (2017, 2019) is also similar to that of planetesimals forming from dust concentrations in turbulent eddies (see Sect. 3.5; Cuzzi et al. 2010; Chambers 2010; Hartlep and Cuzzi 2020).

Singer et al. (2019) show that a power law with an exponent of -3 yields a good fit to the differential size distribution of craters on the dwarf planet Pluto and its moon Charon as observed by the New Horizons mission. Craters with diameters smaller than ~ 13 km are comparatively scarce, though. Since the craters are the result of impacts of other Kuiper belt objects, the size distribution of craters reflects that of these objects. The power-law size distributions of Kuiper belt objects and planetesimals forming via the streaming instability are similarly steep. In addition, a paucity of Kuiper belt objects with diameters less than a few kilometers is implied by the lack of small craters. This is consistent with the streaming instability leading to the formation of planetesimals with typical sizes of tens or hundreds of kilometres (Johansen et al. 2009, 2015; Simon et al. 2016; Abod et al. 2019; SYJ17).

3.5 Other mechanisms facilitating dust concentration and planetesimal formation

In the following, I review mechanisms that lead to an enhancement in the ratio of dust to gas density on a local or a global scale in protoplanetary disks. While some of these mechanisms can induce dust overdensities that are strong enough for direct gravitational collapse and planetesimal formation, most of the mechanisms trigger further dust concentration by the streaming instability.

Dust can be passively concentrated in structures that are caused by gas turbulence: in pressure bumps (Whipple 1972; Haghighipour and Boss 2003), in vortices (Barge and Sommeria 1995; Tanga et al. 1996), and in eddies (Squires and Eaton 1990, 1991; Wang and Maxey 1993). Furthermore, dust accumulates locally at ice lines and in pile-ups, while photoevaporation enhances the global dust-to-gas density ratio. Finally, hydrodynamical instabilities that are similar to the streaming instability in that they result from the mutual drag between gas and dust give rise to dust concentration.

Pressure bumps Pressure bumps induced by the magnetorotational instability (Johansen et al. 2006b, 2007, 2011; Dzyurkevich et al. 2010; Dittrich et al. 2013; Béthune et al. 2016; Riols and Lesur 2018; Riols et al. 2020a) and the vertical shear instability (Stoll and Kley 2016; SJB20) have been studied as sources of dust pile-ups. How dust accumulates in a pressure bump is illustrated in Fig. 3.9. The accumulation arises from variations in the orbital velocity of gas

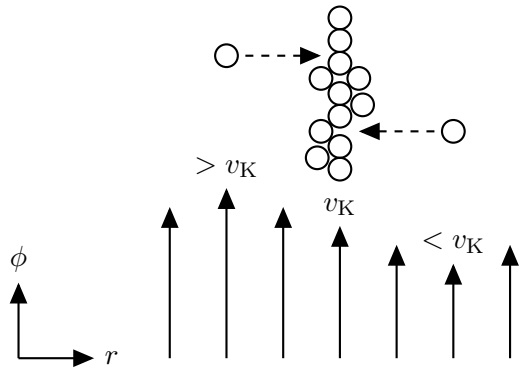

Figure 3.9: Illustration of dust piling up in a gas pressure bump. Solid arrows depict the orbital velocity of the coupled gas and dust. Globally in protoplanetary disks, gas and dust orbit with a sub-Keplerian velocity because the gas is supported by a pressure gradient directed radially away from the star. Locally at a maximum in the gas pressure, the orbital velocity of gas and dust is Keplerian, though. The radial drift of the dust towards the star, which is a consequence of the dust not being supported by a global pressure gradient like the gas, slows down as the dust approaches the gas pressure maximum (dashed arrow). Thus, dust piles up in the maximum. In addition, the orbital velocity is super-Keplerian at the side of the maximum facing the star since the local gas pressure gradient is directed inwards. Dust therefore drifts towards the maximum also from this side (dashed arrow).

and dust around the bump that are referred to as zonal flows: At a local maximum in the gas pressure, both gas and dust orbit with the Keplerian speed. The orbital speed of gas and dust is sub-Keplerian on the outer side of the maximum with respect to the star – like the global one, the local gradient in the gas pressure is directed towards larger radii – but in fact super-Keplerian on its inner side. The latter is because the local pressure gradient is directed towards smaller radii and the centrifugal force thus balances both stellar gravity and pressure gradient. The inwards radial drift of the dust slows down as it approaches a pressure maximum. In addition, dust that is located close to a maximum on its inner side drifts outwards towards the maximum. Consequently, dust piles up in a pressure maximum.

This dust concentration is found to be sufficiently strong to trigger further enhancement by the streaming instability, both in the case of the magnetorotational instability (see Sect. 4.3; Johansen et al. 2007, 2011; Dittrich et al. 2013) and in the case of the vertical shear instability (see Sect. 4.4.1; SJB20). Particularly in the former case, gravitationally unstable dust clumps form if dust with a Stokes number of ~ 0.1 and the canonical ratio of dust to gas surface density in the interstellar medium of 1% are considered (Johansen et al. 2007, 2011; Dittrich et al. 2013). This is also true if the drag of the dust onto the gas and thus the streaming instability are not taken into account (Dittrich et al. 2013). It is interesting to note that in pressure bumps, the fastest growing mode of the linear streaming instability is not the secular mode (see Sect. 3.1; Auffinger and Laibe 2018). The mechanism by which the non-linear instability concentrates dust (see Sect. 3.2) is not associated with pressure bumps, though (Li et al. 2018).

Carrera et al. (submitted) study the formation of planetesimals induced by the streaming instability in a model of a pressure bump that is based on the dust rings observed in protoplanetary disks (see Fig. 1.1). In their model, planetesimals do not form because the dust is concentrated in the pressure bump strongly enough to directly collapse under its self-gravity,

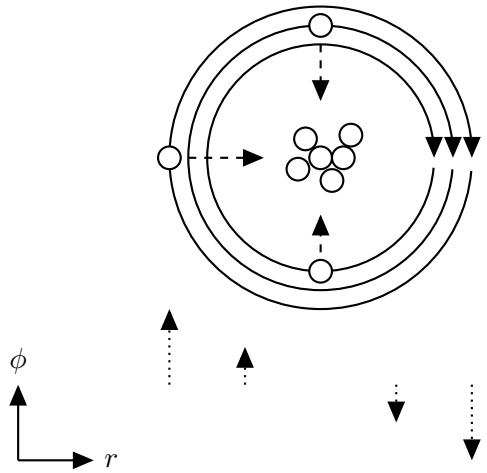

Figure 3.10: Illustration of dust trapping in an anticyclonic vortex in the gas. The dotted arrows show the orbital velocity of gas and dust relative to the orbital velocity at the centre of the vortex. Protoplanetary disks rotate counterclockwise, with the Keplerian orbital velocity decreasing with increasing radial distance to the star (see Eq. 2.24). That is, the formation of cyclonic gas vortices, which rotate counterclockwise like the disk, is inhibited by the Keplerian shear. In contrast, clockwise-rotating anticyclonic vortices in the gas, as the one depicted with solid arrows, are reinforced by the shear. Since the disk rotates counterclockwise, the Coriolis force resulting from the vortical motion is directed towards the centre of the vortex (dashed arrows). The gas in the vortex is stabilised against this Coriolis force by an outwards-directed pressure gradient. Dust that is sufficiently tightly coupled to the gas to follow the vortical motion, on the other hand, drifts towards the centre of the vortex and is trapped there.

but via the streaming instability. Therefore, planetesimal formation does not require dust to be trapped in the pressure bump because its radial drift is completed halted. It is sufficient that the drift is slowed down, resulting in dust concentration that is enhanced by the streaming instability. Planetesimals emerge when a dust-to-gas surface density ratio of 1% and centimetre-sized dust are considered, though not when millimetre-sized dust is taken into account instead. The authors note that the latter might be a result of the limited resolution they employ.

While small dust grains and aggregates pass through the gap which a planet carves into a protoplanetary disk, large aggregates accumulate in the pressure maximum at the outer edge of this gap (e.g., Whipple 1972; Paardekooper and Mellema 2006; Pinilla et al. 2012; Zhu et al. 2012; Weber et al. 2018; Haugbølle et al. 2019; Drążkowska et al. 2019; Eriksson et al. 2020). Eriksson et al. (2020) show that this accumulation results in planetesimal formation via the streaming instability even for dust aggregates as small as 100 µm or 1 mm and a dust-to-gas surface density ratio of 1%.

VORTICES Dust can be trapped in anticyclonic vortices in the gas caused by the magnetorotational instability (Béthune et al. 2016), the subcritical baroclinic instability (see Sect. 4.4.2; Raettig et al. 2015), or the Rossby wave instability (Inaba and Barge 2006; Lyra et al. 2008, 2009b; Meheut et al. 2012; Zhu et al. 2014; Zhu and Stone 2014; Flock et al. 2020)[3]. I show an illustration

[3]The Rossby wave instability is a linear instability arising from a bump in the gas surface density or pressure – induced by, for instance, a planet (Lyra et al. 2009a; Zhu et al. 2014; Zhu and Stone 2014) – and resulting in the

of the mechanism that leads to this trapping in Fig. 3.10. As protoplanetary disks rotate counterclockwise, anticyclonic vortices in them rotate clockwise. Therefore, they amplify the shear resulting from the Keplerian orbital velocity decreasing with increasing radial distance to the star (see Eq. 2.24). In contrast, the formation of cyclonic vortices that rotate counterclockwise is counteracted by the Keplerian shear. Given the orientation of the disk rotation, the rotation of an anticyclonic vortex entails a Coriolis force that is directed towards its centre. The Coriolis force on the gas is balanced by a pressure gradient, with the gas pressure being highest at the centre of the vortex – this state of the gas is called geostrophic.

Dust that is coupled to the gas, on the other hand, is caused by the Coriolis force to spiral towards the centre of the vortex and accumulate there (Barge and Sommeria 1995; Tanga et al. 1996; Johansen et al. 2004). This dust trapping is strongest if the Stokes number of the dust is of order unity since more tightly coupled dust with smaller Stokes numbers follows the vortical motion of the gas, while more loosely coupled dust with larger Stokes numbers is less affected by the vortical gas motion and thus by the Coriolis force (Barge and Sommeria 1995; Tanga et al. 1996; Johansen et al. 2004; Meheut et al. 2012; Raettig et al. 2015). However, dust concentration in gas vortices can lead to their dissolution (Johansen et al. 2004; Inaba and Barge 2006; Raettig et al. 2015): The gas adjusts to the motion of the dust rather than vice versa as soon as the dust density exceeds the gas density and the drag of the dust onto the gas thus dominates over that of the gas onto the dust.

Raettig et al. (2015) find that the subcritical baroclinic instability gives rise to vortices in which the density of dust with a Stokes number of one grows sufficiently high to trigger the streaming instability even if the dust-to-gas surface density ratio is as low as 10^{-4}. This is discussed in more detail in Sect. 4.4.2. The vortices induced by the Rossby wave instability trap dust with Stokes numbers between ~ 0.01 and ~ 10, with the surface density ratio in the vortices exceeding the canonical interstellar medium value by one or two orders of magnitude (Zhu et al. 2014; Zhu and Stone 2014). Enough mass in centimetre-sized dust can accumulate in these vortices for the formation of planets as massive as Mars or Earth (Lyra et al. 2008, 2009a,b; Meheut et al. 2012).

EDDIES The studies of dust concentration in turbulent eddies by Cuzzi et al. (2008, 2010) and Chambers (2010) suggest that they give rise to the formation of planetesimals with sizes of tens to hundreds of kilometers from dust with a stopping time comparable to the turnover time scale at the dissipation scale, corresponding to millimetre-sizes. However, these studies possibly overestimate the efficiency with which such dust is concentrated (Pan et al. 2011; Hartlep and Cuzzi 2020). Hartlep and Cuzzi (2020) find that centimetre-sized dust is required for 10 km- to 100 km-sized planetesimals to emerge. The size distribution of these planetesimals is unimodal, with a peak at ~ 100 km (Cuzzi et al. 2010; Chambers 2010; Hartlep and Cuzzi 2020). This size distribution is comparable to that of primordial asteroids inferred by Delbo' et al. (see Sect. 3.4; 2017, 2019). On the other hand, the streaming instability leads to the formation of planetesimals of similar sizes, but with a different size distribution (see Sect. 3.3). Nonetheless, dust accumulation in turbulent eddies and by the streaming instability occur on different scales: Planetesimals form by collapse of dust clumps with sizes of 10^4 km or less in

formation of vortices (Lovelace et al. 1999; Li et al. 2000, 2001).

the case of turbulent eddies (Cuzzi et al. 2001, 2008; Hartlep and Cuzzi 2020), and of clumps inside filaments with sizes of some to some ten percent of the gas scale height in the case of the streaming instability (see Fig. 3.3). The gas scale height amounts to 0.35 au and 6.25 au at radial distances to the star of 5 au and 50 au in the disk model presented in Appendix A (see Eq. A.7).

Ice lines An ice line, the radial location at which a given molecule – most of the work I discuss here focuses on water – condensates or evaporates[4], is conducive to planetesimal formation in multiple regards. To begin with, the dust-to-gas density ratio is naturally higher outside an ice line, where the respective molecule is present in its solid form, than inside the ice line, where the molecule is gaseous. In particular, the inwards radial motion of the solids is more rapid than that of the vapour (Cuzzi and Zahnle 2004; Ciesla and Cuzzi 2006; Garaud 2007). The density ratio outside the ice line is further enhanced by vapour diffusing over the ice line, from inside to outside, and condensing there (Stevenson and Lunine 1988; Cuzzi and Zahnle 2004; Ciesla and Cuzzi 2006; Garaud 2007; Estrada et al. 2016; Armitage et al. 2016; Schoonenberg and Ormel 2017; Drążkowska and Alibert 2017; Schoonenberg et al. 2018). This also gives rise to larger dust sizes outside the ice line (Ros and Johansen 2013; Ros et al. 2019).

Furthermore, dust piles up inside an ice line because its radial drift is more rapid outside the ice line (Saito and Sirono 2011; Estrada et al. 2016; Ida and Guillot 2016; Schoonenberg and Ormel 2017; Drążkowska and Alibert 2017; Schoonenberg et al. 2018). This is since dust with smaller sizes and thus Stokes numbers drifts more slowly, assuming that the Stokes number is less than one (see Eqs. 2.28 and 3.7). On the one hand, the size of dust is reduced when one of its components evaporates as the dust crosses the respective ice line (Saito and Sirono 2011; Ida and Guillot 2016; Schoonenberg and Ormel 2017). On the other hand, Estrada et al. (2016), Drążkowska and Alibert (2017), and Schoonenberg et al. (2018) find that dust grows to larger sizes outside the water ice line because the relative velocities required for ice aggregates to fragment under mutual collisions are greater than for silicates (see Sect. 2.3). I note, however, that Gundlach et al. (2018) and Musiolik and Wurm (2019) show that water ice is not more prone to sticking when colliding than silicates.

Owing to the effects described above, the dust-to-gas density ratio at an ice line can be sufficiently enhanced for the streaming instability to induce planetesimal formation (Estrada et al. 2016; Armitage et al. 2016; Schoonenberg and Ormel 2017; Drążkowska and Alibert 2017; Schoonenberg et al. 2018). The enhancement is found to be stronger outside the ice line than inside (Estrada et al. 2016; Schoonenberg and Ormel 2017; Drążkowska and Alibert 2017; Schoonenberg et al. 2018). Drążkowska and Alibert (2017) and Schoonenberg et al. (2018) determine the amount of planetesimals forming via the streaming instability in models of the water ice line including sticking and fragmentation of dust aggregates under mutual collisions. The former authors find planetesimals to emerge only outside the ice line and only if the global dust-to-gas surface density ratio amounts to at least 2%, with both the amount of planetesimals forming and the width of the region in which they form increasing with the surface density ratio.

[4]Ice lines exist not only in the radial, but also in the vertical dimension (Krijt et al. 2016a).

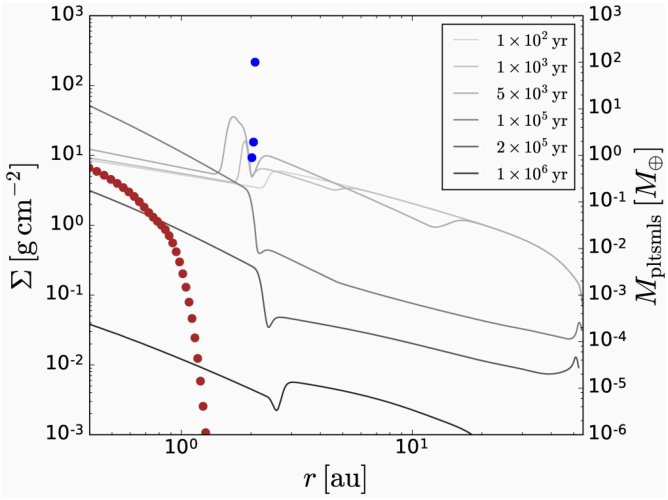

Figure 3.11: Figure adopted from Schoonenberg et al. (2018, their Fig. 11, reproduced with permission ©ESO). Surface density of dust Σ (left ordinate) and mass of planetesimals $M_{\rm pltsmls}$ (right ordinate) as functions of the radial distance to the star r, with the planetesimal mass being given in units of Earth masses $M_\oplus$. The figure represents a model of the water ice line, sticking and fragmentation of colliding dust aggregates, as well as the streaming instability. The global dust-to-gas surface density ratio in the model is equal to 2%. The presence of the water ice line is reflected in a bump in the dust surface density (solid lines). Planetesimals forming outside the ice line and between the ice line and the star are plotted as blue and brown dots, respectively. The total mass of the former planetesimals is as high as ~ 100 Earth masses, while that of latter planetesimals amounts to only a few Earth masses.

While the dependence of the mass in planetesimals on the global surface density ratio is similar in the models by Schoonenberg et al. (2018), ~ 10 Earth masses form even if the surface density ratio is equal to the canonical interstellar medium value. Figure 3.11 depicts the dust surface density and the planetesimal masses in one of their models in which the dust-to-gas surface density ratio is twice as high as that in the interstellar medium. The location of the ice line is evident from a bump in the dust surface density. While planetesimal formation occurs both inside and outside the ice line, the mass in planetesimals is two orders of magnitude higher on the outer side than on the inner side. With regard to the discrepancies between the two studies, I note that Drążkowska and Alibert (2017) assume the streaming instability to give rise to planetesimal formation only if the Stokes number of the dust exceeds 0.01, while Schoonenberg et al. (2018) employ a minimum Stokes number of 0.001. The latter is consistent with the results of the parameter study conducted by Yang et al. (2017), as depicted in Fig 3.4 and given in Eq. 3.28. In the study by Ida and Guillot (2016), enough dust mass can pile up owing to the slower radial dust drift inside an ice line for direct gravitational collapse and planetesimal formation.

An additional effect leading to dust concentration at an ice line arises when the magnetorotational instability is assumed to be the dominant source of turbulence and as such to induce inwards transport of gas mass at the ice line (Kretke and Lin 2007; Brauer et al. 2008; Drążkowska et al. 2013). The protoplanetary disk is considered to be in a steady state and the transport rate of gas mass thus to be equal on the inner and the outer side of the ice line. The magnetorotational instability drives weaker turbulence outside the ice line where the dust density is higher

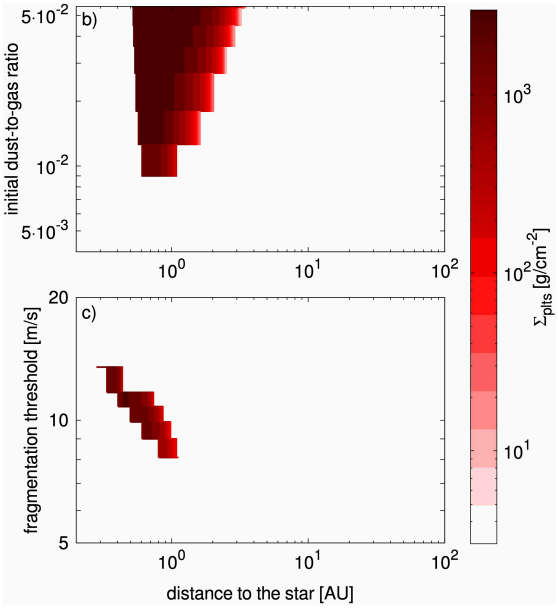

Figure 3.12: Figure adapted from Drążkowska et al. (2016, their Fig. 6, reproduced with permission ©ESO). Surface density of planetesimals $\Sigma_{\rm plts}$ (colour-coded) as a function of the radial distance to the central star in a model including the mutual drag between gas and dust as well as sticking and fragmentation of dust aggregates under mutual collisions. Because radially drifting dust piles up in this region, the streaming instability can induce planetesimal formation at radii ranging from 0.3 au to 3 au. It is evident, though, that planetesimals emerge only if the initial ratio of dust to gas surface density is greater than 1% (upper panel) and the minimum relative velocity resulting in fragmentation of aggregates amounts to between $8\,{\rm m\,s^{-1}}$ and $15\,{\rm m\,s^{-1}}$ (lower panel).

(Sano et al. 2000; Ilgner and Nelson 2006). Since the turbulent strength is less, the gas density must be greater on the outer side for the transport rate to be constant across the ice line. Therefore, the ice line constitutes a bump in the gas pressure in which dust piles up. Weaker gas turbulence further entails lower relative velocities between colliding dust aggregates, which thus can grow to larger sizes outside the ice line (Brauer et al. 2008; Drążkowska et al. 2013). However, I note that a number of hydrodynamical instabilities, including the streaming instability, cause turbulence with a strength that is comparable to or higher than that induced by the magnetorotational instability if the latter is suppressed by non-ideal magnetohydrodynamics effects (see Chapter 4).

DUST PILE-UPS Because the speed of its radial drift depends on the radial distance to the star, dust naturally piles up in protoplanetary disks even if they are considered to be laminar and the gas and dust surface density and gas pressure profiles in them to be smooth (Stepinski and Valageas 1996; Youdin and Shu 2002; Youdin and Chiang 2004; Birnstiel et al. 2012; Drążkowska et al. 2016; Gonzalez et al. 2017a,b). This is true even if dust with a uniform size is taken into account and the drag of the dust on the gas neglected (Stepinski and Valageas 1996; Youdin and Shu 2002).

Drążkowska et al. (2016) present models including growth and fragmentation of dust aggregates under mutual collisions and the mutual drag between gas and dust. In these models,

the dust-to-gas surface density ratio in pile-ups of dust can be high enough for the streaming instability to induce planetesimal formation. I show the surface density of these planetesimals in Fig. 3.12. As can be seen, planetesimals can emerge in a region between radii of 0.3 au and 3 au. Their formation requires the initially uniform dust-to-gas surface density ratio to be equal to the interstellar medium value of 1% or higher and the minimum relative velocity that leads to fragmentation of colliding aggregates to lie in the range between $8\,\mathrm{m\,s^{-1}}$ and $15\,\mathrm{m\,s^{-1}}$. In addition, planetesimal formation occurs only if the radial drift of dust pile-ups slows down because of the drag of the dust onto the gas. This slow-down, which gives rise to the non-linear streaming instability, is explained in Sect. 3.2. The mass in planetesimals forming in the models by Drążkowska et al. (2016) amounts to several tens of Earth masses for a surface density ratio of 1%, and more for higher surface density ratios.

Gonzalez et al. (2017a) study similar models and describe a mechanism that they dub self-induced dust traps (see also Gonzalez et al. 2017b): As the dust density approaches the gas density, the speed of the inward radial drift of the dust decreases, while the gas drifts outwards with increasing speed (see Eqs. 3.6 and 3.7). Thus, a dust overdensity entails the formation of a bump in the gas pressure because of the outward gas drift in the overdensity. The overdensity is enhanced by dust being trapped in this pressure bump. Gonzalez et al. (2017a) find that in these dust traps the dust-to-gas density ratio can increase to order unity as well as that dust grows to Stokes numbers greater than one. These conditions enable planetesimal formation via the streaming instability. Self-induced dust traps emerge in all disk models considered by Gonzalez et al. (2017a), with the initially homogeneous dust-to-gas density ratio in the models ranging from 1% to 5%. I note that they assume that dust aggregates fragment under mutual collisions if their relative velocities amount to at least $10\,\mathrm{m\,s^{-1}}$ to $25\,\mathrm{m\,s^{-1}}$. These threshold values are comparatively high (see Sect. 2.3). The total dust mass concentrated in the dust traps ranges from a few to a few tens of Earth masses and increases with both the initial dust-to-gas density ratio and the minimum relative velocity leading to fragmentation (Gonzalez et al. 2017a).

While self-induced dust traps are related to the mechanism by which the non-linear streaming instability concentrates dust (see Sect. 3.2), there are a few key differences (Gonzalez et al. 2017a). Firstly, self-induced dust traps span tens of astronomical units while the filaments formed by the streaming instability are smaller than an astronomical unit. Secondly, while the streaming instability can be active at all radial distances to the star, self-induced dust traps form at radii of several tens of au. Thirdly, while the streaming instability only requires a global radial gradient in the gas pressure, gradients in the Stokes number of the dust and the dust-to-gas density ratio are further necessary for self-induced dust traps to emerge. Finally, self-induced dust traps develop if only the radial dimension is considered, in contrast to the linear streaming instability (see Sect. 3.1).

PHOTOEVAPORATION During their evolution, protoplanetary disks loose gas owing to photoevaporation. The escaping gas only transports dust with it that is sufficiently tightly coupled to the gas for the drag exerted by the gas to overcome the stellar gravity acting on the dust, corresponding to sizes of at most microns (Takeuchi et al. 2005; Alexander and Armitage 2007). This implies that photoevaporation entails an increase in the dust-to-gas density ratio that is condu-

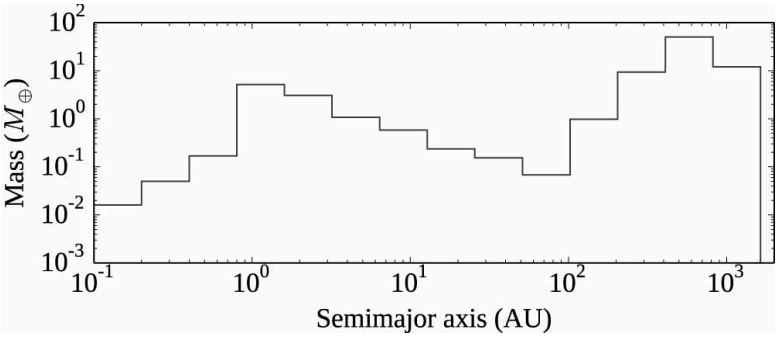

Figure 3.13: Figure adopted from Carrera et al. (2017, their Fig. 11, reproduced with permission ©AAS). Mass in planetesimals as a function of the radial distance to the star. The figure represents a model of a protoplanetary disk that evolves owing to stellar accretion and photoevaporation, collisions of dust aggregates resulting in sticking, bouncing, and fragmentation, as well as planetesimal formation owing to the streaming instability. In addition, the water ice line is taken into account. The spatial distribution of planetesimal mass is shown when the gas component of the disk has dissipated entirely owing to accretion and photoevaporation. At this point, eight Earth masses in planetesimals have emerged in the innermost 3 au, only two Earth masses between 3 au and 100 au, and as much as 73 Earth masses beyond 100 au.

cive to planetesimal formation (Throop and Bally 2005; Alexander and Armitage 2007; Carrera et al. 2017; Ercolano et al. 2017). However, the models presented by Sellek et al. (2020) suggest that the enhancement in the density ratio is not significant because dust that has grown too large to be entrained in the escaping gas is instead lost owing to its inwards radial drift. In particular, since photoevaporation by far-ultraviolet radiation causes a depletion of dust in the outer disk regions, not enough dust drifts towards the inner regions to compensate for the dust drifting away from these regions.

Nevertheless, dust accumulates in the pressure bump at the edge of the gap carved into a protoplanetary disk by photoevaporation (Alexander and Armitage 2007; Carrera et al. 2017; Ercolano et al. 2017). This gap forms because the stellar accretion rate declines with time until at some point the rate at which gas is lost via photoevaporation at a given radial location is greater than the rate at which it is replenished by stellar accretion (e.g., Alexander et al. 2014). This point is reached earliest at the so-called critical radius, the radial location at which photoevaporation is strongest. The gap thus begins to open at this critical radius.

Carrera et al. (2017) study evolution models of protoplanetary disks, the most comprehensive of which includes stellar accretion, photoevaporation by ultraviolet and X-ray radiation, collisional dust growth and the bouncing and fragmentation barriers, the water ice line, as well as planetesimal formation induced by the streaming instability. In this model, within 2.7 Myr several tens of Earth masses in planetesimals form owing to a combination of the streaming instability and photoevaporation by far-ultraviolet radiation at radial distances to the star of 100 au or more. Nevertheless, closer to the star planetesimals formation occurs only afterwards, as a consequence of photoevaporation causing a gap to open in the disk. Figure 3.13 shows the spatial distribution of planetesimal mass when accretion and photoevaporation have lead to the gas in the disk dispersing completely after 4 Myr. In total, eight, two, and 73 Earth masses have formed at radii less than 3 au, between 3 and 100 au, and greater than 100 au, respectively. Ercolano et al. (2017) conduct a similar study of planetesimal formation induced by

the streaming instability and photoevaporation. These authors employ a different photoevaporation model, though, with the photoevaporation being caused by X-ray radiation. In their models, in contrast to the ones by Carrera et al. (2017), only a few Earth masses in planetesimals form in total, and none at radii greater than 100 au.

OTHER INSTABILITIES A non-linear drafting instability occurs when dust sediments through gas in hydrostatic equilibrium (Lambrechts et al. 2016; Capelo et al. 2019). If the drag of the dust onto the gas is neglected, the settling velocity of the dust is determined by the strength of the gravity that causes the settling as well as of the drag by the gas onto the dust which counteracts the settling because gas in hydrostatic equilibrium is at rest (see Sect. 4.1). However, the drag exerted by the dust on the gas leads to dust overdensities sedimenting faster than the surrounding dust. The gas in these overdensities is dragged along by the dust and follows its motion. The ambient gas, on the other hand, moves in the opposite direction as a consequence of momentum conservation. The drag it exerts on the ambient dust impedes the sedimentation of this dust. Thus, the faster-settling dust overdensities accumulate dust ahead of them in the direction of settling, grow in density, and settle even more rapidly. This mechanism results in instability and enhancements of the dust density by an order of magnitude (Lambrechts et al. 2016).

While this instability is related to both the streaming instability and the dust settling instability (see below and Sect. 4.5.2) – particularly, the mechanisms by which the drafting and the non-linear streaming instability (see Sect. 3.2) concentrate dust are very similar – the drafting instability operates in the absence of rotation and thus of the radial dust drift. Like the dust settling instability but in contrast to the streaming instability, the drafting instability can concentrate very small dust aggregates since its growth rate is independent of the dust size on small scales. In fact, the instability grows fastest on small scales, corresponding to hundreds to millions of kilometres in protoplanetary disks. However, it is active only if the initial dust-to-gas density ratio amounts to at least 0.1. It can further be suppressed by the viscosity of the gas. In laboratory experiments including gas and dust grains, Capelo et al. (2019) observe two effects that are reminiscent of the drafting instability but also of the streaming instability: Dust grains approach other grains in their vicinity in the direction of their motion. In addition, grains comprised in dust overdensities move more rapidly through the gas than isolated grains.

Huang et al. (2020) report a meso-scale instability arising at the edges of the dust rings observed in protoplanetary disks (see Fig. 1.1). They conduct simulations in which rings form owing to dust piling up in pressure bumps. If the drag of the dust onto the gas is neglected, the orbital velocity of gas and dust smoothly transitions from super-Keplerian at the inner side of the pressure bump, i.e. on the side of the bump facing the star, to sub-Keplerian at the outer side. Because of the drag exerted by the dust, however, the orbital velocity deviates from this smooth profile in that it is closer to Keplerian within the dust ring forming around the pressure bump. The shear between the gas within and outside of the ring gives rise to the instability. It induces the formation of vortices in which the surface density of 250 µm-sized dust exceeds the gas surface density. I note that this instability is reminiscent of a Kelvin-Helmholtz instability. Huang et al. (2020) find that the instability operates on greater length scales than the

streaming instability. Additionally, they simulate the radial-azimuthal plane, while the linear streaming instability only grows if the vertical dimension is taken into account (see Sect. 3.1).

Other instabilities that result from the mutual drag between gas and dust and cause dust concentration include the dust settling instability (Squire and Hopkins 2018a,b) and the Kelvin-Helmholtz instability induced by the shear between the gas in the dust mid-plane layer and the gas in the adjacent layers (Weidenschilling 1980; Weidenschilling and Cuzzi 1993). These instabilities are reviewed in detail in Sects. 4.5.2 and 4.5.3. The former instability is active only as long as dust sediments and therefore does not lead to concentration that is sufficiently strong for the dust density to exceed the gas density (Krapp et al. 2020). The Kelvin-Helmholtz instability, on the other hand, induces dust overdensities in excess of the Roche density if the dust-to-gas surface density ratio is greater than the one in the interstellar medium by a factor of a few or a few ten (Sekiya 1998; Youdin and Shu 2002; Chiang 2008). However, the streaming instability dominates over the Kelvin-Helmholtz instability if dust with a Stokes number of 0.01 or greater is present (Bai and Stone 2010b).

4
Instabilities and turbulence

In the previous chapter, I detail how the streaming instability arises and how it concentrates dust in filaments, thus inducing planetesimal formation. In this chapter, more specifically in Sect. 4.5.1, the streaming instability is considered as a source of turbulence, which is its fundamental nature as an instability. In addition to the streaming instability, I discuss a number of instabilities that drive turbulence in protoplanetary disks and have been studied in connection with the streaming instability. The strength of the gas turbulence in the disk mid-plane and the dust scale height that these instabilities induce are summarised in Table 4.1. I begin by reviewing observational constraints on disk turbulence.

4.1 Observations

It is challenging to observationally obtain the strength of the turbulence in protoplanetary disks since the turbulent motions are obscured by faster orbital and thermal motions, i.e. the turbulence is subsonic (Flaherty et al. 2018). Recently, high-resolution observations, especially with ALMA, have yielded a number of constraints on the turbulent strength. These mostly stem from either the broadening of molecular emission lines or from the dust scale height.

Line broadening has been studied at (sub-)millimetre-wavelengths in the disks around TW Hydrae (Hughes et al. 2011; Teague et al. 2016, 2018; Flaherty et al. 2018), HD 163296 (Hughes et al. 2011; Flaherty et al. 2015, 2017), DM Tauri (Guilloteau et al. 2012; Flaherty et al. 2020), MWC 480 (Flaherty et al. 2020), and V4046 Sagittarii (Flaherty et al. 2020). Upper limits of the Mach number of the turbulent gas motions of $\lesssim 0.1$ are observed in the outer regions (at distances from the star greater than 10 au) of all of these disks with the exception of DM Tauri. In this disk, Guilloteau et al. (2012) and Flaherty et al. (2020), respectively, infer Mach numbers of 0.4–0.5 and 0.25–0.33. Flaherty et al. (2020) find no indications of either gravitational (see Sect. 4.2) or magnetorotational instability (see Sect. 4.3) being the source of the stronger turbulence in the disk around DM Tauri as it is neither gravitationally unstable nor more strongly ionised by far-ultraviolet and X-ray radiation than MWC480 and V4046 Sagittarii (see also Simon et al. 2018b). Infrared observations indicate the presence of transonic turbulence in the

innermost regions (within a fraction of an astronomical unit) of some disks (Carr et al. 2004; Najita et al. 2009; Doppmann et al. 2011).

The turbulent strength can be derived from the observed vertical dust scale height because the latter is determined by sedimentation owing to the stellar gravity and turbulent diffusion attaining a balance. In the following, I derive an estimate of the dust scale height by equating the settling and the diffusion time scale (e.g., Armitage 2010; Birnstiel et al. 2016)[1]. I consider only dust with a Stokes number much smaller than unity, i.e. dust that is tightly coupled to the gas since its stopping time is much less than the dynamical time scale $1/\Omega_\mathrm{K}$. Thus, it reaches the terminal velocity with which it settles to the mid-plane instantaneously. I further assume a vertical hydrostatic equilibrium of the gas, that is to say there are no systematic vertical gas motions. (This does not exclude random turbulent motions.)

Under these conditions, the gravitational acceleration towards the mid-plane, $-\Omega_\mathrm{K}^2 z$, and the deceleration that is induced by the drag exerted by the gas, $v_{\mathrm{d},z}/t_\mathrm{d,stop}$, can be equated to obtain the settling velocity of the dust

$$v_{\mathrm{d},z} = -\Omega_\mathrm{K}^2 z t_\mathrm{d,stop} = -\Omega_\mathrm{K}\mathrm{St} z. \tag{4.1}$$

The settling time scale, i.e. the time scale over which dust settles from the height z to the mid-plane, amounts to

$$\tau_\mathrm{d,sett} = \frac{z}{|v_{\mathrm{d},z}|} = \frac{1}{\Omega_\mathrm{K}\mathrm{St}}. \tag{4.2}$$

The time scale of the turbulent dust diffusion can be expressed as $\tau_\mathrm{d,diff} \sim z^2/\nu_\mathrm{d,turb}$. Assuming this similarity to be an equality and the turbulent viscosity of the dust to be similar to that of the gas given in Eq. 2.8 yields

$$\tau_\mathrm{d,diff} = \frac{z^2}{\mathcal{M}_{\mathrm{g},z}^2 c_\mathrm{s} H_\mathrm{g}}. \tag{4.3}$$

Sedimentation and diffusion attain an equilibrium at the height at which these two time scales are equal. This height, the dust scale height, can thus be estimated as

$$H_\mathrm{d} = \sqrt{\frac{\mathcal{M}_{\mathrm{g},z}^2 c_\mathrm{s} H_\mathrm{g}}{\Omega_\mathrm{K}\mathrm{St}}} = \sqrt{\frac{\mathcal{M}_{\mathrm{g},z}^2}{\mathrm{St}}} H_\mathrm{g}, \tag{4.4}$$

where I obtain the second equality by using that $H_\mathrm{g} = c_\mathrm{s}/\Omega_\mathrm{K}$ in the thin-disk approximation, i.e. under the assumption that the radial distance to the star is much greater than the height. I note that the more sophisticated derivations by Dubrulle et al. (1995) and Carballido et al. (2006) yield the same equation, with the former authors considering tight coupling between gas and dust as I do, but the latter authors loose coupling. This is despite loosely coupled dust not attaining its terminal velocity before reaching the mid-plane, and therefore oscillating around this plane. These oscillations are excited by turbulence and damped by the drag exerted by the gas. Youdin and Lithwick (2007) propose

$$H_\mathrm{d} = \sqrt{\frac{\mathcal{M}_{\mathrm{g},z}^2}{\mathcal{M}_{\mathrm{g},z}^2 + \mathrm{St}}} H_\mathrm{g} \tag{4.5}$$

[1]The ratio of diffusion to settling time scale is referred to as Péclet number.

to account for the fact that the gas scale height is an upper limit of the dust scale height. The two scale heights are comparable if $\mathrm{St} \ll \mathcal{M}_{\mathrm{g},z}^2$. Otherwise, stronger sedimentation leads to the dust forming a vertically smaller mid-plane layer. From Figure 1.1, it can be seen that the dust scale height in the disk surrounding IM Lupi increases with the radial distance to the star.

Mulders and Dominik (2012) employ a radiative transfer code including dust settling and turbulent diffusion to model the spectral energy distributions of samples of Herbig Ae/Be stars, T Tauri stars[2], and brown dwarfs. They obtain a turbulent α-parameter (see Sect. 2.2; Shakura and Sunyaev 1973) of 10^{-4}, corresponding to a Mach number $\mathcal{M}_{\mathrm{g},z} = \sqrt{\alpha}$ of 0.01, for a typical dust size distribution ranging from sub-microns to millimetres and the canonical dust-to-gas density ratio in the interstellar medium of 1%. This turbulent strength does not vary with the stellar type.

Similar to Mulders and Dominik (2012), Pinte et al. (2016) and Ohashi and Kataoka (2019) apply radiative transfer modelling to fit spatially resolved ALMA observations of the ring-and-gap structure in the disks surrounding HL Tauri (see Fig. 1.1) and HD163296, respectively. Pinte et al. (2016), who presuppose a dust size distribution, infer a scale height of millimetre-sized dust of $\sim$1 au at a radial distance of 100 au in the former disk, which is equivalent to $\sim 10\%$ of the gas scale height. This scale height yields an α-value of the turbulent viscosity of 3×10^{-4} or $\mathcal{M}_{\mathrm{g},z} = 0.017$.

Ohashi and Kataoka (2019), on the other hand, derive both the dust size and the scale height from the polarisation of the dust emission. They find a dust scale height of at most one third and of two thirds, respectively, of the gas scale height inside and outside of the ring located at a radius of 70 au in the disk around HD163296. Furthermore, they estimate a turbulent α-value of $\lesssim 1.5 \times 10^{-3}$ ($\mathcal{M}_{\mathrm{g},z} \lesssim 0.039$) in the gap at $r = 50$ au and a greater value of 0.015–0.3 ($\mathcal{M}_{\mathrm{g},z} = 0.12$–$0.55$) in the gap at $r = 90$ au. However, the latter significantly exceeds the upper limit of the Mach number of $\lesssim 0.06$ at $r \gtrsim 30$ au that Flaherty et al. (2015, 2017) obtain from line broadening observations of this disk.

Assuming that the gaps in the HD163296 disk are caused by planets, Liu et al. (2018) perform simulations to reproduce ALMA observations of both gas and dust in the disk. Like Ohashi and Kataoka (2019), they find a radially increasing turbulent viscosity, with α-values ranging from $\sim 5 \times 10^{-5}$ ($\mathcal{M}_{\mathrm{g}} \approx 0.007$) in the gap at a radius of 60 au to $\sim 7.5 \times 10^{-3}$ ($\mathcal{M}_{\mathrm{g}} \approx 0.09$) at radii greater than 300 au. I note that, while the former turbulent strength is consistent with the upper limits inferred in the studies by Flaherty et al. (2015, 2017) and Ohashi and Kataoka (2019), the latter is in contrast with both studies.

To investigate whether the observed rings in these disks are the result of dust concentration in gas pressure bumps (see Sect. 3.5), Dullemond et al. (2018) compare DSHARP observations of five disks with simulation data. From the measured width of the rings, they derive lower limits of the α-value of the radial gas motions between 10^{-4} and 2×10^{-3} (Mach numbers between 0.01 and 0.045) for a dust size of 200 µm, with these lower limits being proportional to the dust size.

[2] Herbig Ae/Be stars are pre-main sequence stars of spectral types B and A, while T Tauri stars are those of types F, G, K, and M.

4.2 Gravitational instability

A protoplanetary disk, or more generally any rotating gaseous disk, is gravitationally unstable if its self-gravity overcomes rotation and thermal pressure that act to stabilise it (Safronov 1960; Toomre 1964). This condition can be expressed in terms of the dimensionless Toomre Q-parameter, which is given by

$$Q = \frac{c_\mathrm{s}\kappa}{\pi G \Sigma_\mathrm{g}}, \tag{4.6}$$

where Σ_g is the gas surface density and the epicyclic frequency $\kappa = \Omega_\mathrm{K}$ in a disk with Keplerian rotation[3] (e.g., Armitage 2010; Kratter and Lodato 2016). While the sound speed and the epicyclic frequency in the numerator quantify the stabilising effects of thermal pressure and rotation, respectively, the destabilising self-gravity is reflected in $G\Sigma_\mathrm{g}$ in the denominator. Disks with $Q < 1$ are unstable to linear axisymmetric perturbations that cause the formation of axisymmetric rings. Non-axisymmetric linear instability, which induces spiral arms, can also occur for $Q \gtrsim 1$. More generally, the critical value of Q differs from one but remains of order unity if, for instance, differentially instead of uniformly rotating disks or disks with a finite vertical extent rather than razor-thin disks are considered. The instability leads to fragmentation if the gas cooling time scale is sufficiently short, and otherwise saturates in a non-linear state of gravitoturbulence[4] (e.g., Kratter and Lodato 2016).

Gravitational instability requires a disk mass of at least $\sim 10\%$ of the mass of the central star (Kratter and Lodato 2016). Therefore, a disk is more likely to be unstable at an early stage when it and the star it surrounds are still accreting from an envelope. Among a sample of more than a hundred Class II YSOs, which are associated with disks that are no longer embedded in an envelope as I study in this thesis, Andrews et al. (2013) find that only very few exceed the threshold disk-to-star mass ratio necessary for instability. Spiral arms have been observed in a number of disks around Class II stars (Pérez et al. 2016; Huang et al. 2018). However, these spiral arms can not only be caused by gravitational instability, but also by planetary or stellar companions.

Riols et al. (2020b) perform simulations of gravitoturbulent gas and dust with Stokes numbers ranging from 0.0016 to 0.16. The strength of the gas turbulence in their simulations is depicted in Fig 4.1. The turbulence is anisotropic: The Mach number of the vertical motions amounts to ~ 0.01 in the mid-plane and to ~ 0.1 at heights of one gas scale height above and below this plane, while the radial Mach number ranges between 0.1 and 1 at all heights (see also Shi et al. 2016). This turbulence elevates dust with a Stokes number of 0.01 and 0.1 to a scale height of $\sim 70\%$ and $\sim 30\%$, respectively, of the gas scale height. However, Riols et al. (2020b) find both the turbulent strength and the dust scale height to increase with the resolution.

[3] Generally, the square of the epicyclic frequency is given by

$$\kappa^2 = \frac{2\Omega}{r}\frac{\mathrm{d}(\Omega r^2)}{\mathrm{d}r}. \tag{4.7}$$

In a Keplerian disk, $\Omega_\mathrm{K} \propto r^{-3/2}$ (see also Eq. 2.24) and thus $\kappa^2 = \Omega_\mathrm{K}^2$.

[4] It is debated whether gravitoturbulence involves an energy cascade over a range of length scales that is characteristic of turbulence (Kratter and Lodato 2016).

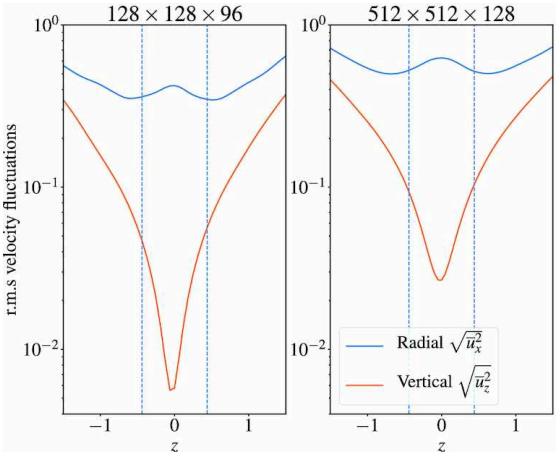

Figure 4.1: Figure adopted from Riols et al. (2020b, their Fig. 1). Radial (blue line) and vertical (orange line) gas velocity relative to the sound speed as a function of the height z in units of gas scale heights. The left and right panel show the velocities in a simulation with a lower and a higher resolution, respectively, with the resolutions being given in the panel captions. The radial Mach number ranges between 0.1 and 1 at all heights. In contrast, the vertical Mach number increases from $\sim 10^{-2}$ in the mid-plane to $\sim 10^{-1}$ one gas scale height away from this plane. The gas motions in both the radial and the vertical dimension are stronger if the resolution is higher.

Dust is concentrated in pressure bumps and vortices that are caused by gravitoturbulence. In two-dimensional simulations of razor-thin disks – the streaming instability operates in the radial-vertical plane and thus not in these simulations – the accumulation of dust with Stokes numbers between 0.1 and 1 is strong enough to lead to the dust collapsing under its self-gravity and forming planetesimals, even if the drag of the dust onto the gas is not included (Gibbons et al. 2014, 2015; Shi et al. 2016). The maximum surface density of the dust is smaller by about an order of magnitude if its self-gravity is not taken into account, but still reaches values of 10^3 to 10^4 times the mean surface density (Gibbons et al. 2012, 2014).

On the other hand, Riols et al. (2020b), who do not consider the self-gravity of the dust, show that the dust concentration is weaker in three- than in two-dimensional simulations. Even when considering dust with the largest Stokes number they simulate, $\mathrm{St} = 0.16$, the dust-to-gas (volume) density ratio exceeds one only occasionally and for not more than a few orbital periods in a three-dimensional simulation. From this, they conclude that the streaming instability is inhibited by gravitoturbulence. I note, however, that the maximum resolution of the simulations by Riols et al. (2020b) amounts to 26 grid cells per gas scale height, which is insufficient to resolve the formation of gravitationally unstable dust clumps owing to the streaming instability (Yang and Johansen 2014).

4.3 Magnetorotational instability

The magnetorotational instability is a linear instability that operates in disks in which the orbital velocity declines with increasing distance to the central source of gravity, such as protoplanetary disks, and which are permeated by a weak magnetic field with a vertical component (Velikhov 1959; Chandrasekhar 1960; Balbus and Hawley 1991).

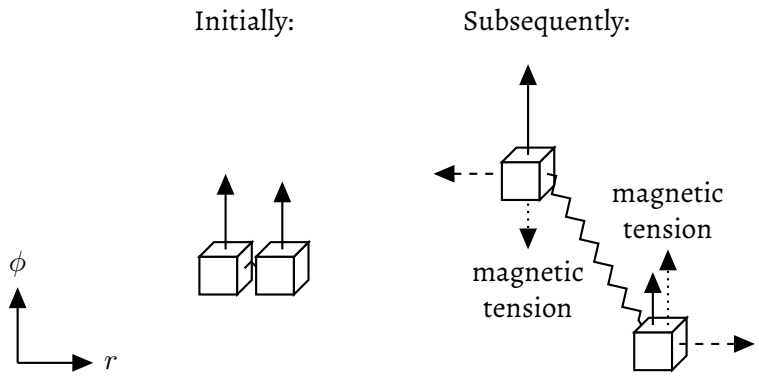

Figure 4.2: Toy model of the magnetorotational instability. The cubes depict two gas parcels, while the zigzag line represents a field line of a vertical magnetic field coupling the parcels. Initially (left), a linear perturbation leads to the parcels being radially displaced from the same to adjacent orbits. Thus, the orbital velocity (solid arrows) of the parcel on the inner orbit is higher than that of the parcel on the outer orbit. The orbital motion of the parcels results in the field line being stretched (right). To counter this stretching, magnetic tension acts to decelerate the parcel on the inner orbit and accelerate that on the outer orbit (dotted arrows) by transporting angular momentum from the former to the latter. However, this only causes further stretching of the field line: On the one hand, since the parcel on the inner orbit slows down, the stellar gravity acting on it is no longer balanced by the centrifugal force. Therefore, the parcel drifts radially inwards. On the other hand, the centrifugal force on the parcel on the outer orbit exceeds the stellar gravity, and the parcel drifts outwards. The magnetic tension grows in strength, while the two parcels drift apart more and more. This leads to instability.

The instability can be explained using the toy model depicted in Fig. 4.2 (e.g., Turner et al. 2014): I consider two gas parcels which are located at the same radius in a protoplanetary disk, i.e. orbiting with the same Keplerian velocity, but at different heights. These parcels are coupled by a field line of a vertical magnetic field. If they are displaced to different radii by a linear perturbation, the one at the larger radius orbits more slowly than the one at the smaller radius since the Keplerian velocity $v_\mathrm{K} \propto r^{-1/2}$ (see Eq. 2.24). This results in a stretching of the field line. Magnetic tension counteracts this stretching by transferring angular momentum from the parcel on the inner orbit to the one on the outer orbit to equalise the orbital velocities of the two parcels. However, this angular momentum transport leads to the field line being stretched even more. This is because the orbital velocity of the parcel on the outer orbit is now super-Keplerian and the centrifugal force, which is no longer balanced by the stellar gravity, causes it to move outwards. The parcel on the inner orbit, on the other hand, orbits with a sub-Keplerian velocity and therefore moves inwards. Further stretching of the field line gives rise to stronger magnetic tension, more angular momentum transfer, the two parcels drifting apart even more, and thus instability. Nevertheless, if the magnetic field is too strong the magnetic tension can prevent the parcels from separating.

In ideal magnetohydrodynamics, it is assumed that the gas is perfectly coupled to the magnetic field – neutral atoms and molecules via collisions with ions and electrons. However, this assumption is valid only if the gas is sufficiently well-ionised. In protoplanetary disks, this is the case in the thermally ionised innermost regions, within 0.1–1 au from the star (Gammie

1996; Latter and Balbus 2012), and at the disk surface which is ionised by stellar far-ultraviolet radiation (Perez-Becker and Chiang 2011)[5].

The bulk of a protoplanetary disk is only weakly ionised, though (e.g., Turner et al. 2014). Therefore, non-ideal magnetohydrodynamic effects must be taken into account:

- Ambipolar diffusion: Ions and electrons are coupled to the magnetic field, neutrals are decoupled. The magnetorotational instability is damped by ambipolar diffusion (Blaes and Balbus 1994; Lesur et al. 2014; Bai 2014, 2015, 2017; Gressel et al. 2015; Simon et al. 2015a).

- Hall effect: Electrons are coupled to the magnetic field, while ions and neutrals are decoupled, the latter owing to collisions with the former. If the vertical component of the magnetic field is aligned with the rotation axis of the disk, the radial and azimuthal field components are enhanced by the Hall shear instability (Kunz 2008; Lesur et al. 2014). This instability results from a feedback loop between Keplerian rotation and the Hall effect: As described above in the context of the toy model, rotation causes an increase in the strength of the azimuthal component. This leads to the Hall effect amplifying the radial component, which in turn results in rotation further enhancing the azimuthal component. As a consequence of the Hall shear instability, gas mass is transported radially inwards and angular momentum outwards, which is conducive to stellar accretion (Lesur et al. 2014; Bai 2014, 2015, 2017; Simon et al. 2015b). If, on the other hand, the vertical magnetic field component and the disk rotation axis are anti-aligned, the Hall effect counteracts the tendency of Keplerian rotation to amplify the azimuthal field component and thus the magnetorotational instability (Wardle 1999).

- Ohmic resistivity: Neutrals are decoupled from the magnetic field, collisions with the neutrals lead to the ions and electrons being decoupled as well. Similar to ambipolar diffusion, Ohmic resistivity suppresses the magnetorotational instability (Gammie 1996; Jin 1996; Lesur et al. 2014; Bai 2014, 2017; Gressel et al. 2015; Simon et al. 2015a).

Which effect dominates depends on the magnetic field strength and the gas density. For a fixed field strength, ambipolar diffusion is most important where the density is low, the Hall effect at intermediate densities, and Ohmic resistivity in high-density regions (e.g., Turner et al. 2014). Given that the density decreases with increasing radius and height in protoplanetary disks, this yields a layered disk structure: Ohmic resistivity is dominant in the mid-plane of the inner disk, the Hall effect at intermediate heights in the inner disk and in the mid-plane at intermediate radii, and ambipolar diffusion in the upper layers of the inner disk, away from the mid-plane at intermediate radii and everywhere in the outer disk regions.

Bai (2014, 2015) performs simulations including all three effects to investigate the strength of the turbulence driven by the magnetorotational instability at various radii and heights. Figure 4.3 shows the gas velocity at $r = 1$ au. Both in the radial and the vertical dimension, it

[5] At the surfaces of protoplanetary disks, magnetically launched winds transport angular momentum away from the disks and thus facilitate stellar accretion (Blandford and Payne 1982; Bai 2014, 2015, 2017; Gressel et al. 2015, 2020; Béthune et al. 2017).

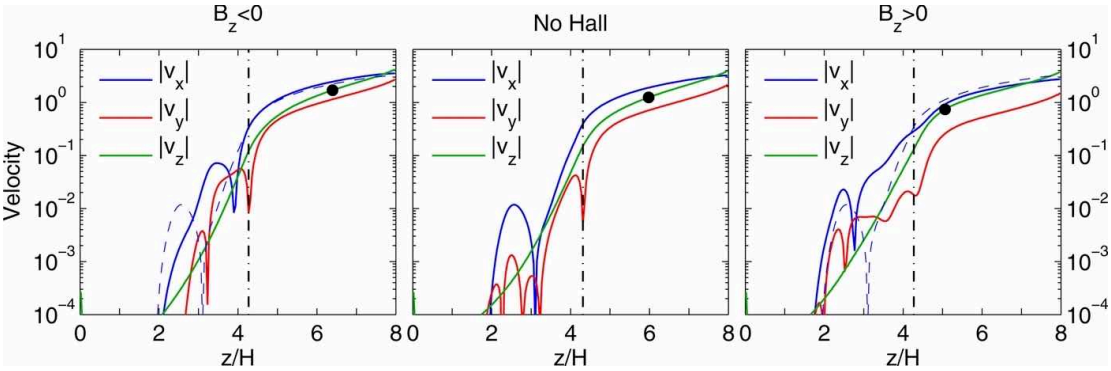

Figure 4.3: Figure adapted from Bai (2014, their Fig. 2, reproduced with permission ©AAS). Gas velocity, expressed in terms of a Mach number, as a function of the height z in units of gas scale heights H. The blue, red, and green lines depict the absolute radial v_x, azimuthal v_y, and vertical v_z velocity components. At heights of up to two gas scale heights, all three components are negligibly small. From about two gas scale heights to the height which marks the transition from disk to magnetically launched disk wind (dash-dotted line), the radial and vertical Mach numbers increase to ~ 0.1. The left and right panel represent a simulation in which the vertical magnetic field component and the disk rotation axis are aligned and anti-aligned, respectively, while the middle panel shows the velocities in a simulation in which the Hall effect is neglected. As can be seen, the Hall effect influences the turbulent strength only marginally.

is negligible within two gas scale heights above and below the mid-plane[6]. From there, the velocity increases to Mach numbers of ~ 0.1 at the disk surface. At radii ranging from 5 au to 60 au, on the other hand, the vertical Mach number amounts to ~ 0.01 in the mid-plane and between 0.1 and 1 at the surface (Bai 2015). A comparison of simulations including and excluding the Hall effect shows that the effect results in a marginally higher and lower turbulent strength if vertical magnetic field component and disk rotation axis are aligned and anti-aligned, respectively (Lesur et al. 2014; Bai 2015). While the above Mach numbers are determined for a ratio of the thermal to the magnetic pressure of 10^5, Simon et al. (2018b) find that at $r = 100$ au values of this ratio greater than 10^3–10^4 and a weak ionisation of the gas are necessary for the magnetorotational instability to drive turbulence with a strength that is consistent with ALMA observations (see Sect. 4.1).

In numerical studies of the dust dynamics that are caused by the magnetorotational instability, of the three effects only ambipolar diffusion has been taken into account as it is the dominant effect in the outer disk regions. Simulations confirm the theoretical prediction that the ratio of the dust to the gas scale height is proportional to $\mathrm{St}^{-1/2}$ (see Eq. 4.4; Xu et al. 2017; Riols and Lesur 2018; Riols et al. 2020a). For a Stokes number of 0.1 and a thermal-to-magnetic pressure ratio of 10^4, the dust-to-gas scale height ratios obtained from simulations range from 4% to 20% (Xu et al. 2017; Riols and Lesur 2018; Yang et al. 2018; Riols et al. 2020a). The scale height ratio increases with the pressure ratio (Riols and Lesur 2018; Riols et al. 2020a).

The magnetorotational instability – even when considering ambipolar diffusion – induces a greater dust scale height than the streaming instability in isolation (see Sect. 4.5.1). Nonetheless, Yang et al. (2018) find that the turbulence driven by the magnetorotational instability

[6]The disk region around the mid-plane in which the magnetorotational instability is strongly suppressed by non-ideal magnetohydrodynamic effects and therefore causes only weak turbulence, if at all, is commonly referred to as dead zone (Gammie 1996).

does not inhibit the formation of filaments by the streaming instability because the magnetorotational instability gives rise to stronger vertical than radial dust diffusion. While in their simulations the Mach number of the turbulent gas velocity is comparable in the radial and vertical dimension, the correlation time is longer in the latter dimension (see also Zhu et al. 2015). That is to say, at a fixed point in space, the vertical gas velocity remains similar for a longer time than the radial one. Yang et al. (2018) conclude that the ability of the streaming instability to concentrate dust is not significantly affected by strong vertical diffusion as long as the radial diffusion is only weak. In simulations of the streaming instability and the magnetorotational instability under the assumption of ideal magnetohydrodynamics, the magnetorotational instability induces pressure bumps in which dust accumulates (see Sect. 3.5), with the streaming instability further enhancing these dust concentrations (Johansen et al. 2007, 2011).

4.4 Purely hydrodynamic instabilities

In this section, I review hydrodynamic instabilities that operate in the absence of dust. I do not discuss the zombie vortex instability because its effect on dust dynamics, and thus on the streaming instability, has not been investigated (Marcus et al. 2013, 2015, 2016; Lesur and Latter 2016; Umurhan et al. 2016b; Barranco et al. 2018). In contrast to the other three purely hydrodynamic instabilities introduced below, this non-linear instability is active if the gas cooling time scale is long, i.e. the gas is locally adiabatic or close to adiabatic (Lesur and Latter 2016; Barranco et al. 2018). Because of their different requirements in terms of cooling time, the four instabilities operate in different regions of protoplanetary disks (Malygin et al. 2017; Pfeil and Klahr 2019).

4.4.1 Vertical shear instability

The vertical shear instability[7] is a linear instability which, as the name indicates, operates if the orbital velocity varies with height (Urpin and Brandenburg 1998; Urpin 2003; Arlt and Urpin 2004; Nelson et al. 2013). The free energy in the resulting shear between vertically adjacent gas layers is the source of energy of the instability (Barker and Latter 2015). Furthermore, a sufficiently short cooling time scale is necessary – optimally, the gas is locally isothermal (Nelson et al. 2013; Lin and Youdin 2015).

Vertical profiles of the orbital velocity are induced by, for example – and somewhat counterintuitively – radial temperature profiles. Such profiles are ubiquitous in protoplanetary disks (Andrews and Williams 2005). A radial temperature gradient gives rise to a misalignment between pressure and density gradient, a state that is referred to as baroclinic[8]. The variation with height of the orbital frequency of a baroclinic gas is a consequence of the Taylor-Proudman theorem. If the gas is in equilibrium, that is to say it is steady in time and there is

[7] The vertical shear instability in differentially rotating protoplanetary disks is related to the Goldreich-Schubert-Fricke instability in differentially rotating stars (Goldreich and Schubert 1967; Fricke 1968).

[8] Gas with a constant temperature and thus aligned density and pressure gradients is called barotropic.

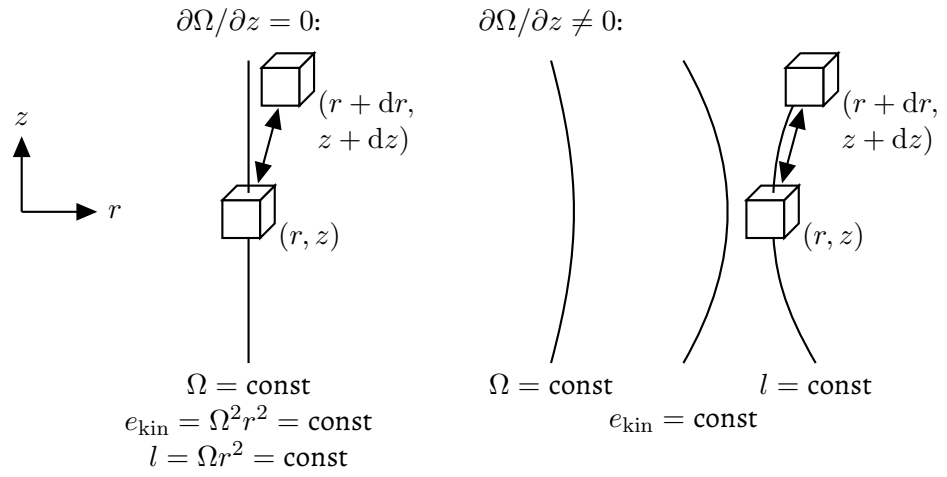

Figure 4.4: Toy model to determine the linear stability of protoplanetary disks in which the orbital frequency Ω is independent of (left) or depends on (right) the height z. While only the radial-vertical plane is shown, the solid lines represent surfaces on which the orbital frequency, the specific kinetic energy e_{kin}, and the specific angular momentum l are constant. Two gas parcels, represented by cubes, at the locations (r, z) and $(r + \mathrm{d}r, z + \mathrm{d}z)$ are interchanged under conservation of their angular momenta. Their orbital frequencies are adjusted to match the ones at their new locations. If afterwards their total kinetic energy is greater than before the interchange, instability can occur. If the rotation is Keplerian only, i.e. $\partial\Omega/\partial z = 0$, the disk is stable according to the Rayleigh criterion. In contrast, a height-dependence of the orbital frequency can result in instability.

no advection, its equation of motion reads

$$0 = \Omega^2 r\hat{r} - \frac{1}{\rho_{\mathrm{g}}}\nabla P + \nabla\Phi_{\mathrm{S}}, \tag{4.8}$$

where Φ_{S} is the stellar gravitational potential. The first term on the right-hand side of the equation represents the centrifugal force. Computing the curl of this equation results in

$$\frac{\partial\Omega^2}{\partial z} r\hat{\phi} = \nabla\frac{1}{\rho_{\mathrm{g}}} \times \nabla P \tag{4.9}$$

since the curl of a gradient and $\partial\Omega/\partial\phi$ are zero. Here, $\hat{\phi}$ is the unit vector in the azimuthal direction.

TOY MODEL Toy models of linear instabilities in protoplanetary disks can be constructed using the following approach (e.g., Barker and Latter 2015; Lyra and Umurhan 2019): Firstly, two gas parcels are interchanged, conserving their angular momenta; secondly, the orbital velocities of the parcels are adapted to their new orbits; and, thirdly, the total energy of the parcels after the interchange is compared to the total energy in the original state. Instability arises if the total energy in the new state is less, i.e. the new state is energetically preferred. This approach is illustrated in Fig. 4.4 for a disk with purely Keplerian rotation, $\partial\Omega/\partial z = 0$, as well as for a disk with a height-dependence of the orbital frequency, $\partial\Omega/\partial z \neq 0$. The figure shows the radial-vertical plane, with surfaces of constant angular frequency Ω, constant specific angular

momentum $l = \Omega r^2$, and constant specific kinetic energy $e_{\mathrm{kin}} = \Omega^2 r^2 = l^2/r^2$ being marked as solid lines. Two gas parcels at the locations (r, z) and $(r + \mathrm{d}r, z + \mathrm{d}z)$ are depicted as cubes.

The total kinetic energy of the two parcels before the interchange can be expressed as

$$e_{\mathrm{kin,init}} = \frac{l^2(r,z)}{r^2} + \frac{l^2(r+\mathrm{d}r, z+\mathrm{d}z)}{(r+\mathrm{d}r)^2} \tag{4.10}$$

and afterwards as

$$e_{\mathrm{kin}} = \frac{l^2(r,z)}{(r+\mathrm{d}r)^2} + \frac{l^2(r+\mathrm{d}r, z+\mathrm{d}z)}{r^2}. \tag{4.11}$$

Expanding the square of the specific angular momentum $l^2(r + \mathrm{d}r, z + \mathrm{d}z)$ in a Taylor series around (r, z) yields

$$l^2(r+\mathrm{d}r, z+\mathrm{d}z) = l^2(r,z) + \frac{\partial l^2(r,z)}{\partial r}\mathrm{d}r + \frac{\partial l^2(r,z)}{\partial z}\mathrm{d}z + \mathcal{O}(\mathrm{d}r^2) + \mathcal{O}(\mathrm{d}z^2). \tag{4.12}$$

If terms of second and higher order are neglected, the difference between the total kinetic energy in the new and in the original state amounts to

$$e_{\mathrm{kin}} - e_{\mathrm{kin,init}} = \left[\frac{\partial l^2(r,z)}{\partial r}\mathrm{d}r + \frac{\partial l^2(r,z)}{\partial z}\mathrm{d}z\right]\left[\frac{1}{r^2} - \frac{1}{(r+\partial r)^2}\right]. \tag{4.13}$$

Instability can occur if this difference is negative. Because the second factor on the right-hand side is always positive, the criterion for instability is

$$\frac{\partial l^2(r,z)}{\partial r}\mathrm{d}r + \frac{\partial l^2(r,z)}{\partial z}\mathrm{d}z < 0. \tag{4.14}$$

In a disk in which the orbital frequency is independent of height, this criterion reduces to the Rayleigh criterion $\partial l^2(r)/\partial r < 0$. Keplerian disks are stable with respect to this criterion because $\Omega_{\mathrm{K}} = v_{\mathrm{K}}/r \propto r^{-3/2}$ (see Eq. 2.24) and thus $l \propto r^{1/2}$. That is, gas parcels that are displaced radially inwards or outwards from their equilibrium state, in which the gravitational and the centrifugal force acting on them are in balance, execute epicyclic oscillations in the radial-azimuthal plane around this state rather than continuing to move inwards or outwards.

In contrast, if the orbital frequency changes with height and the term $\partial l^2(r,z)/\partial z$ is negative (or positive), instability – to be more precise, the vertical shear instability – can arise if the vertical displacement of the two gas parcels $\mathrm{d}z$ is positive (or negative) and large enough compared to the radial displacement $\mathrm{d}r$. Specifically, interchanging the parcels along a surface of constant angular momentum, as shown in Fig. 4.4, leads to a new state that is neither more nor less energetically preferable than the original state. This is since $l^2(r + \mathrm{d}r, z + \mathrm{d}z) = l^2(r, z)$ and therefore $e_{\mathrm{kin}} - e_{\mathrm{kin,init}} = 0$.

VERTICAL BUOYANCY This toy model of the vertical shear instability does not involve the stabilising effect of buoyancy and the consequential necessity of a short gas cooling time scale. To illustrate this, I assume that a vertical density profile ensures that the gas is in hydrostatic equilibrium while the temperature does not depend on height, as among others in the model of

the gas in protoplanetary disks that I present in Appendix A. Under these conditions and if the cooling time is infinitely long, a gas parcel that is displaced upwards adapts to the lower pressure of the gas around it by expanding and cooling. Since this lower ambient pressure results from a decrease in density, but not in temperature, the parcel is denser than the surrounding gas after the displacement. Buoyancy thus causes the parcel to move back downwards. If cooling occurs infinitely rapid, on the other hand, buoyancy does not stabilise the gas. This is because the temperature and therefore also the density of the upwards-moving parcel remain the same as those of the gas surrounding it.

Mathematically, the Schwarzschild criterion[9] can be applied to determine whether linear perturbations in the gas are stabilised by buoyancy. According to this criterion, gas is stable and oscillates around the equilibrium state with the Brunt-Väisälä frequency if this frequency is real. In contrast, if the frequency is imaginary, buoyancy leads to convection. The square of the Brunt-Väisälä frequency is given by

$$\mathcal{N}_z^2 = -\frac{1}{\gamma\rho_\mathrm{g}}\frac{\partial P}{\partial z}\frac{\partial}{\partial z}\ln\left(\frac{P}{\rho_\mathrm{g}^\gamma}\right), \tag{4.15}$$

where γ is the adiabatic index. The last derivative on the right-hand side expresses the dependence of the specific entropy $s \propto \ln(P/\rho_\mathrm{g}^\gamma)$ on height. In the case of locally isothermal gas with a vertically constant temperature, that is to say $\gamma = 1$ and $\partial p/\partial z = c_\mathrm{s}^2\partial\rho_\mathrm{g}/\partial z$, it is equal to

$$\frac{\partial}{\partial z}\ln\left(\frac{P}{\rho_\mathrm{g}^\gamma}\right) = c_\mathrm{s}^2\frac{\partial}{\partial z}\ln\left(\frac{\rho_\mathrm{g}}{\rho_\mathrm{g}}\right) = 0, \tag{4.16}$$

and the Brunt-Väisälä frequency vanishes. If $\gamma > 1$, on the other hand, the specific entropy increases with height. Since the pressure decreases with height, the square of the Brunt-Väisälä frequency is therefore positive.

The vertical shear instability can operate if the cooling time scale is short enough for the destabilising vertical shear to overcome the stabilising buoyancy, that is locally

$$\tau_\mathrm{g,cool} \lesssim \frac{|r\partial\Omega/\partial z|}{\mathcal{N}_z^2} \tag{4.17}$$

(Lin and Youdin 2015)[10]. Under the assumption that the temperature is independent of height, while its dependence on the radial distance to the star can be expressed as a power law with an exponent q, Lin and Youdin (2015) show that instability globally requires

$$\tau_\mathrm{g,cool} < \frac{H_\mathrm{g}|q|}{(\gamma-1)r\Omega_\mathrm{K}}. \tag{4.18}$$

[9]The Schwarzschild criterion is part of the more general Solberg-Høiland criteria for the stability of differentially rotating disks with radial and vertical density and temperature profiles (Tassoul 1978; Rüdiger et al. 2002; Lyra and Umurhan 2019).

[10]The maximum local cooling time scale for which the vertical instability is active is related to the Richardson number $\mathrm{Ri} = \mathcal{N}_z^2/(r\partial\Omega/\partial z)^2$ (Lin and Youdin 2015). This dimensionless number quantifies the ratio of the strengths of buoyancy and shear.

In the gas disk model described in Appendix A, $q = -1/2$ (see Eq. A.1). Since the disk aspect ratio H_g/r is generally less than one, a cooling time that is shorter than the dynamical time scale $1/\Omega_\mathrm{K}$ is thus necessary. I note that the instability operates in the simulations conducted by Stoll and Kley (2014, 2016) and Flock et al. (2017, 2020) which include a radiative transfer model of protoplanetary disks.

LINEAR MODES AND NON-LINEAR SATURATED STATE Two classes of linear modes of the vertical shear instability, body modes and surface modes, have been identified numerically and analytically (Nelson et al. 2013; Barker and Latter 2015; Umurhan et al. 2016a). As predicted by the toy model above, in which instability requires the ratio of vertical $\mathrm{d}z$ to the radial displacement $\mathrm{d}r$ to be sufficiently great, both classes are characterised by their vertical wavelengths being larger than the radial ones. The radial wavelengths of the body modes are longer than those of the surface modes, though.

Numerically studying the surface modes is problematic in two regards: Firstly, the surface modes appear at the artificial vertical boundaries of simulation domains (Nelson et al. 2013; Barker and Latter 2015; Lin and Youdin 2015). Their growth rate increases with the vertical domain extent because the vertical shear is stronger at greater heights (Lin and Youdin 2015). Nonetheless, Barker and Latter (2015) find that the surface modes can as well grow at transitions in the vertical structure of realistic disks in which the temperature varies with height. Secondly, the fastest-growing surface modes are the ones with the shortest wavelengths (Barker and Latter 2015; Lin and Youdin 2015). That is, in simulations convergence with respect to the resolution can only be reached if these modes are either damped by viscosity (Barker and Latter 2015) or if the gas is not locally isothermal. The latter is because reducing the cooling time leads to incremental damping of the fastest-growing modes, as shown by Lin and Youdin (2015).

The growth rate of the body modes is less than that of the surface modes (Nelson et al. 2013; Barker and Latter 2015; Umurhan et al. 2016a). Therefore, they appear later in simulations. In contrast to the surface modes, the body modes occupy the bulk of the disk. They evolve from an odd symmetry relative to the mid-plane – at a given radius, gas moves upwards (downwards) above and downwards (upwards) below the mid-plane – to an even symmetry.

The vertical shear instability attains a non-linear saturated state after $\sim$30 orbital periods or later (Nelson et al. 2013; Stoll and Kley 2014). I show the turbulence that is driven by the instability in this state in Fig. 4.5. In the radial-vertical plane, it is characterised by perturbations with a very small ratio of the radial to the vertical wavelength, by a mirror symmetry with respect to the mid-plane, and by being bent slightly outwards. This curvature is consistent with that of the surfaces of constant angular momentum in the toy model depicted in Fig. 4.4. In three-dimensional simulations, the instability leads to the formation of vortices (Richard et al. 2016; Latter and Papaloizou 2018; Manger and Klahr 2018; Flock et al. 2020). The turbulence induces vertical and radial angular momentum transport, the latter of which aids stellar accretion (Arlt and Urpin 2004; Nelson et al. 2013; Stoll and Kley 2014)[11]. However, this transport also acts to eliminate the temperature structure unless the gas is locally isothermal. Therefore, if this is

[11] In studies of the vertical shear instability, the α-parameter is commonly defined as $\alpha \sim v_{\mathrm{g},r} v_{\mathrm{g},\phi}/c_\mathrm{s}^2$ (e.g. Nelson et al. 2013; Stoll and Kley 2014, 2016; Stoll et al. 2017). This definition is more suitable to quantify angular momentum transfer than the definition I use in this thesis, $\alpha = \mathcal{M}_\mathrm{g}^2$.

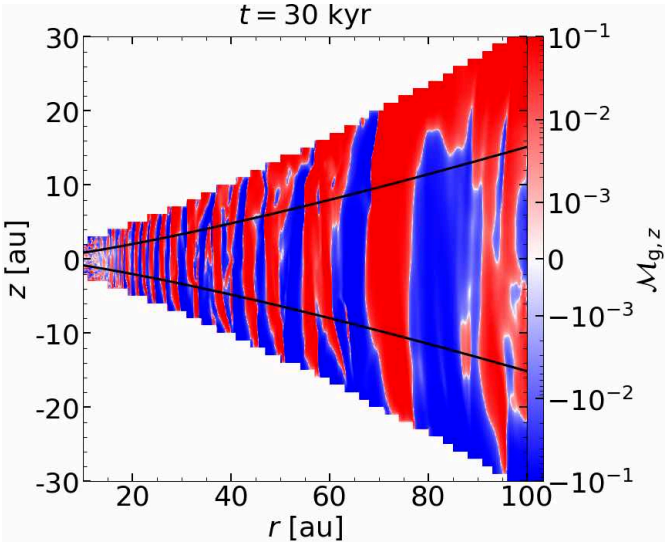

Figure 4.5: Figure adopted from SJB20. Mach number of the vertical gas motions $\mathcal{M}_{g,z}$ as a function of the radial distance r and the height z in a two-dimensional simulation of locally isothermal gas with a radial temperature profile. The turbulence in the simulation is caused by the vertical shear instability in its saturated state. It induces perturbations which are radially small but vertical elongated, slightly bent outwards, and symmetric with respect to the mid-plane. The Mach number is equal to ~ 0.1 at all radii and heights.

not the case, external heating is necessary to maintain the vertical shear and the instability (Stoll and Kley 2014).

Turbulent strength, dust scale height, and interaction with streaming instability

In the three-dimensional radiative transfer simulations of the vertical shear instability performed by Flock et al. (2017), in which the temperature decreases with increasing height, the Mach number of the vertical gas motions ranges between ~ 0.01 in the disk mid-plane and ~ 0.1 at the surface. On the other hand, the Mach number amounts to ~ 0.1 at all heights in the two-dimensional simulations of locally isothermal gas with a vertically constant temperature that we present in SJB20. The instability gives rise to anisotropic turbulence, with the radial velocity of the gas being less than its vertical velocity (Stoll and Kley 2016; Stoll et al. 2017; SJB20). Figure 5 in SJB20 indicates that the radial Mach number ranges between 0.01 and 0.1. Higher turbulent strengths result from stronger vertical shear caused by steeper radial temperature profiles (Nelson et al. 2013; Lin 2019).

The scale height to which dust is elevated by the instability depends on the Stokes number of the dust as well as on the strength of the turbulence and consequently the steepness of the temperature profile (see Eq. 4.5; Lin 2019). In addition, the scale height decreases with increasing ratio of dust to gas surface density if the drag exerted by the dust on the gas is taken into account (Lin 2019; SJB20). The reason for this is the tendency of the dust to sediment towards the mid-plane, which introduces an effective buoyancy in the gas that damps the instability (Lin and Youdin 2017; Lin 2019). To elucidate this, gas and dust can be approximated as a single fluid – a valid approximation if they are tightly coupled owing to their mutual drag

(see Sect. 3.1). While the dust adds to the density of this fluid $\rho_{\mathrm{tot}} = \rho_{\mathrm{g}} + \rho_{\mathrm{d}}$, it does not contribute to its pressure. If the gas is locally isothermal, its equation of state is given by $P = c_{\mathrm{s}}\rho_{\mathrm{g}}$. The one of the fluid can be expressed as $P = c_{\mathrm{s}}(1 - \rho_{\mathrm{d}}/\rho_{\mathrm{tot}})\rho_{\mathrm{tot}}$, though. That is, in contrast to the pure gas the fluid is not locally isothermal and thus stabilised by buoyancy.

Lin (2019) finds that this effective buoyancy leads to the dust scale height decreasing from about the gas scale height to $\sim 5\%$ of it if the dust-to-gas surface density ratio Z increases from 0.01 to 0.1 and dust with a Stokes number of 0.001 is considered. Similarly, the scale height of dust with a higher Stokes number of 0.1 amounts to $\sim 10\%$ of the gas scale height in the simulation with $Z = 0.02$ that is presented in SJB20, but is as low as $\sim 1\%$ in our simulation with $Z = 0.1$.

In SJB20, we study the interaction of the vertical shear instability and the streaming instability. To this end, we compare simulations in which the dust is introduced either at the beginning or after the vertical shear instability has saturated. In the latter case, the vertical shear instability remains the main source of turbulence in the dust layer around the disk mid-plane, although the streaming instability locally drives turbulence. In contrast, the turbulence in the dust layer is caused by the streaming instability if the dust is initialised at the start of the simulations and both instabilities therefore begin to grow at the same time. The fact that the vertical shear instability is suppressed can be explained by the effective buoyancy induced by the dust as well as the streaming instability saturating more rapidly than the vertical shear instability. The vertical shear instability is damped by turbulent viscosity with an α-parameter of at least $\sim 4 \times 10^{-4}$, corresponding to a Mach number of 0.02 (Nelson et al. 2013). The streaming instability gives rise to turbulence with such a strength (see Sect. 4.5.1).

In the simulations conducted by Stoll and Kley (2016) in which only the drag of the gas onto the dust is included, the dust is concentrated radially in short-lived pressure bumps induced by the vertical shear instability (see Sect. 3.5). Dust overdensities arise which exceed the initial density by up to an order of magnitude if the Stokes number of the dust is close to one. Furthermore, dust is trapped in vortices formed by the Rossby wave instability, which in turn is triggered by the vertical shear instability (Flock et al. 2020). A key finding of SJB20 is that, if the drag of the dust onto the gas is taken into account as well, the streaming instability may enhance dust concentrations in pressure bumps caused by the vertical shear instability. The interplay of streaming instability and vertical shear instability gives rise to stronger dust overdensities than the streaming instability in isolation, despite the vertical shear instability inducing larger dust scale heights than the streaming instability (see Sect. 4.5.1). This indicates that a combination of streaming instability and vertical shear instability might lead to planetesimal formation for dust-to-gas surface density ratios and dust sizes for which the streaming instability alone does not (see Sect. 3.2).

4.4.2 Convective overstability and subcritical baroclinic instability

The convective overstability and the subcritical baroclinic instability are related instabilities, the former a linear one operating in the radial-vertical plane and the latter a non-linear one in the radial-azimuthal plane (Klahr and Bodenheimer 2003; Klahr 2004; Petersen et al. 2007a,b; Lesur and Papaloizou 2010; Klahr and Hubbard 2014; Lyra 2014; Latter 2016). While vertical buoyancy can stabilise the vertical shear instability, these instabilities result from the destabil-

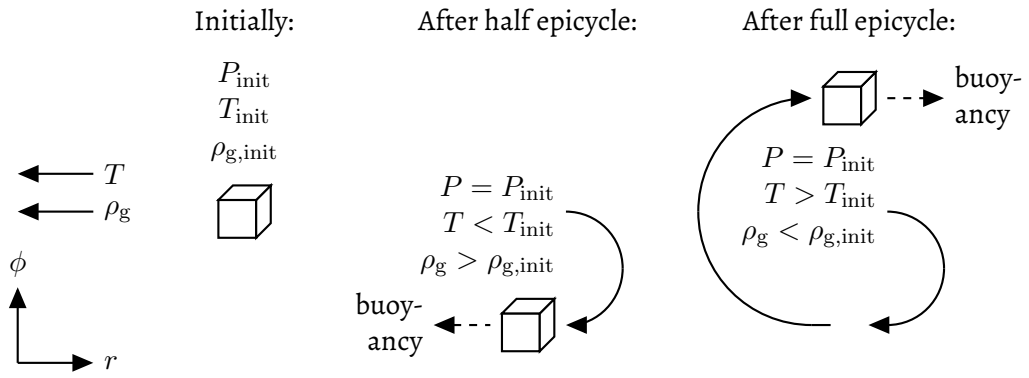

Figure 4.6: Toy model of the convective overstability. A gas parcel with an initial pressure, temperature, and density of $P_{\rm init}$, $T_{\rm init}$, and $\rho_{\rm g,init}$ executes epicyclic motions in the radial-azimuthal plane. The temperature T and density $\rho_{\rm g}$ of the ambient gas decline with increasing radius. During the first half of an epicycle, the parcel moves radially outwards through colder gas. When returning to its initial radial location, it is cooler than initially ($T < T_{\rm init}$). Since its pressure is equal to the initial value ($P = P_{\rm init}$), it it is thus denser ($\rho_{\rm g} > \rho_{\rm g,init}$). Therefore, buoyancy accelerates the radially inwards motion of the parcel in the second half of the epicycle. During this second half, the parcel is in contact with warmer gas. After a full epicycle, it is thus hotter ($T > T_{\rm init}$), but less dense than originally ($\rho_{\rm g} < \rho_{\rm g,init}$). The buoyancy force acting on the parcel is now directed radially outwards and further amplifies its epicyclic motion. This results in instability.

ising effect of radial buoyancy in disks, or regions within disks, in which the entropy decreases with increasing radial distance to the star. The convective overstability is triggered by epicyclic oscillations (Klahr and Hubbard 2014; Lyra 2014; Latter 2016), which can be induced by linear radial perturbations (see Sect. 4.4.1). In contrast, the subcritial baroclinic instability is caused by vortices, i.e. non-linear perturbations (Petersen et al. 2007a,b; Lesur and Papaloizou 2010). In three-dimensional simulations, the subcritical baroclinic instability is the saturated state of the convective overstability as the vortices formed by the latter instability act as seeds for the former (Lyra 2014).

TOY MODEL AND RADIAL BUOYANCY Figure 4.6 depicts a toy model of the convective overstability (Latter 2016; Lyra and Umurhan 2019). In this model, it is assumed that the gas temperature and density decrease with increasing radius as well as that the cooling time scale is finite. The initial pressure, temperature, and density of a gas parcel are denoted by $P_{\rm init}$, $T_{\rm init}$, and $\rho_{\rm g,init}$. The first half of an epicyclic oscillation displaces the parcel radially outwards into colder gas. After half an epicycle, it is thus cooler than initially ($T < T_{\rm init}$). Since the parcel is located at the same radius as initially, its pressure is equal to its initial pressure ($P = P_{\rm init}$), though. Therefore, the parcel is denser than originally ($\rho_{\rm g} > \rho_{\rm g,init}$). Thus, a buoyancy force that is directed radially inwards acts on the parcel and amplifies its epicyclic motion. The second half of this motion brings the parcel into contact with warmer gas. After a full epicycle it returns to its initial radial but not azimuthal location. The pressure of the parcel is the same as the initial pressure ($P = P_{\rm init}$), but its temperature is higher ($T > T_{\rm init}$) and its density thus lower ($\rho_{\rm g} < \rho_{\rm g,init}$). The buoyancy force acting on it is now directed radially outwards and further amplifies the epicyclic oscillation. Instability ensues.

The toy model illustrates that the convective overstability is active only if the gas cooling time is finite. Buoyancy would not amplify the epicyclic oscillations if the cooling time were either infinitely short or infinitely long, that is to say the gas were locally isothermal or locally adiabatic. In the former case, the gas parcel would be heated or cooled to the temperature of the surrounding gas instantaneously, while in the latter case it would not be heated or cooled at all. In either case, the temperature of the parcel would be the same as initially after half an epicycle or a full one. The fact that the instability operates in the radial-vertical plane, not in the radial-azimuthal one as in this model, can be explained by the amplified epicyclic motions being axisymmetric (Lyra and Umurhan 2019). In addition, identical but oppositely directed motions must be executed in vertically adjacent gas layers because of the conservation of mass. A similar toy model can be constructed of the subcritical baroclinic instability (Lesur and Papaloizou 2010; Lyra and Umurhan 2019).

The criterion for linear instability of differentially rotating gas with radial density and temperature profiles can be expressed as

$$\mathcal{N}_r^2 + \kappa^2 < 1. \tag{4.19}$$

It is part of the more general Solberg-Høiland criteria which further include vertical density and temperature profiles (Tassoul 1978; Rüdiger et al. 2002; Lyra and Umurhan 2019). Neglecting the second addend on the left-hand side yields the Schwarzschild criterion in the radial dimension, which is equivalent to the one in the vertical dimension discussed in Sect. 4.4.1. Buoyancy acts destabilising and amplifies epicyclic motions in the case of the convective overstability as well as vortices in the case of the subcritical baroclinic instability if the square of the Brunt-Väisälä frequency

$$\mathcal{N}_r^2 = -\frac{1}{\gamma\rho_\mathrm{g}}\frac{\partial P}{\partial r}\frac{\partial}{\partial r}\ln\left(\frac{P}{\rho_\mathrm{g}^\gamma}\right) < 0. \tag{4.20}$$

The second addend on the left-hand side of Eq. 4.19 reflects the stabilising effect of rotation, with the epicyclic frequency being equal to the Keplerian orbital frequency in Keplerian disks. In fact, if the gas is locally isothermal and the Brunt-Väisälä frequency thus vanishes, Eq. 4.19 reduces to the Rayleigh criterion as introduced in Sect. 4.4.1 since $\kappa = 1/r^3\,\mathrm{d}l^2/\mathrm{d}r$.

That is, the convective overstability – the stability criterion applies to the linear convective overstability, but not necessarily to the non-linear subcritical baroclinic instability – both needs to overcome the stabilising rotation and requires an imaginary Brunt-Väisälä frequency. The former is possible owing to thermal relaxation (Klahr and Hubbard 2014; Lyra 2014) or thermal diffusion (Lesur and Latter 2016) if the gas cooling time is finite. The growth rate of the instability is largest if the cooling time scale is comparable to the dynamical timescale $1/\Omega_\mathrm{K}$ (Klahr and Hubbard 2014; Lyra 2014; Lesur and Latter 2016).

On the other hand, for the Brunt-Väisälä frequency given in Eq. 4.20 to be imaginary, both the pressure and the specific entropy $s \propto \ln(P/\rho_\mathrm{g}^\gamma)$ must decline with increasing radius. This is true for the pressure in protoplanetary disks, but not generally for the entropy (see also Lyra 2014; Lyra and Umurhan 2019). To illustrate this, I assume that the radial density and temperature profiles can be expressed as power laws with the exponents p and q, respectively. Under this assumption, the gradient of the specific entropy $s \propto \ln(\rho_\mathrm{g}^{1-\gamma}T)$ is negative if $(1-\gamma)p + q$ is,

too. In the model of the gas in protoplanetary disks presented in Appendix A, the exponent of the temperature profile amounts to $-1/2$. This exponent is adopted from the minimum mass solar nebula model devised by Hayashi (1981) and is similar to the mean exponent of -0.56 that Andrews and Williams (2005) obtain from an observational survey of more than a hundred disks. Given this exponent and an adiabatic index of $7/5$, i.e. gas that is neither locally isothermal ($\gamma = 1$) nor locally adiabatic ($\gamma = 5/3$), the entropy gradient is negative only if the exponent of the density profile is either close to zero or positive. In contrast, the global density gradient in protoplanetary disks is negative. I note that the convective overstability has been studied only in simulations of regions in disks on a local scale, not of disks on a global scale.

Turbulent strength, dust scale height, and interaction with streaming instability
The convective overstability gives rise to gas turbulence with a Mach number of 0.01–0.1 (Klahr and Hubbard 2014; Lyra 2014). Lyra (2014) shows that this turbulent strength is largely independent of the exponent of the radial temperature profile. However, it increases with the domain size of their simulations without converging. The turbulence driven by the subcritical baroclinic instability is stronger, with its Mach number amounting to 0.1–0.4 if the cooling time scale is comparable to the dynamical time scale (Lyra and Klahr 2011; Raettig et al. 2013). This Mach number, similar to the one induced by the convective overstability, does not vary noticeably with the steepness of the radial pressure gradient (Raettig et al. 2013). Nevertheless, the turbulence is significantly weaker if the cooling time deviates from the dynamical time by one or two orders of magnitude (Lyra and Klahr 2011; Raettig et al. 2013). I note that, from the simulations performed by Raettig et al. (2013), it can be gathered that the Mach number decreases by an order magnitude if the radial extent of the simulation domain is doubled.

Raettig et al. (2015) present simulations of the subcritical baroclinic instability including dust. In Fig. 4.7, I show the vortices in the gas induced by the instability and the trapping of dust in these vortices (see Sect. 3.5). In a simulation of dust with a Stokes number of one and an initial dust-to-gas surface density ratio of 0.01, in which only the drag of the gas onto the dust is included, $\sim 1\%$ of the dust accumulates in overdensities that exceed the gas surface density. Raettig et al. (2015) find that a larger amount of dust is concentrated in the vortices if the drag exerted by the dust on the gas is also taken into account and thus the streaming instability is active. I note, however, that Raettig et al. (2015) simulate the radial-azimuthal plane, while the streaming instability as discovered by Youdin and Goodman (2005) operates in the radial-vertical plane. Nonetheless, overdensities comprise 84% or $56\ \%$ of the dust in a simulation involving the mutual drag between gas and dust with an initial surface density ratio of 10^{-2} or 10^{-4}, respectively. While the former surface density ratio corresponds to the value in the interstellar medium, the latter is two orders of magnitude lower. Dust with smaller Stokes numbers of 0.01 and 0.05 is as well concentrated in vortices, although less strongly than the dust with $\mathrm{St} = 1$ if the drag of the dust onto the gas is not neglected. Nonetheless, gas vortices can disperse if the dust (volume) density in them exceeds the gas (volume) density (Johansen et al. 2004; Inaba and Barge 2006; Raettig et al. 2015). This is since, if the drag exerted by the dust on the gas is stronger than the one by the gas onto the dust, the gas adjusts to the motion of the dust instead of the dust following the vortical motion of the gas.

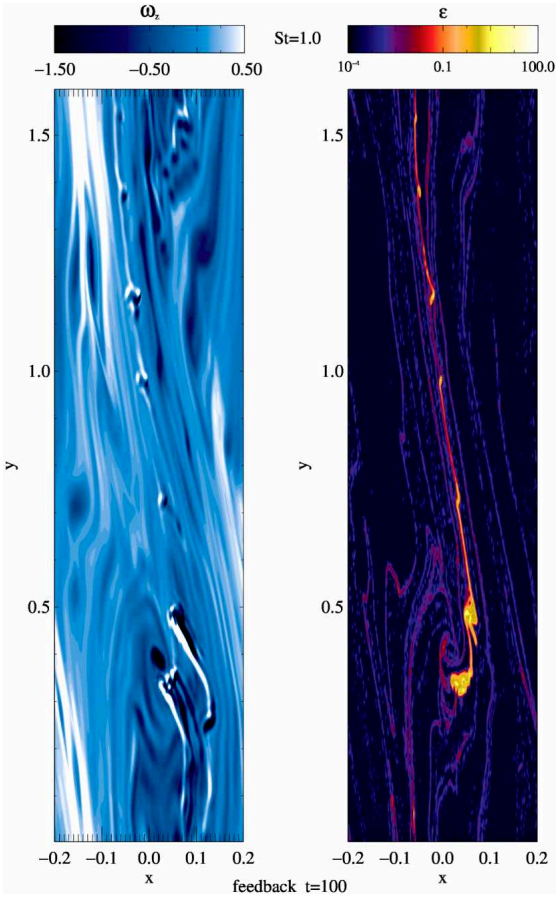

Figure 4.7: Figure adapted from Raettig et al. (2015, their Fig. 3, reproduced with permission ©AAS). Vertical component of the gas vorticity $\omega = \nabla \times v_{\rm g}$, which quantifies the tendency of the gas to rotate (left panel), and dust-to-gas surface density ratio ϵ (right panel) as functions of the radius x and the azimuth y. A simulation of dust with a Stokes number of one, with an initial surface density ratio of 0.01, and including the mutual drag between gas and dust is depicted. In the vortices caused by the subcritical baroclinic instability, the dust is concentrated strongly enough for the surface density ratio to exceed one.

4.5 Hydrodynamic instabilities involving dust

Here, I discuss hydrodynamic instabilities which result from the mutual drag between gas and dust in protoplanetary disks.

4.5.1 Streaming instability

The streaming instability is introduced in detail in Chapter 3. In its saturated state, the instability gives rise to the gas turbulence depicted in Fig. 4.8. Small-scale perturbations can be seen in and close to the disk mid-plane and large-scale perturbations away from it (Li et al. 2018, SJB20). The latter are similar to the ones that the vertical shear instability induces in that their vertical wavelength is much greater than their radial one.

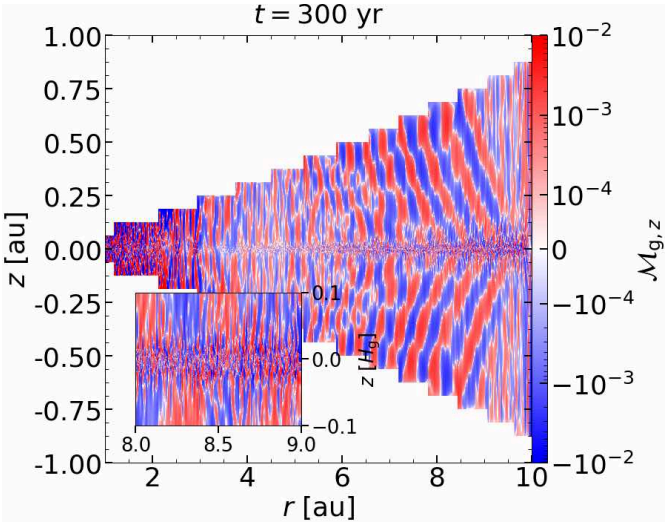

Figure 4.8: Figure adopted from SJB20. Mach number of the vertical gas velocity $\mathcal{M}_{\mathrm{g},z}$ as a function of the radius r and the height z in a simulation of the streaming instability. In and around the mid-plane, which is enlarged in the inlay, the instability induces small-scale perturbations with a Mach number of ~ 0.01. The weaker large-scale perturbations away from the mid-plane, like the perturbations caused by the vertical shear instability, are characterised by a large ratio of vertical to radial wavelength.

In the mid-plane, the turbulence driven by the streaming instability is isotropic (Johansen and Youdin 2007; SJB20). Like the linear growth rate of the instability (Youdin and Goodman 2005), the strength of the turbulence is higher if the radial dust drift is faster, that is to say if either the Stokes number of the dust is closer to unity or the radial gradient in the gas pressure is steeper (see Eqs. 2.28 and 3.7; Carrera et al. 2015; SJB20). Nonetheless, the Mach number of the vertical gas velocity saturates at a value of ~ 0.01 for a Stokes number of ~ 0.05 or a dimensionless pressure gradient parameter, as introduced by Bai and Stone (2010b) and defined in Eq. 2.19, of ~ 0.1 (SJB20). If the Stokes number is reduced from 0.05 to 0.005, the Mach number declines by an order of magnitude to ~ 0.001. In SJB20, we show that the turbulent strength is independent of the dust-to-gas surface density ratio. However, Bai and Stone (2010b) find that the vertical dust diffusion caused by the instability is strongest for a certain surface density ratio which depends on the Stokes number.

Similar to the turbulent strength, the dust scale height induced by the streaming instability increases with the strength of the radial pressure gradient and with the Stokes number approaching one (Carrera et al. 2015; SJB20). Nevertheless, this dependence is comparably weak. The scale height amounts to $\sim 1\%$ of the gas scale height for a wide range of pressure gradient strengths and Stokes numbers between 0.001 and 1 (Yang and Johansen 2014; Carrera et al. 2015; SJB20). If dust with a distribution of Stokes numbers is considered, the instability is triggered by the dust with the largest Stokes numbers and the turbulent strength thus depends on these Stokes number (Bai and Stone 2010b; Schaffer et al. 2018). Consequently, the scale height of dust with the smaller Stokes numbers is greater than it would be if the dust with the largest Stokes numbers were absent. The dust scale height is self-regulating if the streaming instability is the dominant source of turbulence in the dust layer around the mid-plane in

protoplanetary disks. If the dust settled to a scale height smaller than the equilibrium value, the higher density of the dust layer would lead to the instability causing stronger turbulence and vertical diffusion that would lift the dust up to the equilibrium scale height.

Chen and Lin (2020) and Umurhan et al. (2020) analytically investigate the effect of turbulent viscosity and dust diffusion on the streaming instability. Both studies show that turbulence reduces the linear growth rate of the instability, with the latter authors finding that the growth rate is negligible if the turbulent α-parameter is similar to or greater than $\mathrm{St}^{1.5}$, or equivalently $\mathcal{M} \gtrsim \mathrm{St}^{0.75}$. I note that, since in these analyses turbulence is treated as a source of viscosity, they can not cover local structures like pressure bumps or vortices that arise from turbulence driven by a number of the instabilities introduced above. As detailed there and in Sect. 3.5, dust accumulations in these structures can act as seeds for the streaming instability. Furthermore, Gole et al. (submitted) show that the dust concentration caused by the streaming instability is not strong enough for planetesimal formation to ensue in a simulation of dust with a Stokes number of 0.3, a dust-to-gas surface density ratio of 2%, and driven isotropic turbulence with a strength of $\alpha = 0.001$ or $\mathcal{M} = 0.032$. Nevertheless, in this one as well as studies by Chen and Lin (2020) and Umurhan et al. (2020) only isotropic turbulence and dust diffusion is considered. Yet, strong vertical diffusion does not inhibit dust accumulation owing to the streaming instability if it is accompanied by only weak radial diffusion (Yang et al. 2018).

4.5.2 Dust settling instability

The dust settling instability belongs to the class of resonant drag instabilities discovered by Squire and Hopkins (2018a; 2018b; see Sect. 3.1). While these authors find the instability to operate if epicyclic gas motions in the radial-vertical plane are in resonance with both the vertical settling of the dust and the radial dust drift, Zhuravlev (2019) show that it is active also in the absence of radial drift. In contrast to that of the linear streaming instability (Krapp et al. 2019; Zhu and Yang submitted), the growth rate of the linear dust settling instability depends only weakly on whether dust with a uniform size or a size distribution is considered (Krapp et al. 2020). However, turbulent viscosity with an α-parameter of 10^{-4}, corresponding to a Mach number of 0.01, strongly suppresses the linear instability (Krapp et al. 2020; see also Squire and Hopkins 2018b; Zhuravlev 2020). I note, though, that the same limitations apply to the linear analysis of the effect of turbulent viscosity on the dust settling instability as in the case the streaming instability (see Sect. 4.5.1).

The dust settling instability can only operate as long as dust is sedimenting. Nonetheless, the growth rate of the linear instability is largely independent of the Stokes number of the dust and comparable to the Keplerian orbital frequency (Squire and Hopkins 2018b). That is, if dust with Stokes numbers less than one is considered, the growth rate is greater than the inverse of the settling time $1/\tau_{\mathrm{d,sett}} = \Omega_{\mathrm{K}}\mathrm{St}$ (see Eq. 4.2). In addition, for small Stokes numbers the dust settling instability grows faster than the streaming instability (Squire and Hopkins 2018b). This indicates that the dust settling instability, though only transiently, might induce significant turbulence and dust concentration.

Krapp et al. (2020) present a comprehensive analytical and numerical study of the dust settling instability. Since the radial drift of the dust is taken into account, both the dust settling and the streaming instability are active in their simulations. Nevertheless, the dust concentra-

tion in the simulations is not strong enough for the maximum dust density to exceed the gas density noticeably before the dust has settled to the mid-plane. The Mach number of the gas turbulence driven by the instability amounts to ~ 0.05 in both the radial and vertical dimension in simulations with a Stokes number of 0.01 and a dust-to-gas density ratio of 0.1. The Mach number decreases to ~ 0.01 if a lower Stokes number of 0.001 but the same density ratio or if a smaller density ratio of 0.01 but the same Stokes number are considered. Furthermore, the Mach number is less by a factor of a few in a three-dimensional simulation than in the corresponding two-dimensional simulation.

4.5.3 Kelvin-Helmholtz instability

Kelvin-Helmholtz instabilities are linear instabilities that arise from shear, i.e. a difference in velocity, between adjacent gas layers. Here, I review the instability which is caused by the orbital speed of the gas being closer to Keplerian in the mid-plane of protoplanetary disks than away from it owing to the presence of dust (Weidenschilling 1980; Weidenschilling and Cuzzi 1993). As explained in Sects. 2.4 and 3.1, if gas and dust were not coupled via drag, the orbital velocity of the gas would be sub-Keplerian, while the dust would orbit with the Keplerian velocity. Generally in protoplanetary disks, and specifically away from the mid-plane, the ratio of the dust to the gas density is less than one. The coupled gas and dust thus orbit with a speed close to the sub-Keplerian one of the gas. However, in the layer around the mid-plane to which the dust has settled the dust-to-gas density ratio is closer to unity. Therefore, the orbital speed of gas and dust in the dust layer approaches the Keplerian speed. The shear between the gas in vertically adjacent layers with different dust-to-gas density ratios gives rise to the Kelvin-Helmholtz instability.

Instability can occur, although does not necessarily, when the dimensionless Richardson number,

$$\mathrm{Ri} = -\frac{\Omega_\mathrm{K}^2 z}{\rho_\mathrm{tot}} \frac{\partial \rho_\mathrm{tot}/\partial z}{(\partial v_{\mathrm{g},\phi}/\partial z)^2}, \tag{4.21}$$

is less than a threshold value (Chandrasekhar 1961; Chiang 2008). The numerator reflects the stabilising effect of vertical buoyancy, that is to say of the vertical stellar gravity and vertical gradients in the gas and dust density, while the denominator expresses the strength of the destabilising vertical shear. If the forces associated with differential rotation are neglected, the threshold Richardson number amounts to $1/4$ (Chandrasekhar 1961). Analytical and numerical studies show that the threshold value in protoplanetary disks ranges between 0.1 and a few, depending on whether the Coriolis force and the radial shear caused by differential rotation are taken into account as well as on how tightly gas and dust are coupled (Sekiya 1998; Sekiya and Ishitsu 2000; Gómez and Ostriker 2005; Johansen et al. 2006a; Chiang 2008; Barranco 2009; Gerbig et al. 2020).

The Kelvin-Helmholtz instability and the streaming instability operate under the same conditions, but in different planes – the Kelvin-Helmholtz instability in the azimuthal-vertical plane, although it is affected by radial shear, the streaming instability in the radial-vertical plane (Johansen et al. 2006a). Nonetheless, three-dimensional simulations performed by Bai and Stone (2010b) show that, if dust with a Stokes number of 0.01 or larger is present, the

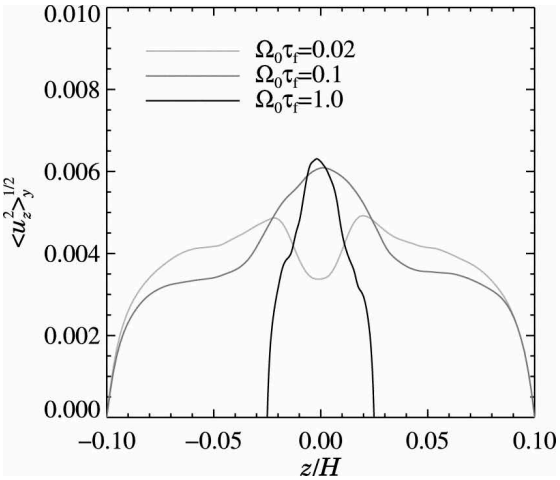

Figure 4.9: Figure adopted from Johansen et al. (2006a, their Fig. 16, reproduced with permission ©AAS). Vertical gas velocity u_z, expressed as a Mach number, as a function of the height z in units of gas scale heights H. Lines in different grey tones represent simulations with varying Stokes numbers of the dust $\Omega_0\tau_f$, with the Stokes numbers being given in the legend. In the mid-plane, the Mach number amounts to ~ 0.05, largely independently of the Stokes number. The Mach number decreases towards the edges of the dust layer, which is located at greater heights if the Stokes number is smaller.

streaming instability dominates over the Kelvin-Helmholtz instability and regulates the dynamics in the dust layer. On the other hand, in contrast to the streaming instability, the Kelvin-Helmholtz instability induces considerable dust concentration even if gas and dust are perfectly coupled, i.e. the dust stopping time is negligible and the Stokes number vanishes (Sekiya 1998; Youdin and Shu 2002; Chiang 2008). This concentration is strong enough for the dust density to exceed the Roche density, that is it can lead to planetesimal formation, if the dust surface density amounts to a few to a few ten percent of the gas surface density. That is, the dust-to-gas surface density ratio is required to exceed the interstellar medium value of 1%.

Figure 4.9 shows the Mach number of the vertical gas motions driven by the Kelvin-Helmholtz instability in simulations conducted by Johansen et al. (2006a). It can be seen that the Mach number does not vary significantly with the Stokes number of the dust, but declines from ~ 0.05 in the mid-plane to zero at the edge of the dust layer. As in the case of the streaming instability, the dust scale height is set by the Kelvin-Helmholtz instability in a self-regulatory manner. If the dust settled to a thinner layer, the difference in orbital speed between this and the vertically adjacent layers would be stronger. Thus, the instability would cause stronger turbulence which would elevate the dust to greater heights. As evident from Fig. 4.9 and theoretically expected (see Eq. 4.5), the scale height increases with decreasing Stokes number (Johansen et al. 2006a). It amounts to $\sim 0.3\%$ of the gas scale height if dust with a Stokes number of 0.1 and a dust-to-gas surface density ratio of 0.01 are considered. Gerbig et al. (2020) find that the dust scale height further depends on the surface density ratio. From $\sim 1.5\%$ of the gas scale height for a surface density ratio of 0.02 and a Stokes number of 0.005, the dust scale height decreases to $\sim 0.5\%$ in their simulations of either a lower surface density ratio of 2×10^{-4} or a larger ratio of 0.1.

Table 4.1: Instabilities

Instability	Radial gas velocity in mid-plane	Vertical gas velocity in mid-plane	Scale height of dust with $\mathrm{St} = 0.1$
Gravitational	$\mathcal{M}_{\mathrm{g},r} = 0.1$–1 (Riols et al. 2020b)	$\mathcal{M}_{\mathrm{g},z} \approx 0.01$ (Riols et al. 2020b)	$H_\mathrm{d} \approx 0.3\, H_\mathrm{g}$(Riols et al. 2020b)
Magneto-rotational	$\mathcal{M}_{\mathrm{g},r} = 0$ at $r = 1$ au (Bai 2014)	$\mathcal{M}_{\mathrm{g},z} = 0$ at $r = 1$ au (Bai 2014), $\mathcal{M}_{\mathrm{g},z} \approx 0.01$ at $r = 5$–60 au (Bai 2015)	$H_\mathrm{d} = 0.04$–$0.2\, H_\mathrm{g}$ (Xu et al. 2017; Riols and Lesur 2018; Yang et al. 2018; Riols et al. 2020a)
Vertical shear	$\mathcal{M}_{\mathrm{g},r} \approx 0.01$–$0.1$ (SJB20)	$\mathcal{M}_{\mathrm{g},z} \approx 0.01$ (Flock et al. 2017), $\mathcal{M}_{\mathrm{g},z} \approx 0.1$ (SJB20)	$H_\mathrm{d} \approx 0.1\, H_\mathrm{g}$ for $Z = 0.02$, $H_\mathrm{d} \approx 0.01\, H_\mathrm{g}$ for $Z = 0.1$ (SJB20)
Convective overstability	$\mathcal{M}_{\mathrm{g},r} = 0.01$–$0.1$ (Klahr and Hubbard 2014; Lyra 2014)	$\mathcal{M}_{\mathrm{g},z} = 0.01$–$0.1$ (Klahr and Hubbard 2014; Lyra 2014)	-
Subcritical baroclinic	$\mathcal{M}_{\mathrm{g},r} \approx 0.1$–$0.4$ (Lyra and Klahr 2011; Raettig et al. 2013)	-	-
Streaming	$\mathcal{M}_{\mathrm{g},r} \approx 0.01$ for $\mathrm{St} = 0.1$ (Johansen and Youdin 2007; SJB20)	$\mathcal{M}_{\mathrm{g},z} \approx 0.01$ for $\mathrm{St} = 0.1$ (Johansen and Youdin 2007; SJB20)	$H_\mathrm{d} \approx 0.1\, H_\mathrm{g}$ (Yang and Johansen 2014; Carrera et al. 2015; SJB20)
Dust settling	$\mathcal{M}_{\mathrm{g},r} \approx 0.01$ for $\mathrm{St} = 0.01$ (Krapp et al. 2020)	$\mathcal{M}_{\mathrm{g},z} \approx 0.01$ for $\mathrm{St} = 0.01$ (Krapp et al. 2020)	-
Kelvin-Helmholtz	-	$\mathcal{M}_{\mathrm{g},z} \approx 0.05$ (Johansen et al. 2006a)	$H_\mathrm{d} \approx 0.003\, H_\mathrm{g}$ for $Z = 0.01$ (Johansen et al. 2006a)

5

Initial mass function of planetesimals formed by the streaming instability

Contribution

In this study, we investigate the birth mass distribution of planetesimals that form owing to the streaming instability, in particular its dependence on the domain size of numerical simulations. To this end, we employed the Pencil Code[1] (Brandenburg and Dobler 2002) to conduct local shearing box simulations (see Sect. 3.1) with larger domain sizes than in other studies of the mass distribution.

To perform the simulations presented in the article, I adopted and modified a simulation setup that was provided by Chao-Chin Yang. No noteworthy changes to the simulation code itself were necessary. Furthermore, I analysed the simulation data, wrote the article and created the figures that can be found in it. Throughout the study, I was supervised by and consulted with Chao-Chin Yang and Anders Johansen.

[1] `http://pencil-code.nordita.org`

A&A 597, A69 (2017)
DOI: 10.1051/0004-6361/201629561

Astronomy & Astrophysics

Initial mass function of planetesimals formed by the streaming instability

Urs Schäfer[1,2], Chao-Chin Yang[2], and Anders Johansen[2]

[1] Hamburg Observatory, University of Hamburg, Gojenbergsweg 112, 21029 Hamburg, Germany
e-mail: urs.schaefer@hs.uni-hamburg.de
[2] Lund Observatory, Department of Astronomy and Theoretical Physics, Lund University, PO Box 43, 22100 Lund, Sweden

Received 20 August 2016 / Accepted 2 November 2016

ABSTRACT

The streaming instability is a mechanism to concentrate solid particles into overdense filaments that undergo gravitational collapse and form planetesimals. However, it remains unclear how the initial mass function of these planetesimals depends on the box dimensions of numerical simulations. To resolve this, we perform simulations of planetesimal formation with the largest box dimensions to date, allowing planetesimals to form simultaneously in multiple filaments that can only emerge within such large simulation boxes. In our simulations, planetesimals with sizes between 80 km and several hundred kilometers form. We find that a power law with a rather shallow exponential cutoff at the high-mass end represents the cumulative birth mass function better than an integrated power law. The steepness of the exponential cutoff is largely independent of box dimensions and resolution, while the exponent of the power law is not constrained at the resolutions we employ. Moreover, we find that the characteristic mass scale of the exponential cutoff correlates with the mass budget in each filament. Together with previous studies of high-resolution simulations with small box domains, our results therefore imply that the cumulative birth mass function of planetesimals is consistent with an exponentially tapered power law with a power-law exponent of approximately −1.6 and a steepness of the exponential cutoff in the range of 0.3–0.4.

Key words. hydrodynamics – instabilities – methods: numerical – planets and satellites: formation – protoplanetary disks

1. Introduction

One of the greatest problems in the theory of planet formation is to explain how millimeter- or centimeter-sized solid particles – in the following referred to as pebbles – grow to kilometer-sized planetesimals. Micron-sized dust grains can grow to pebble sizes by coagulation, but larger particles bounce or fragment under mutual collisions (Güttler et al. 2010; Zsom et al. 2010; Birnstiel et al. 2011). Growth might continue despite this so-called bouncing barrier for very porous ice particles (Wada et al. 2008, 2009) or by mass transfer in high-speed collisions (Wurm et al. 2005; Windmark et al. 2012).

A fundamental problem of planetesimal formation is the time constraint inflicted by the radial drift of solid particles, a problem that persists even under the assumption of perfect sticking. The orbital velocity of the gas in a protoplanetary disk is sub-Keplerian because the gas is supported against the gravity of the central star by a radial pressure gradient. The gas exerts a drag force on the particles in the disk, whose orbital speed would be equal to the Keplerian speed if the gas was not present, causing them to lose angular momentum and drift radially towards the star. The drift velocity depends on the size of the particles, but is in general highest for meter-sized particles in the inner regions of the disk. A particle with a size of 1 m, initially orbiting at a distance of 1 au from the star, drifts towards the star and sublimates in less than 100 years (Adachi et al. 1976; Weidenschilling 1977; Brauer et al. 2007). Hence, there needs to be some mechanism assisting the growth of pebbles into planetesimals, which are sufficiently large for the effect of the drag force exerted on them by the gas to be negligible, on a timescale shorter than the radial drift timescale.

The streaming instability provides a mechanism to concentrate solid materials and form planetesimals despite the poor sticking efficiency of the particles and their radial drift. It was discovered analytically by Youdin & Goodman (2005) and confirmed numerically by Youdin & Johansen (2007), Johansen & Youdin (2007), and Bai & Stone (2010a). The radial drift speed of solid particles decreases with increasing solid-to-gas density ratio because of the drag force exerted by the particles on the gas. A locally enhanced solid-to-gas ratio causes the local orbital velocity of the gas to be closer to Keplerian, and thus a reduction of the local drift speed of the particles. Hence, clusters of particles drift more slowly than isolated particles, and downstream clusters can accumulate upstream isolated particles, further reducing the drift speed of the clusters. Owing to this positive feedback loop, particles can be concentrated into filaments reaching maximum densities of up to several thousand times the local gas density (Bai & Stone 2010a; Johansen et al. 2012; Yang & Johansen 2014; Johansen et al. 2015), sufficient to undergo gravitational collapse and form planetesimals (Johansen et al. 2007; Simon et al. 2016). For this strong clustering of particles to occur, the solid-to-gas column density ratio needs to exceed a critical value (Johansen et al. 2009b; Bai & Stone 2010b), which depends on the radial pressure gradient supporting the gas (Bai & Stone 2010c) and the particle size (Carrera et al. 2015; Yang et al. 2016).

Although several studies have shown that the streaming instability can lead to the formation of planetesimals, their birth mass distribution has not been comprehensively investigated. However, the initial mass function of planetesimals is essential for the study of the formation of planetary systems because it determines the initial conditions for the evolution of the bodies

that planetesimals evolve into, including planets, asteroids, and Kuiper belt objects. The asteroids in the asteroid belt provide a natural sample distribution that can be fitted with a broken power law. Bottke et al. (2005) argue that the current size distribution of asteroids larger than 120 km in diameter represents the birth size distribution of the planetesimals that formed in the asteroid belt (but have been strongly depleted by resonances with Jupiter, independent of their sizes), while smaller asteroids are largely fragments of collisions between the larger ones.

Both Johansen et al. (2015) and Simon et al. (2016) performed numerical simulations of planetesimal formation by the streaming instability and find that the differential distribution of the planetesimal birth masses is well-fitted with a power law with an exponent of about −1.6, albeit with the difference that, while the former observe an exponential tapering of the power-law distribution that constitutes the physical upper mass cutoff, the latter do not include such a tapering in their fits. In this paper, we compare power-law fits with and without exponential cutoff to evaluate how well the high-mass end of the initial mass function is described by an exponential cutoff.

Johansen et al. (2015) find the shape of the initial mass function to be relatively independent of the resolution of the simulations and the solid particle column density. They show that a higher resolution leads to the formation of planetesimals with a wider range of sizes, between 30 km and 120 km in radius in their simulation with the highest resolution because the size of the smallest planetesimal declines with increasing resolution. On the other hand, they observe the size of the largest planetesimal to mainly depend on the particle column density, with smaller column densities yielding smaller sizes. Simon et al. (2016) also studied the dependence of the shape of the birth mass distribution on the resolution of the simulations and obtain the same result. They further find the shape of the distribution to be largely independent of the strength of the self-gravity and the simulation time at which it is initiated, although the masses of the planetesimals are shifted to higher values with the increasing strength of self-gravity. The planetesimals that formed in their simulations typically range in radius from 50 km to a few hundred kilometers.

It remains unclear if the planetesimal initial mass function depends on the dimensions of the simulation box. Both Johansen et al. (2015) and Simon et al. (2016) employed only one box size of 0.2 gas scale heights in the radial, azimuthal, and vertical directions. However, Yang & Johansen (2014) find that, while in the simulations with this box size, the solid particles are concentrated by the streaming instability into only one axisymmetric filament, multiple of these filaments form in simulations with larger box dimensions. This raises the question of whether the mass budget of planetesimal formation, and thus the shape of the initial mass function, is different when not only one filament is observed. In this paper, we study simulations with three different box sizes, the smallest of which is equal to that employed by Johansen et al. (2015) and Simon et al. (2016), while the others are two and four times larger, respectively, in the radial and azimuthal directions, which permits investigating planetesimal formation in several filaments. Furthermore, in simulations with larger box sizes, more planetesimals emerge, yielding better statistics in particular for the determination of the initial mass function.

The paper is structured as follows: in Sect. 2, the simulation setup, i.e. the initial conditions and the parameters that govern the evolution of the simulations are described. In Sect. 3, we present our results regarding the formation of planetesimals by the streaming instability and their radial migration. Further, we comment on the issue of permitting the mutual accretion of sink particles, which we use to model planetesimals. In Sect. 4, we discuss whether the planetesimal birth mass distribution is exponentially tapered and how its shape depends on the dimensions of the simulation box as well as the resolution. We conclude in Sect. 5.

Table 1. Simulation specifications.

Name	$L_x\,[H_g] \times L_y\,[H_g] \times L_z\,[H_g]^a$	Resolution $[H_g^{-1}]$	$N_x \times N_y \times N_z{}^b$
run_0.2_320	$0.2 \times 0.2 \times 0.2$	320	$64 \times 64 \times 64$
run_0.4_320	$0.4 \times 0.4 \times 0.2$	320	$128 \times 128 \times 64$
run_0.8_320	$0.8 \times 0.8 \times 0.2$	320	$256 \times 256 \times 64$
run_0.2_640	$0.2 \times 0.2 \times 0.2$	640	$128 \times 128 \times 128$
run_0.4_640	$0.4 \times 0.4 \times 0.2$	640	$256 \times 256 \times 128$

Notes. [(a)] Box dimensions in the x-, y-, and z-directions, where H_g is the gas scale height. [(b)] Number of grid cells in the x-, y-, and z-directions.

2. Simulation setup

We conduct three-dimensional computer simulations with the Pencil Code[1], a hybrid code for gas, for which the magnetohydrodynamic equations are solved on a fixed grid, with Lagrangian particles representing solid bodies. The code employs sixth-order finite differences in space and third-order Runge-Kutta steps in time.

We use the shearing box approximation (Goldreich & Lynden-Bell 1965), i.e. we assume that the size of the simulation box is small compared to the distance to the central star of the protoplanetary disk. Hence, the curvature of the disk is neglected and the stellar gravity is linearized. The rectangular simulation box is aligned such that the x-, y-, and z-directions correspond to the radial, azimuthal, and vertical directions, respectively, and co-rotates with the Keplerian velocity at its origin. For both gas and particles, sheared periodic boundary conditions are employed at the radial and azimuthal boundaries and periodic boundary conditions at the vertical boundaries (Hawley et al. 1995; Brandenburg et al. 1995; Youdin & Johansen 2007; Johansen et al. 2009a).

In total, we perform five simulations with three different simulation box dimensions and two different resolutions, as listed in Table 1. The two smaller boxes have a size of 0.2 and 0.4 gas scale heights, respectively, in the radial and azimuthal directions with a resolution of either 320 or 640 grid cells per scale height, while the largest box has a radial and azimuthal size of 0.8 scale heights with a resolution of 320 grid cells per scale height. All simulation boxes have a vertical size of 0.2 scale heights. The names of the simulations are composed of the radial and azimuthal dimension as the first number and the resolution as the second number.

2.1. Gas

The simulation box is filled with an isothermal, non-magnetized gas with an isothermal equation of state $p_g = c_s^2 \rho_g$, where p_g and ρ_g are the pressure and density, respectively, and c_s is the (constant) sound speed. While the gas density is initially constant in the radial and azimuthal direction, it is stratified in the vertical direction because we take into consideration the vertical gravity of the central star, which causes both gas and solid particles to sediment to the mid-plane at $z = 0$. This background density stratification is determined by the equilibrium between vertical

[1] http://pencil-code.nordita.org/

gravity and vertical pressure gradient, and is given by

$$\rho_{\rm g}(z) = \rho_{\rm g,0} \exp\left(-\frac{z^2}{2H_{\rm g}^2}\right), \tag{1}$$

where $H_{\rm g} = c_{\rm s}/\Omega_{\rm K}$ is the gas scale height, $\Omega_{\rm K} = 2\pi/P_{\rm K}$ the Keplerian orbital frequency, and $P_{\rm K}$ the Keplerian orbital period. Here and in the following, the subscript zero refers to the mid-plane. As formulated in Yang & Johansen (2014), we subtract the background density stratification from the equations of the motion for the gas to numerically balance this equilibrium state down to machine precision.

Since the gas density is initially radially constant, there is no radial pressure gradient to support the gas and cause it to orbit with sub-Keplerian speed. Hence, a background pressure gradient set by the dimensionless parameter

$$\Pi = -\frac{1}{2}\frac{H_{\rm g}}{R}\frac{\partial \ln(p_{\rm g,0})}{\partial \ln(R)} = 0.05, \tag{2}$$

where R is the orbital distance, is imposed. We refer to this parameter as Π adopting the notation by Bai & Stone (2010b). The resulting sub-Keplerian orbital velocity of the gas is given by $v_{\rm g} = v_{\rm K} - \Delta v$, where $v_{\rm K} = \Omega_{\rm K} R$ is the Keplerian orbital velocity and $\Delta v = \Pi c_{\rm s} = 0.05 c_{\rm s}$, which is a representative value at orbital distances of the order of 1 au in a typical protoplanetary disk (Hayashi 1981; Bai & Stone 2010b; Bitsch et al. 2015).

2.2. Particles

Two types of Lagrangian particles are employed in the simulations: super-particles and sink particles to model pebbles and planetesimals, respectively. To achieve a good load balancing among the processors, we use the particle block domain decomposition algorithm implemented by Johansen et al. (2011). For the calculation of the mutual drag forces between the gas and the super-particles and the mutual gravitational forces between the super-particles and the sink particles, we apply the triangular shaped cloud scheme to map the particle masses and velocities onto the grid, and similarly interpolate the back-reaction drag forces and the self-gravitational forces onto the particles (Hockney & Eastwood 1981; Youdin & Johansen 2007; Johansen et al. 2007).

The gravitational potential of the super-particles as well as the sink particles is computed by solving Poisson's equation using the fast Fourier transform algorithm (Gammie 2001), which entails gravitational softening. The softening length is of the order of the grid cell edge length. Even though the gravitational potential of the particles is vertically periodic, the particles are concentrated in a thin layer around the mid-plane such that their dynamics are not affected by the periodic potential away from the mid-plane.

We neglect the contribution of the gas to the gravitational potential under the assumption that the gas component of the protoplanetary disk is not in the gravitationally unstable regime. Indeed, in our simulations the gas density deviates by at most 2% from the mid-plane density $\rho_{\rm g,0}$, the gas density perturbations are thus very small compared to the super-particle densities in the filaments when planetesimals form, which are of the order of the Roche density (see below).

The sedimentation of the super-particles to the mid-plane that is due to the vertical stellar gravity induces turbulence as a result of either the streaming instability or the Kelvin-Helmholtz instability, which are both caused by the mutual drag forces between the gas and the super-particles (Bai & Stone 2010b). This turbulence stirs up the super-particles, and hence counteracts the sedimentation. To give sedimentation and turbulence time to attain an equilibrium, in our simulations self-gravity is not introduced until $t = 25\ P_{\rm K}$. Its strength is then gradually increased from zero over $10\ P_{\rm K}$ until it reaches its final value at $t = 35\ P_{\rm K}$ since initiating self-gravity instantaneously with full strength could cause significant impulses on the particles. While we initiate self-gravity at a simulation time at which the super-particles have already formed filaments, Johansen et al. (2015) introduced self-gravity with full strength at the start of their simulations and observe qualitatively the same planetesimal birth mass distribution as we do.

We achieve this gradual initiation of the self-gravity by substituting

$$\Gamma = \begin{cases} 0 & t \le 25\ P_{\rm K}, \\ \frac{1}{2}\gamma\left(1 - \cos\left[\frac{\pi(t-25\ P_{\rm K})}{10\ P_{\rm K}}\right]\right) & 25\ P_{\rm K} < t < 35\ P_{\rm K}, \\ \gamma & t \ge 35\ P_{\rm K}, \end{cases} \tag{3}$$

where the dimensionless self-gravity parameter

$$\gamma = \frac{4\pi G \rho_{\rm g,0}}{\Omega_{\rm K}^2} \tag{4}$$

and G is the gravitational constant, into the right-hand side of Poisson's equation. We choose $G = P_{\rm K}^{-2}\rho_{\rm g,0}^{-1}$, and thus $\gamma = 1/\pi = 0.318$. We note that Simon et al. (2016) find the shape of the initial mass function of the planetesimals formed in their simulations of the streaming instability to be relatively independent of both the simulation time at which self-gravity is introduced and the strength of the self-gravity. The Roche density depends on the self-gravity parameter γ and is given by

$$\rho_{\rm R} = \frac{9\Omega_{\rm K}^2}{4\pi G} = \frac{9\rho_{\rm g,0}}{\gamma} = 28.3\rho_{\rm g,0}. \tag{5}$$

Each super-particle represents a large number of equally sized pebbles because it is computationally infeasible to simulate the pebbles individually. While the mass of a super-particle is equal to the total mass of the pebbles it models, its friction time is the same as that of an individual constituent pebble.

The mass of the super-particles is determined by the initial solid-to-gas column density ratio and their initial number. We set the solid-to-gas ratio

$$Z = \frac{\Sigma_{\rm p,init}}{\Sigma_{\rm g,init}}, \tag{6}$$

where $\Sigma_{\rm p,init}$ and

$$\Sigma_{\rm g,init} = \sqrt{2\pi} H_{\rm g} \rho_{\rm g,0} \tag{7}$$

are the initial column densities of the super-particles and the gas, respectively, to $Z = 0.02$. This value corresponds to the critical solid-to-gas ratio necessary for strong clustering of pebbles due to the streaming instability to occur (Johansen et al. 2009b; Bai & Stone 2010b,c; Carrera et al. 2015), and is slightly higher than the solar metallicity. The initial number of super-particles is set equal to the total number of grid cells. The super-particles are randomly distributed among the entire simulation box to seed the streaming instability.

The Stokes number of the super-particles $\tau_{\rm f} = \Omega_{\rm K} t_{\rm f}$, where $t_{\rm f}$ is the friction time, is set to $\tau_{\rm f} = \pi/10 = 0.314$, which, at an orbital distance of 2.5 au in the Minimum Mass Solar Nebula (MMSN), corresponds to a size of approximately 25 cm

(Bai & Stone 2010b; Johansen et al. 2015). While we employ only one fixed particle size, Bai & Stone (2010b) performed simulations with particles of a range of sizes. They find that the particle-gas dynamics are dominated by the most massive particles, and that the critical solid-to-gas ratio required for strong particle clustering owing to the streaming instability is determined by the total mass of all particles.

After self-gravity has attained its full strength at $t = 35\ P_{\rm K}$, every super-particle comprised in a cluster whose super-particle density $\rho_{\rm p}$ exceeds a threshold value $\rho_{\rm p,thres}$ is replaced by a sink particle. This sink particle creation threshold is set to $\rho_{\rm p,thres} = 200\,\rho_{\rm g,0}$, i.e. about seven times the Roche density (see Eq. (5)). We note that Johansen et al. (2015) compared simulations similar to ours with three different threshold values and find the masses of the sink particles emerging in their simulations to be largely independent of the threshold above a value of five times the Roche density.

The simulation time at which the formation of sink particles is introduced is arbitrary since both the gravitationally bound super-particle clusters that exist beforehand and the sink particles that emerge from them afterwards represent planetesimals. Owing to the limited resolution of the gravitational forces the behavior of many super-particles inside one grid cell is comparable to that of a few sink particles. Nevertheless, the computational expense of the simulations is lowered substantially by the introduction of sink particles.

Super-particles within the accretion radius of a sink particle, which is set equal to one grid cell edge length, are accreted by it, i.e. the super-particle mass and momentum are added to the sink particle mass and momentum, respectively, and the super-particle is removed. This accretion, however, might in parts be artificial because the physical accretion radius, i.e. the Bondi radius for pebble accretion (Ormel & Klahr 2010; Lambrechts & Johansen 2012), could be smaller than the simulated accretion radius, especially in the case of less massive sink particles. On the other hand, since the mutual gravitational forces between the super-particles and the sink particles within one grid cell can only be computed inaccurately, the chosen accretion radius corresponds to the highest accuracy our numerical simulations can offer.

We further permit sink particles to accrete one another. This accretion is handled analogously to the super-particle accretion, and might as well be partially artificial. Nevertheless, it is required because in a super-particle cluster exceeding the sink particle creation threshold, all super-particles are replaced by sink particles. That is, the gravitational collapse of a super-particle cluster results in the creation of a cluster of sink particles, of which only one should persist to represent one new-born planetesimal. See Sect. 3.2 for further discussion of this topic.

2.3. Units and scaling relations

We report our results using the Keplerian orbital period at the origin of the simulation box $P_{\rm K}$, the gas scale height $H_{\rm g}$, and the mid-plane gas density $\rho_{\rm g,0}$ as the units of time, length, and density, respectively. We note that a shearing box freely scales with these units until self-gravity is initiated at $t = 25\ P_{\rm K}$. Afterwards,

$$\rho_{\rm g,0} = \frac{\gamma \Omega_{\rm K}^2}{4\pi G} = \frac{\pi\gamma}{G P_{\rm K}^2} \tag{8}$$

(see Eq. (4)), and hence the unit of mass $[M] = H_{\rm g}^3 \rho_{\rm g,0} = \pi\gamma\, G^{-1}\, H_{\rm g}^3 P_{\rm K}^{-2}$.

In the following, relations for the scaling of relevant quantities and units with the orbital distance R, the temperature T, and the mass of the central star $M_{\rm S}$ are given. A mean atomic weight of $\mu = 2.33$ is used and the scaling relations for $\rho_{\rm g,0}$ and $[M]$ are calculated applying those for $P_{\rm K}$ and $H_{\rm g}$:

$$P_{\rm K} = 4.0 \left(\frac{R}{2.5\ {\rm au}}\right)^{3/2} \left(\frac{M_{\rm S}}{1\ M_\odot}\right)^{-1/2} {\rm yr} \tag{9}$$

$$\Omega_{\rm K} = 1.6 \left(\frac{R}{2.5\ {\rm au}}\right)^{-3/2} \left(\frac{M_{\rm S}}{1\ M_\odot}\right)^{1/2} {\rm yr}^{-1} \tag{10}$$

$$c_{\rm S} = 0.80 \left(\frac{T}{180\ {\rm K}}\right)^{1/2} {\rm km\ s}^{-1} \tag{11}$$

$$H_{\rm g} = 0.11 \left(\frac{R}{2.5\ {\rm au}}\right)^{3/2} \left(\frac{T}{180\ {\rm K}}\right)^{1/2} \left(\frac{M_{\rm S}}{1\ M_\odot}\right)^{-1/2} {\rm au} \tag{12}$$

$$\rho_{\rm g,0} = 9.4 \times 10^{-10} \left(\frac{\gamma}{\pi^{-1}}\right) \left(\frac{R}{2.5\ {\rm au}}\right)^{-3} \left(\frac{M_{\rm S}}{1\ M_\odot}\right) {\rm g\ cm}^{-3} \tag{13}$$

$$[M] = 4.2 \times 10^{27} \left(\frac{\gamma}{\pi^{-1}}\right) \left(\frac{R}{2.5\ {\rm au}}\right)^{3/2} \left(\frac{T}{180\ {\rm K}}\right)^{3/2} \times \left(\frac{M_{\rm S}}{1\ M_\odot}\right)^{-1/2} {\rm g}. \tag{14}$$

Hereafter, we use the above scaling relations, the properties of the asteroid belt, i.e. an orbital distance of $R = 2.5$ au, a temperature of $T = 180$ K, and a stellar mass of $M_{\rm S} = 1\ M_\odot$, and the chosen strength of the self-gravity $\gamma = 1/\pi$ to convert simulation units into physical units. For example, the mid-plane gas density $\rho_{\rm g,0} = 9.4 \times 10^{-10}$ g cm^{-3}, which is almost one order of magnitude greater than the corresponding value in the MMSN, $\rho_{\rm g,0} = 1.1 \times 10^{-10}$ g cm^{-3} (Hayashi 1981; Bai & Stone 2010b). The streaming instability has been shown to form planetesimals for pebble column densities similar to that in the MMSN (Johansen et al. 2015). Nevertheless, we choose this comparably high gas density and thus high solid density to promote planetesimal formation, enabling us to better constrain the initial mass function of planetesimals.

3. Evolution of the simulations

Apart from the use of self-gravity and sink particles to model planetesimals, our simulation setup is identical with that applied by Yang & Johansen (2014). Hence, we find our simulations to be consistent with their simulations until $t = 25\ P_{\rm K}$, when self-gravity is introduced (compare the evolution of the pebble density in the simulation time span $20\ P_{\rm K} \le t \le 25\ P_{\rm K}$ shown in Fig. 1 with their Fig. 3). We thus only report on the evolution of our simulations between $t = 25\ P_{\rm K}$ and the end of the simulations, $t = 40\ P_{\rm K}$.

3.1. Planetesimal formation and migration

If self-gravity is not taken into account the streaming instability concentrates pebbles into axisymmetric filaments that are elongated in the azimuthal direction (Johansen & Youdin 2007; Johansen et al. 2009b; Bai & Stone 2010b; Yang & Johansen 2014). In Figs. 1 and 2, we show how self-gravity causes these filaments to fragment into pebble clusters that undergo gravitational collapse and form planetesimals. In the first $5\ P_{\rm K}$ after self-gravity has been initiated, the filaments begin to disperse because the pebbles accumulate into clusters owing to their mutual gravitational attraction (upper panels of Fig. 2). At $t = 35\ P_{\rm K}$,

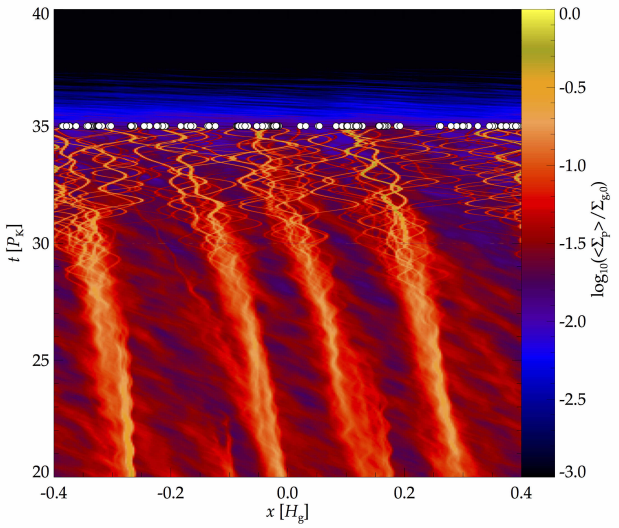

Fig. 1. Pebble column density Σ_p, integrated over the vertical dimension and averaged over the azimuthal dimension of the simulation box, as a function of radial location x and simulation time t for the simulation with the largest box size, *run_0.8_320*. Locations at which sink particles emerge are indicated with white dots. Though every pebble cluster forms in one of the filaments, they migrate up to the distance to one of the adjacent filaments. All sink particles emerge as soon as their formation is initiated at $t = 35\ P_K$, and they emerge nearly evenly distributed among the entire radial extent of the box owing to the radial migration of the pebble clusters.

when the self-gravity reaches its full strength, these clusters contain most pebbles available in the simulation, and the filaments are no longer observable (lower left panel).

At this point, we commence the formation of sink particles. Almost all pebble clusters exceed the sink particle creation threshold, consequently the pebbles in each of these clusters are replaced by sink particles which merge into one massive sink particle that represents the gravitationally collapsed cluster. At $t = 35.1\ P_K$, this sink particle merging process is for the most part completed (lower right panel). However, a few low-mass pebble clusters do not turn into sink particles. All sink particles emerge instantly at $t = 35\ P_K$, as can be seen from Fig. 1, but a couple of clusters remain at $t = 35.1\ P_K$ (three such clusters can be spotted in the lower right panel of Fig. 2). Although they are not sufficiently dense to exceed the sink particle creation threshold, these clusters probably represent gravitationally bound planetesimals with low masses.

We observe that the planetesimals on average move through more than half of the radial extent of the simulation boxes. Figure 1 shows that each pebble cluster forms in one of the filaments, but that they migrate in the radial direction, some of them only marginally, others the entire distance to one of the adjacent filaments. As a result, the sink particles emerge almost evenly distributed among the whole radial dimension of the box. From Fig. 3, it can be seen that the sink particles continue this radial migration, they on average pass through over half of, a few of them even through the whole radial extent of the box. The mean standard deviation of the radial displacement of the sink particles from the locations at which they emerge, averaged over and weighted by the lifetime of every sink particle and then averaged over all sink particles in a simulation, amounts to between 26% and 36% of the radial box size in each of the five simulations. We note that the extent of the migration in the radial direction increases with the box size without converging for the box sizes we consider. The radial motions result from the mutual gravitational scattering of sink particles that closely pass by each other. It remains to be investigated whether planetesimals are composed of not only pebbles from the filament they form in, but also of an appreciable amount of pebbles from filaments they migrate to.

3.2. Mutual sink particle accretion

For the sink particles to realistically represent new-born planetesimals, only one of them should be allowed to form from every pebble cluster that undergoes gravitational collapse. However, this requires a precise determination of the extent of each cluster, which entails several issues, for instance the treatment of overlapping clusters. Therefore, we replace every super-particle that is part of a cluster that exceeds the sink particle creation threshold by a sink particle and allow the sink particles to accrete one another until only one of them remains. We observe that in our five simulations, on average 81% of all accreted sink particles are accreted within $0.1\ P_K$ after their formation, i.e. until $t = 35.1\ P_K$, because in all simulations all sink particles emerge togather at $t = 35\ P_K$. Therefore, the merging process of sink particles that emerged from the same pebble cluster is probably largely completed at this point (see the lower right panel of Fig. 2), and most of the mutual sink particle accretions are a part of this process.

On the other hand, we note that the merging of sink particles afterwards may be artificial. The accuracy of the calculation of the gravitational forces between sink particles is limited by the resolution, hence we cannot determine whether two sink particles that encounter one another inside a grid cell collide or pass by each other. Nevertheless, we find the latter to be more probable. Taking into account gravitational focusing, the maximum impact parameter leading to a collision of two sink particles

$$b_{\max} = \sqrt{(r_1 + r_2)^2 + \frac{2G(m_1 + m_2)(r_1 + r_2)}{\Delta v^2}}, \tag{15}$$

where m_i are the masses of the two sink particles, r_i their radii, which are calculated from m_i using a solid body density of 3 g cm^{-3}, and Δv is their relative velocity (see, e.g., Armitage 2007). The mean maximum impact parameter $\langle b_{\max} \rangle$, averaged over all mutual sink particle accretions in all five simulations where the lifetime of the accreted sink particle is greater than $0.1\ P_K$ and weighted by the lifetimes of the accreted sink particles, amounts to only 3.5% of the grid cell edge length. Mutual accretions of three or more sink particles at the same simulation time are not included in this statistic because we cannot infer their outcome. We note, though, that the sink particle data are not written out after each simulation time step, but every $0.01\ P_K$. Thus, we can only imprecisely determine the simulation time at which a sink particle merging occurs and the maximum impact parameter for this encounter.

4. Initial mass function

4.1. Best-fitting parameters

We fit the cumulative mass distribution of the sink particles that emerge in our simulations using two functional forms: an integrated power law and a power law with an exponential cutoff. We choose to fit the cumulative mass distributions because, in particular for small numbers of sink particles, they are less affected by noise than the differential mass distributions and can thus be fitted more accurately.

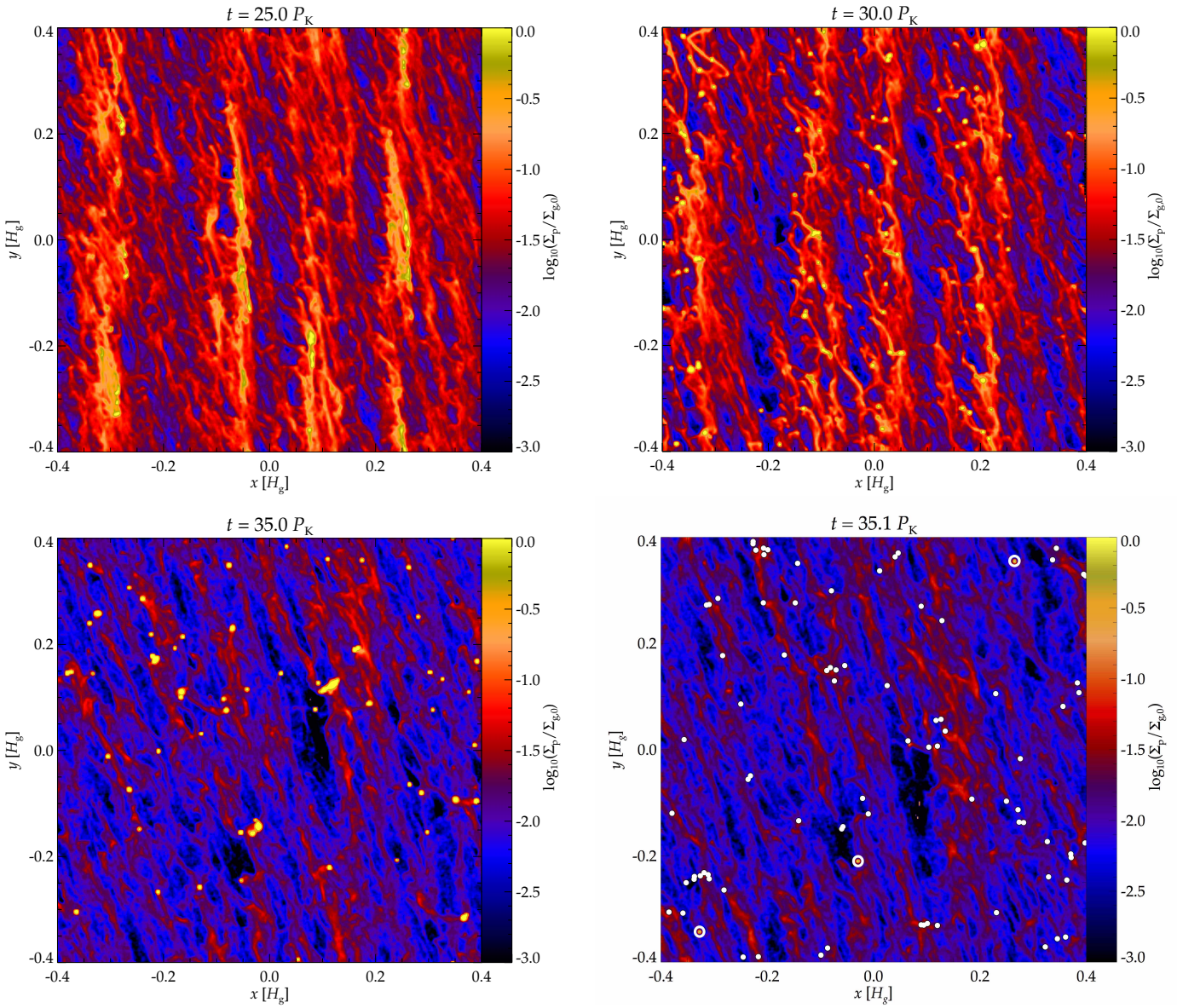

Fig. 2. Pebble column density Σ_p, integrated over the vertical dimension of the simulation box, as a function of radial location x and azimuthal location y at four different simulation times $t = 25\ P_K$ (*top left panel*), $t = 30\ P_K$ (*top right panel*), $t = 35\ P_K$ (*bottom left panel*), and $t = 35.1\ P_K$ (*bottom right panel*) for the simulation with the largest box size, *run_0.8_320*. In the *lower right panel*, sink particles are plotted as white dots and three pebble clusters are indicated using white circles. After self-gravity has been initiated at $t = 25\ P_K$, the pebbles aggregate into clusters and the axisymmetric filaments disperse (*upper panels*). When the self-gravity attains its full strength at $t = 35\ P_K$, most pebbles are concentrated in clusters and the filaments are no longer visible (*lower left panel*). At this point, we introduce the formation of sink particles, and the pebbles comprised in all but the three encircled clusters are replaced by sink particles. The sink particles emerging from the same pebble cluster undergo a merging process until only one of them remains. This process is largely completed at $t = 35.1\ P_K$ (*lower right panel*).

The integrated power law can be expressed as

$$\frac{N_>(M)}{N_{\rm tot}} = \frac{1}{1-\alpha}\left[\left(\frac{M_{\rm max}}{M_{\rm pow}}\right)^{1-\alpha} - \left(\frac{M}{M_{\rm pow}}\right)^{1-\alpha}\right], \tag{16}$$

where $N_>$ is the number of sink particles with masses greater than M, $N_{\rm tot}$ is their total number and $M_{\rm max}$ their maximum mass, and $M_{\rm pow}$ and α are fitting parameters. Since the formation of planetesimals by the streaming instability is a stochastic process and the actual $M_{\rm max}$ in a simulation might differ significantly from the $M_{\rm max}$ of the ensemble-averaged mass distribution of the sink particles for this model, we treat $M_{\rm max}$ as a fitting parameter.

The exponentially tapered power law is given by

$$\frac{N_>(M)}{N_{\rm tot}} = \left(\frac{M}{M_{\rm pow}}\right)^{-\alpha} \exp\left[-\left(\frac{M}{M_{\rm exp}}\right)^{\beta}\right], \tag{17}$$

where $M_{\rm exp}$ and β are fitting parameters. The condition $N_>(M_{\rm min})/N_{\rm tot} = 1$, where $M_{\rm min}$ is the minimum sink particle mass, can be used to eliminate one of the fitting parameters in Eq. (17). We choose to eliminate the characteristic mass of the power-law part, $M_{\rm pow}$, which is then given by

$$M_{\rm pow} = M_{\rm min}\ \exp\left[\frac{1}{\alpha}\left(\frac{M_{\rm min}}{M_{\rm exp}}\right)^{\beta}\right]. \tag{18}$$

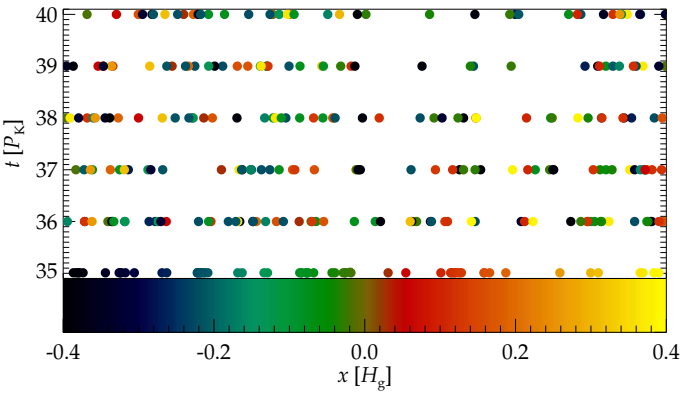

Fig. 3. Radial locations x of sink particles which are not accreted before $t = 36\ P_K$, color-coded according to the locations at which they emerge, as functions of the simulation time t for the simulation with the largest box size, *run_0.8_320*. On average, the motions of the sink particles span more than half of the radial extent of the simulation box, a couple of them even migrate through the entire radial dimension of the box.

Substituting Eq. (18) into (17) yields

$$\frac{N_>(M)}{N_{\rm tot}} = \left(\frac{M}{M_{\rm min}}\right)^{-\alpha} \exp\left[\left(\frac{M_{\rm min}}{M_{\rm exp}}\right)^{\beta} - \left(\frac{M}{M_{\rm exp}}\right)^{\beta}\right]. \tag{19}$$

We use Eq. (19) to fit the sink particle data because we find the resulting fits to be better than the ones we obtain applying Eq. (17). For the same reason as $M_{\rm max}$ in Eq. (16), $M_{\rm min}$ is treated as a fitting parameter.

To investigate the dependence of the shape of the initial mass function on the resolution and particularly the dimensions of the simulation box, we determine an individual initial mass function for every simulation. At first, we employ the least-squares method to fit Eqs. (16) and (19) to the sink particle data at each Keplerian orbital period between $t = 36\ P_K$ and the end of the simulations, $t = 40\ P_K$. In all five simulations, all sink particles emerge at once at the simulation time at which their formation is initiated, $t = 35\ P_K$, but we begin the fitting at $t = 36\ P_K$ to give the sink particles that emerge from the same pebble cluster time to merge into one. Averaged over this period, we then calculate mean values of the fitting parameters that do not vary significantly with time and are thus probably relatively unaffected by artificial sink particle merging.

In the left panel and the right panel of Fig. 4 we show the sink particle mass distributions as well as the fitted integrated power laws and power laws with exponential tapering for the two simulations with the largest numbers of sink particles, the one with the largest box size, *run_0.8_320*, and the one with the middle box size and the higher resolution, *run_0.4_640*, respectively, at $t = 40\ P_K$. In the legends for both fits, the standard deviation σ of the actual $N_>(M)/N_{\rm tot}$ for the sink particle masses M from the fitted $N_>(M)/N_{\rm tot}$ is given.

We find that the exponential tapered power laws fit the mass distributions better than the integrated power laws. The standard deviations for the power-law fits without exponential cutoff are larger, not only at $t = 40\ P_K$ as shown in the figure, but also at other simulation times. We further note that the shallower exponential cutoff represents the high-mass end of the distributions better than the steeper cutoff of the integrated power law, and that the exponential tapering better reproduces the smooth change of the slope of the distributions. Hence, we limit our further analysis to the power-law fits with exponential cutoff.

4.2. Power-law fits with and without exponential tapering

In Fig. 5 the best-fitting parameters $M_{\rm min}$, α, $M_{\rm exp}$, and β in Eq. (19) are shown for $t = 36\ P_K$ to $t = 40\ P_K$ for all of our simulations. In the case of the simulation with the smallest box dimensions and the lower resolution, *run_0.2_320*, the small number of sink particles persisting after $t = 36\ P_K$ does not permit to properly fit a power law and an exponential cutoff. The parameters α, $M_{\rm exp}$, and β are approximately constant in time for all simulations apart from $M_{\rm exp}$ for the simulation with the middle box dimensions and the lower resolution, *run_0.4_320*, which seems to converge to an upper limit. In Table 2, we list mean values of these three parameters, averaged over the simulation time span from $t = 36\ P_K$ to $t = 40\ P_K$.

Similar to $M_{\rm exp}$ for *run_0.4_320*, the fitted minimum mass $M_{\rm min}$ increases with time for the simulation with the largest box size, *run_0.8_320*, and the one with the middle box size and the higher resolution, *run_0.4_640*, but appears to saturate at an upper limit. The increase of $M_{\rm min}$ and $M_{\rm exp}$ is likely due to both pebble accretion by the sink particles – as less and less pebbles remain towards the end of the simulations (see Fig. 1), both masses converge to an upper limit – and possibly artificial merging of sink particles. In contrast to this, for *run_0.4_320* and the simulation with the smallest box dimensions and the higher resolution, *run_0.2_640*, $M_{\rm min}$ is roughly constant. To provide a comparable value for each simulation despite these differences in the time dependence, in Table 2 we list the best-fitting values at $t = 40\ P_K$ for all simulations (except for *run_0.2_320*, for which only the value at $t = 36\ P_K$ is available). A comparison of these values shows that $M_{\rm min}$ declines with both increasing box dimensions and increasing resolution if the value for *run_0.2_320* is disregarded.

The best-fitting values of the exponent of the power-law component α for all simulations vanish. This is because a lower limit for the sizes of the pebble clusters, and thus the sink particle masses, is set by the resolution, which even in the case of the higher resolution is too large for low-mass sink particles that would constitute the power-law part to emerge. Both Johansen et al. (2015) and Simon et al. (2016) fit the differential mass distribution with a power-law exponent of about −1.6, corresponding to $\alpha = 0.6$. Since the higher resolution we employ, $640\ H_g^{-1}$, is the lowest one that is considered in these papers, to properly study the power-law distribution higher resolutions than $640\ H_g^{-1}$ seem to be required.

We find the mass scale of the exponential cutoff $M_{\rm exp}$ to correlate with the mass budget in every filament. The parameter $M_{\rm exp}$ should increase with the distance between the filaments because, if the distance is larger, more pebbles can be accreted by the planetesimals forming in each filament. In Col. 6 of Table 2, the numbers of filaments $N_{\rm f}$ we observe in our simulations are listed. One, three, and four filaments form in the simulation boxes with radial and azimuthal dimensions of 0.2 H_g, 0.4 H_g, and 0.8 H_g, respectively. Therefore, the mass reservoir of pebbles in each filament is similar for the smallest and the largest box sizes, but smaller for the middle box sizes. We indeed see that the mean values of $M_{\rm exp}$ for *run_0.2_320* and *run_0.8_320* are similar, but larger than the one for *run_0.4_320*. Likewise, the mean value for *run_0.2_640* is greater than that for *run_0.4_640*. Even though the mean values for the two simulations with the middle box size differ by more than one standard deviation, we note that the best-fitting values for *run_0.4_320* increase with time with a range enclosing the mean value for *run_0.4_640*. Hence, we find $M_{\rm exp}$ to be largely independent of the resolution.

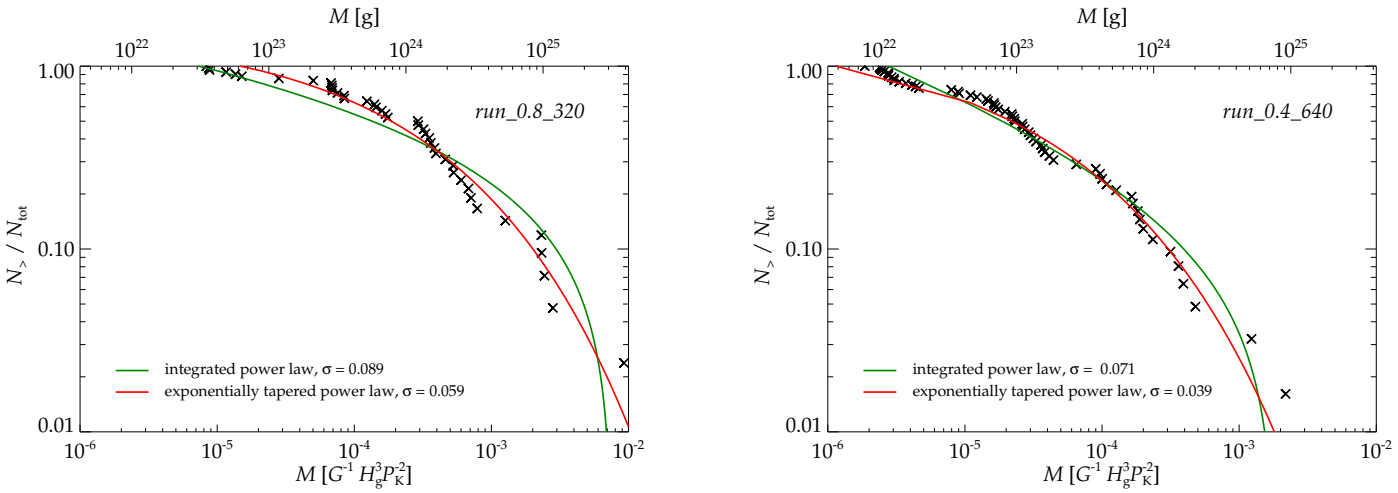

Fig. 4. Cumulative mass distributions of sink particles (black crosses) and fitted integrated power laws (Eq. (16), green lines) and power laws with exponential cutoff (Eq. (19), red lines) at $t = 40\ P_K$ for the two simulations with the largest numbers of sink particles: the one with the largest box dimensions, *run_0.8_320*, (*left panel*) and the one with the middle box dimensions and the higher resolution, *run_0.4_640* (*right panel*). Standard deviations of the actual $N_>/N_{tot}$ (black crosses) from the fitted $N_>/N_{tot}$ are given in the legends. The standard deviations for the integrated power laws are up to twice as large as those for the exponentially tapered power laws. In addition, it can be seen that the shallower exponential cutoffs fit the actual cutoffs more accurately than the steeper cutoffs of the integrated power laws and better replicate the smooth change of the slope of the mass distributions. We thus find the power laws with exponential tapering to represent the mass distributions better than the integrated power laws.

Table 2. Best-fitting parameters.

Name	M_{min} $[G^{-1}\ H_g^3 P_K^{-2}]^a$	$\langle\alpha\rangle^b$	$\langle M_{exp}\rangle$ $[G^{-1}\ H_g^3 P_K^{-2}]^b$	$\langle\beta\rangle^b$	$N_f{}^c$
run_0.2_320	$(1.9 \pm 3.8) \times 10^{-7}$	0.0002 ± 0.0097	$(1.85 \pm 0.32) \times 10^{-4}$	0.324 ± 0.025	1
run_0.4_320	$(1.9 \pm 0.3) \times 10^{-5}$	0.0057 ± 0.0094	$(2.31 \pm 0.14) \times 10^{-5}$	0.284 ± 0.004	3
run_0.8_320	$(1.5 \pm 0.2) \times 10^{-5}$	0.0045 ± 0.0022	$(1.32 \pm 0.02) \times 10^{-4}$	0.375 ± 0.003	4
run_0.2_640	$(4.7 \pm 2.8) \times 10^{-6}$	0.0147 ± 0.0085	$(5.05 \pm 0.41) \times 10^{-5}$	0.294 ± 0.007	1
run_0.4_640	$(1.2 \pm 0.1) \times 10^{-6}$	0.0097 ± 0.0011	$(1.82 \pm 0.02) \times 10^{-5}$	0.352 ± 0.002	3

Notes. Listed errors are standard errors. $^{(a)}$ Best-fitting values at $t = 36\ P_K$ in the case of *run_0.2_320* and at $t = 40\ P_K$ in the case of the other simulations. $^{(b)}$ Mean values, averaged over $36\ P_K \le t \le 40\ P_K$. $^{(c)}$ Number of filaments.

With the mean values of the exponent of the exponential cutoff β ranging from 0.28 to 0.38, the exponential cutoff is rather smooth. Johansen et al. (2015) fit their data by eye using $\beta = 4/3$, which is a significantly steeper cutoff, but this steep cutoff might be an artefact of the small box size they employed, in which only a few massive planetesimals formed. The best-fitting values for the two simulations with the largest number of sink particles, *run_0.8_320* and *run_0.4_640*, are nearly equal, but somewhat greater than the values for *run_0.4_320* and *run_0.2_640*, which are also roughly equal. This indicates that only in the former two simulations enough sink particles emerge to completely capture the high-mass end of the mass distribution. However, the mean values for all simulations lie in a rather small range of 0.1, hence we find β to be relatively independent of the box size and the resolution.

Substituting the best-fitting parameters listed in Table 2 into the cumulative (Eq. (19)) or the differential mass distribution,

$$\frac{dN}{dM} = \frac{1}{M}\left[\alpha + \beta\left(\frac{M}{M_{exp}}\right)^{\beta}\right]\left(\frac{M}{M_{pow}}\right)^{-\alpha} \times \exp\left[\left(\frac{M_{min}}{M_{exp}}\right)^{\beta} - \left(\frac{M}{M_{exp}}\right)^{\beta}\right], \quad (20)$$

yields an initial mass function for each simulation. The cumulative mass distribution can be converted to a cumulative size distribution,

$$\frac{N_>(R)}{N_{tot}} = \left(\frac{R}{R_{min}}\right)^{-3\alpha} \exp\left[\left(\frac{R_{min}}{R_{exp}}\right)^{3\beta} - \left(\frac{R}{R_{exp}}\right)^{3\beta}\right], \quad (21)$$

where R is the radius of every sink particle and the minimum radius R_{min} and the radius scale of the exponential tapering R_{exp} can be calculated from M_{min} and M_{exp}, respectively, using a solid density of 3 g cm^{-3}.

Table 3. Sink particle statistics.

Name	N_{tot}	M_{min} $[G^{-1}\ H_g^3 P_K^{-2}]$	M_{max} $[G^{-1}\ H_g^3 P_K^{-2}]$	$\langle M\rangle$ $[G^{-1}\ H_g^3 P_K^{-2}]$
run_0.2_320	4	5.9×10^{-5}	1.6×10^{-3}	4.8×10^{-4}
run_0.4_320	15	7.8×10^{-6}	4.3×10^{-3}	4.9×10^{-4}
run_0.8_320	42	8.3×10^{-6}	9.3×10^{-3}	6.9×10^{-4}
run_0.2_640	7	1.0×10^{-5}	1.5×10^{-3}	2.6×10^{-4}
run_0.4_640	62	1.9×10^{-6}	2.2×10^{-3}	1.2×10^{-4}

In Table 3, we list the number N_{tot}, minimum mass M_{min}, maximum mass M_{max}, and mean mass $\langle M\rangle$ of the sink particles at the end of our five simulations, $t = 40\ P_K$. In the case of the two simulations with the smallest box dimensions, we observe less than ten sink particles, and the best-fitting parameters for these simulations are therefore afflicted with comparably large errors (see Fig. 5). We find the actual M_{min} and $\langle M\rangle$ to be of the order of the fitted M_{min} and M_{exp}, respectively (compare with Cols. 2 and 4 of Table 2). For *run_0.8_320* and *run_0.4_640*, the 10% of the sink particles which are most massive contain 66% and 70%, respectively, of the total sink particle mass. That is, in our simulations the most massive sink particles dominate the total mass.

As stated above, a higher resolution enables us to observe the formation of smaller pebble clusters, and thus less massive sink particles. Hence, N_{tot} increases and both M_{min} and $\langle M\rangle$ decline with increasing resolution. Like Johansen et al. (2015) and Simon et al. (2016), we find the maximum mass M_{max} to be relatively independent of the resolution.

We expect the number of planetesimals to increase with the number of filaments, and thus with the radial box dimension,

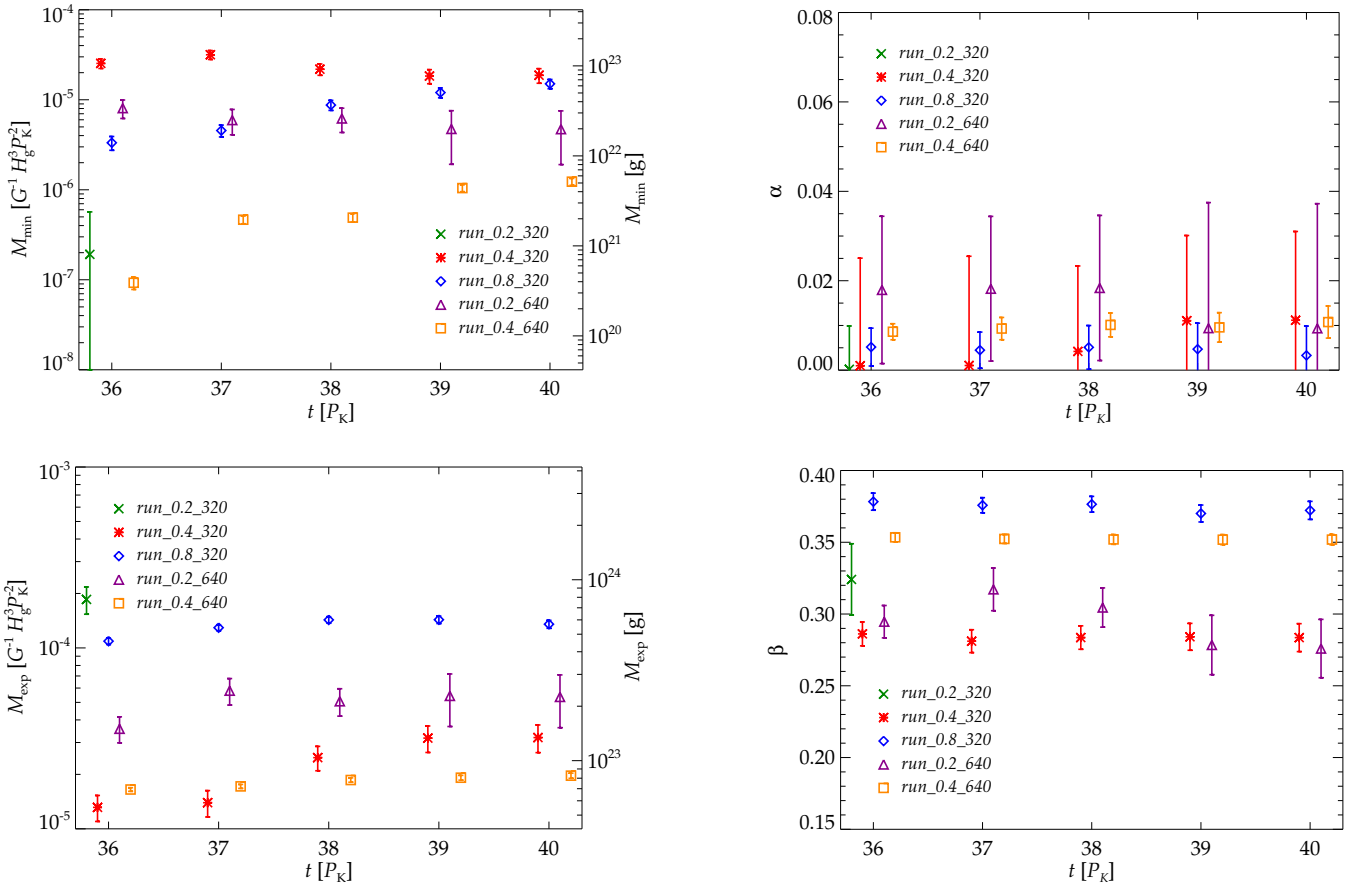

Fig. 5. Best-fitting parameters $M_{\rm min}$ (*upper left panel*), α (*upper right panel*), $M_{\rm exp}$ (*lower left panel*), and β (*lower right panel*) of the exponentially tapered power law (Eq. (19)) at every Keplerian orbital period between $t = 36\ P_{\rm K}$ and $t = 40\ P_{\rm K}$ for all five simulations. Standard errors are plotted as error bars. In the case of the simulation with the smallest box size and the lower resolution, *run_0.2_320*, only parameter values for $t = 36\ P_{\rm K}$ are plotted because afterwards only four sink particles persist, which prevents us from properly fitting the mass distributions with a power law and an exponential tapering.

and with the length of the filaments, i.e. the azimuthal box dimension. Analogously to the mass scale of the exponential cutoff $M_{\rm exp}$, as discussed above, we further expect $\langle M \rangle$ to increase with the distance between the filaments. Our findings are consistent with these expectations, with the exception of $\langle M \rangle$ for *run_0.2_320*. One and three filaments form in *run_0.2_320* and *run_0.4_320*, respectively (see Col. 6 of Table 2), therefore the value for the former simulation should be greater than the one for the latter simulation, yet it is slightly smaller. This shows that, at least at the lower resolution, the smallest boxes, in which only one filament forms, might be too small to accurately capture the mass budget of each filament.

Furthermore, $M_{\rm min}$ and $M_{\rm max}$ in general increase with the box dimensions, but we find $M_{\rm min}$ to considerably decrease if the box size is increased from 0.2 $H_{\rm g}$ to 0.4 $H_{\rm g}$ in the radial and azimuthal directions. This also indicates that the smallest box dimensions might not capture the sink particle mass distribution as well as the larger boxes. However, it may also be a stochastic effect because, especially for a small number of sink particles, the ensemble-averaged values of $M_{\rm min}$ and $M_{\rm max}$ might differ significantly from the actual values.

5. Summary and discussion

We have investigated the formation of planetesimals by the streaming instability in numerical simulations with three different box sizes and two different resolutions. In particular, we have studied the initial mass function of these planetesimals, employing the largest box dimensions to date with radial and azimuthal sizes of up to 0.8 gas scale heights. These large box sizes have enabled us to study planetesimal formation in multiple axisymmetric filaments formed by the streaming instability and to yield better statistics because more planetesimals emerge in simulations with larger box sizes.

In the absence of self-gravity, the streaming instability concentrates pebbles into axisymmetric filaments. After self-gravity has been introduced, these filaments disperse within about ten Keplerian orbital periods because the pebbles accumulate into clusters that undergo gravitational collapse and form planetesimals. We have observed that, after their formation, the planetesimals on average migrate through more than half of the radial dimension of the simulation box owing to mutual gravitational scattering. The extent of the radial migration does not converge for the box sizes we have taken into consideration. Further studies could provide insights regarding the implications of the migration through multiple filaments for the dependence of the composition of planetesimals on the orbital distance.

The radii of the planetesimals formed in our simulations, which depend on the strength of the self-gravity and thus on the solid particle column density, range from 80 km to 620 km. We have compared power-law fits to their cumulative mass distribution with and without exponential tapering and have found that a rather shallow exponential cutoff fits the distribution better than the steeper cutoff of an integrated power law. Johansen et al.

(2015) also find the initial mass function to be represented best by an exponentially tapered power law, although they studied planetesimals that are smaller than the ones formed in our simulations. In their simulation with the highest resolution, the planetesimal radii amount to between 30 km and 120 km. In contrast to this, Simon et al. (2016) find that a power law without exponential tapering is suitable to fit the birth mass distribution of planetesimals with radii between 50 km and a few hundred kilometers.

We have found a value of the exponent of the exponential cutoff of about 0.3 to 0.4, which is largely invariant under changes in the box size and the resolution, but considerably smaller than the value of 4/3 that Johansen et al. (2015) determine, which is based on a much smaller number of massive planetesimals that formed in a small simulation domain. However, the resolutions we have considered are insufficient to constrain the shape of the power-law part and to investigate its dependence on the box dimensions because the planetesimals that formed in our simulations are too large to constitute a power-law distribution at the low-mass end of the initial mass function.

Both the characteristic mass of the exponential cutoff and the mean mass of the planetesimals correlate with the pebble mass budget in every filament. In this regard, we have found indications that a simulation box with a size of 0.2 gas scale heights in the radial, azimuthal, and vertical directions, in which only one filament emerges, may be too small to properly capture the mass reservoir. This is consistent with the observation by Yang & Johansen (2014) that box dimensions of 0.2 scale heights in the radial and azimuthal directions are too small to capture all scales relevant for the streaming instability, and is further supported by Li et al. (in prep.) finding that the density distribution function of solid particles is consistent only for boxes with radial and azimuthal sizes of at least 0.4 scale heights.

The current size distribution of the asteroids in the asteroid belt with diameters between 120 km and several hundred kilometers, corresponding to the sizes of the planetesimals that emerge in our simulations, is well-fitted with a power law. This power law, which Bottke et al. (2005) argue represents the primordial asteroid size distribution, is in contrast to the exponential cutoff we (and Johansen et al. 2015) find. Subsequent pebble accretion therefore appears to be necessary to convert the exponential tapering of the birth size distribution into the power law observed in the asteroid belt (Johansen et al. 2015).

It is interesting to compare the initial mass function of planetesimals to the classical concept of an initial mass function of stars. The formation of stars is comparable to the formation of planetesimals by the streaming instability insofar as both stars and planetesimals form by gravitational collapse, the former from molecular cloud cores, and the latter from pebble clusters. The differential mass distribution of stars with masses greater than about 1 $M_\odot$ is given by a power law with an exponent of approximately −2.3 (Salpeter 1955; Massey 1998; Chabrier 2003). That is, the total stellar mass is dominated by the least massive stars, in contrast to the total mass of the planetesimals we have observed in our simulations, which is dominated by the most massive ones. It has been argued that there is a physical upper mass cutoff of the stellar initial mass function, but massive stars are rare and short-lived, and their mass distribution is therefore difficult to observe (Zinnecker & Yorke 2007).

Johansen et al. (2015) and Simon et al. (2016) investigated the dependence of the shape of the planetesimal initial mass function on the resolution, the pebble column density, the strength of the self-gravity, and the simulation at which self-gravity is initiated. We have complemented these parameter studies with an analysis of the box-size dependence, but how, for instance, the solid-to-gas ratio, the friction time of the pebbles, the radial gas pressure gradient, and the vertical box size affect the shape of the birth mass distribution remains to be investigated. Finally, the streaming instability has been shown to operate in protoplanetary disks with turbulence driven by the magnetorotational instability (Johansen et al. 2007). It remains to be seen how turbulence and magnetic fields influence the shape of the initial mass function.

Acknowledgements. We thank Piero Ranalli for his advice on how to calculate the standard errors of the fitting parameters. We further thank the anonymous referee for providing comments and questions that helped to improve the paper. The simulations presented in this paper were performed on resources provided by the Swedish National Infrastructure for Computing (SNIC), the Alarik system at Lunarc at Lund University and the Beskow system at the PDC Center for High Performance Computing at the KTH Royal Institute of Technology. This research was supported by the European Research Council under ERC Starting Grant agreement 278675-PEBBLE2PLANET. A.J. is thankful for financial support from the Knut and Alice Wallenberg Foundation and from the Swedish Research Council (grant 2014-5775).

References

Adachi, I., Hayashi, C., & Nakazawa, K. 1976, Prog. Theor. Phys., 56, 1756
Armitage, P. J. 2007, ArXiv Astrophysics e-prints [arXiv:astro-ph/0701485]
Bai, X.-N., & Stone, J. M. 2010a, ApJS, 190, 297
Bai, X.-N., & Stone, J. M. 2010b, ApJ, 722, 1437
Bai, X.-N., & Stone, J. M. 2010c, ApJ, 722, L220
Birnstiel, T., Ormel, C. W., & Dullemond, C. P. 2011, A&A, 525, A11
Bitsch, B., Johansen, A., Lambrechts, M., & Morbidelli, A. 2015, A&A, 575, A28
Bottke, W. F., Durda, D. D., Nesvorný, D., et al. 2005, Icarus, 175, 111
Brandenburg, A., Nordlund, Å., Stein, R. F., & Torkelsson, U. 1995, ApJ, 446, 741
Brauer, F., Dullemond, C. P., Johansen, A., et al. 2007, A&A, 469, 1169
Carrera, D., Johansen, A., & Davies, M. B. 2015, A&A, 579, A43
Chabrier, G. 2003, PASP, 115, 763
Gammie, C. F. 2001, ApJ, 553, 174
Goldreich, P., & Lynden-Bell, D. 1965, MNRAS, 130, 125
Güttler, C., Blum, J., Zsom, A., Ormel, C. W., & Dullemond, C. P. 2010, A&A, 513, A56
Hawley, J. F., Gammie, C. F., & Balbus, S. A. 1995, ApJ, 440, 742
Hayashi, C. 1981, Prog. Theor. Phys. Suppl., 70, 35
Hockney, R. W., & Eastwood, J. W. 1981, Computer Simulation Using Particles (New York: McGraw-Hill)
Johansen, A., & Youdin, A. 2007, ApJ, 662, 627
Johansen, A., Oishi, J. S., Mac Low, M.-M., et al. 2007, Nature, 448, 1022
Johansen, A., Youdin, A., & Klahr, H. 2009a, ApJ, 697, 1269
Johansen, A., Youdin, A., & Mac Low, M.-M. 2009b, ApJ, 704, L75
Johansen, A., Klahr, H., & Henning, T. 2011, A&A, 529, A62
Johansen, A., Youdin, A. N., & Lithwick, Y. 2012, A&A, 537, A125
Johansen, A., Mac Low, M.-M., Lacerda, P., & Bizzarro, M. 2015, Sci. Adv., 1, 1500109
Lambrechts, M., & Johansen, A. 2012, A&A, 544, A32
Massey, P. 1998, in The Stellar Initial Mass Function, 38th Herstmonceux Conference, eds. G. Gilmore, & D. Howell, ASP Conf. Ser., 142, 17
Ormel, C. W., & Klahr, H. H. 2010, A&A, 520, A43
Salpeter, E. E. 1955, ApJ, 121, 161
Simon, J. B., Armitage, P. J., Li, R., & Youdin, A. N. 2016, ApJ, 822, 55
Wada, K., Tanaka, H., Suyama, T., Kimura, H., & Yamamoto, T. 2008, ApJ, 677, 1296
Wada, K., Tanaka, H., Suyama, T., Kimura, H., & Yamamoto, T. 2009, ApJ, 702, 1490
Weidenschilling, S. J. 1977, MNRAS, 180, 57
Windmark, F., Birnstiel, T., Güttler, C., et al. 2012, A&A, 540, A73
Wurm, G., Paraskov, G., & Krauss, O. 2005, Icarus, 178, 253
Yang, C.-C., & Johansen, A. 2014, ApJ, 792, 86
Yang, C.-C., Johansen, A., & Carrera, D. 2016, A&A, submitted [arXiv:1611.07014]
Youdin, A. N., & Goodman, J. 2005, ApJ, 620, 459
Youdin, A., & Johansen, A. 2007, ApJ, 662, 613
Zinnecker, H., & Yorke, H. W. 2007, ARA&A, 45, 481
Zsom, A., Ormel, C. W., Güttler, C., Blum, J., & Dullemond, C. P. 2010, A&A, 513, A57

6

The coexistence of the streaming instability and the vertical shear instability in protoplanetary disks

Contribution

This study began with the notion of employing the FLASH Code[1] (Fryxell et al. 2000) to conduct the first-ever two-dimensional global simulations of the streaming instability with Lagrangian particles representing the dust. Previous numerical studies of the instability almost exclusively used the local shearing box approximation. Only Kowalik et al. (2013) conducted two- and three-dimensional global simulations of the streaming instability, but modelled the dust as a fluid on a Eulerian grid. Our global simulations were computationally feasible because of the capability of the FLASH Code to perform adaptive mesh refinement (AMR). This allowed us to locally increase the resolution where particles are concentrated and the streaming instability is active. In contrast, in previous studies of the instability simulation codes with a uniform grid had been employed.

For the purpose of conducting these simulations, I implemented and tested a number of extensions and modifications in the FLASH Code, including

- a unit[2] to simulate the mutual drag between gas and dust, which is based on the cloud-in-cell algorithm included in the code for mapping between grid and particles that model gas and dust, respectively (see Appendix B of the article),
- an adaptation for cylindrical geometries of the Leapfrog algorithm for the time integration of particles (see Appendix A of the article; Boris 1970),
- a unit to model a temperature distribution in connection with an isothermal equation of state,

[1] `http://flash.uchicago.edu/site/flashcode/`

[2] The FLASH Code is organised in units. Each unit consists of one or several routines that jointly control an aspect of the simulations conducted with the code.

- a modification of the polytropic equation of state unit that permits the treatment of the polytropic constant as a local rather than a global constant,
- a routine to handle particles that move into obstacle blocks, i.e. blocks of grid cells that are excluded from the simulation domain,
- an AMR criterion to enhance the local resolution if a threshold number of particles per cell is exceeded,
- modifications to the simulation boundary conditions to account for the differences in temperature and orbital velocity between guard and non-guard cells[3],
- and a simulation setup to perform the simulations presented in the article.

The presence of the vertical shear instability in test simulations of these implementations lead us to study the interaction of the streaming instability and the vertical shear instability, which had not been investigated before. While in previous studies the streaming instability has been considered predominantly as a mechanism for planetesimal formation, we focus on the instability as a source of turbulence. Under supervision and in collaboration with Anders Johansen and Robi Banerjee, I conducted, analysed, and visualised the simulations and wrote the article.

[3]The domains of FLASH Code simulations are divided into blocks. Every block consists of several non-guard cells that are surrounded by a layer of guard cells. While the data in the non-guard cells are computed locally, the data in the guard cells are either received from adjacent blocks or calculated based on the simulation boundary conditions.

A&A 635, A190 (2020)
https://doi.org/10.1051/0004-6361/201937371

Astronomy & Astrophysics

The coexistence of the streaming instability and the vertical shear instability in protoplanetary disks

Urs Schäfer[1,2], Anders Johansen[2], and Robi Banerjee[1]

[1] Hamburg Observatory, University of Hamburg, Gojenbergsweg 112, 21029 Hamburg, Germany
e-mail: urs.schaefer@hs.uni-hamburg.de
[2] Lund Observatory, Department of Astronomy and Theoretical Physics, Lund University, Box 43, 22100 Lund, Sweden

Received 20 December 2019 / Accepted 14 February 2020

ABSTRACT

The streaming instability is a leading candidate mechanism to explain the formation of planetesimals. However, the role of this instability in the driving of turbulence in protoplanetary disks, given its fundamental nature as a linear hydrodynamical instability, has so far not been investigated in detail. We study the turbulence that is induced by the streaming instability as well as its interaction with the vertical shear instability. For this purpose, we employ the FLASH Code to conduct two-dimensional axisymmetric global disk simulations spanning radii from 1 to 100 au, including the mutual drag between gas and dust as well as the radial and vertical stellar gravity. If the streaming instability and the vertical shear instability start their growth at the same time, we find the turbulence in the dust midplane layer to be primarily driven by the streaming instability. The streaming instability gives rise to vertical gas motions with a Mach number of up to $\sim 10^{-2}$. The dust scale height is set in a self-regulatory manner to about 1% of the gas scale height. In contrast, if the vertical shear instability is allowed to saturate before the dust is introduced into our simulations, then it continues to be the main source of the turbulence in the dust layer. The vertical shear instability induces turbulence with a Mach number of $\sim 10^{-1}$ and thus impedes dust sedimentation. Nonetheless, we find the vertical shear instability and the streaming instability in combination to lead to radial dust concentration in long-lived accumulations that are significantly denser than those formed by the streaming instability alone. Therefore, the vertical shear instability may promote planetesimal formation by creating weak overdensities that act as seeds for the streaming instability.

Key words. instabilities – turbulence – methods: numerical – planets and satellites: formation – protoplanetary disks – hydrodynamics

1. Introduction

Turbulence crucially influences various stages of the formation of planets: such as (1) the vertical settling of dust grains to a midplane layer whose thickness is determined by the equilibrium between sedimentation and turbulent diffusion (Dubrulle et al. 1995; Johansen & Klahr 2005; Fromang & Papaloizou 2006; Youdin & Lithwick 2007); (2) collisional grain growth (Ormel & Cuzzi 2007; Birnstiel et al. 2010); (3) planetesimal formation owing to passive concentration of grains (Barge & Sommeria 1995; Johansen et al. 2007; Cuzzi et al. 2008); and (4) planetary migration (Nelson & Papaloizou 2004; Oishi et al. 2007; Yang et al. 2009, 2012; Baruteau et al. 2011).

However, it is challenging to observationally constrain the strength of the turbulence in the gas and the dust in protoplanetary disks, whose motions are coupled via drag. This is particularly because these turbulent motions are weaker than both the thermal gas motions and the orbital motions of gas and dust (Flaherty et al. 2018).

Recently, high-resolution ALMA observations of protoplanetary disks permitted a number of authors to assess the turbulent strength in these disks: Flaherty et al. (2015, 2017, 2018) derive upper limits of the strength of the turbulent vertical gas motions in the disks surrounding HD 163296 and TW Hya from the non-thermal broadening of molecular emission lines. These upper limits correspond to Mach numbers of the order of 0.01[1].

Pinte et al. (2016) employ a model of micron- to millimeter-sized grains in the disk around HL Tau to estimate the strength of their vertical turbulent diffusion from the observed dust scale height, which is equal to ∼10% of the gas scale height. These latter authors also find a Mach number of ∼0.01. Similarly, Ohashi & Kataoka (2019) constrain the dust grain sizes and dust scale height in the disk around HD 163296 using polarization measurements of the dust emission. From a grain size of ∼100 μm and a scale height of less than one-third of the gas scale height inside the ring that is located at an orbital radius of 70 au in this disk, these latter authors infer an upper limit of the Mach number of the vertical gas velocity of ∼0.01. On the other hand, from the dust-to-gas scale height ratio of two-thirds outside of the ring the authors estimate a Mach number of the order of 0.1.

Furthermore, Dullemond et al. (2018) obtain a lower limit on the strength of the radial turbulent motions from the width of the dust rings that characterize the majority of the observed disks. This limit also amounts to a Mach number of about 0.01 for grains of 0.2 mm in size, but is proportional to the grain size.

[1] Here and in the following, we report turbulent strength in terms of Mach numbers rather than turbulent α-parameters (Shakura & Sunyaev 1973). This is to avoid confusion with the α-parameter associated with angular momentum transport. Based on a mixing length approach and assuming that the eddy turn-over timescale is similar to the inverse of the orbital frequency – a valid assumption for the instabilities that we investigate in this paper, the streaming instability (Youdin & Goodman 2005) and the vertical shear instability (Nelson et al. 2013) – the turbulent α-parameter can be approximated as the square of the Mach number.

In addition to the uncertainties in the observational determination of the turbulent strength, the physical processes that are the dominant sources of protoplanetary disk turbulence remain to be theoretically established. In large fractions of disks, particularly in the midplane, magnetohydrodynamic (MHD) turbulence is suppressed because of nonideal MHD effects (Gressel et al. 2015; Bai 2017). Turbulence in these regions must therefore be driven either from the MHD turbulent disk surface (Oishi & Mac Low 2009; Bai 2015) or by purely hydrodynamic instabilities.

One of the most promising among the hydrodynamical instabilities is the vertical shear instability (Arlt & Urpin 2004; Nelson et al. 2013), which is similar to the Goldreich-Schubert-Fricke instability in differentially rotating stars (Goldreich & Schubert 1967; Fricke 1968). It arises when the disk rotation profile depends on the height. This can, for instance, be due to baroclinity, which is a misalignment between the density and the pressure gradient, resulting from a radial temperature profile. The source of energy of the instability is the free energy associated with the vertical shear (Barker & Latter 2015).

The vertical shear instability can overcome both the radial angular momentum gradient, as its modes are characterized by a large radial-to-vertical wavenumber ratio, and the vertical buoyancy if the gas cooling timescale is sufficiently short (Nelson et al. 2013; Lin & Youdin 2015). Analytical and numerical analyses of the linear growth of the instability have found two classes of modes: short-wavelength surface modes with higher growth rates and vertically global body modes with lower growth rates. The former appear at the artificial vertical simulation domain boundary, where the vertical shear is strongest – although natural transitions in the density can also give rise to these modes. Their growth rate increases with the vertical shear at the boundary, and thus with vertical domain size (Nelson et al. 2013; Barker & Latter 2015; Lin & Youdin 2015).

In nonlinear simulations, the vertical shear instability grows over at least approximately 30 orbital periods until it attains a saturated state (Stoll & Kley 2014; Flock et al. 2017). The Mach numbers of the turbulent vertical motions in this state are of the order of 10^{-2} to 10^{-1} (Flock et al. 2017). This turbulent strength is higher if the radial temperature gradient is steeper (Nelson et al. 2013; Lin 2019). Perturbations associated with the surface modes appear first and grow towards the disk midplane. The later emerging body modes are characterized by perturbations that evolve from an odd symmetry with respect to the midplane into an even symmetry, and therefore the instability saturates last in this plane (Nelson et al. 2013; Stoll & Kley 2014).

The turbulence that is induced by the vertical shear instability entails angular momentum being transported radially outwards and vertically away from the midplane. Since the latter eliminates the vertical shear, external heating (of locally non-isothermal disks) is necessary to sustain the instability (Stoll & Kley 2014). In numerical models including dust and the drag exerted on it by the gas, the turbulence further gives rise to vertical dust motions, and radial motions leading to accumulation in overdensities of up to five times the initial dust density (Stoll & Kley 2016; Flock et al. 2017).

However, Lin & Youdin (2017) and Lin (2019) show that, if the drag back-reaction of the dust onto the gas is taken into account as well, the dust, which sediments to the midplane, introduces an effective vertical buoyancy – it "weighs down" the gas – that can quench the vertical shear instability. If they are tightly coupled, gas and dust can be described as a single fluid, with a density equal to the sum of the gas and the dust density, but a pressure that is solely due to the gas. We assume that the pure gas is locally isothermal, that is, its cooling timescale is infinitely short. Under this assumption, the equation of state of the mixture is given by $P = c_s^2\rho_g = c_s^2(1-\rho_d/\rho_{tot})\rho_{tot}$, where P is the gas pressure, c_s the sound speed, and ρ_g, ρ_d, and ρ_{tot} are the gas, dust, and total density, respectively. In other words, the gas-dust mixture is not locally isothermal, and its cooling timescale is finite. As noted above, the instability is suppressed by vertical buoyancy if the cooling timescale is too long.

The streaming instability (Youdin & Goodman 2005; Youdin & Johansen 2007; Johansen & Youdin 2007) results from the inwards radial drift of dust, which is caused by the difference in orbital velocity between the gas and the dust as well as their mutual coupling via drag. In contrast to the dust, the gas orbits with a sub-Keplerian velocity because it is supported against the radial stellar gravity by a pressure gradient. This pressure gradient constitutes a source of free energy that is tapped by the streaming instability (Youdin & Johansen 2007). The linear growth rate of the instability is highest if the dust drift is fastest, that is when the dust stopping time is comparable to the inverse of the orbital frequency (Weidenschilling 1977), and if the dust-to-gas density ratio is slightly greater than one (Youdin & Goodman 2005). Physical interpretations of the instability have been devised by Lin & Youdin (2017) and Squire & Hopkins (2018).

The turbulence that the streaming instability gives rise to in its nonlinear regime can result in dust concentration in axisymmetric filaments. In these filaments, the dust accumulates in clumps that are sufficiently dense to collapse under their self-gravity and form planetesimals (Johansen et al. 2007; Bai & Stone 2010b; Yang & Johansen 2014; Simon et al. 2016; Schäfer et al. 2017). However, whether the streaming instability causes dust accumulation that is strong enough for planetesimal formation depends on the dust-to-gas surface density ratio and the size of the dust (Johansen et al. 2009; Bai & Stone 2010b; Carrera et al. 2015; Yang et al. 2017, 2018), as well as the strength of the radial pressure gradient (Bai & Stone 2010c). The required surface density ratio is higher than 1% – the canonical value in the interstellar medium – for all dust sizes. It can be enhanced sufficiently to reach the critical value globally by photoevaporation (Carrera et al. 2017; Ercolano et al. 2017), and locally in radial dust pile-ups (Drążkowska et al. 2016) or at ice lines (Ida & Guillot 2016; Schoonenberg & Ormel 2017; Schoonenberg et al. 2018; Drążkowska & Alibert 2017).

Observations of binaries among the Trans-Neptunian objects provide evidence for planetesimal formation owing to the streaming instability: their observed orbital inclinations relative to their heliocentric orbit as well as the ones that are found in simulations of binary formation by gravitational collapse are predominantly prograde (Grundy et al. 2019; Nesvorný et al. 2010, 2019). In contrast, dynamical binary capture leads to either mostly retrograde inclinations or a similar number of prograde and retrograde ones, depending on the capture mechanism (Schlichting & Sari 2008).

While it is considered to be and is studied as one of the most promising mechanisms to induce planetesimal formation, the streaming instability has received comparably little attention as a process to drive turbulence, although this is its fundamental effect. Moreover, the streaming instability has been studied numerically almost exclusively in local shearing box simulations. Only Kowalik et al. (2013) present global two- and three-dimensional simulations, which reproduce the dust accumulation in dense axisymmetric filaments.

In this paper, we study the streaming instability as a source of turbulence, employing axisymmetric global simulations with

considerably larger domains than the ones that were simulated by Kowalik et al. (2013). In contrast to these authors, we model the dust as Lagrangian particles rather than as a pressureless fluid, and take into account the vertical stellar gravity, which leads to the dust sedimenting to the midplane. We further apply adaptive mesh refinement to enhance the resolution of the dust midplane layer.

The paper is structured as follows: in Sect. 2, the simulations, their initial conditions, and the parameters that govern their evolution are described. In Sects. 3–5, respectively, we present our study of the turbulence in models of the vertical shear instability only, both the vertical shear and the streaming instability, and the streaming instability only. Implications and limitations of the study are discussed in Sect. 6. We summarize our results in Sect. 7.

2. Numerical model

We perform two-dimensional numerical simulations of the gas and the dust components of protoplanetary disks, including the mutual drag between the two components as well as the radial and the vertical stellar gravity. Magnetic fields, the self-gravity of the gas and the dust, and (nonnumerical) viscosity are neglected. We employ version 4.5 of the adaptive-mesh refinement (AMR) finite volume code FLASH Code[2] (Fryxell et al. 2000).

2.1. Domains, boundary conditions, and resolutions

The cylindrical, axisymmetric simulation domains extend from either 1 to 10 au or from 10 to 100 au in the radial dimension and 1 or 2 gas scale heights above and below the midplane in the vertical dimension. Since in our model the gas scale height increases nonlinearly with the radius (see Eq. (9)), the domains are shaped like isosceles trapezoids with curved rather than straight legs. To model this shape as accurately as possible with respect to the initial resolution, we initially create rectangular domains with a vertical size of two or four gas scale heights at the outer radial boundary. From these domains, we then exclude all blocks of 10×10 grid cells whose distance to the midplane is greater than one or two local gas scale heights. For this purpose, we apply the obstacle block implementation that is included in the FLASH Code[3].

Diode conditions are applied at both the radial and the vertical boundaries, that is, the boundaries are permeable to gas and dust moving out of the domain, but reflect gas and dust that would move into it. At the vertical boundaries, the pressure in the guard cells is quadratically interpolated to maintain hydrostatic equilibrium. The temperature in the guard cells at all boundaries is reset to the initial value because we find this to be conducive to the stability of our simulations. In addition, the orbital velocity is corrected to account for the difference in temperature and stellar gravity between the guard and the nonguard cells[3].

The FLASH Code employs the PARAMESH package (MacNeice et al. 2000) to perform block-structured AMR. In other words, the domain is subdivided into blocks of 10×10 grid cells, which as a whole are refined or derefined if a refinement or derefinement criterion is fulfilled in any cell inside them. To resolve the gas and dust dynamics that are induced by the streaming instability in the disk midplane, we apply a (de-) refinement criterion which is based on the spatial dust distribution: the resolution is doubled if more than ten particles, which we use to model the dust, are located in one cell. On the other hand, the resolution is halved if no particles remain in a cell[3]. In addition, we initially increase the resolution of the midplane density at the inner radial domain boundary by a factor of two or of four where the ratio of the gas density to the midplane density at the inner radial domain boundary exceeds 1 or 10%, respectively.

In the domains with a radial size of 9 au, the fiducial initial and maximum resolution amount to 160 and 5120 cells per astronomical unit, respectively, while in the domains with an extent of 90 au they are equal to 10 and 320 cells per astronomical unit, respectively. At the maximum resolution, this corresponds to more than 200 cells per gas scale height at all radii, which has been shown to be sufficient to resolve the formation of gravitationally unstable dust clumps owing to the streaming instability in local shearing box simulations (Yang & Johansen 2014). To investigate whether or not our findings are dependent on resolution, we also conduct simulations with a doubled initial and maximum resolution.

The simulation names and parameters are compiled in Table 1. Sets of simulations which are analyzed in different sections are separated by a double horizontal line. All names are composed of (1) the gas equation of state (isothermal or adiabatic); (2) the dust-to-gas surface density ratio (this is omitted if dust is not included in a simulation); and (3) the radial simulation domain size. Where applicable, the names further indicate that (4) the vertical domain extent amounts to four gas scale heights; (5) the resolution is twice the fiducial resolution; (6) the dust particles are introduced after 50 kyr rather than at the beginning of the simulation; (7) the initial dust-to-gas scale height ratio is set to 1 or 100%, with the fiducial value being 10%; and (8) the dust particle size deviates from the fiducial size of $a = 3$ cm.

2.2. Gas

The equations of motion of the gas can be expressed as

$$\frac{\partial \rho_\mathrm{g}}{\partial t} + \nabla \cdot \left(\rho_\mathrm{g} \boldsymbol{v}_\mathrm{g}\right) = 0 \text{ and} \tag{1}$$

$$\frac{\partial \boldsymbol{v}_\mathrm{g}}{\partial t} + \left(\boldsymbol{v}_\mathrm{g} \cdot \nabla\right) \boldsymbol{v}_\mathrm{g} = -\frac{1}{\rho_\mathrm{g}} \nabla P - \nabla \Phi_\mathrm{S} + \frac{\rho_\mathrm{d}}{\rho_\mathrm{g}} \frac{\boldsymbol{v}_\mathrm{d} - \boldsymbol{v}_\mathrm{g}}{t_\mathrm{stop}}, \tag{2}$$

where $\boldsymbol{v}$ is the velocity, and the subscripts g and d refer to the gas and the dust, respectively. The stellar gravitational potential is given by $\Phi_\mathrm{S} = -GM_\mathrm{S}/\sqrt{r^2 + z^2}$, where G is the gravitational constant, $M_\mathrm{S} = 1\ M_\odot$ is the stellar mass, and r and z, respectively, are the radial distance to the star and the height above or below the disk midplane. The last term on the right-hand side of Eq. (2) results from the drag exerted by the dust on the gas, with t_stop being the stopping time (see Sect. 2.3).

To close the system of equations, we consider either an isothermal or an adiabatic equation of state. In the former case, the pressure is calculated as

$$P = \frac{RT}{\mu} \rho_\mathrm{g}, \tag{3}$$

where R is the ideal gas constant, T the temperature, and $\mu = 2.33$ the mean molecular weight[3]. In this case, the adiabatic index $\gamma = 1$. To model the latter case, we employ a polytropic equation of state that is given by

$$P = K \rho_\mathrm{g}^\gamma, \tag{4}$$

[2] http://flash.uchicago.edu/site/flashcode/

[3] Please address code requests regarding the modifications to the FLASH Code that we have implemented to conduct the simulations presented in this paper to urs.schaefer@hs.uni-hamburg.de. We note that we are not permitted to re-distribute the FLASH Code or any of its parts.

Table 1. Simulation parameters.

Simulation name	Equation of state	Z [%] [a]	Dust particle size [b]	L_z [H_g] [c]	L_r [au] [d]	Δx_{init} [au] [e]	Δx_{min} [au] [f]	t_{end} [kyr] [g]
iso_Lr=90au [h]	Isothermal	–	–	2	90	0.1	3.125×10^{-3}	70
iso_Lr=90au_Lz=4Hg [h]	Isothermal	–	–	4	90	0.1	3.125×10^{-3}	70
iso_Lr=90au_Lz=4Hg_dou_res [h]	Isothermal	–	–	4	90	0.05	1.56×10^{-3}	70
iso_Z=0.02_Lr=90au_Lz=4Hg	Isothermal	2	a = 3 cm	4	90	0.1	3.125×10^{-3}	30
iso_Z=0.02_Lr=90au_Lz=4Hg_tdinit=50kyr [i]	Isothermal	2	a = 3 cm	4	90	0.1	3.125×10^{-3}	55
iso_Z=0.02_Lr=90au_Lz=4Hg_tdinit=50kyr_Hdinit=0.01Hginit [i,j]	Isothermal	2	a = 3 cm	4	90	0.1	3.125×10^{-3}	55
iso_Z=0.04_Lr=90au_Lz=4Hg_tdinit=50kyr [i]	Isothermal	4	a = 3 cm	4	90	0.1	3.125×10^{-3}	55
iso_Z=0.1_Lr=90au_Lz=4Hg_tdinit=50kyr [i]	Isothermal	10	a = 3 cm	4	90	0.1	3.125×10^{-3}	55
adi_Lr=9au [h]	Adiabatic	–	–	2	9	6.25×10^{-3}	1.95×10^{-4}	0.3
adi_Z=0.02_Lr=9au	Adiabatic	2	a = 3 cm	2	9	6.25×10^{-3}	1.95×10^{-4}	0.3
adi_Z=0.02_Lr=90au	Adiabatic	2	a = 3 cm	2	90	0.1	3.125×10^{-3}	2.5
adi_Z=0.02_Lr=9au_Hdinit=Hginit [k]	Adiabatic	2	a = 3 cm	2	9	6.25×10^{-3}	1.95×10^{-4}	0.4
adi_Z=0.02_Lr=90au_Hdinit=Hginit [k]	Adiabatic	2	a = 3 cm	2	90	0.1	3.125×10^{-3}	2.5
adi_Z=0.01_Lr=9au	Adiabatic	1	a = 3 cm	2	9	6.25×10^{-3}	1.95×10^{-4}	0.3
adi_Z=0.01_Lr=90au	Adiabatic	1	a = 3 cm	2	90	0.1	3.125×10^{-3}	2.5
adi_Z=0.02_Lr=9au_dou_res	Adiabatic	2	a = 3 cm	2	9	3.125×10^{-3}	9.76×10^{-5}	0.3
adi_Z=0.02_Lr=90au_dou_res	Adiabatic	2	a = 3 cm	2	90	0.05	1.56×10^{-3}	2.5
adi_Z=0.02_Lr=90au_a=3mm	Adiabatic	2	a = 3 mm	2	9	6.25×10^{-3}	1.95×10^{-4}	6
adi_Z=0.02_Lr=90au_taustop=0.1	Adiabatic	2	τ_{stop} = 0.1	2	90	0.05	1.56×10^{-3}	3.5

Notes. [a]Dust-to-gas surface density ratio. [b]Given either as a size a or as a dimensionless stopping time τ_{stop}. [c]Vertical domain extent, where H_g is the gas scale height. (Approximate value, see text.) [d]Radial domain size. [e]Initial grid cell edge length. [f]Minimum grid cell edge length (at maximum resolution). [g]Time after which simulation ends. [h]No dust particles included. [i]Dust particles initialized after $t_{d,init}$ = 50 kyr. [j]Initial dust scale height equal to 1% of gas scale height. [k]Initial dust scale height equal to gas scale height.

where $K = RT\rho_g^{1-\gamma}/\mu$ is the polytropic constant and the adiabatic index $\gamma = 5/3$[3]. While it is a local constant in time, the polytropic constant depends on the global temperature and density distributions (see Eqs. (5)–(7)). If the gas is locally adiabatic, the vertical shear instability is stabilized by vertical buoyancy.

The initial temperature is adopted from the minimum mass solar nebula (MMSN) model (Hayashi 1981),

$$T = 280\ \mathrm{K} \left(\frac{r}{1\ \mathrm{au}}\right)^{-1/2}. \tag{5}$$

The steepness of this profile is in agreement with that of power-law fits to observed temperature distributions (Andrews & Williams 2005). The radial temperature gradient gives rise to a variation of the orbital speed with height. This vertical shear in turn is the source of energy of the vertical shear instability.

The gas initially orbits with a sub-Keplerian velocity, which is determined by the balance between stellar gravity, centrifugal force, and pressure gradient. It is furthermore in vertical hydrostatic equilibrium. As it is vertically isothermal, the vertical density profile is thus given by

$$\rho_g = \rho_g(z=0) \exp\left[-\frac{\gamma G M_S}{c_s^2}\left(\frac{1}{r} - \frac{1}{\sqrt{r^2+z^2}}\right)\right], \tag{6}$$

where $c_s = (\gamma RT/\mu)^{1/2} \propto r^{-1/4}$ (see Eq. (5)) is the sound speed. We set the initial midplane density to

$$\rho_g(z=0) = 10^{-9}\ \mathrm{g\,cm^{-3}} \left(\frac{r}{1\ \mathrm{au}}\right)^{-9/4}. \tag{7}$$

Numerically integrating over Eq. (6) yields the surface density

$$\Sigma_g = \int_{-1\ H_g}^{1\ H_g} \rho_g\, \mathrm{d}z = 10^3\ \mathrm{g\,cm^{-2}} \left(\frac{r}{1\ \mathrm{au}}\right)^{-1}, \tag{8}$$

where

$$H_g = \sqrt{\frac{c_s^2 r^3 (2\gamma G M_S - c_s^2 r)}{(c_s^2 r - \gamma G M_S)^2}}, \tag{9}$$

is the gas scale height. This surface density profile is shallower than the one in the MMSN model (Hayashi 1981), but is consistent with that of observed young, massive protoplanetary disks (Andrews et al. 2009, 2010).

We note that Eq. (8) gives the surface density as the density integrated over two gas scale heights, not integrated from $-\infty$ to ∞ as in the commonly used definition. Consequently, the total mass $M_{g,tot}$ in each of our domains depends not only on the radial, but also on the vertical domain extent:

$$M_{g,tot} = \begin{cases} 7.1 \times 10^{-3}\ M_\odot \left(\frac{L_r}{9\ \mathrm{au}}\right) & L_z \approx 2\ H_g \text{ or} \\ 8.0 \times 10^{-3}\ M_\odot \left(\frac{L_r}{9\ \mathrm{au}}\right) & L_z \approx 4\ H_g, \end{cases} \tag{10}$$

where L_r and L_z are the radial and vertical domain size, respectively.

The orbital speed can be expressed as $v_{g,\phi} = v_K - \Pi c_s$, where

$$v_K = \sqrt{\frac{G M_S}{(r^2+z^2)^{3/2}} r^2} \tag{11}$$

is the Keplerian speed. We adopt the dimensionless parameter Π, which is introduced by Bai & Stone (2010b) to indicate the strength of the radial pressure gradient

$$\Pi = -\frac{1}{2 c_s \rho_g \Omega_K} \frac{\mathrm{d}P}{\mathrm{d}r}, \tag{12}$$

where $\Omega_K = v_K/r$ is the Keplerian orbital frequency. In the midplane, the parameter is equal to

$$\Pi(z=0) = 4.6 \times 10^{-2} \frac{1}{\sqrt{\gamma}} \left(\frac{r}{1\ \mathrm{au}}\right)^{1/4}; \tag{13}$$

(see Eqs. (5) and (7)).

2.3. Dust

We model the dust as Lagrangian particles using the massive active particle implementation that is included in the FLASH Code. We adopt an approach that is commonly used in local shearing box studies of the streaming instability (Youdin & Johansen 2007; Bai & Stone 2010a): the mass and momentum of every simulated particle are equal to the total mass and momentum of a large number of dust pebbles, while the drag coupling to the gas is the same as that of a single pebble.

The dust is initially uniformly distributed in the radial dimension. The mass of the dust particles is determined by their total number $N_\mathrm{d} = 10^6$, the dust-to-gas surface density ratio Z, and the gas surface density. It can be expressed as

$$m_\mathrm{d} = \frac{1}{N_\mathrm{d}} \int_{L_r} 2\pi r \Sigma_\mathrm{d}\, \mathrm{d}r = \frac{Z}{N_\mathrm{d}} \int_{L_r} 2\pi r \Sigma_\mathrm{g}\, \mathrm{d}r. \tag{14}$$

Because the gas surface density is inversely proportional to the radius (see Eq. (8)), the mass of all particles in a simulation is given by

$$\begin{aligned} m_\mathrm{d} &= 1.27 \times 10^{23}\ \mathrm{g} \left(\frac{Z}{0.01}\right)\left(\frac{L_r}{9\ \mathrm{au}}\right) \\ &= 0.14\ M_\mathrm{Ceres} \left(\frac{Z}{0.01}\right)\left(\frac{L_r}{9\ \mathrm{au}}\right), \end{aligned} \tag{15}$$

where $M_\mathrm{Ceres} = 9.3 \times 10^{23}$ g is the mass of Ceres. The simulated dust-to-gas surface density ratios range from $Z = 0.01$ to $Z = 0.1$, with $Z = 0.02$ being the fiducial value. We verified that our results are converged with respect to the total number of particles by comparing simulations with $N_\mathrm{d} = 5 \times 10^5$ and $N_\mathrm{d} = 10^6$.

The initial vertical positions are randomly sampled from a Gaussian distribution with a scale height of 10% of the gas scale height. This scale height is in agreement with the thickness of the dust midplane layer observed by Pinte et al. (2016). To investigate the dependence of our findings on the initial scale height, we additionally perform simulations with a dust-to-gas scale height ratio of 0.01 and of 1. The noise in the vertical distribution serves as a seed for the streaming instability. A comparison of simulations with two different vertical distributions has shown that our results do not noticeably depend on the random seed.

We simulate dust with a fixed size of $a = 3$ cm or of $a = 3$ mm, or with a fixed dimensionless stopping time, which is equivalent to the Stokes number, of $\tau_\mathrm{stop} = 0.1$. Even if $a = 3$ cm, the dust is smaller than the gas mean free path length at all densities in our model. Under this condition, that is to say in the Epstein regime, the dimensionless stopping time in the midplane is given by

$$\begin{aligned} \tau_\mathrm{stop}(z=0) &= t_\mathrm{stop}(z=0)\Omega_\mathrm{K}(z=0) = \frac{a\rho_\mathrm{s}}{c_\mathrm{s}\rho_\mathrm{g}(z=0)}\Omega_\mathrm{K}(z=0) \\ &= 6 \times 10^{-4}\ \frac{1}{\sqrt{\gamma}} \left(\frac{a}{3\ \mathrm{mm}}\right)\left(\frac{r}{1\ \mathrm{au}}\right), \end{aligned} \tag{16}$$

where $\rho_\mathrm{s} = 1\ \mathrm{g\,cm^{-3}}$ is the dust material density (see also Eq. (7)).

We note that the collisional growth to sizes greater than millimeters is prevented by dust grains bouncing or fragmenting under mutual collisions (Güttler et al. 2010; Zsom et al. 2010; Birnstiel et al. 2011), except for in the innermost regions of protoplanetary disks (Birnstiel et al. 2012) and at ice lines (Ros & Johansen 2013; Ros et al. 2019). However, simulating centimeter-sized grains allows us to probe dimensionless stopping times of the order of $\tau_\mathrm{stop} = 0.1$. These are pertinent to a study of the turbulence that is driven by the streaming instability since the linear growth rate of the instability is highest if the dimensionless stopping time is close to one (Youdin & Goodman 2005).

The dust particles initially orbit with the Keplerian speed (see Eq. (11)). They are initialized either at the beginning of the simulations or after 50 kyr. The latter is to give the vertical shear instability time to attain a saturated state before the introduction of the dust. To advance the particles in time, we use the Leapfrog algorithm, which was adapted for cylindrical geometries by Boris (1970), as detailed in Appendix A[3].

The implementation of the mutual drag between the gas and the dust is based on the cloud-in-cell mapping between the grid and the particles that is included in the FLASH Code. The algorithm can be described as follows: firstly, the gas properties are mapped to the particles. Secondly, for each particle, the stopping time (see Eq. (16)) and the change in velocity due to the drag exerted by the gas is computed. The corresponding change in particle momentum is then mapped to the grid. Finally, the change of the gas velocity in every grid cell is calculated from the particle momentum change. A more detailed description of the implementation can be found in Appendix B[3].

3. Vertical shear instability

In this section, we verify that our model can reproduce the findings of previous studies of the vertical shear instability, in particular the turbulent strength in its saturated state, despite the comparably small vertical domain sizes we consider. For this purpose, we analyze our model of locally isothermal gas in which dust is not included.

In Fig. 1, the vertical gas motions in the model are depicted. The characteristic perturbations that the vertical shear instability gives rise to are reproduced. The perturbations are bent outwards, their radial wavelength is much less than their vertical wavelength, and they are symmetric with respect to the midplane in the saturated state of the instability (compare with, e.g., Figs. 2 and 3 of Nelson et al. 2013 and Fig. 2 of Stoll & Kley 2014).

We find that the strength of the turbulence induced by the vertical shear instability depends on the extent of the vertical domain. This can be seen from Fig. 2, in which we depict the vertical gas velocity in our models with a vertical domain size of two and of four gas scale heights. Throughout the simulations, the turbulence is considerably weaker in the vertically smaller domain than in the vertically larger one. The reason for this is likely that the vertical shear at the vertical domain boundaries is less in smaller domains, which entails a decline of the linear growth rate of the surface modes of the instability (Lin & Youdin 2015).

In the vertically larger domain, the vertical shear instability saturates at a Mach number of the vertical gas velocity of $\mathcal{M}_{\mathrm{g},z} \approx 0.1$. This value does not depend significantly on the resolution and is consistent with the Mach number which Flock et al. (2017) find. This is regardless of the fact that these authors simulate a domain with an aspect ratio of $z/r = 0.35$, while our domain extends to between $z/r = 0.17$ at $r = 10$ au and $z/r = 0.3$ at $r = 100$ au. Furthermore, Flock et al. (2017) employ a radiative transfer model rather than assuming the gas to be locally isothermal as we do. Therefore, in the following we investigate the vertical shear instability and its coexistence with the streaming instability using our model with a vertical domain size of two gas scale heights above and below the midplane.

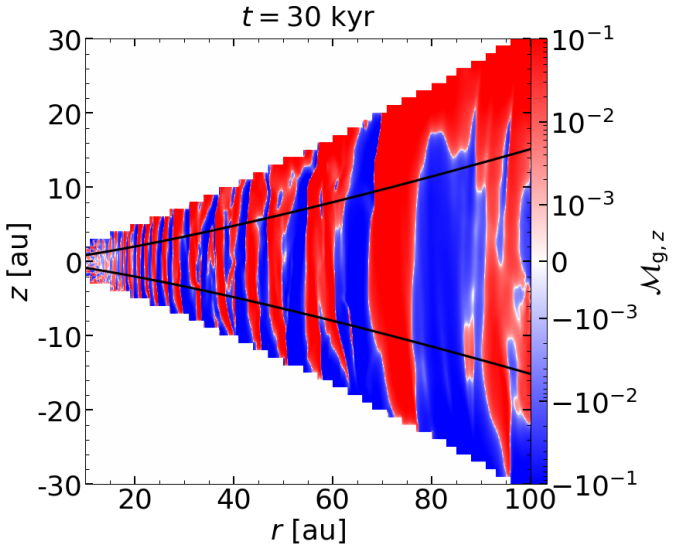

Fig. 1. Mach number of the vertical gas velocity $\mathcal{M}_{g,z}$ as a function of radius r and height z in a simulation including a locally isothermal gas, but no particles (*iso_Lr=90au_Lz=4Hg*). The simulation domain spans four gas scale heights in the vertical dimension. Black lines mark one gas scale height above and below the midplane. After 30 kyr, the vertical shear instability has saturated at all radii and heights; it gives rise to perturbations which are characterized by a radial-to-vertical wavelength ratio much smaller than unity, by being bent outwards, and by a mirror symmetry relative to the midplane.

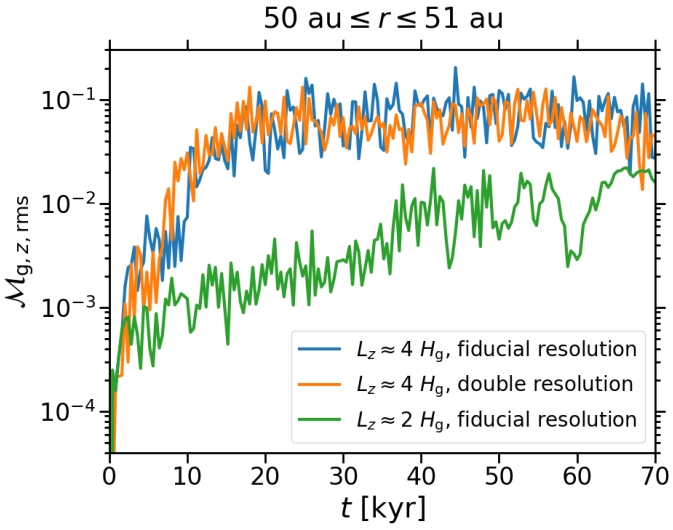

Fig. 2. Root mean square of $\mathcal{M}_{g,z}$ as a function of time t. The root mean square is computed using the mass-weighted average over the vertical domain size and over 1 au extending from $r = 50$ to 51 au. In the domain with a vertical dimension of four gas scale heights (blue and orange lines), the Mach number saturates at $\mathcal{M}_{g,z,rms} \approx 10^{-1}$. This value is consistent with the one which Flock et al. (2017) find in their numerical study of the vertical shear instability. The turbulent strength is similar in the simulation with the fiducial resolution (*iso_Lr=90au_Lz=4Hg*; blue line) and the one with the doubled resolution (*iso_Lr=90au_Lz=4Hg_dou_res*; orange line); however, it remains lower until the simulations end in the domain with a vertical size of two gas scale heights (simulation *iso_Lr=90au*; green line).

4. Coexistence of vertical shear instability and streaming instability

Using our model with dust and an isothermal gas equation of state, we investigate how the vertical shear instability and the streaming instability interact. We consider two scenarios: in the scenario that we refer to as *SIwhileVSI*, the streaming instability grows simultaneously with the vertical shear instability. In the scenario referred to here as *SIafterVSI*, on the other hand, the streaming instability is not active before the vertical shear instability has saturated. We model the latter scenario by introducing the dust into the simulations after 50 kyr. At this point, the vertical shear instability has reached a saturated state at all radii (see Fig. 1).

4.1. Source of turbulence

Figure 3 shows the Mach number of the vertical gas motions in *SIwhileVSI* (left panel) and *SIafterVSI* (right panel). In both scenarios, away from the midplane the vertical shear instability is the primary source of turbulence and induces the characteristic large-scale perturbations (compare with Fig. 1). However, in the midplane, small-scale perturbations can be seen at all radii in the former scenario. Similar perturbations exist in the latter scenario, although only at certain radii and not as limited in vertical extent. These small-scale perturbations are not present in our model of the vertical shear instability only. They resemble the perturbations that Li et al. (2018) observe in the midplane of their local shearing box simulations of the streaming instability (see their Fig. 2).

In Fig. 4, we compare the time-dependence of the Mach number in the two scenarios. The mass-weighted vertical average of the Mach number is depicted, that is, the turbulent strength in the midplane is weighted more heavily than the strength away from it. In *SIafterVSI*, we find that the initialization of the dust does not cause the Mach number to deviate significantly from the value of $\mathcal{M}_{g,z} \approx 0.1$ induced by the vertical shear instability after it has saturated (compare with Fig. 2).

In contrast, in the *SIwhileVSI* scenario the Mach number saturates at a lower value of $\mathcal{M}_{g,z} \approx 0.01$. In the local shearing box simulations without vertical stellar gravity presented by Johansen & Youdin (2007), the streaming instability drives turbulence with a similar strength. After saturation, the Mach number does not vary significantly until, owing to its radial drift, locally no dust is left. Subsequently, it increases to approximately the value the vertical shear instability in its saturated state gives rise to in *SIafterVSI*.

Figure 5 shows the ratio of the radial to the vertical Mach number in both scenarios. The turbulent velocity in the radial direction is significantly less than the one in the vertical direction in *SIafterVSI*. This is consistent with Stoll & Kley (2016) and Stoll et al. (2017) showing that the vertical shear instability drives anisotropic turbulence. On the other hand, in *SIwhileVSI* the radial and the vertical Mach number are comparable near and in the midplane. Johansen & Youdin (2007) find the streaming instability to cause isotropic turbulence.

From the fact that the turbulence is comparably weak and isotropic as well as from the presence of small-scale perturbations that are not observable in our model of the vertical shear instability only, we conclude that the streaming instability is the primary source of turbulence in the dust midplane layer if it starts to operate at the same time as the vertical shear instability. One possible explanation for this is that the streaming instability grows faster in turbulent strength than the vertical shear instability. This is evident when comparing the time taken for the vertical shear instability (see Fig. 2) and the streaming instability (see the right panel of Fig. 4) to saturate.

However, the turbulence is mainly driven by the vertical shear instability if it has attained a saturated state before the

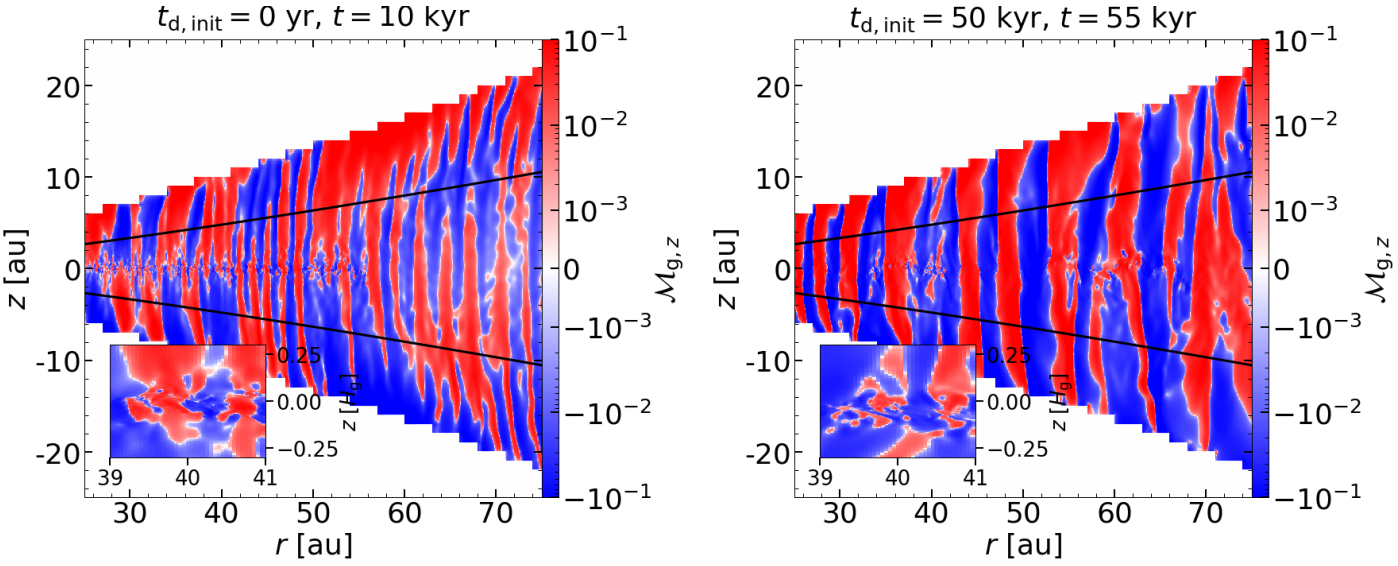

Fig. 3. Mach number $\mathcal{M}_{\mathrm{g},z}$ as a function of r and z in two simulations with dust and an isothermal gas equation of state. As in the dust-free equivalent (compare with Fig. 1), the vertical shear instability induces large-scale perturbations away from the midplane. In the simulation *iso_Z=0.02_Lr=90au_Lz=4Hg* (*left panel*), in which we initialize the dust at the beginning, small-scale perturbations can be seen at all radii in the midplane. These perturbations are also observable in the simulation *iso_Z=0.02_Lr=90au_Lz=4Hg_tdinit=50kyr* (*right panel*), in which the dust is introduced after 50 kyr, although not at all radii and extending to greater heights. The inlays with a vertical extent of 0.6 gas scale heights show the enlarged perturbations. However, such small-scale perturbations do not exist in the corresponding simulation without dust.

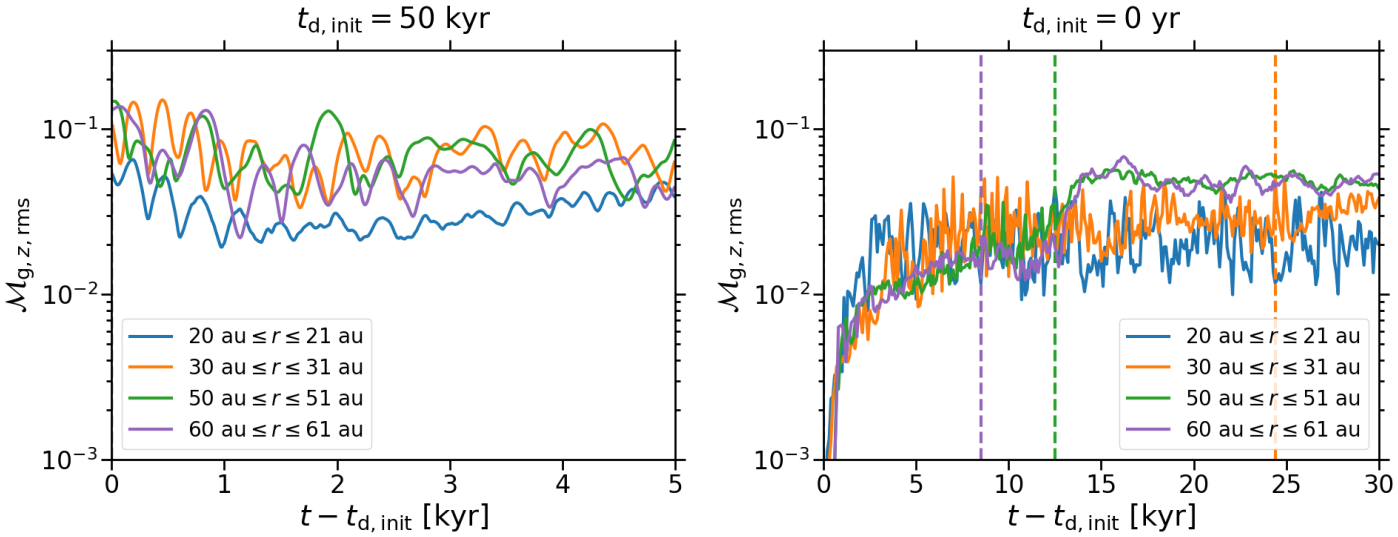

Fig. 4. Root mean square of $\mathcal{M}_{\mathrm{g},z}$, averaged over the vertical domain extent and the radii given in the legend, as a function of t after the initialization of the dust at $t_{\mathrm{d,init}}$. The mean is weighted by mass, i.e., more weight is assigned to the Mach number in the midplane than to the one away from it. In the simulation *iso_Z=0.02_Lr=90au_Lz=4Hg_tdinit=50kyr* (*left panel*), the vertical shear instability has saturated before the dust is introduced. The Mach number remains approximately constant at a value $\mathcal{M}_{\mathrm{g},z,\mathrm{rms}} \approx 10^{-1}$ after the dust initialization (compare with Fig. 2). That is, in this simulation the vertical shear instability is the primary source of turbulence in the midplane. In contrast, in the simulation *iso_Z=0.02_Lr=90au_Lz=4Hg* (*right panel*), in which the vertical shear instability and the streaming instability begin to grow at the same time, the Mach number saturates at a lower value of $\mathcal{M}_{\mathrm{g},z,\mathrm{rms}} \approx 10^{-2}$. After no dust remains at a radius because of its radial drift (this point is marked with a dashed line), the Mach number increases until it is approximately equal to the value at the same radius in the simulation *iso_Z=0.02_Lr=90au_Lz=4Hg_tdinit=50kyr*. We find that, as long as dust is present, the streaming instability drives the turbulence in the midplane in the simulation *iso_Z=0.02_Lr=90au_Lz=4Hg*.

streaming instability can begin to grow. In this state, we find it to give rise to turbulence with a higher Mach number than the streaming instability in *SIwhileVSI*. Nevertheless, we note that the small-scale perturbations, which we find to be induced by the streaming instability at all radii in *SIwhileVSI*, are also observable locally in the *SIafterVSI* scenario (see the right panel of Fig. 3).

The vertical shear instability would likely be the main source of turbulence in *SIwhileVSI* as well if the dust grains were too small to settle and trigger the streaming instability before the vertical shear instability had saturated. Equating a saturation timescale of 30 orbital periods (Stoll & Kley 2014) with the settling timescale as given by Eq. (10) of Chiang & Youdin (2010) yields a critical dimensionless dust stopping time of ∼0.005.

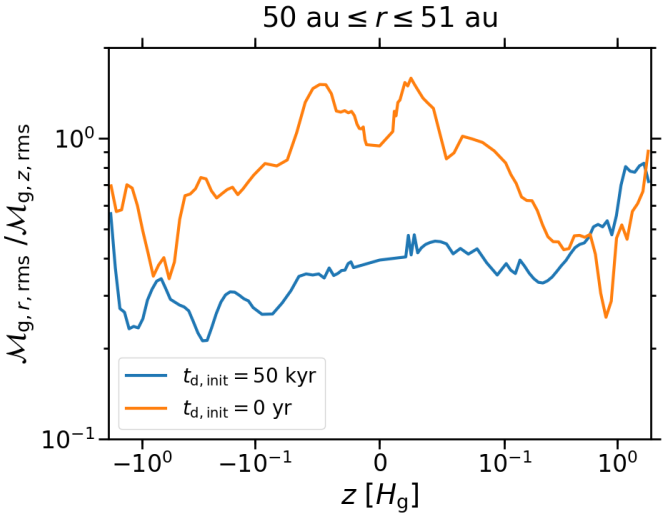

Fig. 5. Ratio of the root mean square Mach number of the radial gas velocity $\mathcal{M}_{g,r}$ to the root mean square of $\mathcal{M}_{g,z}$ as a function of z in units of gas scale heights. The abscissa is scaled linearly between −0.1 and 0.1 gas scale heights and logarithmically otherwise. To compute the root mean square, we take the mass-weighted average over $r = 50$ to 51 au and the average over 1 kyr through $t = 55$ kyr in the case of the simulation *iso_Z=0.02_Lr=90au_Lz=4Hg_tdinit=50kyr* (blue line) and through $t = 10$ kyr in the case of the simulation *iso_Z=0.02_Lr=90au_Lz=4Hg* (orange line). Away from the midplane, the radial-to-vertical Mach number ratio is less than unity in both simulations. While this anisotropy extends over all heights if the dust is introduced after 50 kyr, the Mach number ratio is close to one in the midplane if the dust is initialized at the start. This is indicative of the vertical shear instability being the primary source of turbulence in the midplane in the former case, but the streaming instability in the latter case.

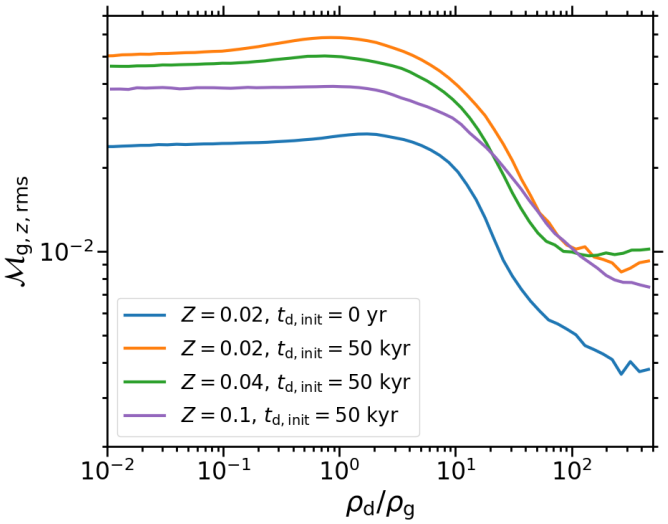

Fig. 6. Root mean square of $\mathcal{M}_{g,z}$ as a function of the dust-to-gas density ratio ρ_d/ρ_g. The orange, green, and purple lines represent the turbulent strength in simulations in which we initialize the dust after the vertical shear instability has saturated. The strength at low to intermediate values of the volume density ratio in the three simulations is marginally smaller if the dust-to-gas surface density ratio is greater. Nevertheless, the Mach number is higher in all of these simulations than in the simulation in which we introduce the dust at the start (blue line). We find that the stronger turbulence in the former simulations is driven by the vertical shear instability, while the weaker turbulence in the latter one is caused by the streaming instability. Independent of the source of the turbulence, its strength decreases at dust densities larger than the gas density in all four simulations.

However, since simulating such small dust grains as particles is computationally very expensive, we do not explore this scenario.

4.2. Dependence of turbulent strength on dust density

As explained in Sect. 1, settling dust introduces an effective vertical gas buoyancy that can suppress the vertical shear instability. This is a second possible reason – besides the more rapid growth in turbulent strength of the streaming instability – why the streaming instability is the source of turbulence in the dust layer in the scenario *SIwhileVSI*.

Lin (2019) performs simulations of the vertical shear instability which include dust from the beginning, as in the *SIwhileVSI* scenario. This latter author shows that the dust-induced buoyancy leads to a decrease in the Mach number in the midplane from $\mathcal{M}_{g,z} \approx 10^{-1}$ to $\mathcal{M}_{g,z} \approx 10^{-2}$ if the dust-to-gas surface density or the stopping time of the dust exceed a threshold value. These threshold values are correlated: for a surface density ratio of 1%, the critical dimensionless stopping time of the dust is equal to 0.005 (see their Fig. 5). For a stopping time of 0.001, the critical surface density ratio amounts to 3% (see their Fig. 9). This is consistent with the Mach number of $\mathcal{M}_{g,z} \approx 10^{-2}$ we find in *SIwhileVSI*, in which the surface density ratio is equal to 2%[4] and the stopping time of the dust ranges from 0.046 to 0.46.

[4] The loss of gas mass through the domain boundaries of our simulations leads to an increase of the dust-to-gas surface density ratio with time. This effect is negligible if we simulate the dust over a time-span of 5 kyr or less (see Table 1). It is significant, however, in the simulation *iso_Z=0.02_Lr=90au_Lz=4Hg*, which ends after 30 kyr. At this point, the surface density ratio has increased to 2.6%.

However, while Lin (2019) associates the turbulence in the midplane of their simulations with the vertical shear instability, we find it to be driven by the streaming instability if both instabilities begin to operate at the same time. Lin (2019) notes that they apply a diffusive numerical scheme which probably suppresses the growth of the streaming instability. In addition, they model tightly coupled dust and gas employing a one-fluid approach.

To investigate whether the vertical shear instability is quenched by the dust-induced buoyancy in the *SIafterVSI* scenario, we analyze how the turbulent strength depends on the dust density. We note that this analysis does not involve information about the spatial distribution of the dust. In other words, the strength at a certain dust density is the sum of the bulk motions of regions with this density and the internal turbulence in these regions.

In Fig. 6, the Mach number is shown as a function of the dust-to-gas density ratio in both scenarios. Overall, the Mach number is higher in *SIafterVSI* (orange, green, and purple lines) than in *SIwhileVSI* (blue line). This is consistent with stronger turbulence in the dust layer being induced by the vertical shear instability in the former scenario, and weaker turbulence by the streaming instability in the latter scenario.

In the *SIafterVSI* scenario, at low to intermediate dust-to-gas volume density ratios the Mach number decreases with increasing dust-to-gas surface density ratio, although only slightly. This can be explained by the vertical shear instability being suppressed if the surface density ratio, that is, the total dust mass, is greater, which leads to the vertical bulk motions of regions with these volume density ratios being weaker.

Furthermore, the vertical shear instability is gradually quenched if the dust density increases to values greater than the gas density. The Mach number is as low as $\mathcal{M}_{g,z} \approx 0.01$ for

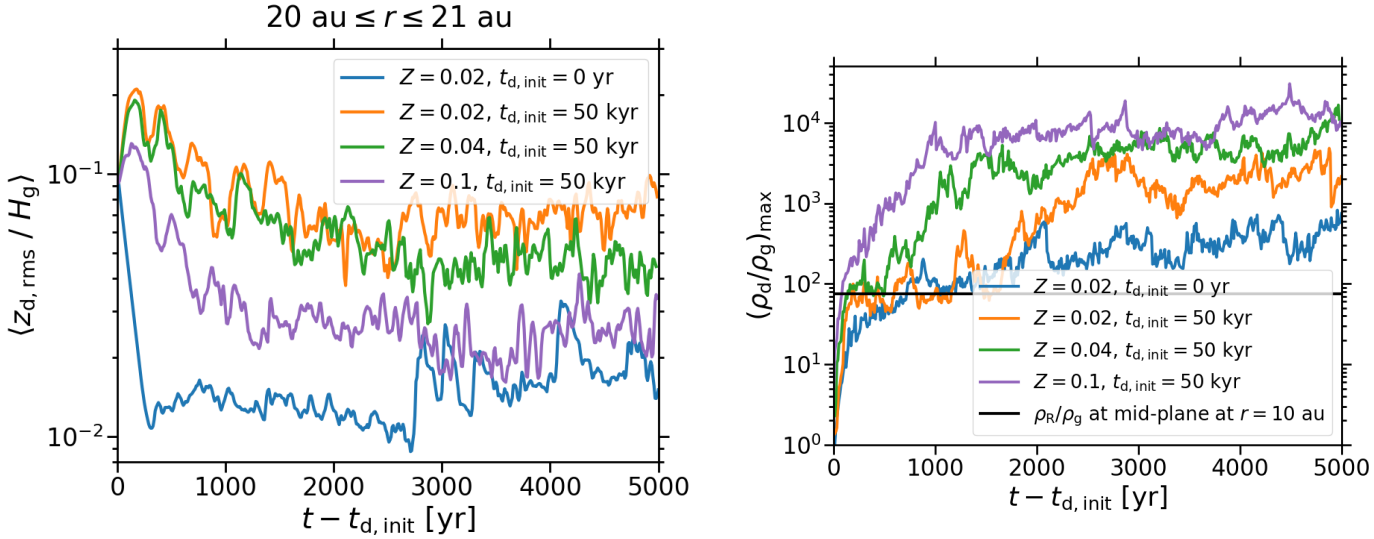

Fig. 7. Ratio of the dust scale height to the gas scale height H_g (*left panel*) and maximum of the dust-to-gas density ratio ρ_d/ρ_g (*right panel*) as functions of t after the dust is introduced at $t_{d,init}$. We compute the dust scale height as the root mean square of the vertical particle positions z_d, and average the scale height ratio over 1 au spanning from $r = 20$ to 21 au. For a dust-to-gas surface density ratio of $Z = 2\%$, the dust scale height amounts to ∼1% of the gas scale height if the streaming instability induces the vertical diffusion of the dust (blue line). On the other hand, it is equal to ∼10% for the same surface density ratio if the diffusion is caused by the vertical shear instability (orange line). The scale height which is induced by the vertical shear instability decreases with increasing surface density ratio (green and purple line). However, it is higher than the value that the streaming instability gives rise to for all surface density ratios that we consider. In contrast, the maximum dust volume density is significantly smaller if the streaming instability drives the turbulence in the dust layer than if the turbulence is caused by the vertical shear instability. In the former case, the dust-to-gas volume density ratio amounts to a few hundred for a surface density ratio of 2%. In the latter case, on the other hand, it exceeds 10^3 for the same surface density ratio, and 10^4 for a surface density ratio of 10%. In all cases, the maximum dust density is greater than the Roche density ρ_R in the midplane at the inner radial boundary of the simulation domains, i.e., the maximum Roche density in the simulations. The ratio of this Roche density to the gas density is marked as a black line.

the highest density ratios. This turbulent strength is similar to that caused by the streaming instability throughout the dust layer in the *SIwhileVSI* scenario. However, we note that even in the regions with the highest density ratios in *SIafterVSI*, the Mach number is greater than in the regions with the same density ratios in *SIwhileVSI*. This is because the vertical shear instability gives rise to stronger bulk motions of these regions in the former scenario than the streaming instability in the latter scenario.

The turbulent strength that the streaming instability induces in the scenario *SIwhileVSI* is also lower if the density ratio exceeds a few. This is in agreement with Johansen et al. (2009) who find that the collision speeds of dust grains in the filaments forming in their simulations of the streaming instability are smaller if the dust density is higher.

4.3. Vertical and radial dust concentration

The dust-to-gas scale height ratio in *SIwhileVSI* (blue line) and *SIafterVSI* (orange, green, and purple lines) is shown in the left panel of Fig. 7. In the former scenario, the streaming instability is the source of turbulence in the dust layer. The dust sedimentation and the vertical diffusion of the dust which it causes reach a balance at a dust-to-gas scale height ratio of ∼1% (see also Sect. 5).

Since the vertical shear instability drives stronger turbulence than the streaming instability, we find the equilibrium dust scale height to be greater in the *SIafterVSI* scenario. On the other hand, it decreases with increasing dust-to-gas surface density ratio in this latter scenario: for a ratio of 2%, the dust scale height amounts to ∼10% of the gas scale height. In comparison, if the ratio is equal to 10% the scale height is close to the value in *SIwhileVSI*. We show in Sect. 5 that the scale height which is induced by the streaming instability is largely independent of the surface density ratio.

The dust settling to smaller scale heights for higher surface density ratios is most probably a consequence of the vertical shear instability being more suppressed by the dust-induced buoyancy. Lin (2019) finds the instability to diffuse dust with a dimensionless stopping time of 0.001 to a scale height that is similar to the gas scale height if the surface density ratio amounts to 1%, but that the dust scale height is an order of magnitude smaller if the ratio is equal to 5% (see their Fig. 9). These scale heights are significantly greater than the ones in the *SIafterVSI* scenario. This is likely because we simulate dust with stopping times of between 0.046 and 0.46, which is more weakly coupled to the gas and is therefore less elevated by the vertical gas motions.

To investigate whether or not in the *SIafterVSI* scenario the vertical shear instability can be quenched if the dust is initialized with a smaller scale height and thus a higher midplane density, we conducted a simulation with an initial surface density ratio of 2% and an initial dust scale height of 1% of the gas scale height rather than the fiducial value of 10%. Despite this scale height being comparable to the one which is induced by the streaming instability in the *SIwhileVSI* scenario and the initial midplane dust-to-gas density ratio being of order unity, we find that the vertical shear instability is not noticeably affected. The dust is elevated to a dust-to-scale height ratio of ∼10% in less than an orbital period in this simulation.

In the right panel of Fig. 7, we depict the maximum dust-to-gas density ratio in the two scenarios. We note that this maximum is stochastic and dependent on the resolution (Johansen & Youdin 2007; Bai & Stone 2010c). Nonetheless, we find the

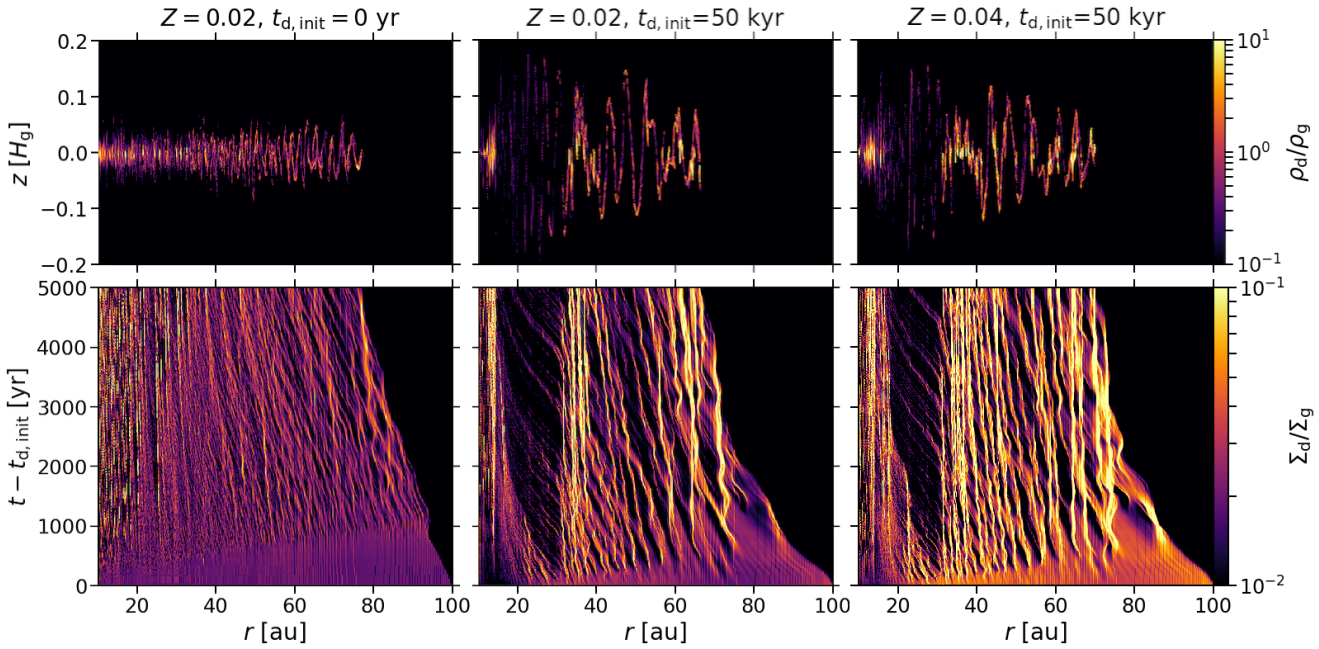

Fig. 8. Dust-to-gas volume density ratio ρ_d/ρ_g as a function of r and z (*upper panels*) as well as dust-to-gas surface density ratio Σ_d/Σ_g as functions of r and t (*lower panels*). *The upper panels show the* spatial dust distribution 5 kyr after the dust initialization. We compare a simulation in which the turbulence in the dust layer is driven by the streaming instability (*left panels*) and two simulations in which the vertical shear instability is the main source of turbulence (*middle and right panels*). For the same dust-to-gas surface density ratio of $Z = 0.02$, the dust scale height is smaller, but the radial dust concentration is weaker in the former case. (The values of Z are specified in the titles.) In the latter case, more dust is accumulated in overdensities if the surface density ratio is higher. Some of the accumulations are sufficiently dense for their radial drift to cease almost entirely.

maximum dust density to exceed the maximum Roche density,

$$\rho_{\mathrm{R,max}} = \frac{9\Omega_{\mathrm{K}}(r = 10\ \mathrm{au},\ z = 0)}{4\pi G}, \tag{17}$$

in both scenarios. In other words, if the dust self-gravity were included in our model, local dust overdensities could undergo gravitational collapse and form planetesimals. This is in line with expectations for the *SIwhileVSI* scenario since the surface density ratio of 2% in this scenario exceeds the critical value for the dust concentration by the streaming instability to be strong enough to lead to planetesimal formation (Carrera et al. 2015; Yang et al. 2017).

If the radial concentration of the dust were comparable in both scenarios, the maximum dust density would by tendency be greater in *SIwhileVSI* because the dust scale height is smaller in this scenario. On the contrary, we find the maximum dust density to be considerably higher in *SIafterVSI*. The maximum of the density ratio amounts to a few hundred in *SIwhileVSI*, but to a few thousand for the same surface density ratio in *SIafterVSI*, and to more than 10^4 for higher surface density ratios. We investigate the radial dust concentration in the following.

In the upper panels of Fig. 8, we show the spatial dust distribution 5 kyr after the dust is introduced in *SIwhileVSI* (left panel) and in *SIafterVSI* (middle and right panels). In agreement with what can be seen from Fig. 7, the oscillating dust midplane layer extends to greater heights in the latter scenario than in the former. In addition, the dust is more uniformly distributed in the radial dimension in the former scenario. Interestingly, the region between $r = 15$ and 30 au is depleted of dust in both simulations of the *SIafterVSI* scenario that are presented in Fig. 8. The reason for this depletion is unclear.

The time- and radius-dependence of the dust-to-gas surface density ratio in *SIwhileVSI* is depicted in the lower-left panel of Fig. 8. The streaming instability causes the dust to radially accumulate in overdensities. Comparable, azimuthally elongated filaments are found in three-dimensional simulations of the instability (Johansen et al. 2007; Bai & Stone 2010b; Kowalik et al. 2013). As noted above, the dust concentration in this scenario is sufficiently strong for the streaming instability to induce planetesimal formation.

From the lower-middle and lower-right panels, it can be seen that similar, but significantly denser dust concentrations form in *SIafterVSI*. If the surface density ratio is higher, that is to say the total dust mass is greater, more dust is contained in overdensities. The radial drift of overdensities is reduced in both scenarios. However, it is only in the *SIafterVSI* scenario that some of the accumulations are dense enough for their radial drift to be nearly completely halted.

Stoll & Kley (2016) perform simulations of the vertical shear instability in which dust and the drag exerted on it by the gas are included. These latter authors find that pressure fluctuations which are induced by the vertical shear instability lead to a radial concentration of the dust. This concentration is strongest if the dimensionless stopping time of the dust is close to unity. Nevertheless, because they do not take the drag back-reaction of the dust on the gas into account, the radial drift speed does not depend on the dust density in their simulations.

In the vicinity of the dust overdensities in the *SIafterVSI* scenario, we find the streaming instability to contribute to the driving of turbulence. At the end of the simulation of the *SIafterVSI* scenario with a surface density ratio of 2% – 55 kyr after the beginning of the simulation and 5 kyr after the initialization of the dust – several overdensities can be found between $r = 30$ au and 40 au, and around 60 au (see the lower-middle panel of Fig. 8). From the right panel of Fig. 3, it is evident that at this time and these radii small-scale perturbations are present. We associate these perturbations with the streaming instability because they are not observable in our model of the vertical shear

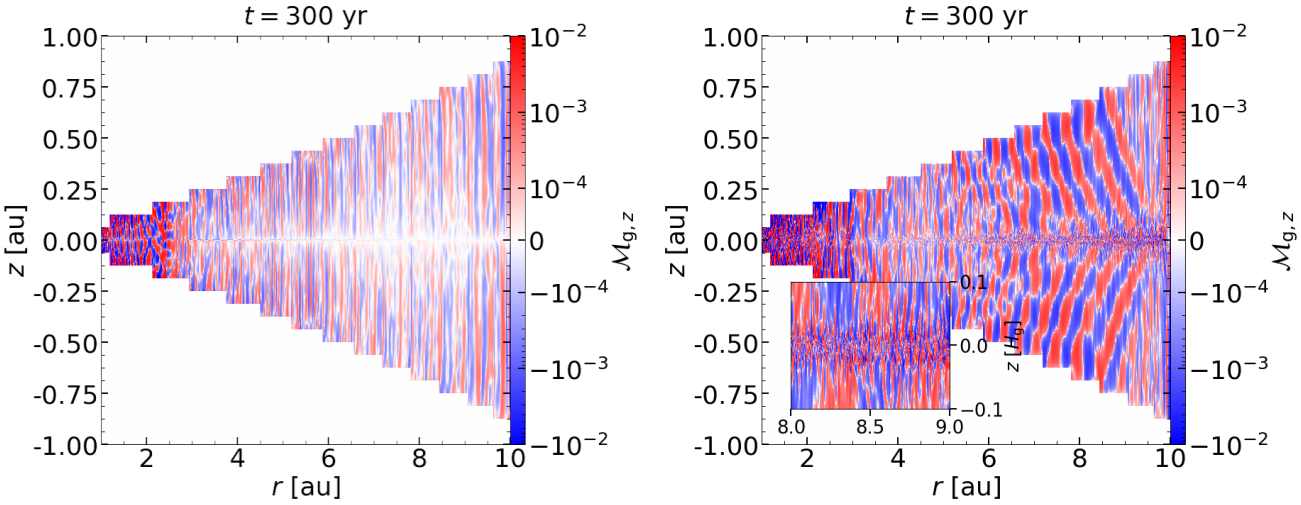

Fig. 9. Mach number of the vertical gas velocity as a function of r and z in simulations of dust and a locally adiabatic gas. The Mach number at radii of less than ∼3 au is similarly high in the simulation without (*adi_Lr=9au*; *left panel*) or with dust (*adi_Z=0.02_Lr=9au*; *right panel*). This is in spite of the streaming instability operating in the latter simulation, but not in the former one. At larger radii in the simulation that includes dust, the streaming instability induces large-scale perturbations with $\mathcal{M}_{g,z} \approx 10^{-3}$ away from the midplane. These perturbations are similar in shape to the ones caused by the vertical shear instability, but they are weaker, are bent inwards rather than outwards, and are not symmetric with respect to the midplane (compare with Fig. 1). In the inlay, which extends to 0.1 gas scale heights H_g above and below the midplane, small-scale perturbations with $\mathcal{M}_{g,z} \approx 10^{-2}$ in the midplane can be seen.

instability only. Therefore, it is most probably a combination of the vertical shear instability and the streaming instability that induces the dust accumulation in this scenario. We speculate that the vertical shear instability first concentrates the dust in weak overdensities, as shown by Stoll & Kley (2016). Subsequently, the streaming instability causes the growth of these seeds to the dense accumulations that we find in our simulations.

The fact that the dust is radially more concentrated in *SIafterVSI* despite its vertical diffusion being stronger in this scenario is consistent with the results of the numerical study by Yang et al. (2018). These latter authors show that the radial dust concentration owing to the streaming instability is not significantly affected by the vertical dust diffusion that is induced by nonideal MHD turbulence.

5. Global simulations of the streaming instability

To study the vertical and radial gas motions induced by the streaming instability, as well as the dust scale height, we employ our model including dust and locally adiabatic gas. Because the gas is locally adiabatic, the vertical shear instability is quenched by vertical buoyancy.

The Mach number of the vertical motions in this model as well as its dust-free equivalent are shown in Fig. 9. Since in the latter model (left panel) the streaming instability is not active, the turbulence in this model is most probably a numerical artifact caused by vertical shear that results from imperfect boundary conditions. At radii greater than ∼3 au, this artificial turbulence is negligibly weak compared to the turbulence driven by the streaming instability in the model with dust (right panel). However, at smaller radii, we cannot distinguish between artificial turbulence and turbulence caused by the streaming instability. We therefore exclude these radii from the following analysis.

In the model including dust, the streaming instability induces small-scale perturbations with a turbulent strength of $\mathcal{M}_{g,z} \approx 0.01$ in the dust midplane layer (see the inlay in the right panel) and somewhat weaker large-scale perturbations away from it. The small-scale perturbations are similar to the ones caused by streaming instability in the model in which both this latter instability and the vertical shear instability operate (see Fig. 3). We find both kinds of perturbations to be largely isotropic (see also Fig. 5).

The large-scale perturbations resemble the perturbations caused by the vertical shear instability in that their radial-to-vertical wavelength ratio is much less than one (see Fig. 1). In contrast to these, their symmetry is odd with respect to the midplane and they are bent inwards. This bending of the perturbations can be explained by gas moving both vertically away from the midplane and radially outwards, the latter being caused by the inward radial drift of the dust and the conservation of angular momentum.

In the local shearing box simulations presented by Li et al. (2018), the streaming instability gives rise to the same two kinds of perturbations with a similar turbulent strength (compare with their Fig. 2). However, the large-scale perturbations observed by these latter authors are bent outwards rather than inwards. Nevertheless, these perturbations are likely suppressed by the stronger ones caused by the vertical shear instability under more realistic conditions, that is, in simulations including heating and cooling by radiation rather than an adiabatic equation of state (Stoll & Kley 2014; Flock et al. 2017).

5.1. Vertical gas velocity and dust scale height

In Fig. 10, we show the dust-to-gas scale height ratio as well as the Mach number of the vertical gas velocity in the midplane after dust settling and vertical diffusion have reached an equilibrium. We find both the dust scale height and the turbulent strength to be similar in the model with a dust-to-gas surface density ratio of 2% and the model with a ratio of 1%. The equilibrium scale height and the Mach number do not depend significantly on the initial dust scale height either, regardless of the increase in time taken for the dust to sediment to the midplane if the scale height is greater. Furthermore, our results are converged with respect to resolution.

Bai & Stone (2010b) study local shearing box simulations of the streaming instability with surface density ratios of 1, 2, or 3%. These latter authors derive the strength of the vertical

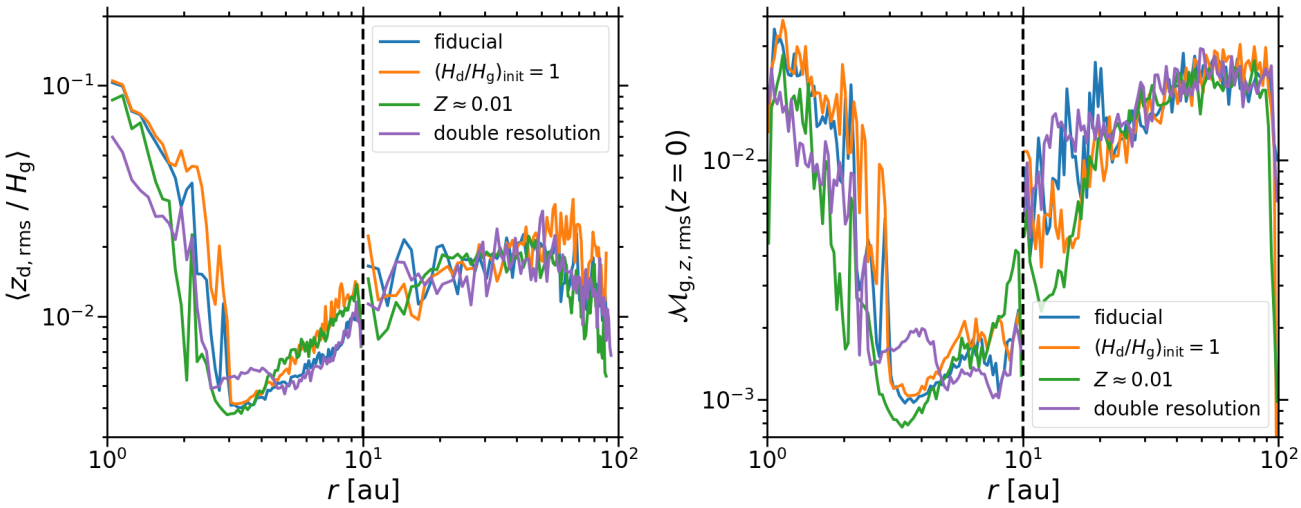

Fig. 10. Ratio of the dust scale height, as the root mean square of z_d, to the gas scale height H_g (*left panel*) as well as mass-weighted root mean square of $\mathcal{M}_{g,z}$ in the midplane (*right panel*). Both quantities are depicted as functions of r. To compute the root mean square, we average over 50 or 500 yr after the dust scale height has reached an equilibrium value in the simulation domains spanning 1 au $\leq r \leq$ 10 au or 10 au $\leq r \leq$ 100 au, respectively. The dashed line marks the boundary between these domains. The model with an initial dust-to-gas scale height ratio of $(H_d/H_g)_{init} = 0.1$, a dust-to-gas surface density ratio of $Z = 2\%$, and the fiducial resolution (blue line) is shown together with the models that deviate from this fiducial one in that $(H_d/H_g)_{init} = 1$, that $Z = 1\%$ (green line), or that the initial and maximum resolution are doubled (purple line). While both the dust scale height and the Mach number depend on the radius, they are largely independent of the initial dust scale height, the surface density ratio, and the resolution.

diffusion as well as the scale height of the dust from fitting a Gaussian distribution to the vertical dust density profile. In contrast to us, they find the vertical diffusion to be stronger and the scale height to increase with the dust-to-gas surface density ratio if the ratio is less than a threshold value. Above this threshold value, which depends on the particle size, the turbulent strength decreases again, and the dust settles to smaller scale heights.

The dust scale height is equal to ∼1% of the gas scale height at all radii in our model. The streaming instability gives rise to a similar dust scale height in our model in which both this latter instability and the vertical shear instability are active and begin to grow at the same time (see the left panel of Fig. 7). Comparable dust scale heights are further found in local shearing box simulations, for example, the ones that were conducted by Yang & Johansen (2014) and Carrera et al. (2015). For these scale heights and the dust-to-gas surface density ratios of the order of 1% which we simulate, the ratio of the dust to the gas density in the midplane is of order unity, and the linear growth rate of the instability is largest (Youdin & Goodman 2005).

The thickness of the dust layer is set in a self-regulatory manner if the turbulent diffusion of the dust is caused by the streaming instability (Bai & Stone 2010b): if the dust scale height is greater than the equilibrium value, the instability induces weaker turbulence, which does not balance the dust settling towards the midplane. On the other hand, if the scale height is less than the equilibrium value, the instability drives overly strong turbulence, which lifts the dust away from the midplane.

At radii $r \gtrsim 10$ au, the Mach number is consistent with the observed values of the order of 10^{-2} (Flaherty et al. 2015, 2017, 2018; Pinte et al. 2016; Ohashi & Kataoka 2019). The turbulent strength is comparable in our model in which both the vertical shear instability and the streaming instability operate, but the latter drives the turbulence in the dust layer. Pinte et al. (2016) and Ohashi & Kataoka (2019) derive the turbulent strength from the dust scale height, which is regulated by the streaming instability if it is the main source of turbulence in the dust layer of protoplanetary disks. We note that these latter authors observe a dust-to-gas scale height ratio of 10% and one-third, respectively, which is an order of magnitude larger than the ratio we find. This can be explained by the fact that these latter authors consider micron- and millimeter-sized dust grains, which are elevated to greater heights than the centimeter-sized ones in the simulations that we present in Fig. 10.

5.2. Dependence of turbulent strength on dust stopping time and radial gas pressure gradient

We find that the strength of the turbulence that is driven by the streaming instability, like the linear growth rate of the instability (Youdin & Goodman 2005), increases with the speed of the radial dust drift. The drift is faster if the dimensionless stopping time of the dust is closer to one and the radial gas pressure gradient is stronger. Both quantities increase with the radius in our model of dust with a fixed size (see Eqs. (13) and (16)). From Fig. 10, it is evident that both the Mach number and the dust scale height are also consequently greater at larger radii.

To analyze the extent to which the turbulent strength depends on the stopping time and the magnitude of the pressure gradient individually, we compare three simulations with different dimensionless stopping times: in one, it is fixed at 0.1, while in the other two it ranges from 0.0046 to 0.046 and from 0.046 to 0.46, respectively. The Mach number in each of these simulations is depicted in Fig. 11 as a function of the radius and the pressure gradient strength. We find an equivalent radius-dependence of the dust scale height in the three simulations.

The turbulent strength increases with both the dimensionless pressure gradient parameter and the dimensionless stopping time until it saturates for respective values of $\Pi \approx 0.1$ and of $\tau_{stop} \approx 0.05$. This is consistent with Bai & Stone (2010a,b) finding the scale height of the dust and its vertical diffusion to increase with the strength of the pressure gradient and the stopping time. The dependence on the pressure gradient strength is evident when considering only the simulation with a fixed stopping time (blue line in the figure).

At all radii in the simulation with a dimensionless stopping time of 0.1 and the simulation with stopping times greater

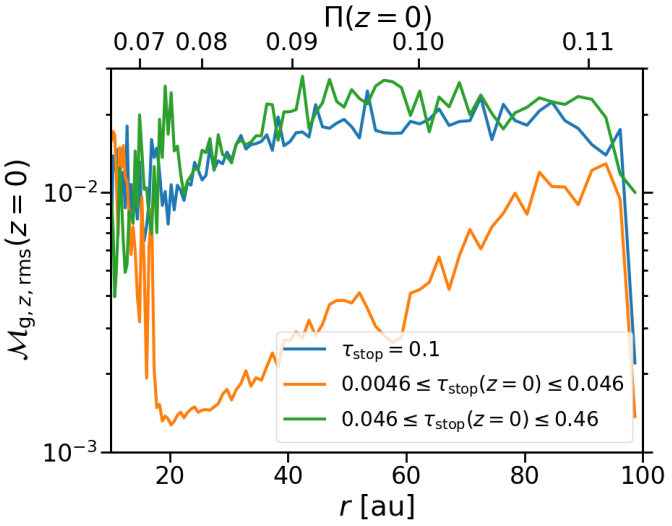

Fig. 11. Root mean square of $\mathcal{M}_{g,z}$ in the midplane as a function of r (lower abscissa) and the dimensionless gas pressure gradient parameter Π in the midplane (upper abscissa). The root mean square is calculated using the mass-weighted mean over 500 yr after an equilibrium value of the dust scale height is reached. In the simulation *adi_Z=0.02_Lr=90au_taustop=0.1* (blue line), in which the dimensionless dust stopping time τ_{stop} is fixed at 0.1, the Mach number increases with the pressure gradient parameter if $\Pi \lesssim 0.09$, but is approximately constant if the pressure gradient is stronger. The Mach number in this one and the simulation *adi_Z=0.02_Lr=90au* (green line), in which the stopping time increases from 0.046 to 0.46, is comparable at all radii. That is, the turbulent strength does not depend significantly on the stopping time in this stopping time regime. The Mach number is lower overall, but depends more strongly on the radius in the simulation *adi_Z=0.02_Lr=90au_a=3mm* (orange line) in which the stopping time ranges from 0.0046 to 0.046. In this regime, the turbulent strength increases with both the strength of the pressure gradient and the stopping time.

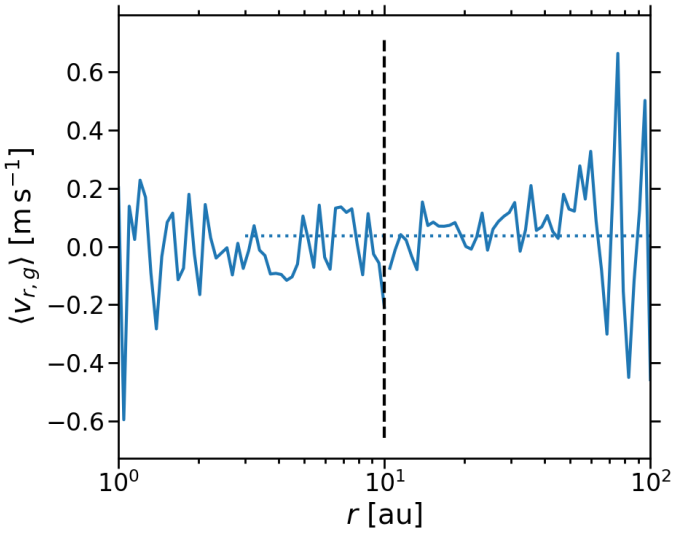

Fig. 12. Radial gas velocity (solid line) as a function of r in the simulations *adi_Z=0.02_Lr=9au* and *adi_Z=0.02_Lr=90au*. (The dashed lines marks the boundary between the domains of the two simulations.) The velocity is computed as the mass-weighted average over the vertical domain extent and a time-span of 50 and 500 yr, respectively, after an equilibrium dust scale height has been attained in each simulation. The average radial velocity at $r \geq 3$ au is plotted as a dotted line and amounts to 0.035 m s^{-1}. This outward motion is caused by the dust drifting radially inwards and its angular momentum being transferred to the gas. However, it is evident that the mean of the velocity is less than its standard deviation, which is equal to 0.16 m s^{-1}. This is a result of the turbulent motions caused by the streaming instability.

than 0.046 (green line), the turbulent strength is about the same, and therefore it is largely independent of the stopping time if $\tau_{stop} \gtrsim 0.05$. In contrast, in the simulation with stopping times of less than 0.046 (orange line) the turbulence is overall weaker, but its strength increases more strongly with the radius than in the other two simulations. That is, if $\tau_{stop} \lesssim 0.05$ the strength depends not only on the pressure gradient magnitude, but also on the stopping time.

5.3. Radial gas velocity

In Fig. 12, we show the radial velocity of the gas. The gas moves outward on average as a consequence of the inward radial drift of the dust and, as the total angular momentum is conserved, the transfer of angular momentum from the dust to the gas. Yet, the turbulent motions that are induced by the streaming instability lead to the variance in the gas velocity being greater than the speed of this mean outward motion. That is, the streaming instability does not cause a sustained inward transport of gas mass (and outward transport of angular momentum) that contributes to the observed stellar accretion (Alcalá et al. 2017).

6. Discussion

6.1. Implications for turbulence and planetesimal formation in protoplanetary disks

We have studied the interaction of two instabilities, the vertical shear instability and the streaming instability. Both instabilities appear to be robust: operation of the vertical shear instability requires a vertical rotation profile and a sufficiently short gas cooling timescale. Lin & Youdin (2015) show that in the MMSN model, the instability can grow between $r \approx 5$ and 50 au. On the other hand, only dust and a radial gas pressure gradient are necessary for the streaming instability to be active.

We considered two scenarios: in the first scenario, the vertical shear instability and the streaming instability start to grow at the same time. In this scenario, the turbulence in the dust layer is driven by the streaming instability. If the vertical shear instability has already saturated beforehand, as is the case in the second scenario, it remains the main source of turbulence even while the streaming instability is active.

It is unclear which of these scenarios is more realistic: Monte-Carlo simulations of dust coagulation show that (sub-)micron-sized grains grow to millimeter- or centimeter-sized aggregates within 10^3 to 10^4 orbital periods (Zsom et al. 2010; Lorek et al. 2018). However, the point at which dust growth commences during the formation of a protoplanetary disk is unclear, as is the point at which the conditions in a disk become conducive to the growth of the vertical shear instability and the streaming instability.

The vertical shear instability gives rise to stronger turbulence, and thus a stronger vertical dust diffusion, than the streaming instability. Nonetheless, we find this instability, in combination with the streaming instability, to cause the dust to be substantially more concentrated in the radial dimension than the streaming instability alone. We note that previous studies show the dust accumulation owing to the streaming instability to be sufficient to lead to planetesimal formation for the dust-to-gas surface density ratios we consider.

In other words, for a given dust size, the critical surface density ratio that is required for planetesimal formation may

be significantly lower if not only the streaming instability, but both the vertical shear instability and the streaming instability together induce the dust concentration. The critical surface density ratio exceeds 1% for all dust sizes in the former case (Carrera et al. 2015; Yang et al. 2017), but might be lower than this canonical interstellar medium value in the latter case.

6.2. Limitations of our numerical study

Both the linear vertical shear instability (Nelson et al. 2013; Barker & Latter 2015) and the linear streaming instability (Youdin & Goodman 2005) are axisymmetric in nature. Nonetheless, slight deviations from this symmetry are found in simulations of the nonlinear regime of both the former instability (Nelson et al. 2013; Stoll & Kley 2014) and the latter one (Kowalik et al. 2013). These deviations are not captured by our two-dimensional simulations.

Umurhan et al. (2019) and Chen & Lin (2020) analytically examined the linear streaming instability in connection with the α-model for protoplanetary disk turbulence (Shakura & Sunyaev 1973). These latter authors find that turbulence reduces the growth rate of the instability compared to the purely laminar case. However, this analysis is not applicable if the streaming instability itself is the dominant source of turbulence.

Similarly, Gole et al. (2020) study planetesimal formation owing to the streaming instability in local shearing box simulations with driven Kolmogorov-like turbulence that is not affected by the presence of the dust. In the simulations of these latter authors, planetesimals formation is hampered by turbulence and quenched if the turbulent Mach number is greater than $\sim 10^{-2}$.

We studied only models with a single dust size (or a single dimensionless dust stopping time). Krapp et al. (2019) show that the linear growth rate of the streaming instability can decrease if multiple dust species with a distribution of sizes rather than a single species are simulated. Nevertheless, simulations of the nonlinear streaming instability including dust size distributions do not seem to show indications of this effect (Bai & Stone 2010b; Schaffer et al. 2018).

Furthermore, we did not take into account other hydrodynamic instabilities like the convective overstability (Klahr & Hubbard 2014; Lyra 2014), the subcritical baroclinic instability (Klahr & Bodenheimer 2003; Klahr 2004; Lyra 2014), or the zombie vortex instability (Marcus et al. 2015, 2016; Lesur & Latter 2016). These instabilities do not operate in our model because the former two require finite gas cooling timescales – we simulate either a locally adiabatic or a locally isothermal gas – while the latter is three-dimensional.

In addition, our simulations do not include magnetic fields. Cui & Bai (2020) study the vertical shear instability in nonideal MHD simulations. These latter authors find that magnetized disk winds and the vertical shear instability can coexist. Under conditions that are typical of protoplanetary disks, the instability induces a comparable turbulent strength in their simulations and in purely hydrodynamical ones like ours. Nonetheless, if the magnetization is enhanced or the gas is more strongly coupled to the magnetic field, the instability causes weaker turbulence.

7. Summary

We present two-dimensional axisymmetric global numerical simulations of protoplanetary disks spanning orbital radii between 1 and 100 au. The simulations include Lagrangian particles to model the dust, the mutual drag between dust and gas, and the radial and vertical stellar gravity. We used the FLASH Code to conduct these simulations, which allowed us to apply adaptive mesh refinement to increase the resolution locally in and close to the dust layer in the midplane of the disks.

Employing these simulations, we investigated the turbulence driven by the vertical shear instability and that driven by the streaming instability individually, as well as the interaction of the two instabilities. The results of our study can be summarized as follows:

- We conducted simulations of the vertical shear instability only, with vertical domain extents of one or two gas scale heights above and below the midplane. Only the latter vertical size is sufficient to reproduce the turbulent strength found by previous numerical studies of vertically larger domains. The Mach number of the vertical gas motions is of the order of 10^{-1} in the saturated state of the instability (Flock et al. 2017).
- If both the vertical shear instability and the streaming instability start to grow simultaneously, we find the turbulence in the dust midplane layer to be mainly driven by the streaming instability. This is most likely the result of a combination of two effects: in the midplane, the streaming instability grows faster in turbulent strength than the vertical shear instability. Furthermore, the weight of the dust induces an effective buoyancy in the gas that quenches the vertical shear instability (Lin & Youdin 2017; Lin 2019).
- The vertical dust settling and the turbulent diffusion that is induced by the streaming instability attain an equilibrium if the dust-to-gas scale height ratio is equal to $\sim$1%. The dust scale height is set in a self-regulatory way if the streaming instability gives rise to the diffusion of the dust (Bai & Stone 2010b): if the scale height is less than the equilibrium value, then the turbulent strength is greater than the equilibrium strength, and the dust is lifted away from the midplane.
- We show that the streaming instability drives isotropic turbulence with a Mach number of up to $\sim 10^{-2}$. This is in agreement with observed values in protoplanetary disks (Flaherty et al. 2015, 2017, 2018; Pinte et al. 2016; Ohashi & Kataoka 2019). In particular, Pinte et al. (2016) and Ohashi & Kataoka (2019) obtain this Mach number from the scale height of the dust disks surrounding HL Tau and HD 163296, respectively; that is, they would probe the turbulent strength induced by the streaming instability if this instability were the primary source of turbulence in the dust layer of protoplanetary disks.
- Both the equilibrium dust scale height and the Mach number that are induced by the streaming instability are largely independent of the dust-to-gas surface density ratio and the initial dust scale height. The turbulent strength, and with it the scale height, increases with the speed of the radial dust drift. In other words, the turbulence is stronger if the dust stopping time or the radial gas pressure gradient is greater. The strength saturates for dimensionless stopping times of $\sim$0.05 and dimensionless pressure gradient parameters, as defined by Bai & Stone (2010b), of $\sim$0.1.
- In contrast, if the vertical shear instability has attained a saturated state before we introduce the dust into our simulations, then this instability remains the primary source of turbulence in the dust layer; it gives rise to stronger turbulence than the streaming instability, which elevates the dust to greater scale heights. For a dust-to-gas surface density ratio of 2%, the instability induces a Mach number of $\sim 10^{-1}$ and a dust scale height of $\sim$10% of the gas scale height. Nevertheless, if the surface density ratio is higher, the instability is more strongly quenched by the dust-induced buoyancy.

– We find that a combination of the vertical shear instability and the streaming instability leads to a considerably stronger radial concentration of the dust than the streaming instability only. The dust accumulations are dense enough for their radial drift to be halted almost completely. This is despite the vertical shear instability inducing stronger vertical diffusion than the streaming instability. We speculate that the vertical shear instability induces the formation of weak overdensities that seed the streaming instability. The streaming instability in turn causes strong dust concentration that would likely lead to planetesimal formation in simulations including the self-gravity of the dust.

Acknowledgements. We thank the anonymous referee and Chao-Chin Yang for their constructive feedback that helped to improve this paper. To analyze and visualize the simulations, the Python packages yt (`http://yt-project.org`) (Turk et al. 2011), Matplotlib (`https://matplotlib.org`) (Hunter 2007), and NumPy (`https://numpy.org`) (Oliphant 2006) have been used. The FLASH Code has in part been developed by the DOE NNSA-ASC OASCR Flash Center at the University of Chicago. Computational resources employed to conduct the simulations presented in this paper were provided by the Regionales Rechenzentrum at the University of Hamburg, by the Norddeutscher Verbund für Hoch- und Höchstleistungsrechnen (HLRN), and by the Swedish Infrastructure for Computing (SNIC) at LUNARC at Lund University. US thanks the University of Hamburg for granting him a scholarship to fund his doctoral studies. A.J. is thankful for research support by the European Research Council (ERC Consolidator Grant 724687-PLANETESYS), the Knut and Alice Wallenberg Foundation (Wallenberg Academy Fellow Grant 2017.0287), and the Swedish Research Council (Project Grant 2018-04867). US and R.B. gratefully acknowledge financial support by the Deutsche Forschungsgemeinschaft (DFG), grant BA 3706/18-1. R.B. is thankful for support by the Excellence Cluster 2121 "Quantum Universe" which is funded by the DFG.

References

Alcalá, J. M., Manara, C. F., Natta, A., et al. 2017, A&A, 600, A20
Andrews, S. M., & Williams, J. P. 2005, ApJ, 631, 1134
Andrews, S. M., Wilner, D. J., Hughes, A. M., Qi, C., & Dullemond, C. P. 2009, ApJ, 700, 1502
Andrews, S. M., Wilner, D. J., Hughes, A. M., Qi, C., & Dullemond, C. P. 2010, ApJ, 723, 1241
Arlt, R., & Urpin, V. 2004, A&A, 426, 755
Bai, X.-N. 2015, ApJ, 798, 84
Bai, X.-N. 2017, ApJ, 845, 75
Bai, X.-N., & Stone, J. M. 2010a, ApJS, 190, 297
Bai, X.-N., & Stone, J. M. 2010b, ApJ, 722, 1437
Bai, X.-N., & Stone, J. M. 2010c, ApJ, 722, L220
Barge, P., & Sommeria, J. 1995, A&A, 295, L1
Barker, A. J., & Latter, H. N. 2015, MNRAS, 450, 21
Baruteau, C., Fromang, S., Nelson, R. P., & Masset, F. 2011, A&A, 533, A84
Birnstiel, T., Dullemond, C. P., & Brauer, F. 2010, A&A, 513, A79
Birnstiel, T., Ormel, C. W., & Dullemond, C. P. 2011, A&A, 525, A11
Birnstiel, T., Klahr, H., & Ercolano, B. 2012, A&A, 539, A148
Boris, J. P. 1970, Proceedings of the Fourth Conference on the Numerical Simulation of Plasmas, 3
Carrera, D., Johansen, A., & Davies, M. B. 2015, A&A, 579, A43
Carrera, D., Gorti, U., Johansen, A., & Davies, M. B. 2017, ApJ, 839, 16
Chapman, S., & Cowling, T. G. 1970, The mathematical theory of non-uniform gases. An account of the kinetic theory of viscosity, thermal conduction and diffusion in gases, 3rd edn. (Cambridge: Cambridge University Press)
Chen, K., & Lin, M.-K. 2020, ApJ, 891, 132
Chiang, E., & Youdin, A. N. 2010, Ann. Rev. Earth Planet. Sci., 38, 493
Cui, C., & Bai, X.-N. 2020, ApJ, 891, 30
Cuzzi, J. N., Hogan, R. C., & Shariff, K. 2008, ApJ, 687, 1432
Delzanno, G. L., & Camporeale, E. 2013, J. Comput. Phys., 253, 259
Drążkowska, J., & Alibert, Y. 2017, A&A, 608, A92
Drążkowska, J., Alibert, Y., & Moore, B. 2016, A&A, 594, A105
Dubrulle, B., Morfill, G., & Sterzik, M. 1995, Icarus, 114, 237
Dullemond, C. P., Birnstiel, T., Huang, J., et al. 2018, ApJ, 869, L46
Ercolano, B., Jennings, J., Rosotti, G., & Birnstiel, T. 2017, MNRAS, 472, 4117
Flaherty, K. M., Hughes, A. M., Rosenfeld, K. A., et al. 2015, ApJ, 813, 99
Flaherty, K. M., Hughes, A. M., Rose, S. C., et al. 2017, ApJ, 843, 150
Flaherty, K. M., Hughes, A. M., Teague, R., et al. 2018, ApJ, 856, 117
Flock, M., Nelson, R. P., Turner, N. J., et al. 2017, ApJ, 850, 131
Fricke, K. 1968, ZAp, 68, 317
Fromang, S., & Papaloizou, J. 2006, A&A, 452, 751
Fryxell, B., Olson, K., Ricker, P., et al. 2000, ApJS, 131, 273
Goldreich, P., & Schubert, G. 1967, ApJ, 150, 571
Gole, D. A., Simon, J. B., Li, R., Youdin, A. N., & Armitage, P. J. 2020, ApJ, submitted [arXiv:2001.10000]
Gressel, O., Turner, N. J., Nelson, R. P., & McNally, C. P. 2015, ApJ, 801, 84
Grundy, W., Noll, K., Roe, H., et al. 2019, Icarus, in press
Güttler, C., Blum, J., Zsom, A., Ormel, C. W., & Dullemond, C. P. 2010, A&A, 513, A56
Hayashi, C. 1981, Prog. Theor. Phys. Suppl., 70, 35
Hunter, J. D. 2007, Comput. Sci. Eng., 9, 90
Ida, S., & Guillot, T. 2016, A&A, 596, L3
Johansen, A., & Klahr, H. 2005, ApJ, 634, 1353
Johansen, A., & Youdin, A. 2007, ApJ, 662, 627
Johansen, A., Oishi, J. S., Mac Low, M.-M., et al. 2007, Nature, 448, 1022
Johansen, A., Youdin, A., & Mac Low M.-M. 2009, ApJ, 704, L75
Klahr, H. 2004, ApJ, 606, 1070
Klahr, H. H., & Bodenheimer, P. 2003, ApJ, 582, 869
Klahr, H., & Hubbard, A. 2014, ApJ, 788, 21
Kowalik, K., Hanasz, M., Wóltański, D., & Gawryszczak, A. 2013, MNRAS, 434, 1460
Krapp, L., Benítez-Llambay, P., Gressel, O., & Pessah, M. E. 2019, ApJ, 878, L30
Laibe, G., & Price, D. J. 2011, MNRAS, 418, 1491
Lesur, G. R. J., & Latter, H. 2016, MNRAS, 462, 4549
Li, R., Youdin, A. N., & Simon, J. B. 2018, ApJ, 862, 14
Lin, M.-K. 2019, MNRAS, 485, 5221
Lin, M.-K., & Youdin, A. N. 2015, ApJ, 811, 17
Lin, M.-K., & Youdin, A. N. 2017, ApJ, 849, 129
Lorek, S., Lacerda, P., & Blum, J. 2018, A&A, 611, A18
Lyra, W. 2014, ApJ, 789, 77
MacNeice, P., Olson, K. P., Mobarry, C., de Fainchtein, R., & Packer, C. 2000, Comput. Phys. Commun., 126, 330
Marcus, P. S., Pei, S., Jiang, C.-H., et al. 2015, ApJ, 808, 87
Marcus, P. S., Pei, S., Jiang, C.-H., & Barranco, J. A. 2016, ApJ, 833, 148
Mignone, A., Flock, M., & Vaidya, B. 2019, ApJS, 244, 38
Nelson, R. P., & Papaloizou, J. C. B. 2004, MNRAS, 350, 849
Nelson, R. P., Gressel, O., & Umurhan, O. M. 2013, MNRAS, 435, 2610
Nesvorný, D., Youdin, A. N., & Richardson, D. C. 2010, AJ, 140, 785
Nesvorný, D., Li, R., Youdin, A. N., Simon, J. B., & Grundy, W. M. 2019, Nat. Astron., 364
Ohashi, S., & Kataoka, A. 2019, ApJ, 886, 103
Oishi, J. S., & Mac Low M.-M. 2009, ApJ, 704, 1239
Oishi, J. S., Mac Low, M.-M., & Menou, K. 2007, ApJ, 670, 805
Oliphant, T. E. 2006, A guide to NumPy (USA: Trelgol Publishing)
Ormel, C. W., & Cuzzi, J. N. 2007, A&A, 466, 413
Pinte, C., Dent, W. R. F., Ménard, F., et al. 2016, ApJ, 816, 25
Ros, K., & Johansen, A. 2013, A&A, 552, A137
Ros, K., Johansen, A., Riipinen, I., & Schlesinger, D. 2019, A&A, 629, A65
Schäfer, U., Yang, C.-C., & Johansen, A. 2017, A&A, 597, A69
Schaffer, N., Yang, C.-C., & Johansen, A. 2018, A&A, 618, A75
Schlichting, H. E., & Sari, R. 2008, ApJ, 686, 741
Schoonenberg, D., & Ormel, C. W. 2017, A&A, 602, A21
Schoonenberg, D., Ormel, C. W., & Krijt, S. 2018, A&A, 620, A134
Shakura, N. I., & Sunyaev, R. A. 1973, A&A, 24, 337
Simon, J. B., Armitage, P. J., Li, R., & Youdin, A. N. 2016, ApJ, 822, 55
Squire, J., & Hopkins, P. F. 2018, MNRAS, 477, 5011
Stoll, M. H. R., & Kley, W. 2014, A&A, 572, A77
Stoll, M. H. R., & Kley, W. 2016, A&A, 594, A57
Stoll, M. H. R., Kley, W., & Picogna, G. 2017, A&A, 599, L6
Turk, M. J., Smith, B. D., Oishi, J. S., et al. 2011, ApJS, 192, 9
Umurhan, O. M., Estrada, P. R., & Cuzzi, J. N. 2019, ApJ, submitted [arXiv:1906.05371]
Weidenschilling, S. J. 1977, MNRAS, 180, 57
Yang, C.-C., & Johansen, A. 2014, ApJ, 792, 86
Yang, C.-C., & Johansen, A. 2016, ApJS, 224, 39
Yang, C.-C., Mac Low, M.-M., & Menou, K. 2009, ApJ, 707, 1233
Yang, C.-C., Mac Low, M.-M., & Menou, K. 2012, ApJ, 748, 79
Yang, C.-C., Johansen, A., & Carrera, D. 2017, A&A, 606, A80
Yang, C.-C., Mac Low, M.-M., & Johansen, A. 2018, ApJ, 868, 27
Youdin, A. N., & Goodman, J. 2005, ApJ, 620, 459
Youdin, A., & Johansen, A. 2007, ApJ, 662, 613
Youdin, A. N., & Lithwick, Y. 2007, Icarus, 192, 588
Zsom, A., Ormel, C. W., Güttler, C., Blum, J., & Dullemond, C. P. 2010, A&A, 513, A57

Appendix A: Leapfrog algorithm for cylindrical geometries

A.1. Implementation

We implement a second-order-accurate, explicit Leapfrog algorithm for the time integration of particles in cylindrical geometries. The algorithm is based on the one developed by Boris (1970) for charged particles in simulations including electric and magnetic fields. It has been described as well by, for example, Delzanno & Camporeale (2013).

For the update of the vertical components of the particle velocity and position, we adopt the Leapfrog algorithm for Cartesian geometries that is part of the FLASH Code:

$$v_{z,i}^{1/2} = v_{z,i}^{0} + \frac{1}{2} a_{z,i}^{0} \Delta t^{0}, \tag{A.1}$$

$$v_{z,i}^{n+1/2} = v_{z,i}^{n-1/2} + A_n a_{z,i}^{n} + B_n a_{z,i}^{n-1}, \text{ and} \tag{A.2}$$

$$z_i^{n+1} = z_i^{n} + v_{z,i}^{n+1/2} \Delta t^{n}, \tag{A.3}$$

where z_i^n, $v_{z,i}^n$, and $a_{z,i}^n$ are the vertical position, velocity, and acceleration of the ith particle at the nth time-step Δt^n, respectively. The acceleration is computed employing cloud-in-cell mapping between the grid and the particles; in our simulations, it is due to the stellar gravity only. We explain in Appendix B how we take account of the acceleration caused by the drag of the gas onto the particles. The coefficients A_n and B_n are given by

$$A_n = \frac{1}{2}\Delta t^{n} + \frac{1}{3}\Delta t^{n-1} + \frac{1}{6}\frac{\Delta t^{n^2}}{\Delta t^{n-1}} \text{ and} \tag{A.4}$$

$$B_n = \frac{1}{6}\left(\Delta t^{n-1} - \frac{\Delta t^{n^2}}{\Delta t^{n-1}}\right). \tag{A.5}$$

The radial and azimuthal velocity and position components are advanced as in Cartesian coordinates, followed by a transformation from these to cylindrical coordinates:

1. The velocity is calculated as in a Cartesian geometry, i.e., inertial forces are disregarded:

$$v_{\{r,\phi\},i}^{1/2'} = v_{\{r,\phi\},i}^{0} + \frac{1}{2} a_{\{r,\phi\},i}^{0} \Delta t^{0} \text{ and} \tag{A.6}$$

$$v_{\{r,\phi\},i}^{n+1/2'} = v_{\{r,\phi\},i}^{n-1/2} + A_n a_{\{r,\phi\},i}^{n} + B_n a_{\{r,\phi\},i}^{n-1}, \tag{A.7}$$

   where the subscript $\{r, \phi\}$ denotes the radial or azimuthal component.
2. The position is updated in Cartesian geometry and then transformed from Cartesian to cylindrical geometry:

$$x_i^{n+1} = r_i^{n} + v_{r,i}^{n+1/2'} \Delta t^{n}, \tag{A.8}$$

$$y_i^{n+1} = v_{\phi,i}^{n+1/2'} \Delta t^{n}, \tag{A.9}$$

$$r_i^{n+1} = \sqrt{x_i^{n+1^2} + y_i^{n+1^2}}, \text{ and} \tag{A.10}$$

$$\phi_i^{n+1} = \phi_i^{n} + \alpha_i^{n+1}, \tag{A.11}$$

   where r_i^n and ϕ_i^n are the radial and azimuthal position, respectively, and the angle α_i^{n+1} can be computed as

$$\alpha_i^{n+1} = \arccos\left(\frac{x_i^{n+1}}{r_i^{n+1}}\right) = \arcsin\left(\frac{y_i^{n+1}}{r_i^{n+1}}\right). \tag{A.12}$$

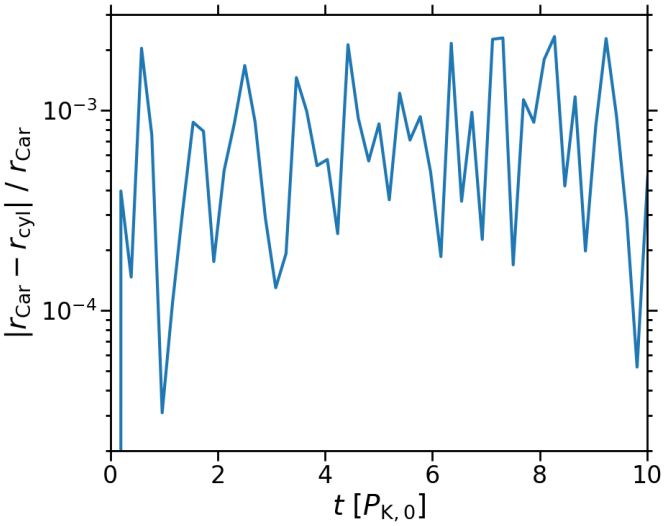

Fig. A.1. Error of the radial coordinate r_{cyl} that is computed by our implementation of the Leapfrog algorithm for cylindrical geometries relative to the coordinate $r_{Car} = \sqrt{x^2 + y^2}$ that is calculated by the already implemented algorithm for Cartesian geometries. We conduct two equivalent simulations of a particle in a point mass gravitational potential, one applying the former and one the latter algorithm. Both simulations end after ten Keplerian orbital periods at the initial position of the particle $P_{K,0}$. As can be seen, the relative error, while varying, is at most 2×10^{-3}.

3. The velocity is corrected to reflect the transformation from Cartesian to cylindrical geometry, which entails the consideration of inertial forces:

$$v_{r,i}^{n+1/2} = \cos\left(\alpha_i^{n+1}\right) v_{r,i}^{n+1/2'} + \sin\left(\alpha_i^{n+1}\right) v_{\phi,i}^{n+1/2'} \text{ and} \tag{A.13}$$

$$v_{\phi,i}^{n+1/2} = -\sin\left(\alpha_i^{n+1}\right) v_{r,i}^{n+1/2'} + \cos\left(\alpha_i^{n+1}\right) v_{\phi,i}^{n+1/2'}. \tag{A.14}$$

The velocity at a full time-step can be computed from the one at a half time step as follows:

$$\boldsymbol{v}_i^{n} = \boldsymbol{v}_i^{n-1/2} + \frac{1}{2}\left(A_n \boldsymbol{a}_i^{n} + B_n \boldsymbol{a}_i^{n-1}\right). \tag{A.15}$$

We note that this full-step velocity is second-order accurate, while the error in the half-step velocity is proportional to the time-step.

A.2. Test

We test our implementation using the Leapfrog algorithm for Cartesian geometries that is already included in the FLASH Code as a benchmark: we conduct two analogous simulations of a particle in the gravitational potential of a point mass, one with a two-dimensional cylindrical and one with a three-dimensional Cartesian geometry.

The initial position of the particle, relative to the position of the point mass, can be expressed as $(r, z) = (3\text{ au}, -1\text{ au})$ in cylindrical and by $(x, y, z) = (3\text{ au}, 0\text{ au}, -1\text{ au})$ in Cartesian coordinates. To establish an initial balance between the centrifugal and the radial gravitational force which are exerted on the particle, we set its velocity to

$$\begin{cases} v_\phi = \sqrt{\frac{GM}{\left(r^2+z^2\right)^{3/2}} r^2} & \text{(cylindrical geometry) or} \\ v_y = \sqrt{\frac{GM}{\left(x^2+y^2+z^2\right)^{3/2}} \left(x^2+y^2\right)} & \text{(Cartesian geometry),} \end{cases} \tag{A.16}$$

where $M = 1\,M_\odot$ is the point mass. Cloud-in-cell mapping is applied to calculate the gravitational acceleration of the particle. The grid cell edge length is fixed at 0.025 au.

In Fig. A.1, we show the relative error of the cylindrical radial coordinate $r_{\rm cyl}$ with respect to the coordinate $r_{\rm Car} = \sqrt{x^2 + y^2}$ in Cartesian geometry. As is evident, the error does not exceed 2×10^{-3} throughout the simulations.

Appendix B: Drag

B.1. Implementation

For our implementation of the drag exerted by the gas on the dust and vice versa, we take advantage of the first-order cloud-in-cell mapping between the grid and the particles that is part of the FLASH Code.

For each of the radial, azimuthal, and vertical velocity components, we execute the following steps:

1. The gas density, pressure, and velocity component are mapped to the particles.
2. For every particle:
   (a) The full-step dust velocity component is calculated from the stored half-step component according to Eq. (A.15).
   (b) The dust stopping time $t_{\rm d,stop}$ is computed as

$$t_{\rm d,stop} = \begin{cases} \frac{\rho_{\rm s} a}{\rho_{\rm g} c_{\rm s}} & a \le 9/4\,\lambda_{\rm g,mfp} \text{ (Epstein regime) or} \\ \frac{4\rho_{\rm s} a^2}{9\rho_{\rm g} c_{\rm s} \lambda_{\rm g,mfp}} & a > 9/4\,\lambda_{\rm g,mfp} \text{ (Stokes regime),} \end{cases} \tag{B.1}$$

   where $\lambda_{\rm g,mfp} = 1/(\sigma_{\rm g} n_{\rm g}) = \mu m_H/(\sigma_{\rm g}\rho_{\rm g})$ is the gas mean free path length, $n_{\rm g}$ the gas number density, $\sigma_{\rm g} = 2 \times 10^{-15}$ cm^2 the molecular collision cross section (Chapman & Cowling 1970), and $c_{\rm s} = \gamma P/\rho_{\rm g}$ the sound speed.
   (c) To the stored dust half-step velocity component, the drag source term $-\Delta v_{\rm d,drag} = -(v_{\rm d} - v_{\rm g})/t_{\rm d,stop}\,\Delta t$ is added, where $v_{\rm d}$ and $v_{\rm g}$ are the (full-step) dust and gas velocity components, respectively, and Δt is the current time-step.
3. The change in dust momentum $\Delta p_{\rm d,drag} = m_{\rm d}\Delta v_{\rm d,drag}$ is mapped to the grid.
4. The drag source term $\Delta v_{\rm g,drag} = \Delta p_{\rm d,drag}/(\rho_{\rm g} V)$ is added to the gas velocity in each grid cell, where V is the cell volume.

We employ the global minimum of the particle stopping time and the gas stopping time $t_{\rm g,stop} = \rho_{\rm g}/\rho_{\rm d}\,t_{\rm d,stop}$ as an upper limit of the simulation time-step.

B.2. Test

To evaluate our algorithm, we adopt the test problem introduced by Laibe & Price (2011) and applied by Bai & Stone (2010a), Mignone et al. (2019) as well as Yang & Johansen (2016), who refer to it as DUSTYBOX, particle-gas deceleration, and uniform streaming test, respectively. This problem provides an opportunity to simultaneously test the drag that is exerted by the gas on the dust and the drag back-reaction of the dust onto the gas. In addition, it allows us to compare the numeric solution computed by our algorithm to an analytic one.

We conduct simulations with a two-dimensional cylindrical geometry, as this is the geometry of the simulations we present in the main text. Dust and gas initially move in the radial direction with $v_{{\rm d},r,{\rm init}} = c_{\rm s}$ and $v_{{\rm g},r,{\rm init}} = -c_{\rm s}$, respectively. The dust and gas density as well as the gas temperature are constant. The equations of motion of the dust and the gas reduce to

$$\frac{{\rm d}v_{{\rm d},r}}{{\rm d}t} = -\frac{v_{{\rm d},r} - v_{{\rm g},r}}{t_{\rm d,stop}} \text{ and} \tag{B.2}$$

$$\frac{{\rm d}v_{{\rm g},r}}{{\rm d}t} = \epsilon\frac{v_{{\rm d},r} - v_{{\rm g},r}}{t_{\rm d,stop}}, \tag{B.3}$$

where ϵ is the solid-to-gas density ratio. The dust and the gas velocity can be solved for analytically, yielding

$$\begin{aligned} v_{{\rm d},r}(t) = {} & v_{{\rm d},r,{\rm init}} \exp\left[-(1+\epsilon)\frac{t}{t_{\rm d,stop}}\right] \\ & + v_{{\rm com},r,{\rm init}}\left(1 - \exp\left[-(1+\epsilon)\frac{t}{t_{\rm d,stop}}\right]\right) \text{ and} \end{aligned} \tag{B.4}$$

$$\begin{aligned} v_{{\rm g},r}(t) = {} & v_{{\rm g},r,{\rm init}} \exp\left[-(1+\epsilon)\frac{t}{t_{\rm d,stop}}\right] \\ & + v_{{\rm com},r,{\rm init}}\left(1 - \exp\left[-(1+\epsilon)\frac{t}{t_{\rm d,stop}}\right]\right), \end{aligned} \tag{B.5}$$

where

$$v_{{\rm com},r,{\rm init}} = \frac{v_{{\rm g},r,{\rm init}} + \epsilon v_{{\rm p},r,{\rm init}}}{1+\epsilon} \tag{B.6}$$

is the initial velocity of the center of mass of dust and gas.

The displacement of every dust particle relative to its initial position is given by

$$\begin{aligned} \Delta r_{\rm d}(t) &= r_{\rm d}(t) - r_{\rm d,init} \\ &= \frac{(v_{{\rm d},r,{\rm init}} - v_{{\rm com},r,{\rm init}})\,t_{\rm d,stop}}{1+\epsilon}\left(1 - \exp\left[-(1+\epsilon)\frac{t}{t_{\rm d,stop}}\right]\right) \\ &\quad + v_{{\rm com},r,{\rm init}}\,t. \end{aligned} \tag{B.7}$$

Initially, one particle is positioned at the center of every cell.

It is natural to choose the dust stopping time $t_{\rm d,stop}$ and the sound speed $c_{\rm s}$ as the units of time and velocity, respectively. The unit of length is therefore $c_{\rm s}\,t_{\rm d,stop}$. The domains of our simulations span 100 $c_{\rm s}\,t_{\rm d,stop}$ in the radial dimension. The domain boundaries are periodic, which is necessary to maintain a constant dust and gas density and to conserve the total momentum of dust and gas. The simulations end after 3 $t_{\rm d,stop}$.

We employ two quantities to measure the accuracy of our implementation: the absolute error of the total momentum with respect to the initial value and the absolute error of the particle displacement relative to the analytic solution (see Eq. (B.7)). In upper and lower panels of Fig. B.1, respectively, we show the momentum and the displacement error at the end of simulations with varying time-steps Δt (left panels), grid cell edge lengths Δx (middle panels), and solid-to-gas density ratios ϵ (right panels).

First and foremost, we note that our drag algorithm should not be used in combination with the periodic boundary implementation that is part of the FLASH Code[5]. In the figure, we mark with red crosses the errors in simulations in which particles cross the domain boundaries. The absolute error of the total momentum, while generally of the order of 10^{-10} or 10^{-9} otherwise, can be larger than unity in these simulations (see the upper panels).

[5] This issue does not affect the simulations that are presented in the main text since we apply diode conditions at the boundaries of their domains.

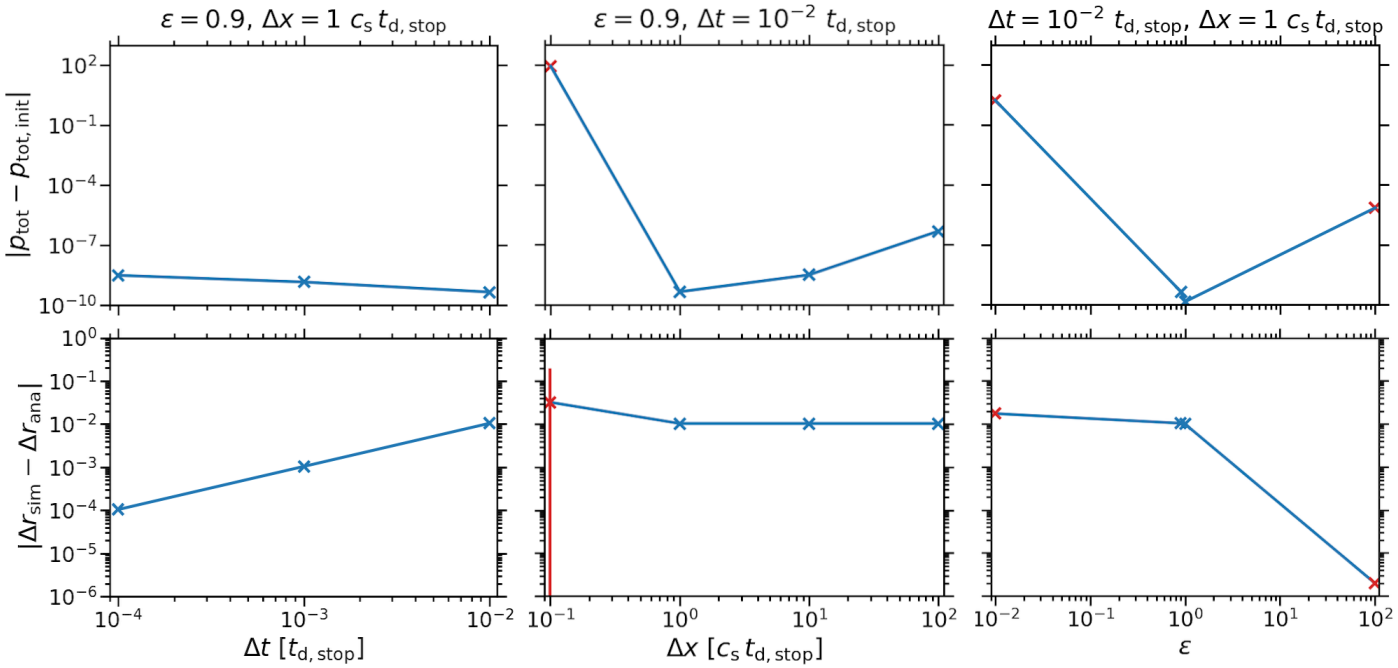

Fig. B.1. Absolute error of the total momentum p_{tot} of dust and gas relative to the initial total momentum $p_{tot,init}$ (*upper panels*) and mean absolute error of the simulated particle displacement Δr_{sim} with respect to the analytic solution Δr_{ana} (see Eq. (B.7); *lower panels*). In the latter case, the mean is calculated by averaging over all particles, with the standard deviations plotted as error bars. (With one exception, the standard deviations are too small for the error bars to be visible, though.) Both the momentum and the displacement errors are computed after 3 $t_{d,stop}$. We show the errors as functions of the time-step Δt (*left panels*), of the grid cell edge length Δx (*middle panels*), and of the dust-to-gas density ratio ϵ (*right panels*). In the title of every column of panels, the fixed values of the other two quantities are given. Simulations in which particles cross the domain boundaries are marked with red crosses. The error in the total momentum can exceed one in these simulations, but is in general of the order of 10^{-10} to 10^{-9} otherwise. The error in the displacement increases linearly with the time-step since our drag algorithm is first-order accurate. On the other hand, it is independent of the cell size for sizes of at least 1 $c_s\ t_{d,stop}$. At these resolutions, the particles are displaced by less than half a cell within 3 $t_{d,stop}$ and therefore do not transverse the boundaries. The error for the fiducial dust-to-gas density ratio of $\epsilon = 0.9$ amounts to 10^{-2}; while for a ratio of $\epsilon = 0.01$ it is greater by a factor of a few, it is as small as $\sim 10^{-6}$ if the ratio is equal to $\epsilon = 100$. This is despite a number of particles crossing the boundaries if the density ratio is much less or much greater than the fiducial value.

We choose $\epsilon = 0.9$ as the fiducial dust-to-gas density ratio and $\Delta x = 1\ c_s\ t_{d,stop}$ as the fiducial resolution. This is to reduce the influence of the boundary conditions on our examination of the drag implementation as much as possible. For the fiducial density ratio, the analytic displacement remains less than 0.436 $c_s\ t_{d,stop}$, that is, less than half a cell edge length at the fiducial resolution, within 3 $t_{d,stop}$. Indeed, no particle crosses the boundaries in our simulations with this density ratio and the fiducial or a lower resolution.

From the lower-left panel of the figure, it can be seen that our implementation is first-order accurate in time. For the fiducial time-step of $\Delta t = 10^{-2}$, the absolute error of the displacement amounts to 1%. If the time-step is ten or a hundred times smaller, the error is less by one order or two orders of magnitude, respectively.

Reducing the resolution by a factor of ten or a hundred with respect to the fiducial resolution does not lead to an increase in the displacement error (see the lower-middle panel). This is despite the displacement within 3 $t_{d,stop}$ not being resolved even at the fiducial resolution. Nonetheless, the momentum error is greater at lower resolutions; it is of the order of 10^{-7} in the simulation with a resolution of a hundredth of the fiducial resolution, in which only one particle is present. On the other hand, if the resolution is higher than the fiducial one, the error in both the displacement and the total momentum is considerable. This is because a large number of particles transverse the domain boundaries.

Compared to the error for the fiducial dust-to-gas density ratio, the displacement error increases by a factor of a few for low density ratios, but decreases by orders of magnitude for high ratios. This is evident from the lower-right panel, in which the errors in simulations with the fiducial density ratio as well as $\epsilon = 0.01$, $\epsilon = 1$, and $\epsilon = 100$ are shown. A number of particles cross the boundaries in both the simulation with the highest density ratio and the one with the lowest ratio. Thus, the error in the total momentum, though not the error in the displacement, is significantly greater for these ratios than for the fiducial one.

7 Outlook

The streaming instability affects the bottom-up growth from dust to planets in two regards. On the one hand, it drives turbulence in the dust layer around the mid-plane of protoplanetary disks. On the other hand, it induces dust concentration in gravitationally unstable clumps that collapse and form planetesimals. Both of these aspects are studied in this thesis. In SYJ17, we employ three-dimensional local shearing box simulations to investigate the initial mass distribution of the planetesimals and particularly its high-mass end. In SJB20, we conduct two-dimensional global simulations to study the instability as a source of turbulence, including how this turbulence interacts with that caused by the vertical shear instability.

The simulations presented in SJB20 are the first multi-dimensional global simulations of the streaming instability including Lagrangian particles to model the dust, and the second ever in general (after Kowalik et al. 2013). Future global simulations of the instability could provide answers to a variety of questions which, if at all, have only been touched on so far:

- How does the streaming instability interact with other instabilities? Do these interactions promote dust concentration and thus facilitate planetesimal formation? Apart from the vertical shear instability in SJB20, among the purely (magneto-)hydrodynamic instabilities only the magnetorotational and the subcritical baroclinic instability have been studied in connection with the streaming instability, and only in local shearing box simulations (Johansen et al. 2007, 2011; Balsara et al. 2009; Tilley et al. 2010; Raettig et al. 2015; Yang et al. 2018). These simulations show that dust accumulations in pressure bumps and vortices induced by the magnetorotational, the subcritical baroclinic, and the vertical shear instability are enhanced by the streaming instability (Johansen et al. 2007, 2011; Raettig et al. 2015; SJB20).

- What is the extent and the separation of the filaments in which dust is concentrated by the streaming instability, in which planetesimals form and from which they accrete? In shearing box simulations, Yang and Johansen (2014) and Li et al. (2018) find a typical separation of $0.15 - 0.2$ gas scale heights, while Abod et al. (2019) show that the radial width varies with the strength of the radial gas pressure gradient. While planetesimals emerging form radially larger filaments are more numerous and more massive (Abod et al.

2019; SYJ17), planetesimals typically accrete dust from more than one filament owing to migration in the radial direction (SYJ17).

- With what efficiency is dust mass converted to planetesimal mass? How is the mass in planetesimals distributed in protoplanetary disks? What are the implications of this mass distribution for the subsequent stages of planet formation? One-dimensional global models show the formation of tens or hundreds of Earth masses in planetesimals locally in dust pile-ups in the inner disk regions (Drążkowska et al. 2016), at the water ice line (Drążkowska and Alibert 2017; Schoonenberg et al. 2018), and at the outer edges of the gaps carved in disks by planets (Eriksson et al. 2020). A comparable total mass in planetesimals emerges globally in the one-dimensional disk evolution models including accretion and photoevaporation by Carrera et al. (2017) – in their most comprehensive models the water ice line is taken into account as well – but at most a few Earth masses in similar models by Ercolano et al. (2017).

The two-dimensional global simulations in SJB20 can be improved upon by considering more realistic models of gas and dust in protoplanetary disks. This includes dust size distributions (Bai and Stone 2010b; Schaffer et al. 2018; Krapp et al. 2019; Zhu and Yang submitted) which are informed by the barriers to collisional growth constituted by bouncing, fragmentation, and radial drift (Drążkowska et al. 2016, 2019) rather than a single dust size; disk evolution owing to stellar accretion, jets and disk winds, as well as photoevaporation (Carrera et al. 2017; Ercolano et al. 2017); ice lines (Schoonenberg and Ormel 2017; Drążkowska and Alibert 2017; Schoonenberg et al. 2018); and planets (Eriksson et al. 2020). Even more potential lies in three-dimensional simulations with self-gravity because only in these the gravitational collapse of dust clumps and the formation of planetesimals can be investigated.

Acknowledgments

Mein erster Dank gebührt Robi Banerjee, der mich in die theoretische und numerische Astrophysik eingeführt und mit Sternentstehung und den Unzulänglichkeiten astrophysikalischer Software vertraut gemacht hat. I am also deeply grateful to Anders Johansen and Chao-Chin Yang for introducing me to the fascinating world of protoplanetary disks and planet formation and for teaching me how to write papers. Thanks to all three of you for our discussions, your advice, and your support!

Danke auch an meine Kollegen aus Robis Arbeitsgruppe, besonders Gunther Lukat, Manuel Jung, Simon Selg und Bastian Körtgen, für technischen Support, physikalischen Support und Diskussionen über Gott und die Welt.

I am equally thankful to Anders' group and the others at Lund Observatory for being so kind and welcoming whenever I visited Lund. I especially thank Thomas Ronnet and Sebastian Lorek as large parts of Sects. 2.2 and 2.3 are based on discussions with them.

Allen voran bin ich Katharina dankbar, für viel mehr als ich hier in Worte fassen kann. Insbesondere aber danke, dass du diese Arbeit Korrektur gelesen hast, auch wenn wir nicht die gleiche Mathematik sprechen.

Bibliography

Abod, C. P., Simon, J. B., Li, R., et al. The Mass and Size Distribution of Planetesimals Formed by the Streaming Instability. II. The Effect of the Radial Gas Pressure Gradient. *ApJ*, 883(2): 192, 2019.

Adachi, I., Hayashi, C., and Nakazawa, K. The gas drag effect on the elliptical motion of a solid body in the primordial solar nebula. *Progress of Theoretical Physics*, 56:1756–1771, 1976.

Adams, F. C., Lada, C. J., and Shu, F. H. Spectral Evolution of Young Stellar Objects. *ApJ*, 312: 788, 1987.

Agurto-Gangas, C., Pineda, J. E., Szűcs, L., et al. Revealing the dust grain size in the inner envelope of the Class I protostar Per-emb-50. *A&A*, 623:A147, 2019.

Akimkin, V. V., Ivlev, A. V., and Caselli, P. Inhibited Coagulation of Micron-size Dust Due to the Electrostatic Barrier. *ApJ*, 889(1):64, 2020.

Alexander, R., Pascucci, I., Andrews, S., et al. The Dispersal of Protoplanetary Disks. In Beuther, H., Klessen, R. S., Dullemond, C. P., and Henning, T., editors, *Protostars and Planets VI*, page 475, 2014.

Alexander, R. D. and Armitage, P. J. Dust dynamics during protoplanetary disc clearing. *MNRAS*, 375(2):500–512, 2007.

Andre, P., Ward-Thompson, D., and Barsony, M. Submillimeter Continuum Observations of rho Ophiuchi A: The Candidate Protostar VLA 1623 and Prestellar Clumps. *ApJ*, 406:122, 1993.

Andrews, S. M. and Williams, J. P. Circumstellar Dust Disks in Taurus-Auriga: The Submillimeter Perspective. *ApJ*, 631(2):1134–1160, 2005.

Andrews, S. M., Wilner, D. J., Hughes, A. M., et al. Protoplanetary Disk Structures in Ophiuchus. *ApJ*, 700(2):1502–1523, 2009.

Andrews, S. M., Wilner, D. J., Hughes, A. M., et al. Protoplanetary Disk Structures in Ophiuchus. II. Extension to Fainter Sources. *ApJ*, 723(2):1241–1254, 2010.

Andrews, S. M., Rosenfeld, K. A., Kraus, A. L., and Wilner, D. J. The Mass Dependence between Protoplanetary Disks and their Stellar Hosts. *ApJ*, 771(2):129, 2013.

Arlt, R. and Urpin, V. Simulations of vertical shear instability in accretion discs. *A&A*, 426: 755–765, 2004.

Armitage, P. J. *Astrophysics of Planet Formation*. Cambridge: Cambridge University Press, 2010.

Armitage, P. J., Eisner, J. A., and Simon, J. B. Prompt Planetesimal Formation beyond the Snow Line. *ApJ*, 828(1):L2, 2016.

Auffinger, J. and Laibe, G. Linear growth of streaming instability in pressure bumps. *MNRAS*, 473(1):796–805, 2018.

Bacciotti, F., Girart, J. M., Padovani, M., et al. ALMA Observations of Polarized Emission toward the CW Tau and DG Tau Protoplanetary Disks: Constraints on Dust Grain Growth and Settling. *ApJ*, 865(2):L12, 2018.

Bai, X.-N. Hall-effect-Controlled Gas Dynamics in Protoplanetary Disks. I. Wind Solutions at the Inner Disk. *ApJ*, 791(2):137, 2014.

Bai, X.-N. Hall Effect Controlled Gas Dynamics in Protoplanetary Disks. II. Full 3D Simulations toward the Outer Disk. *ApJ*, 798(2):84, 2015.

Bai, X.-N. Global Simulations of the Inner Regions of Protoplanetary Disks with Comprehensive Disk Microphysics. *ApJ*, 845(1):75, 2017.

Bai, X.-N. and Stone, J. M. Particle-gas Dynamics with Athena: Method and Convergence. *ApJS*, 190:297–310, 2010a.

Bai, X.-N. and Stone, J. M. Dynamics of Solids in the Midplane of Protoplanetary Disks: Implications for Planetesimal Formation. *ApJ*, 722(2):1437–1459, 2010b.

Bai, X.-N. and Stone, J. M. The Effect of the Radial Pressure Gradient in Protoplanetary Disks on Planetesimal Formation. *ApJ*, 722:L220–L223, 2010c.

Balbus, S. A. and Hawley, J. F. A Powerful Local Shear Instability in Weakly Magnetized Disks. I. Linear Analysis. *ApJ*, 376:214, 1991.

Balsara, D. S., Tilley, D. A., Rettig, T., and Brittain, S. D. Dust settling in magnetorotationally driven turbulent discs - I. Numerical methods and evidence for a vigorous streaming instability. *MNRAS*, 397(1):24–43, 2009.

Barge, P. and Sommeria, J. Did planet formation begin inside persistent gaseous vortices? *A&A*, 295:L1–L4, 1995.

Barker, A. J. and Latter, H. N. On the vertical-shear instability in astrophysical discs. *MNRAS*, 450(1):21–37, 2015.

Barranco, J. A. Three-Dimensional Simulations of Kelvin-Helmholtz Instability in Settled Dust Layers in Protoplanetary Disks. *ApJ*, 691(2):907–921, 2009.

Barranco, J. A., Pei, S., and Marcus, P. S. Zombie Vortex Instability. III. Persistence with Nonuniform Stratification and Radiative Damping. *ApJ*, 869(2):127, 2018.

Baruteau, C., Crida, A., Paardekooper, S. J., et al. Planet-Disk Interactions and Early Evolution of Planetary Systems. In Beuther, H., Klessen, R. S., Dullemond, C. P., and Henning, T., editors, *Protostars and Planets VI*, page 667, 2014.

Benecchi, S. D., Noll, K. S., Grundy, W. M., et al. The correlated colors of transneptunian binaries. *Icarus*, 200(1):292–303, 2009.

Béthune, W., Lesur, G., and Ferreira, J. Self-organisation in protoplanetary discs. Global, non-stratified Hall-MHD simulations. *A&A*, 589:A87, 2016.

Béthune, W., Lesur, G., and Ferreira, J. Global simulations of protoplanetary disks with net magnetic flux. I. Non-ideal MHD case. *A&A*, 600:A75, 2017.

Birnstiel, T., Klahr, H., and Ercolano, B. A simple model for the evolution of the dust population in protoplanetary disks. *A&A*, 539:A148, 2012.

Birnstiel, T., Fang, M., and Johansen, A. Dust Evolution and the Formation of Planetesimals. *Space Sci. Rev.*, 205(1-4):41–75, 2016.

Blaes, O. M. and Balbus, S. A. Local Shear Instabilities in Weakly Ionized, Weakly Magnetized Disks. *ApJ*, 421:163, 1994.

Blandford, R. D. and Payne, D. G. Hydromagnetic flows from accretion disks and the production of radio jets. *MNRAS*, 199:883–903, 1982.

Blum, J. Dust Evolution in Protoplanetary Discs and the Formation of Planetesimals. What Have We Learned from Laboratory Experiments? *Space Sci. Rev.*, 214(2):52, 2018.

Blum, J. and Wurm, G. The growth mechanisms of macroscopic bodies in protoplanetary disks. *ARA&A*, 46:21–56, 2008.

Blum, J., Gundlach, B., Krause, M., et al. Evidence for the formation of comet 67P/Churyumov-Gerasimenko through gravitational collapse of a bound clump of pebbles. *MNRAS*, 469:S755–S773, 2017.

Boris, J. P. Relativistic plasma simulation-optimization of a hybrid code. *Proceedings of the Fourth Conference on the Numerical Simulation of Plasmas*, pages 3–67, 1970.

Boss, A. P. Evolution of the Solar Nebula. V. Disk Instabilities with Varied Thermodynamics. *ApJ*, 576(1):462–472, 2002.

Boss, A. P. Giant Planet Formation by Disk Instability in Low Mass Disks? *ApJ*, 725(2):L145–L149, 2010.

Bottke, W. F., Durda, D. D., Nesvorný, D., et al. The fossilized size distribution of the main asteroid belt. *Icarus*, 175(1):111–140, 2005.

Brandenburg, A. and Dobler, W. Hydromagnetic turbulence in computer simulations. *Computer Physics Communications*, 147(1-2):471–475, 2002.

Brauer, F., Dullemond, C. P., Johansen, A., et al. Survival of the mm-cm size grain population observed in protoplanetary disks. *A&A*, 469(3):1169–1182, 2007.

Brauer, F., Henning, T., and Dullemond, C. P. Planetesimal formation near the snow line in MRI-driven turbulent protoplanetary disks. *A&A*, 487(1):L1–L4, 2008.

Capelo, H. L., Moláček, J., Lambrechts, M., et al. Observation of aerodynamic instability in the flow of a particle stream in a dilute gas. *A&A*, 622:A151, 2019.

Carballido, A., Fromang, S., and Papaloizou, J. Mid-plane sedimentation of large solid bodies in turbulent protoplanetary discs. *MNRAS*, 373(4):1633–1640, 2006.

Carr, J. S., Tokunaga, A. T., and Najita, J. Hot H_2O Emission and Evidence for Turbulence in the Disk of a Young Star. *ApJ*, 603(1):213–220, 2004.

Carrasco-González, C., Sierra, A., Flock, M., et al. The Radial Distribution of Dust Particles in the HL Tau Disk from ALMA and VLA Observations. *ApJ*, 883(1):71, 2019.

Carrera, D., Johansen, A., and Davies, M. B. How to form planetesimals from mm-sized chondrules and chondrule aggregates. *A&A*, 579:A43, 2015.

Carrera, D., Gorti, U., Johansen, A., and Davies, M. B. Planetesimal Formation by the Streaming Instability in a Photoevaporating Disk. *ApJ*, 839(1):16, 2017.

Carrera, D., Simon, J. B., Li, R., et al. Protoplanetary Disk Rings as Sites for Planetesimal Formation. *ApJ*, submitted.

Chabrier, G. Galactic Stellar and Substellar Initial Mass Function. *PASP*, 115(809):763–795, 2003.

Chambers, J. E. Planetesimal formation by turbulent concentration. *Icarus*, 208(2):505–517, 2010.

Chandrasekhar, S. The Stability of Non-Dissipative Couette Flow in Hydromagnetics. *Proceedings of the National Academy of Science*, 46(2):253–257, 1960.

Chandrasekhar, S. *Hydrodynamic and hydromagnetic stability*. Oxford: Clarendon, 1961.

Chapman, S. and Cowling, T. G. *The mathematical theory of non-uniform gases. an account of the kinetic theory of viscosity, thermal conduction and diffusion in gases*. Cambridge: University Press, 1970.

Chen, K. and Lin, M.-K. How Efficient Is the Streaming Instability in Viscous Protoplanetary Disks? *ApJ*, 891(2):132, 2020.

Chiang, E. Vertical Shearing Instabilities in Radially Shearing Disks: The Dustiest Layers of the Protoplanetary Nebula. *ApJ*, 675(2):1549–1558, 2008.

Ciesla, F. J. and Cuzzi, J. N. The evolution of the water distribution in a viscous protoplanetary disk. *Icarus*, 181(1):178–204, 2006.

Cuzzi, J. N. and Hogan, R. C. Blowing in the wind. I. Velocities of chondrule-sized particles in a turbulent protoplanetary nebula. *Icarus*, 164(1):127–138, 2003.

Cuzzi, J. N. and Zahnle, K. J. Material Enhancement in Protoplanetary Nebulae by Particle Drift through Evaporation Fronts. *ApJ*, 614(1):490–496, 2004.

Cuzzi, J. N., Hogan, R. C., Paque, J. M., and Dobrovolskis, A. R. Size-selective Concentration of Chondrules and Other Small Particles in Protoplanetary Nebula Turbulence. *ApJ*, 546(1): 496–508, 2001.

Cuzzi, J. N., Hogan, R. C., and Shariff, K. Toward Planetesimals: Dense Chondrule Clumps in the Protoplanetary Nebula. *ApJ*, 687(2):1432–1447, 2008.

Cuzzi, J. N., Hogan, R. C., and Bottke, W. F. Towards initial mass functions for asteroids and Kuiper Belt Objects. *Icarus*, 208(2):518–538, 2010.

Davies, M. B., Adams, F. C., Armitage, P., et al. The Long-Term Dynamical Evolution of Planetary Systems. In Beuther, H., Klessen, R. S., Dullemond, C. P., and Henning, T., editors, *Protostars and Planets VI*, page 787, 2014.

Delbo', M., Walsh, K., Bolin, B., et al. Identification of a primordial asteroid family constrains the original planetesimal population. *Science*, 357(6355):1026–1029, 2017.

Delbo', M., Avdellidou, C., and Morbidelli, A. Ancient and primordial collisional families as the main sources of X-type asteroids of the inner main belt. *A&A*, 624:A69, 2019.

Delsanti, A. and Jewitt, D. The Solar System Beyond The Planets. In Blondel, P. and Mason, J. W., editors, *Solar System Update*, page 267, 2006.

Dittrich, K., Klahr, H., and Johansen, A. Gravoturbulent Planetesimal Formation: The Positive Effect of Long-lived Zonal Flows. *ApJ*, 763(2):117, 2013.

Dohnanyi, J. S. Collisional Model of Asteroids and Their Debris. *J. Geophys. Res.*, 74:2531–2554, 1969.

Doppmann, G. W., Najita, J. R., Carr, J. S., and Graham, J. R. Warm H_2O and OH Disk Emission in V1331 Cyg. *ApJ*, 738(1):112, 2011.

Draine, B. T. On the Submillimeter Opacity of Protoplanetary Disks. *ApJ*, 636(2):1114–1120, 2006.

Drążkowska, J. and Alibert, Y. Planetesimal formation starts at the snow line. *A&A*, 608:A92, 2017.

Drążkowska, J. and Dullemond, C. P. Can dust coagulation trigger streaming instability? *A&A*, 572:A78, 2014.

Drążkowska, J., Windmark, F., and Dullemond, C. P. Planetesimal formation via sweep-up growth at the inner edge of dead zones. *A&A*, 556:A37, 2013.

Drążkowska, J., Alibert, Y., and Moore, B. Close-in planetesimal formation by pile-up of drifting pebbles. *A&A*, 594:A105, 2016.

Drążkowska, J., Li, S., Birnstiel, T., et al. Including Dust Coagulation in Hydrodynamic Models of Protoplanetary Disks: Dust Evolution in the Vicinity of a Jupiter-mass Planet. *ApJ*, 885 (1):91, 2019.

Dubrulle, B., Morfill, G., and Sterzik, M. The dust subdisk in the protoplanetary nebula. *Icarus*, 114(2):237–246, 1995.

Dullemond, C. P., Birnstiel, T., Huang, J., et al. The Disk Substructures at High Angular Resolution Project (DSHARP). VI. Dust Trapping in Thin-ringed Protoplanetary Disks. *ApJ*, 869: L46, 2018.

Duquennoy, A. and Mayor, M. Multiplicity among solar-type stars in the solar neighbourhood. II - Distribution of the orbital elements in an unbiased sample. *A&A*, 500:337–376, 1991.

Dzyurkevich, N., Flock, M., Turner, N. J., et al. Trapping solids at the inner edge of the dead zone: 3-D global MHD simulations. *A&A*, 515:A70, 2010.

Elliot, J. L., Kern, S. D., Clancy, K. B., et al. The Deep Ecliptic Survey: A Search for Kuiper Belt Objects and Centaurs. II. Dynamical Classification, the Kuiper Belt Plane, and the Core Population. *AJ*, 129(2):1117–1162, 2005.

Ercolano, B., Jennings, J., Rosotti, G., and Birnstiel, T. X-ray photoevaporation's limited success in the formation of planetesimals by the streaming instability. *MNRAS*, 472(4):4117–4125, 2017.

Eriksson, L. E. J., Johansen, A., and Liu, B. Pebble drift and planetesimal formation in protoplanetary discs with embedded planets. *A&A*, 635:A110, 2020.

Estrada, P. R., Cuzzi, J. N., and Morgan, D. A. Global Modeling of Nebulae with Particle Growth, Drift, and Evaporation Fronts. I. Methodology and Typical Results. *ApJ*, 818(2):200, 2016.

Fedele, D., Carney, M., Hogerheijde, M. R., et al. ALMA unveils rings and gaps in the protoplanetary system HD 169142: signatures of two giant protoplanets. *A&A*, 600:A72, 2017.

Flaherty, K., Hughes, A. M., Simon, J. B., et al. Measuring Turbulent Motion in Planet-forming Disks with ALMA: A Detection around DM Tau and Nondetections around MWC 480 and V4046 Sgr. *ApJ*, 895(2):109, 2020.

Flaherty, K. M., Hughes, A. M., Rosenfeld, K. A., et al. Weak Turbulence in the HD 163296 Protoplanetary Disk Revealed by ALMA CO Observations. *ApJ*, 813(2):99, 2015.

Flaherty, K. M., Hughes, A. M., Rose, S. C., et al. A Three-dimensional View of Turbulence: Constraints on Turbulent Motions in the HD 163296 Protoplanetary Disk Using DCO^+. *ApJ*, 843(2):150, 2017.

Flaherty, K. M., Hughes, A. M., Teague, R., et al. Turbulence in the TW Hya Disk. *ApJ*, 856(2): 117, 2018.

Flock, M., Nelson, R. P., Turner, N. J., et al. Radiation Hydrodynamical Turbulence in Protoplanetary Disks: Numerical Models and Observational Constraints. *ApJ*, 850(2):131, 2017.

Flock, M., Turner, N. J., Nelson, R. P., et al. Gas and Dust Dynamics in Starlight-heated Protoplanetary Disks. *ApJ*, 897(2):155, 2020.

Fraser, W. C., Bannister, M. T., Pike, R. E., et al. All planetesimals born near the Kuiper belt formed as binaries. *Nature Astronomy*, 1:0088, 2017a.

Fraser, W. C., Bannister, M. T., Pike, R. E., et al. Corrigendum: All planetesimals born near the Kuiper belt formed as binaries. *Nature Astronomy*, 1:0138, 2017b.

Fricke, K. Instabilität stationärer Rotation in Sternen. *ZAp*, 68:317, 1968.

Friedrich, J. M., Weisberg, M. K., Ebel, D. S., et al. Chondrule size and related physical properties: A compilation and evaluation of current data across all meteorite groups. *Chemie der Erde / Geochemistry*, 75(4):419–443, 2015.

Fromang, S. and Papaloizou, J. Dust settling in local simulations of turbulent protoplanetary disks. *A&A*, 452(3):751–762, 2006.

Fryxell, B., Olson, K., Ricker, P., et al. FLASH: An Adaptive Mesh Hydrodynamics Code for Modeling Astrophysical Thermonuclear Flashes. *ApJS*, 131(1):273–334, 2000.

Gammie, C. F. Layered Accretion in T Tauri Disks. *ApJ*, 457:355, 1996.

Garaud, P. Growth and Migration of Solids in Evolving Protostellar Disks. I. Methods and Analytical Tests. *ApJ*, 671(2):2091–2114, 2007.

Garaud, P., Meru, F., Galvagni, M., and Olczak, C. From Dust to Planetesimals: An Improved Model for Collisional Growth in Protoplanetary Disks. *ApJ*, 764(2):146, 2013.

Garcia, A. J. L. and Gonzalez, J.-F. Evolution of porous dust grains in protoplanetary discs - I. Growing grains. *MNRAS*, 493(2):1788–1800, 2020a.

Garcia, A. J. L. and Gonzalez, J.-F. Erratum: Evolution of porous dust grains in protoplanetary discs - I. Growing grains. *MNRAS*, 493(4):6119–6119, 2020b.

Gerbig, K., Murray-Clay, R. A., Klahr, H., and Baehr, H. Requirements for Gravitational Collapse in Planetesimal Formation—The Impact of Scales Set by Kelvin-Helmholtz and Nonlinear Streaming Instability. *ApJ*, 895(2):91, 2020.

Gibbons, P. G., Rice, W. K. M., and Mamatsashvili, G. R. Planetesimal formation in self-gravitating discs. *MNRAS*, 426(2):1444–1454, 2012.

Gibbons, P. G., Mamatsashvili, G. R., and Rice, W. K. M. Planetesimal formation in self-gravitating discs - the effects of particle self-gravity and back-reaction. *MNRAS*, 442(1):361–371, 2014.

Gibbons, P. G., Mamatsashvili, G. R., and Rice, W. K. M. Planetesimal formation in self-gravitating discs - dust trapping by vortices. *MNRAS*, 453(4):4232–4243, 2015.

Gladman, B., Marsden, B. G., and Vanlaerhoven, C. Nomenclature in the Outer Solar System. In Barucci, M. A., Boehnhardt, H., Cruikshank, D. P., et al., editors, *The Solar System Beyond Neptune*, page 43, 2008.

Goldreich, P. and Lynden-Bell, D. II. Spiral arms as sheared gravitational instabilities. *MNRAS*, 130:125, 1965.

Goldreich, P. and Schubert, G. Differential Rotation in Stars. *ApJ*, 150:571, 1967.

Goldreich, P. and Ward, W. R. The Formation of Planetesimals. *ApJ*, 183:1051–1062, 1973.

Goldreich, P., Lithwick, Y., and Sari, R. Formation of Kuiper-belt binaries by dynamical friction and three-body encounters. *Nature*, 420(6916):643–646, 2002.

Gole, D. A., Simon, J. B., Li, R., et al. Turbulence Regulates the Rate of Planetesimal Formation via Gravitational Collapse. *ApJ*, submitted.

Gómez, G. C. and Ostriker, E. C. The Effect of the Coriolis Force on Kelvin-Helmholtz-driven Mixing in Protoplanetary Disks. *ApJ*, 630(2):1093–1106, 2005.

Gonzalez, J. F., Laibe, G., and Maddison, S. T. Self-induced dust traps: overcoming planet formation barriers. *MNRAS*, 467(2):1984–1996, 2017a.

Gonzalez, J. F., Laibe, G., and Maddison, S. T. Erratum: Self-induced dust traps: overcoming planet formation barriers. *MNRAS*, 472(1):1162–1162, 2017b.

Greene, T. P., Wilking, B. A., Andre, P., et al. Further Mid-Infrared Study of the rho Ophiuchi Cloud Young Stellar Population: Luminosities and Masses of Pre–Main-Sequence Stars. *ApJ*, 434:614, 1994.

Gressel, O., Turner, N. J., Nelson, R. P., and McNally, C. P. Global Simulations of Protoplanetary Disks With Ohmic Resistivity and Ambipolar Diffusion. *ApJ*, 801(2):84, 2015.

Gressel, O., Ramsey, J. P., Brinch, C., et al. Global Hydromagnetic Simulations of Protoplanetary Disks with Stellar Irradiation and Simplified Thermochemistry. *ApJ*, 896(2):126, 2020.

Grundy, W. M., Noll, K. S., Nimmo, F., et al. Five new and three improved mutual orbits of transneptunian binaries. *Icarus*, 213(2):678–692, 2011.

Grundy, W. M., Noll, K. S., Roe, H. G., et al. Mutual orbit orientations of transneptunian binaries. *Icarus*, 334:62–78, 2019.

Grundy, W. M., Bird, M. K., Britt, D. T., et al. Color, composition, and thermal environment of Kuiper Belt object (486958) Arrokoth. *Science*, 367(6481):aay3705, 2020.

Guilloteau, S., Dutrey, A., Wakelam, V., et al. Chemistry in disks. VIII. The CS molecule as an analytic tracer of turbulence in disks. *A&A*, 548:A70, 2012.

Gundlach, B. and Blum, J. The Stickiness of Micrometer-sized Water-ice Particles. *ApJ*, 798 (1):34, 2015.

Gundlach, B., Schmidt, K. P., Kreuzig, C., et al. The tensile strength of ice and dust aggregates and its dependence on particle properties. *MNRAS*, 479(1):1273–1277, 2018.

Güttler, C., Krause, M., Geretshauser, R. J., et al. The Physics of Protoplanetesimal Dust Agglomerates. IV. Toward a Dynamical Collision Model. *ApJ*, 701(1):130–141, 2009.

Güttler, C., Blum, J., Zsom, A., et al. The outcome of protoplanetary dust growth: pebbles, boulders, or planetesimals?. I. Mapping the zoo of laboratory collision experiments. *A&A*, 513: A56, 2010.

Haghighipour, N. and Boss, A. P. On Gas Drag-Induced Rapid Migration of Solids in a Nonuniform Solar Nebula. *ApJ*, 598(2):1301–1311, 2003.

Haisch, J. Karl E., Lada, E. A., and Lada, C. J. Disk Frequencies and Lifetimes in Young Clusters. *ApJ*, 553(2):L153–L156, 2001.

Harsono, D., Bjerkeli, P., van der Wiel, M. H. D., et al. Evidence for the start of planet formation in a young circumstellar disk. *Nature Astronomy*, 2:646–651, 2018.

Hartlep, T. and Cuzzi, J. N. Cascade Model for Planetesimal Formation by Turbulent Clustering. *ApJ*, 892(2):120, 2020.

Haugbølle, T., Weber, P., Wielandt, D. P., et al. Probing the Protosolar Disk Using Dust Filtering at Gaps in the Early Solar System. *AJ*, 158(2):55, 2019.

Hayashi, C. Structure of the Solar Nebula, Growth and Decay of Magnetic Fields and Effects of Magnetic and Turbulent Viscosities on the Nebula. *Progress of Theoretical Physics Supplement*, 70:35–53, 1981.

Helled, R., Bodenheimer, P., Podolak, M., et al. Giant Planet Formation, Evolution, and Internal Structure. In Beuther, H., Klessen, R. S., Dullemond, C. P., and Henning, T., editors, *Protostars and Planets VI*, page 643, 2014.

Huang, J., Andrews, S. M., Pérez, L. M., et al. The Disk Substructures at High Angular Resolution Project (DSHARP). III. Spiral Structures in the Millimeter Continuum of the Elias 27, IM Lup, and WaOph 6 Disks. *ApJ*, 869(2):L43, 2018.

Huang, P., Li, H., Isella, A., et al. Meso-scale Instability Triggered by Dust Feedback in Dusty Rings: Origin and Observational Implications. *ApJ*, 893(2):89, 2020.

Hughes, A. M., Wilner, D. J., Andrews, S. M., et al. Empirical Constraints on Turbulence in Protoplanetary Accretion Disks. *ApJ*, 727(2):85, 2011.

Hughes, A. M., Duchêne, G., and Matthews, B. C. Debris Disks: Structure, Composition, and Variability. *ARA&A*, 56:541–591, 2018.

Ida, S. and Guillot, T. Formation of dust-rich planetesimals from sublimated pebbles inside of the snow line. *A&A*, 596:L3, 2016.

Ilgner, M. and Nelson, R. P. On the ionisation fraction in protoplanetary disks. I. Comparing different reaction networks. *A&A*, 445(1):205–222, 2006.

Inaba, S. and Barge, P. Dusty Vortices in Protoplanetary Disks. *ApJ*, 649(1):415–427, 2006.

Jacquet, E., Balbus, S., and Latter, H. On linear dust-gas streaming instabilities in protoplanetary discs. *MNRAS*, 415(4):3591–3598, 2011.

Jaupart, E. and Laibe, G. Channels for streaming instability in dusty discs. *MNRAS*, 492(4): 4591–4598, 2020.

Jin, L. Damping of the Shear Instability in Magnetized Disks by Ohmic Diffusion. *ApJ*, 457: 798, 1996.

Johansen, A. and Lambrechts, M. Forming Planets via Pebble Accretion. *Annual Review of Earth and Planetary Sciences*, 45(1):359–387, 2017.

Johansen, A. and Youdin, A. Protoplanetary Disk Turbulence Driven by the Streaming Instability: Nonlinear Saturation and Particle Concentration. *ApJ*, 662(1):627–641, 2007.

Johansen, A., Andersen, A. C., and Brandenburg, A. Simulations of dust-trapping vortices in protoplanetary discs. *A&A*, 417:361–374, 2004.

Johansen, A., Henning, T., and Klahr, H. Dust Sedimentation and Self-sustained Kelvin-Helmholtz Turbulence in Protoplanetary Disk Midplanes. *ApJ*, 643(2):1219–1232, 2006a.

Johansen, A., Klahr, H., and Henning, T. Gravoturbulent Formation of Planetesimals. *ApJ*, 636(2):1121–1134, 2006b.

Johansen, A., Oishi, J. S., Mac Low, M.-M., et al. Rapid planetesimal formation in turbulent circumstellar disks. *Nature*, 448(7157):1022–1025, 2007.

Johansen, A., Youdin, A., and Mac Low, M.-M. Particle Clumping and Planetesimal Formation Depend Strongly on Metallicity. *ApJ*, 704(2):L75–L79, 2009.

Johansen, A., Klahr, H., and Henning, T. High-resolution simulations of planetesimal formation in turbulent protoplanetary discs. *A&A*, 529:A62, 2011.

Johansen, A., Youdin, A. N., and Lithwick, Y. Adding particle collisions to the formation of asteroids and Kuiper belt objects via streaming instabilities. *A&A*, 537:A125, 2012.

Johansen, A., Blum, J., Tanaka, H., et al. The Multifaceted Planetesimal Formation Process. In Beuther, H., Klessen, R. S., Dullemond, C. P., and Henning, T., editors, *Protostars and Planets VI*, page 547, 2014.

Johansen, A., Mac Low, M.-M., Lacerda, P., and Bizzarro, M. Growth of asteroids, planetary embryos, and Kuiper belt objects by chondrule accretion. *Science Advances*, 1:1500109, 2015.

Jutzi, M. and Asphaug, E. The shape and structure of cometary nuclei as a result of low-velocity accretion. *Science*, 348(6241):1355–1358, 2015.

Kataoka, A., Tanaka, H., Okuzumi, S., and Wada, K. Fluffy dust forms icy planetesimals by static compression. *A&A*, 557:L4, 2013.

Kataoka, A., Muto, T., Momose, M., et al. Millimeter-wave Polarization of Protoplanetary Disks due to Dust Scattering. *ApJ*, 809(1):78, 2015.

Kataoka, A., Tsukagoshi, T., Pohl, A., et al. The Evidence of Radio Polarization Induced by the Radiative Grain Alignment and Self-scattering of Dust Grains in a Protoplanetary Disk. *ApJ*, 844(1):L5, 2017.

Kirchschlager, F. and Bertrang, G. H. M. Self-scattering of non-spherical dust grains. The limitations of perfect compact spheres. *A&A*, 638:A116, 2020.

Klahr, H. The Global Baroclinic Instability in Accretion Disks. II. Local Linear Analysis. *ApJ*, 606(2):1070–1082, 2004.

Klahr, H. and Bodenheimer, P. Formation of Giant Planets by Concurrent Accretion of Solids and Gas inside an Anticyclonic Vortex. *ApJ*, 639(1):432–440, 2006.

Klahr, H. and Hubbard, A. Convective Overstability in Radially Stratified Accretion Disks under Thermal Relaxation. *ApJ*, 788(1):21, 2014.

Klahr, H. and Schreiber, A. Turbulence Sets the Length Scale for Planetesimal Formation: Local 2D Simulations of Streaming Instability and Planetesimal Formation. *ApJ*, 901(1):54, 2020.

Klahr, H. H. and Bodenheimer, P. Turbulence in Accretion Disks: Vorticity Generation and Angular Momentum Transport via the Global Baroclinic Instability. *ApJ*, 582(2):869–892, 2003.

Kofman, W., Herique, A., Barbin, Y., et al. Properties of the 67P/Churyumov-Gerasimenko interior revealed by CONSERT radar. *Science*, 349(6247):2.639, 2015.

Kornet, K., Stepinski, T. F., and Różyczka, M. Diversity of planetary systems from evolution of solids in protoplanetary disks. *A&A*, 378:180–191, 2001.

Kothe, S., Blum, J., Weidling, R., and Güttler, C. Free collisions in a microgravity many-particle experiment. III. The collision behavior of sub-millimeter-sized dust aggregates. *Icarus*, 225(1):75–85, 2013.

Kowalik, K., Hanasz, M., Wóltański, D., and Gawryszczak, A. Streaming instability in the quasi-global protoplanetary discs. *MNRAS*, 434(2):1460–1468, 2013.

Krapp, L., Benítez-Llambay, P., Gressel, O., and Pessah, M. E. Streaming Instability for Particle-size Distributions. *ApJ*, 878(2):L30, 2019.

Krapp, L., Youdin, A. N., Kratter, K. M., and Benítez-Llambay, P. Dust Settling Instability in Protoplanetary Discs. *MNRAS*, 2020.

Kratter, K. and Lodato, G. Gravitational Instabilities in Circumstellar Disks. *ARA&A*, 54:271–311, 2016.

Kretke, K. A. and Lin, D. N. C. Grain Retention and Formation of Planetesimals near the Snow Line in MRI-driven Turbulent Protoplanetary Disks. *ApJ*, 664(1):L55–L58, 2007.

Krijt, S., Ormel, C. W., Dominik, C., and Tielens, A. G. G. M. Erosion and the limits to planetesimal growth. *A&A*, 574:A83, 2015.

Krijt, S., Ciesla, F. J., and Bergin, E. A. Tracing Water Vapor and Ice During Dust Growth. *ApJ*, 833(2):285, 2016a.

Krijt, S., Ormel, C. W., Dominik, C., and Tielens, A. G. G. M. A panoptic model for planetesimal formation and pebble delivery. *A&A*, 586:A20, 2016b.

Kroupa, P. On the variation of the initial mass function. *MNRAS*, 322(2):231–246, 2001.

Kunz, M. W. On the linear stability of weakly ionized, magnetized planar shear flows. *MNRAS*, 385(3):1494–1510, 2008.

Lada, C. J. Star formation: from OB associations to protostars. In Peimbert, M. and Jugaku, J., editors, *Star Forming Regions*, volume 115 of *IAU Symposium*, page 1, 1987.

Lada, C. J. and Wilking, B. A. The nature of the embedded population in the rho Ophiuchi dark cloud : mid-infrared observations. *ApJ*, 287:610–621, 1984.

Lambrechts, M., Johansen, A., Capelo, H. L., et al. Spontaneous concentrations of solids through two-way drag forces between gas and sedimenting particles. *A&A*, 591:A133, 2016.

Latter, H. N. On the convective overstability in protoplanetary discs. *MNRAS*, 455(3):2608–2618, 2016.

Latter, H. N. and Balbus, S. The dynamics of inner dead-zone boundaries in protoplanetary discs. *MNRAS*, 424(3):1977–1990, 2012.

Latter, H. N. and Papaloizou, J. Vortices and the saturation of the vertical shear instability in protoplanetary discs. *MNRAS*, 474(3):3110–3124, 2018.

Lesur, G. and Papaloizou, J. C. B. The subcritical baroclinic instability in local accretion disc models. *A&A*, 513:A60, 2010.

Lesur, G., Kunz, M. W., and Fromang, S. Thanatology in protoplanetary discs. The combined influence of Ohmic, Hall, and ambipolar diffusion on dead zones. *A&A*, 566:A56, 2014.

Lesur, G. R. J. and Latter, H. On the survival of zombie vortices in protoplanetary discs. *MNRAS*, 462(4):4549–4554, 2016.

Li, H., Finn, J. M., Lovelace, R. V. E., and Colgate, S. A. Rossby Wave Instability of Thin Accretion Disks. II. Detailed Linear Theory. *ApJ*, 533(2):1023–1034, 2000.

Li, H., Colgate, S. A., Wendroff, B., and Liska, R. Rossby Wave Instability of Thin Accretion Disks. III. Nonlinear Simulations. *ApJ*, 551(2):874–896, 2001.

Li, R., Youdin, A. N., and Simon, J. B. On the Numerical Robustness of the Streaming Instability: Particle Concentration and Gas Dynamics in Protoplanetary Disks. *ApJ*, 862(1):14, 2018.

Li, R., Youdin, A. N., and Simon, J. B. Demographics of Planetesimals Formed by the Streaming Instability. *ApJ*, 885(1):69, 2019.

Li, Z. Y., Banerjee, R., Pudritz, R. E., et al. The Earliest Stages of Star and Planet Formation: Core Collapse, and the Formation of Disks and Outflows. In Beuther, H., Klessen, R. S., Dullemond, C. P., and Henning, T., editors, *Protostars and Planets VI*, page 173, 2014.

Lin, M.-K. Dust settling against hydrodynamic turbulence in protoplanetary discs. *MNRAS*, 485(4):5221–5234, 2019.

Lin, M.-K. and Youdin, A. N. Cooling Requirements for the Vertical Shear Instability in Protoplanetary Disks. *ApJ*, 811(1):17, 2015.

Lin, M.-K. and Youdin, A. N. A Thermodynamic View of Dusty Protoplanetary Disks. *ApJ*, 849 (2):129, 2017.

Lin, Z.-Y. D., Li, Z.-Y., Yang, H., et al. Validating scattering-induced (sub)millimetre disc polarization through the spectral index, wavelength-dependent polarization pattern, and polarization spectrum: the case of HD 163296. *MNRAS*, 496(1):169–181, 2020.

Liu, B., Lambrechts, M., Johansen, A., et al. Pebble-driven planet formation around very low-mass stars and brown dwarfs. *A&A*, 638:A88, 2020.

Liu, H. B. The Anomalously Low (Sub)Millimeter Spectral Indices of Some Protoplanetary Disks May Be Explained By Dust Self-scattering. *ApJ*, 877(2):L22, 2019.

Liu, S.-F., Jin, S., Li, S., et al. New Constraints on Turbulence and Embedded Planet Mass in the HD 163296 Disk from Planet-Disk Hydrodynamic Simulations. *ApJ*, 857(2):87, 2018.

Lorek, S., Lacerda, P., and Blum, J. Local growth of dust- and ice-mixed aggregates as cometary building blocks in the solar nebula. *A&A*, 611:A18, 2018.

Lovelace, R. V. E., Li, H., Colgate, S. A., and Nelson, A. F. Rossby Wave Instability of Keplerian Accretion Disks. *ApJ*, 513(2):805–810, 1999.

Lyra, W. Convective Overstability in Accretion Disks: Three-dimensional Linear Analysis and Nonlinear Saturation. *ApJ*, 789(1):77, 2014.

Lyra, W. and Klahr, H. The baroclinic instability in the context of layered accretion. Self-sustained vortices and their magnetic stability in local compressible unstratified models of protoplanetary disks. *A&A*, 527:A138, 2011.

Lyra, W. and Umurhan, O. M. The Initial Conditions for Planet Formation: Turbulence Driven by Hydrodynamical Instabilities in Disks around Young Stars. *PASP*, 131(1001):072001, 2019.

Lyra, W., Johansen, A., Klahr, H., and Piskunov, N. Embryos grown in the dead zone. Assembling the first protoplanetary cores in low mass self-gravitating circumstellar disks of gas and solids. *A&A*, 491(3):L41–L44, 2008.

Lyra, W., Johansen, A., Klahr, H., and Piskunov, N. Standing on the shoulders of giants. Trojan Earths and vortex trapping in low mass self-gravitating protoplanetary disks of gas and solids. *A&A*, 493(3):1125–1139, 2009a.

Lyra, W., Johansen, A., Zsom, A., et al. Planet formation bursts at the borders of the dead zone in 2D numerical simulations of circumstellar disks. *A&A*, 497(3):869–888, 2009b.

Lyra, W., Youdin, A. N., and Johansen, A. Evolution of MU69 from a binary planetesimal into contact by Kozai-Lidov oscillations and nebular drag. *Icarus*, submitted.

Mac Low, M.-M. and Klessen, R. S. Control of star formation by supersonic turbulence. *Reviews of Modern Physics*, 76(1):125–194, 2004.

Macías, E., Espaillat, C. C., Osorio, M., et al. Characterization of Ring Substructures in the Protoplanetary Disk of HD 169142 from Multiwavelength Atacama Large Millimeter/submillimeter Array Observations. *ApJ*, 881(2):159, 2019.

Malygin, M. G., Klahr, H., Semenov, D., et al. Efficiency of thermal relaxation by radiative processes in protoplanetary discs: constraints on hydrodynamic turbulence. *A&A*, 605:A30, 2017.

Mamajek, E. E. Initial Conditions of Planet Formation: Lifetimes of Primordial Disks. In Usuda, T., Tamura, M., and Ishii, M., editors, *American Institute of Physics Conference Series*, volume 1158, pages 3–10, 2009.

Manara, C. F., Morbidelli, A., and Guillot, T. Why do protoplanetary disks appear not massive enough to form the known exoplanet population? *A&A*, 618:L3, 2018.

Manger, N. and Klahr, H. Vortex formation and survival in protoplanetary discs subject to vertical shear instability. *MNRAS*, 480(2):2125–2136, 2018.

Marcus, P. S., Pei, S., Jiang, C.-H., and Hassanzadeh, P. Three-Dimensional Vortices Generated by Self-Replication in Stably Stratified Rotating Shear Flows. *Phys. Rev. Lett.*, 111(8): 084501, 2013.

Marcus, P. S., Pei, S., Jiang, C.-H., et al. Zombie Vortex Instability. I. A Purely Hydrodynamic Instability to Resurrect the Dead Zones of Protoplanetary Disks. *ApJ*, 808(1):87, 2015.

Marcus, P. S., Pei, S., Jiang, C.-H., and Barranco, J. A. Zombie Vortex Instability. II. Thresholds to Trigger Instability and the Properties of Zombie Turbulence in the Dead Zones of Protoplanetary Disks. *ApJ*, 833(2):148, 2016.

Markiewicz, W. J., Mizuno, H., and Voelk, H. J. Turbulence induced relative velocity between two grains. *A&A*, 242(1):286–289, 1991.

Mathis, J. S., Rumpl, W., and Nordsieck, K. H. The size distribution of interstellar grains. *ApJ*, 217:425–433, 1977.

McKee, C. F. and Ostriker, E. C. Theory of Star Formation. *ARA&A*, 45(1):565–687, 2007.

McKinnon, W. B., Richardson, D. C., Marohnic, J. C., et al. The solar nebula origin of (486958) Arrokoth, a primordial contact binary in the Kuiper Belt. *Science*, 367(6481):eaay6620, 2020.

Meheut, H., Meliani, Z., Varniere, P., and Benz, W. Dust-trapping Rossby vortices in protoplanetary disks. *A&A*, 545:A134, 2012.

Miotello, A., Testi, L., Lodato, G., et al. Grain growth in the envelopes and disks of Class I protostars. *A&A*, 567:A32, 2014.

Morbidelli, A., Bottke, W. F., Nesvorný, D., and Levison, H. F. Asteroids were born big. *Icarus*, 204(2):558–573, 2009.

Mulders, G. D. and Dominik, C. Probing the turbulent mixing strength in protoplanetary disks across the stellar mass range: no significant variations. *A&A*, 539:A9, 2012.

Mulders, G. D., Pascucci, I., and Apai, D. An Increase in the Mass of Planetary Systems around Lower-mass Stars. *ApJ*, 814(2):130, 2015.

Musiolik, G. and Wurm, G. Contacts of Water Ice in Protoplanetary Disks—Laboratory Experiments. *ApJ*, 873(1):58, 2019.

Najita, J. R. and Kenyon, S. J. The mass budget of planet-forming discs: isolating the epoch of planetesimal formation. *MNRAS*, 445(3):3315–3329, 2014.

Najita, J. R., Doppmann, G. W., Carr, J. S., et al. High-Resolution K-Band Spectroscopy of MWC 480 and V1331 Cyg. *ApJ*, 691(1):738–748, 2009.

Nakagawa, Y., Sekiya, M., and Hayashi, C. Settling and growth of dust particles in a laminar phase of a low-mass solar nebula. *Icarus*, 67(3):375–390, 1986.

Nelson, R. P., Gressel, O., and Umurhan, O. M. Linear and non-linear evolution of the vertical shear instability in accretion discs. *MNRAS*, 435(3):2610–2632, 2013.

Nesvorný, D., Youdin, A. N., and Richardson, D. C. Formation of Kuiper Belt Binaries by Gravitational Collapse. *AJ*, 140(3):785–793, 2010.

Nesvorný, D., Brož, M., and Carruba, V. Identification and Dynamical Properties of Asteroid Families. In Michel, P., DeMeo, F. E., and Bottke, W. F., editors, *Asteroids IV*, pages 297–321, 2015.

Nesvorný, D., Li, R., Youdin, A. N., et al. Trans-Neptunian binaries as evidence for planetesimal formation by the streaming instability. *Nature Astronomy*, 3:808–812, 2019.

Noll, K. S., Grundy, W. M., Stephens, D. C., et al. Evidence for two populations of classical transneptunian objects: The strong inclination dependence of classical binaries. *Icarus*, 194 (2):758–768, 2008.

Ohashi, S. and Kataoka, A. Radial Variations in Grain Sizes and Dust Scale Heights in the Protoplanetary Disk around HD 163296 Revealed by ALMA Polarization Observations. *ApJ*, 886(2):103, 2019.

Ohashi, S., Kataoka, A., van der Marel, N., et al. Solving Grain Size Inconsistency between ALMA Polarization and VLA Continuum in the Ophiuchus IRS 48 Protoplanetary Disk. *ApJ*, 900(1):81, 2020.

Okuzumi, S. Electric Charging of Dust Aggregates and its Effect on Dust Coagulation in Protoplanetary Disks. *ApJ*, 698(2):1122–1135, 2009.

Okuzumi, S. Erratum: "Electric Charging of Dust Aggregates and its Effect on Dust Coagulation in Protoplanetary Disks". *ApJ*, 793(2):143, 2014.

Okuzumi, S., Tanaka, H., Kobayashi, H., and Wada, K. Rapid Coagulation of Porous Dust Aggregates outside the Snow Line: A Pathway to Successful Icy Planetesimal Formation. *ApJ*, 752(2):106, 2012.

Ormel, C. W. and Cuzzi, J. N. Closed-form expressions for particle relative velocities induced by turbulence. *A&A*, 466(2):413–420, 2007.

Paardekooper, S. J. and Mellema, G. Dust flow in gas disks in the presence of embedded planets. *A&A*, 453(3):1129–1140, 2006.

Pan, L., Padoan, P., Scalo, J., et al. Turbulent Clustering of Protoplanetary Dust and Planetesimal Formation. *ApJ*, 740(1):6, 2011.

Pätzold, M., Andert, T., Hahn, M., et al. A homogeneous nucleus for comet 67P/Churyumov-Gerasimenko from its gravity field. *Nature*, 530(7588):63–65, 2016.

Pérez, L. M., Carpenter, J. M., Chand ler, C. J., et al. Constraints on the Radial Variation of Grain Growth in the AS 209 Circumstellar Disk. *ApJ*, 760(1):L17, 2012.

Pérez, L. M., Chandler, C. J., Isella, A., et al. Grain Growth in the Circumstellar Disks of the Young Stars CY Tau and DoAr 25. *ApJ*, 813(1):41, 2015.

Pérez, L. M., Carpenter, J. M., Andrews, S. M., et al. Spiral density waves in a young protoplanetary disk. *Science*, 353(6307):1519–1521, 2016.

Perez-Becker, D. and Chiang, E. Surface Layer Accretion in Conventional and Transitional Disks Driven by Far-ultraviolet Ionization. *ApJ*, 735(1):8, 2011.

Petersen, M. R., Julien, K., and Stewart, G. R. Baroclinic Vorticity Production in Protoplanetary Disks. I. Vortex Formation. *ApJ*, 658(2):1236–1251, 2007a.

Petersen, M. R., Stewart, G. R., and Julien, K. Baroclinic Vorticity Production in Protoplanetary Disks. II. Vortex Growth and Longevity. *ApJ*, 658(2):1252–1263, 2007b.

Pfeil, T. and Klahr, H. Mapping the Conditions for Hydrodynamic Instability on Steady-State Accretion Models of Protoplanetary Disks. *ApJ*, 871(2):150, 2019.

Pinilla, P., Benisty, M., and Birnstiel, T. Ring shaped dust accumulation in transition disks. *A&A*, 545:A81, 2012.

Pinte, C., Dent, W. R. F., Ménard, F., et al. Dust and Gas in the Disk of HL Tauri: Surface Density, Dust Settling, and Dust-to-gas Ratio. *ApJ*, 816(1):25, 2016.

Raettig, N., Lyra, W., and Klahr, H. A Parameter Study for Baroclinic Vortex Amplification. *ApJ*, 765(2):115, 2013.

Raettig, N., Klahr, H., and Lyra, W. Particle Trapping and Streaming Instability in Vortices in Protoplanetary Disks. *ApJ*, 804(1):35, 2015.

Raghavan, D., McAlister, H. A., Henry, T. J., et al. A Survey of Stellar Families: Multiplicity of Solar-type Stars. *ApJS*, 190(1):1–42, 2010.

Richard, S., Nelson, R. P., and Umurhan, O. M. Vortex formation in protoplanetary discs induced by the vertical shear instability. *MNRAS*, 456(4):3571–3584, 2016.

Riols, A. and Lesur, G. Dust settling and rings in the outer regions of protoplanetary discs subject to ambipolar diffusion. *A&A*, 617:A117, 2018.

Riols, A., Lesur, G., and Menard, F. Ring formation and dust dynamics in wind-driven protoplanetary discs: global simulations. *A&A*, 639:A95, 2020a.

Riols, A., Roux, B., Latter, H., and Lesur, G. Dust dynamics and vertical settling in gravitoturbulent protoplanetary discs. *MNRAS*, 493(4):4631–4642, 2020b.

Robinson, J. E., Fraser, W. C., Fitzsimmons, A., and Lacerda, P. Investigating Gravitational Collapse of a Pebble Cloud to form Transneptunian Binaries. *A&A*, accepted.

Ros, K. and Johansen, A. Ice condensation as a planet formation mechanism. *A&A*, 552:A137, 2013.

Ros, K., Johansen, A., Riipinen, I., and Schlesinger, D. Effect of nucleation on icy pebble growth in protoplanetary discs. *A&A*, 629:A65, 2019.

Rüdiger, G., Arlt, R., and Shalybkov, D. Hydrodynamic stability in accretion disks under the combined influence of shear and density stratification. *A&A*, 391:781–787, 2002.

Safronov, V. S. On the gravitational instability in flattened systems with axial symmetry and non-uniform rotation. *Annales d'Astrophysique*, 23:979, 1960.

Safronov, V. S. *Evoliutsiia doplanetnogo oblaka.* Moscow: Nauka, 1969.

Saito, E. and Sirono, S.-i. Planetesimal Formation by Sublimation. *ApJ*, 728(1):20, 2011.

Salpeter, E. E. The Luminosity Function and Stellar Evolution. *ApJ*, 121:161, 1955.

Sano, T., Miyama, S. M., Umebayashi, T., and Nakano, T. Magnetorotational Instability in Protoplanetary Disks. II. Ionization State and Unstable Regions. *ApJ*, 543(1):486–501, 2000.

Schaffer, N., Yang, C.-C., and Johansen, A. Streaming instability of multiple particle species in protoplanetary disks. *A&A*, 618:A75, 2018.

Schlichting, H. E. and Sari, R. The Ratio of Retrograde to Prograde Orbits: A Test for Kuiper Belt Binary Formation Theories. *ApJ*, 686(1):741–747, 2008.

Schoonenberg, D. and Ormel, C. W. Planetesimal formation near the snowline: in or out? *A&A*, 602:A21, 2017.

Schoonenberg, D., Ormel, C. W., and Krijt, S. A Lagrangian model for dust evolution in protoplanetary disks: formation of wet and dry planetesimals at different stellar masses. *A&A*, 620:A134, 2018.

Schreiber, A. and Klahr, H. Azimuthal and Vertical Streaming Instability at High Dust-to-gas Ratios and on the Scales of Planetesimal Formation. *ApJ*, 861(1):47, 2018.

Seizinger, A. and Kley, W. Bouncing behavior of microscopic dust aggregates. *A&A*, 551:A65, 2013.

Sekiya, M. Quasi-Equilibrium Density Distributions of Small Dust Aggregations in the Solar Nebula. *Icarus*, 133(2):298–309, 1998.

Sekiya, M. and Ishitsu, N. Shear instabilities in the dust layer of the solar nebula I. The linear analysis of a non-gravitating one-fluid model without the Coriolis and the solar tidal forces. *Earth, Planets, and Space*, 52:517–526, 2000.

Sekiya, M. and Onishi, I. K. Two Key Parameters Controlling Particle Clumping Caused by Streaming Instability in the Dead-zone Dust Layer of a Protoplanetary Disk. *ApJ*, 860(2):140, 2018.

Sellek, A. D., Booth, R. A., and Clarke, C. J. The evolution of dust in discs influenced by external photoevaporation. *MNRAS*, 492(1):1279–1294, 2020.

Shakura, N. I. and Sunyaev, R. A. Black holes in binary systems. Observational appearance. *A&A*, 24:337–355, 1973.

Shariff, K. and Cuzzi, J. N. The Spherically Symmetric Gravitational Collapse of a Clump of Solids in a Gas. *ApJ*, 805(1):42, 2015.

Sheppard, S. S. and Jewitt, D. Extreme Kuiper Belt Object 2001 QG_{298} and the Fraction of Contact Binaries. *AJ*, 127(5):3023–3033, 2004.

Shi, J.-M., Zhu, Z., Stone, J. M., and Chiang, E. Dust dynamics in 2D gravito-turbulent discs. *MNRAS*, 459(1):982–998, 2016.

Simon, J. B., Hughes, A. M., Flaherty, K. M., et al. Signatures of MRI-driven Turbulence in Protoplanetary Disks: Predictions for ALMA Observations. *ApJ*, 808(2):180, 2015a.

Simon, J. B., Lesur, G., Kunz, M. W., and Armitage, P. J. Magnetically driven accretion in protoplanetary discs. *MNRAS*, 454(1):1117–1131, 2015b.

Simon, J. B., Armitage, P. J., Li, R., and Youdin, A. N. The Mass and Size Distribution of Planetesimals Formed by the Streaming Instability. I. The Role of Self-gravity. *ApJ*, 822(1):55, 2016.

Simon, J. B., Armitage, P. J., Youdin, A. N., and Li, R. Evidence for Universality in the Initial Planetesimal Mass Function. *ApJ*, 847(2):L12, 2017.

Simon, J. I., Cuzzi, J. N., McCain, K. A., et al. Particle size distributions in chondritic meteorites: Evidence for pre-planetesimal histories. *Earth and Planetary Science Letters*, 494:69–82, 2018a.

Simon, J. I., Cuzzi, J. N., McCain, K. A., et al. Corrigendum to "Particle size distributions in chondritic meteorites: Evidence for pre-planetesimal histories". *Earth and Planetary Science Letters*, 502:293–295, 2018b.

Singer, K. N., McKinnon, W. B., Gladman, B., et al. Impact craters on Pluto and Charon indicate a deficit of small Kuiper belt objects. *Science*, 363(6430):955–959, 2019.

Squire, J. and Hopkins, P. F. Resonant Drag Instability of Grains Streaming in Fluids. *ApJ*, 856(1):L15, 2018a.

Squire, J. and Hopkins, P. F. Resonant drag instabilities in protoplanetary discs: the streaming instability and new, faster growing instabilities. *MNRAS*, 477(4):5011–5040, 2018b.

Squire, J. and Hopkins, P. F. Physical models of streaming instabilities in protoplanetary discs. *MNRAS*, 498(1):1239–1251, 2020.

Squires, K. D. and Eaton, J. K. Particle response and turbulence modification in isotropic turbulence. *Physics of Fluids A*, 2(7):1191–1203, 1990.

Squires, K. D. and Eaton, J. K. Preferential concentration of particles by turbulence. *Physics of Fluids A*, 3(5):1169–1178, 1991.

Stammler, S. M., Drążkowska, J., Birnstiel, T., et al. The DSHARP Rings: Evidence of Ongoing Planetesimal Formation? *ApJ*, 884(1):L5, 2019.

Steinpilz, T., Joeris, K., Jungmann, F., et al. Electrical charging overcomes the bouncing barrier in planet formation. *Nature Physics*, 16(2):225–229, 2019.

Stepinski, T. F. and Valageas, P. Global evolution of solid matter in turbulent protoplanetary disks. I. Aerodynamics of solid particles. *A&A*, 309:301–312, 1996.

Stern, S. A., Weaver, H. A., Spencer, J. R., et al. Initial results from the New Horizons exploration of 2014 MU_{69}, a small Kuiper Belt object. *Science*, 364(6441):eaaw9771, 2019.

Stevenson, D. J. and Lunine, J. I. Rapid formation of Jupiter by diffusive redistribution of water vapor in the solar nebula. *Icarus*, 75(1):146–155, 1988.

Stoll, M. H. R. and Kley, W. Vertical shear instability in accretion disc models with radiation transport. *A&A*, 572:A77, 2014.

Stoll, M. H. R. and Kley, W. Particle dynamics in discs with turbulence generated by the vertical shear instability. *A&A*, 594:A57, 2016.

Stoll, M. H. R., Kley, W., and Picogna, G. Anisotropic hydrodynamic turbulence in accretion disks. *A&A*, 599:L6, 2017.

Takeuchi, T. and Lin, D. N. C. Radial Flow of Dust Particles in Accretion Disks. *ApJ*, 581(2): 1344–1355, 2002.

Takeuchi, T., Clarke, C. J., and Lin, D. N. C. The Differential Lifetimes of Protostellar Gas and Dust Disks. *ApJ*, 627(1):286–292, 2005.

Tanga, P., Babiano, A., Dubrulle, B., and Provenzale, A. Forming Planetesimals in Vortices. *Icarus*, 121(1):158–170, 1996.

Tapia, C., Lizano, S., Sierra, A., et al. Exploring the Grain Properties in the Disk of HL Tau with an Evolutionary Model. *ApJ*, 887(2):244, 2019.

Tassoul, J.-L. *Theory of rotating stars*. Princeton: Princeton University Press, 1978.

Tazzari, M., Testi, L., Ercolano, B., et al. Multiwavelength analysis for interferometric (sub-)mm observations of protoplanetary disks. Radial constraints on the dust properties and the disk structure. *A&A*, 588:A53, 2016.

Teague, R., Guilloteau, S., Semenov, D., et al. Measuring turbulence in TW Hydrae with ALMA: methods and limitations. *A&A*, 592:A49, 2016.

Teague, R., Henning, T., Guilloteau, S., et al. Temperature, Mass, and Turbulence: A Spatially Resolved Multiband Non-LTE Analysis of CS in TW Hya. *ApJ*, 864(2):133, 2018.

Testi, L., Birnstiel, T., Ricci, L., et al. Dust Evolution in Protoplanetary Disks. In Beuther, H., Klessen, R. S., Dullemond, C. P., and Henning, T., editors, *Protostars and Planets VI*, page 339, 2014.

Thirouin, A. and Sheppard, S. S. Light Curves and Rotational Properties of the Pristine Cold Classical Kuiper Belt Objects. *AJ*, 157(6):228, 2019.

Thomas, P. C., Binzel, R. P., Gaffey, M. J., et al. Impact excavation on asteroid 4 Vesta: Hubble Space Telescope results. *Science*, 277:1492–1495, 1997.

Throop, H. B. and Bally, J. Can Photoevaporation Trigger Planetesimal Formation? *ApJ*, 623 (2):L149–L152, 2005.

Tilley, D. A., Balsara, D. S., Brittain, S. D., and Rettig, T. Dust settling in magnetorotationally-driven turbulent discs - II. The pervasiveness of the streaming instability and its consequences. *MNRAS*, 403(1):211–228, 2010.

Toomre, A. On the gravitational stability of a disk of stars. *ApJ*, 139:1217–1238, 1964.

Turner, N. J., Fromang, S., Gammie, C., et al. Transport and Accretion in Planet-Forming Disks. In Beuther, H., Klessen, R. S., Dullemond, C. P., and Henning, T., editors, *Protostars and Planets VI*, page 411, 2014.

Umurhan, O. M., Nelson, R. P., and Gressel, O. Linear analysis of the vertical shear instability: outstanding issues and improved solutions. *A&A*, 586:A33, 2016a.

Umurhan, O. M., Shariff, K., and Cuzzi, J. N. Critical Layers and Protoplanetary Disk Turbulence. *ApJ*, 830(2):95, 2016b.

Umurhan, O. M., Estrada, P. R., and Cuzzi, J. N. Streaming Instability in Turbulent Protoplanetary Disks. *ApJ*, 895(1):4, 2020.

Urpin, V. A comparison study of the vertical and magnetic shear instabilities in accretion discs. *A&A*, 404:397–403, 2003.

Urpin, V. and Brandenburg, A. Magnetic and vertical shear instabilities in accretion discs. *MNRAS*, 294(3):399–406, 1998.

Velikhov, E. Stability of an ideally conducting liquid flowing between cylinders rotating in a magnetic field. *Journal of Experimental and Theoretical Physics*, 36(9):995–998, 1959.

Wada, K., Tanaka, H., Suyama, T., et al. Collisional Growth Conditions for Dust Aggregates. *ApJ*, 702(2):1490–1501, 2009.

Wada, K., Tanaka, H., Suyama, T., et al. The Rebound Condition of Dust Aggregates Revealed by Numerical Simulation of Their Collisions. *ApJ*, 737(1):36, 2011.

Wahlberg Jansson, K. and Johansen, A. Formation of pebble-pile planetesimals. *A&A*, 570:A47, 2014.

Wahlberg Jansson, K. and Johansen, A. Radially resolved simulations of collapsing pebble clouds in protoplanetary discs. *MNRAS*, 469:S149–S157, 2017.

Wang, L. P. and Maxey, M. R. Settling velocity and concentration distribution of heavy particles in homogeneous isotropic turbulence. *Journal of Fluid Mechanics*, 256:27–68, 1993.

Wardle, M. The Balbus-Hawley instability in weakly ionized discs. *MNRAS*, 307(4):849–856, 1999.

Weber, P., Benítez-Llambay, P., Gressel, O., et al. Characterizing the Variable Dust Permeability of Planet-induced Gaps. *ApJ*, 854(2):153, 2018.

Weidenschilling, S. J. Aerodynamics of solid bodies in the solar nebula. *MNRAS*, 180:57–70, 1977a.

Weidenschilling, S. J. The Distribution of Mass in the Planetary System and Solar Nebula. *Ap&SS*, 51(1):153–158, 1977b.

Weidenschilling, S. J. Dust to planetesimals: Settling and coagulation in the solar nebula. *Icarus*, 44(1):172–189, 1980.

Weidenschilling, S. J. and Cuzzi, J. N. Formation of Planetesimals in the Solar Nebula. In Levy, E. H. and Lunine, J. I., editors, *Protostars and Planets III*, page 1031, 1993.

Weidling, R. and Blum, J. Free collisions in a microgravity many-particle experiment. IV. - Three-dimensional analysis of collision properties. *Icarus*, 253:31–39, 2015.

Weidling, R., Güttler, C., Blum, J., and Brauer, F. The Physics of Protoplanetesimal Dust Agglomerates. III. Compaction in Multiple Collisions. *ApJ*, 696(2):2036–2043, 2009.

Weidling, R., Güttler, C., and Blum, J. Free collisions in a microgravity many-particle experiment. I. Dust aggregate sticking at low velocities. *Icarus*, 218(1):688–700, 2012.

Whipple, F. L. On certain aerodynamic processes for asteroids and comets. In Elvius, A., editor, *From Plasma to Planet*, page 211, 1972.

Williams, D. R. and Wetherill, G. W. Size Distribution of Collisionally Evolved Asteroidal Populations: Analytical Solution for Self-Similar Collision Cascades. *Icarus*, 107(1):117–128, 1994.

Windmark, F., Birnstiel, T., Güttler, C., et al. Planetesimal formation by sweep-up: how the bouncing barrier can be beneficial to growth. *A&A*, 540:A73, 2012a.

Windmark, F., Birnstiel, T., Ormel, C. W., and Dullemond, C. P. Breaking through: The effects of a velocity distribution on barriers to dust growth. *A&A*, 544:L16, 2012b.

Windmark, F., Birnstiel, T., Ormel, C. W., and Dullemond, C. P. Breaking through: the effects of a velocity distribution on barriers to dust growth (Corrigendum). *A&A*, 548:C1, 2012c.

Winn, J. N. Planet Occurrence: Doppler and Transit Surveys. In Deeg, H. J. and Belmonte, J. A., editors, *Handbook of Exoplanets*, page 195, 2018.

Xu, Z., Bai, X.-N., and Murray-Clay, R. A. Pebble Accretion in Turbulent Protoplanetary Disks. *ApJ*, 847(1):52, 2017.

Yang, C.-C. and Johansen, A. On the Feeding Zone of Planetesimal Formation by the Streaming Instability. *ApJ*, 792(2):86, 2014.

Yang, C. C., Johansen, A., and Carrera, D. Concentrating small particles in protoplanetary disks through the streaming instability. *A&A*, 606:A80, 2017.

Yang, C.-C., Mac Low, M.-M., and Johansen, A. Diffusion and Concentration of Solids in the Dead Zone of a Protoplanetary Disk. *ApJ*, 868(1):27, 2018.

Yang, H. and Li, Z.-Y. The Effects of Dust Optical Properties on the Scattering-induced Disk Polarization by Millimeter-sized Grains. *ApJ*, 889(1):15, 2020.

Yoshimatsu, R., Araújo, N. A., Wurm, G., et al. Self-charging of identical grains in the absence of an external field. *Scientific Reports*, 7:39996, 2017.

Youdin, A. and Johansen, A. Protoplanetary Disk Turbulence Driven by the Streaming Instability: Linear Evolution and Numerical Methods. *ApJ*, 662(1):613–626, 2007.

Youdin, A. N. and Chiang, E. I. Particle Pileups and Planetesimal Formation. *ApJ*, 601(2): 1109–1119, 2004.

Youdin, A. N. and Goodman, J. Streaming Instabilities in Protoplanetary Disks. *ApJ*, 620(1): 459–469, 2005.

Youdin, A. N. and Lithwick, Y. Particle stirring in turbulent gas disks: Including orbital oscillations. *Icarus*, 192(2):588–604, 2007.

Youdin, A. N. and Shu, F. H. Planetesimal Formation by Gravitational Instability. *ApJ*, 580(1): 494–505, 2002.

Zhu, Z. and Stone, J. M. Dust Trapping by Vortices in Transitional Disks: Evidence for Non-ideal Magnetohydrodynamic Effects in Protoplanetary Disks. *ApJ*, 795(1):53, 2014.

Zhu, Z. and Yang, C.-C. Streaming Instability with Multiple Dust Species: I. Favourable Conditions for the Linear Growth. *MNRAS*, submitted.

Zhu, Z., Nelson, R. P., Dong, R., et al. Dust Filtration by Planet-induced Gap Edges: Implications for Transitional Disks. *ApJ*, 755(1):6, 2012.

Zhu, Z., Stone, J. M., Rafikov, R. R., and Bai, X.-n. Particle Concentration at Planet-induced Gap Edges and Vortices. I. Inviscid Three-dimensional Hydro Disks. *ApJ*, 785(2):122, 2014.

Zhu, Z., Stone, J. M., and Bai, X.-N. Dust Transport in MRI Turbulent Disks: Ideal and Non-Ideal MHD With Ambipolar Diffusion. *ApJ*, 801(2):81, 2015.

Zhu, Z., Zhang, S., Jiang, Y.-F., et al. One Solution to the Mass Budget Problem for Planet Formation: Optically Thick Disks with Dust Scattering. *ApJ*, 877(2):L18, 2019.

Zhuravlev, V. V. On the nature of the resonant drag instability of dust streaming in protoplanetary disc. *MNRAS*, 489(3):3850–3869, 2019.

Zhuravlev, V. V. The resonant drag instability of dust streaming in turbulent protoplanetary disc. *MNRAS*, 494(1):1395–1410, 2020.

Zsom, A., Ormel, C. W., Güttler, C., et al. The outcome of protoplanetary dust growth: pebbles, boulders, or planetesimals? II. Introducing the bouncing barrier. *A&A*, 513:A57, 2010.

A
Gas disk model

Here, I describe the model of the gas in protoplanetary disks that is used in Chapters 2, 3, and 4 as well as in SJB20.

The temperature profile is adopted from the minimum mass solar nebula model (Hayashi 1981). It is based on the assumption that the disk acts as a black body with no internal or external heating mechanisms other than the irradiation from the central star, the Sun. Under these conditions, the luminosity absorbed by the disk, $L_{\rm abs} = \pi r_{\rm outer}^2 F_\odot$, is equal to the luminosity emitted by it, $L_{\rm emi} = 4\pi r_{\rm outer}^2 \sigma T^4$. Here, $F_\odot = L_\odot/(4\pi r^2)$ is the Solar flux density, $L_\odot$ the Solar luminosity, r the radial distance to the Sun, $r_{\rm outer}$ the radial distance between outer disk edge and Sun, σ the Stefan-Boltzmann constant, and T the temperature. Thus, the temperature is given by

$$T = \left(\frac{L_\odot}{16\pi\sigma r^2}\right)^{1/4} = 280\ \mathrm{K}\ \left(\frac{r}{1\ \mathrm{au}}\right)^{-1/2}. \tag{A.1}$$

The steepness of this temperature profile is consistent with observations (Andrews and Williams 2005). The temperature does not vary with height. The equation of state is assumed to be isothermal, $P = c_{\rm s}^2 \rho_{\rm g}$, where P is the pressure, $c_{\rm s} = \sqrt{RT/\mu} \propto r^{-1/4}$ the sound speed, R the ideal gas constant, $\mu = 2.33$ the mean molecular weight, and $\rho_{\rm g}$ the density.

The density in the disk mid-plane can be expressed as

$$\rho_{\rm g}(z=0) = 10^{-9}\ \mathrm{g\,cm^{-3}}\ \left(\frac{r}{1\ \mathrm{au}}\right)^{-9/4}, \tag{A.2}$$

where z is the height above or below the mid-plane. The gas is in vertical hydrostatic equilibrium. That is, the stellar gravitational potential

$$\Phi_{\rm S} = -\frac{GM_{\rm S}}{\sqrt{r^2+z^2}}, \tag{A.3}$$

where G is the gravitational constant and $M_{\rm S} = 1\ M_\odot$ the stellar mass, is balanced by a density

profile. This profile can be calculated by considering the vertical component of the momentum equation,

$$\begin{aligned} \frac{1}{\rho_\mathrm{g}}\frac{\partial P}{\partial z} &= -\frac{\partial \Phi_\mathrm{S}}{\partial z} \\ \Leftrightarrow \frac{c_\mathrm{s}^2}{\rho_\mathrm{g}}\frac{\partial \rho_\mathrm{g}}{\partial z} &= -\frac{GM_\mathrm{S} z}{\left(r^2+z^2\right)^{3/2}} \\ \Leftrightarrow \int_{\rho_\mathrm{g}(z=0)}^{\rho_\mathrm{g}(z)} \frac{1}{\rho'_\mathrm{g}}\,\mathrm{d}\rho'_\mathrm{g} &= -\frac{GM_\mathrm{S}}{c_\mathrm{s}^2}\int_0^z \frac{z'}{\left(r^2+z'^2\right)^{3/2}}\,\mathrm{d}z', \end{aligned} \tag{A.4}$$

which results in

$$\rho_\mathrm{g} = \rho_\mathrm{g}(z=0)\exp\left[-\frac{GM_\mathrm{S}}{c_\mathrm{s}^2}\left(\frac{1}{r}-\frac{1}{\sqrt{r^2+z^2}}\right)\right]. \tag{A.5}$$

The surface density can be computed by numerically integrating the above equation,

$$\Sigma_\mathrm{g} = \int_{z\to-\infty}^{z\to\infty} \rho_\mathrm{g}\,\mathrm{d}z = 1.26\times10^3\ \mathrm{g\,cm^{-2}}\left(\frac{r}{1\ \mathrm{au}}\right)^{-1}. \tag{A.6}$$

Observed surface density profiles are comparably steep (Andrews et al. 2009, 2010), while the minimum mass solar nebula profile is shallower. The latter is constructed by augmenting the amount of hydrogen and helium in the Solar System planets until their composition matches the Solar composition and then spreading the enhanced mass of every planet uniformly over an annulus centred on its orbit (Weidenschilling 1977b; Hayashi 1981).

The gas scale height H_g is defined by $\rho_\mathrm{g}(z=0)/e = \rho_\mathrm{g}(z=H_\mathrm{g})$, which yields

$$H_\mathrm{g} = \sqrt{\frac{c_\mathrm{s}^2 r^3(2GM_\mathrm{S}-c_\mathrm{s}^2 r)}{(c_\mathrm{s}^2 r - GM_\mathrm{S})^2}} = 0.047\ \mathrm{au}\left(\frac{r}{1\ \mathrm{au}}\right)^{5/4}. \tag{A.7}$$

B
Symbols

In the tables below, the symbols, sub- and superscripts, and constants used in this thesis are listed and explained:

Table B.1: Symbols

Symbol	Meaning	Definition
a (Chapter 2, SJB20)	dust size	Chapter 2, Eq. 2.13; SJB20, Table 1
$\boldsymbol{a}$ (SJB20, see also Table B.2)	acceleration	
$\dot{a}$	dust growth rate	Chapter 2, Eq. 2.29
a_{boun}	threshold dust size for bouncing	Chapter 2, Eq. 2.14
a_{drift}	threshold dust size for radial drift	Chapter 2, Eqs. 2.30, 2.31
a_{frag}	threshold dust size for fragmentation	Chapter 2, Eq. 2.16
A_n	coefficient for calculation of acceleration in Leapfrog algorithm	SJB20, Eq. A.4
α (Chapters 2, 3, 4)	dimensionless parameter quantifying turbulence and angular momentum transport (Shakura and Sunyaev 1973)	
α (SYJ17)	exponent of power-law part of planetesimal initial mass function	Table 2
α (SJB20)	angle for calculation of position and velocity in Leapfrog algorithm	Eq. A.12

Symbol	Meaning	Definition
$b_{\max}$	maximum impact parameter for sink particle collisions	SYJ17, Eq. 15
B_n	coefficient for calculation of acceleration in Leapfrog algorithm	SJB20, Eq. A.5
β (Chapter 2)	dust opacity spectral index	
β (SYJ17)	exponent of exponential cutoff of planetesimal initial mass function	Table 2
c_{s}	sound speed	$c_{\mathrm{s}} = \sqrt{RT/\mu}$; SYJ17, Eq. 11
e_{kin} (see also Table B.2)	specific kinetic energy	$e_{\mathrm{kin}} = \Omega^2 r^2 = l^2/r^2$
η	dissipation scale	
f_{d}, f_{g}	ratio of dust, gas density to total density of gas and dust	$f_{\mathrm{d}} = \rho_{\mathrm{d}}/\rho_{\mathrm{tot}}$, $f_{\mathrm{g}} = \rho_{\mathrm{g}}/\rho_{\mathrm{tot}}$
$\boldsymbol{F}_{\mathrm{drag}}$	drag force	
$F_\odot$	Solar flux density	$F_\odot = L_\odot/(4\pi r^2)$
γ, Γ (Chapter 3, SYJ17)	dimensionless self-gravity parameter	Chapter 3, Eqs. 3.30, 3.35; SYJ17: $\gamma = 1/\pi$, Eqs. 3, 4
γ (Chapter 4, SJB20)	adiabatic index	
H_{d}	dust scale height	Chapter 4, Eqs. 4.4, 4.5
H_{g}	gas scale height	SYJ17: $H_{\mathrm{g}} = c_{\mathrm{s}}/\Omega_{\mathrm{K}}$, Eq. 12; SJB20, Eq. 9; Appendix A, Eq. A.7
$(H_{\mathrm{d}}/H_{\mathrm{g}})_{\mathrm{init}}$	initial dust-to-gas scale height ratio	SJB20, Table 1
i	imaginary unit	
k (k_x, k_z)	wave number (in radial, vertical dimension)	$k = \sqrt{k_x^2 + k_z^2}$
K	polytropic constant	$K = RT\rho_{\mathrm{g}}^{1-\gamma}/\mu$
κ	epicyclic frequency	Chapter 4, Eq. 4.7, $\kappa = \Omega_{\mathrm{K}}$
κ_λ	dust opacity	$\kappa_\lambda \propto \lambda^{-\beta}$
l	specific angular momentum	$l = \Omega^2 r$
L (Chapter 2)	injection scale	
L (SYJ17, SJB20; see also Table B.2)	simulation domain size	SYJ17, Table 1; SJB20, Table 1
L_{abs}, L_{emi}	absorbed, emitted luminosity of protoplanetary disk	$L_{\mathrm{abs}} = \pi r_{\mathrm{outer}}^2 F_\odot$, $L_{\mathrm{emi}} = 4\pi r_{\mathrm{outer}}^2 \sigma T^4$
λ	wavelength	
$\lambda_{\mathrm{g,mfp}}$	gas mean free path length	$\lambda_{\mathrm{g,mfp}} = 1/(\sigma_{\mathrm{g}} n_{\mathrm{g}}) = \mu m_{\mathrm{H}}/(\sigma_{\mathrm{g}}\rho_{\mathrm{g}})$

Symbol	Meaning	Definition
λ_{G}	threshold wavelength for linear gravitational instability	Chapter 3, Eq. 3.38
m, M (Chapter 3, SYJ17; see also Table B.2)	planetesimal / sink particle mass	$[M] = \rho_{\mathrm{g},0} H_{\mathrm{g}}^3 = \pi\gamma\, H_{\mathrm{g}}^3 P_{\mathrm{K}}^{-2}$; Chapter 3, Eq. 3.34; SYJ17, Eq. 14, Table 3
m_{c}	dust clump mass	
m_{d}	dust (particle) mass	SJB20, Eqs. 14, 15
M (SJB20)	point mass	$M = 1\, M_\odot$
$\langle M \rangle$	mean planetesimal / sink particle mass	SYJ17, Table 3
M_{char}	characteristic planetesimal mass	Chapter 3, Eqs. 3.33, 3.36
$M_{\mathrm{g,tot}}$	total gas mass	SJB20, Eq. 10
M_{G}	gravitational mass (Abod et al. 2019)	Chapter 3, Eqs. 3.37, 3.39
M_{min}, M_{max}	minimum, maximum planetesimal / sink particle mass	SYJ17, Table 3
M_{pow}, M_{exp}	characteristic mass of power-law part, exponential cutoff of planetesimal initial mass function	SYJ17, Eq. 18, Table 2
M_{S}	stellar mass	SJB20, Appendix A: $M_{\mathrm{S}} = 1\, M_\odot$
$\mathcal{M}$ (see also Table B.2)	Mach number	
μ	mean molecular weight	$\mu = 2.33$
n (see also Table B.2)	number density	$\mathrm{d}n_{\mathrm{d}}/\mathrm{d}a \propto a^{-q}$
N	planetesimal / sink particle number	Chapter 3, Eqs. 3.31, 3.32; SYJ17, Eq. 20
N_{d}	dust particle number	
N_{f}	filament number	SYJ17, Table 2
N_{tot}	total number of planetesimals / sink particles	SYJ17, Table 3
N_{x}, N_{y}, N_{z}	number of grid cells in the x-,y-,z-dimension	SYJ17, Table 1
$N_>(M)$, $N_>(R)$	number of planetesimals / sink particles with masses, radii greater than M, R	Chapter 3, Eq. 3.29; SYJ17, Eqs. 16, 17, 19, 21
$\mathcal{N}_r, \mathcal{N}_z$	Brunt-Väisälä frequency of oscillations caused by buoyancy in the radial, vertical dimension	Chapter 4, Eqs. 4.15, 4.20

Symbol	Meaning	Definition
$\nu_{\mathrm{g,mol}}$	molecular gas viscosity	Chapter 2, Eq. 2.5
ν_{turb} (see also Table B.2)	turbulent viscosity	Chapter 2, Eqs. 2.6, 2.7, 2.8
ω	wave frequency	
Ω	orbital frequency	
Ω_{K}	Keplerian orbital frequency	$\Omega_{\mathrm{K}} = 2\pi/P_{\mathrm{K}} = v_{\mathrm{K}}/r$; SYJ17, Eq. 10
p	power-law exponent of radial density profile	
p_{g}	gas pressure	$p_{\mathrm{g}} = c_{\mathrm{s}}^2 \rho_{\mathrm{g}}$
p_{tot}	total momentum of gas and dust	
$\Delta \boldsymbol{p}_{\mathrm{d,drag}}$	change in dust momentum owing to drag exerted by gas	$\Delta \boldsymbol{p}_{\mathrm{d,drag}} = m_{\mathrm{d}} \boldsymbol{v}_{\mathrm{d,drag}}$
P (see also Table B.2)	gas pressure	SJB20, Eqs. 3, 4; Appendix A: $P = c_{\mathrm{s}}^2 \rho_{\mathrm{g}}$
P_{K}	Keplerian orbital period	SYJ17, Eq. 9
$P_{\mathrm{K},0}$	Keplerian orbital period at initial position of particle	
Π	dimensionless pressure gradient parameter (Bai and Stone 2010b)	Chapter 2, Eqs. 2.19, 2.20; SYJ17, Eq. 2; SJB20, Eqs. 12, 13
ϕ	azimuthal coordinate	
$\hat{\phi}$	unit vector in azimuthal direction	
Φ_{S}	stellar gravitational potential	$\Phi_{\mathrm{S}} = -GM_{\mathrm{S}}/\sqrt{r^2 + z^2}$
q (Chapter 2)	power-law exponent of dust size distribution	
q (Chapter 4)	power-law exponent of radial temperature profile	
Q	dimensionless Toomre parameter for gravitational instability (Toomre 1964)	Chapter 4, Eq. 4.6
r (Chapters 2, 3, 4, SJB20, Appendix A; see also Table B.2)	radial coordinate	
r, R (Chapter 3, SYJ17; see also Table B.2)	planetesimal / sink particle radius	
$\hat{r}$	unit vector in radial direction	
r_{c}	dust clump radius	Chapter 3, Eq. 3.27

Symbol	Meaning	Definition
r_{cyl}, r_{Car}	radial coordinate in cylindrical, Cartesian geometry	
r_{S}	radial distance between dust clump and star	
r_{H}	Hill radius	Chapter 3, Eq. 3.25
r_{outer}	radial distance between outer protoplanetary disk edge and star	
r_0	radial distance between centre of protoplanetary disk region and star in shearing box approximation	
Δr_{d} (Δr_{sim}, Δr_{ana})	(simulated, analytic) radial displacement of dust particle relative to initial position	SJB20, Eq. B.7
R (SYJ17)	orbital distance	
R_{exp}	radius scale of exponential cutoff of planetesimal initial mass function	
Re	Reynolds number	Chapter 2, Eq. 2.4
Ri	Richardson number	Chapter 4, Eq. 4.21
ρ (see also Table B.2)	density	SYJ17, Eqs. 1, 8, 13; SJB20, Eqs. 6, 7; Appendix A, Eqs. A.2, A.5
ρ_{c}	dust clump density	
$\rho_{\mathrm{p,thres}}$	threshold density for sink particle creation	$\rho_{\mathrm{p,thres}} = 200\,\rho_{\mathrm{g},0}$
ρ_{R} (see also Table B.2)	Roche density	Chapter 3, Eq. 3.26; SYJ17, Eq. 5; SJB20, Eq. 17
ρ_{s}	solid density	$\rho_{\mathrm{s}} = 1\ \mathrm{g\,cm^{-3}}$
ρ_{tot}	total density of gas and dust	$\rho_{\mathrm{tot}} = \rho_{\mathrm{g}} + \rho_{\mathrm{d}}$
s	specific gas entropy	$s \propto \ln(P/\rho_{\mathrm{g}}^{\gamma}) \propto \ln(T\rho_{\mathrm{g}}^{1-\gamma})$
St	Stokes number	$\mathrm{St} \equiv \tau_{\mathrm{stop}} = \Omega_{\mathrm{K}} t_{\mathrm{stop}}$; Chapter 2, Eq. 2.32
$\mathrm{St}_{\mathrm{boun}}$	threshold Stokes number for bouncing	Chapter 2, Eq. 2.12
$\mathrm{St}_{\mathrm{drift}}$	threshold Stokes number for radial drift	Chapter 2, Eq. 2.33
$\mathrm{St}_{\mathrm{frag}}$	threshold Stokes number for fragmentation	$\mathrm{St}_{\mathrm{frag}} = \Delta v_{\mathrm{frag}}^2/(2\mathcal{M}_{\mathrm{g}}^2 c_{\mathrm{s}}^2)$; Chapter 2, Eq. 2.15

Symbol	Meaning	Definition
$\mathrm{St}_{\mathrm{turb}}$	threshold Stokes number for dust being stirred by gas turbulence	Chapter 2, Eq. 2.9
σ_{d}	dust cross section	
$\sigma_{\mathrm{d,coll}}$	dust collision cross section	$\sigma_{\mathrm{d}} = 4\pi a^2$
σ_{g}	molecular collision cross section	$\sigma_{\mathrm{g}} = 2 \times 10^{-15}$ cm^2 (Chapman and Cowling 1970)
Σ (see also Table B.2)	surface density	SYJ17, Eq. 7; SJB20, Eq. 8; Appendix A, Eq. A.6
t	time	
$t_{\mathrm{d,init}}$	time of dust initialisation	SJB20, Table 1
t_{end}	time of simulation end	SJB20, Table 1
t_{f}	friction/stopping time	
t_{stop} (see also Table B.2)	stopping/friction time	Chapter 2, Eq. 2.2; SJB20: $t_{\mathrm{stop}} \equiv t_{\mathrm{d,stop}}$, Eq. B.1; $t_{\mathrm{g,stop}} = \rho_{\mathrm{g}}/\rho_{\mathrm{d}}\, t_{\mathrm{d,stop}}$
T (see also Table B.2)	temperature	SJB20, Eq. 5; Appendix A, Eq. A.1
$\tau_{\mathrm{d,coll}}$	dust collision time scale	$\tau_{\mathrm{d,coll}} = 1/(n_{\mathrm{d}}\sigma_{\mathrm{d,coll}}\Delta v_{\mathrm{d,Bm}})$
$\tau_{\mathrm{d,diff}}$	time scale of vertical dust diffusion	Chapter 4, Eq. 4.3
$\tau_{\mathrm{d,drift}}$	time scale of radial dust drift	$\tau_{\mathrm{d,drift}} = r/v_{\mathrm{d},r}$
$\tau_{\mathrm{d,grow}}$	dust growth time scale	$\tau_{\mathrm{d,grow}} = a/\dot{a}$
$\tau_{\mathrm{d,sett}}$	dust settling time scale	Chapter 4, Eq. 4.2
τ_{η}	eddy turnover time scale at dissipation scale	
τ_{f}	dimensionless friction/stopping time	$\tau_{\mathrm{f}} = \Omega_{\mathrm{K}} t_{\mathrm{f}} = \pi/10$
$\tau_{\mathrm{g,cool}}$	gas cooling time scale	Chapter 4, Eqs. 4.17, 4.18
τ_{L}	eddy turnover time scale at injection scale	
τ_{stop}	dimensionless stopping/friction time	$\tau_{\mathrm{stop}} \equiv \mathrm{St} = \Omega_{\mathrm{K}} t_{\mathrm{stop}}$; SJB20, Table 1, Eq. 16
Δt (see also Table B.2)	time step	
$\boldsymbol{v}$ (see also Table B.2)	velocity	
$v_{\mathrm{com},r,\mathrm{init}}$	radial velocity of center of mass of gas and dust	SJB20, Eq. B.6
$v_{\mathrm{g},\eta}$	gas velocity at dissipation scale	
$v_{\mathrm{g,L}}$	gas velocity at injection scale	

Symbol	Meaning	Definition
$v_{\mathrm{g,therm}}$	mean thermal gas velocity	$v_{\mathrm{g,therm}} = \sqrt{8/\pi}\, c_{\mathrm{s}}$
v_{K}	Keplerian orbital speed	Chapter 2, Eq. 2.24; SYJ17: $v_{\mathrm{K}} = \Omega_{\mathrm{K}} R$; SJB20, Eq. 11
$v_{r,\mathrm{init}}$ (see also Table B.2)	initial radial velocity	$v_{\mathrm{d},r,\mathrm{init}} = -v_{\mathrm{g},r,\mathrm{init}} = c_{\mathrm{s}}$
$\Delta \boldsymbol{v}$ (Chapter 2)	relative velocity of dust and gas	
Δv (SYJ17)	relative sink particle velocity	
$\Delta \boldsymbol{v}_{\mathrm{drag}}$ (see also Table B.2)	change in velocity caused by drag	$\Delta \boldsymbol{v}_{\mathrm{d,drag}} = (\boldsymbol{v}_{\mathrm{d}} - \boldsymbol{v}_{\mathrm{g}})/t_{\mathrm{d,stop}}\, \Delta t$, $\Delta \boldsymbol{v}_{\mathrm{g,drag}} = \Delta \boldsymbol{p}_{\mathrm{p,drag}}/(\rho_{\mathrm{g}} V)$
V	cell volume	
$\Delta v_{\mathrm{d,boun}}$	relative dust velocity leading to bouncing	Chapter 2, Eq. 2.11
$\Delta v_{\mathrm{d,Bm}}$	mean relative dust velocity owing to Brownian motion	Chapter 2, Eq. 2.1
$\Delta v_{\mathrm{d,frag}}$	relative dust velocity leading to fragmentation	$\Delta v_{\mathrm{d,frag}} = 100\ \mathrm{cm\ s^{-1}}$
$\Delta v_{\mathrm{d,turb}}$	relative dust velocity owing to gas turbulence	Chapter 2, Eq. 2.10
x (Chapter 3, SYJ17)	radial coordinate	
x (SJB20; see also Table B.2)	x-coordinate	
Δx	grid cell size	SJB20, Table 1
y (Chapter 3, SYJ17)	azimuthal coordinate	
y (SJB20; see also Table B.2)	y-coordinate	
z (see also Table B.2)	vertical coordinate	
Z	dust-/solid-to-gas surface density ratio	Chapters 3, 4, SJB20: $Z = \Sigma_{\mathrm{d}}/\Sigma_{\mathrm{g}}$; SJB20, Table 1; SYJ17: $Z = \Sigma_{\mathrm{p}}/\Sigma_{\mathrm{g}}$
Z_{thres}	threshold dust-to-gas surface density ratio for filament and planetesimal formation owing to streaming instability	Chapter 3, Eq. 3.28

Table B.2: Sub- and superscripts

Sub-/superscript	Meaning
d	dust
g	gas
i	particle index
init	initial
max	maximum
min	minimum
n	time step index
p	particle
ϕ	azimuthal
r	radial
RMS	root mean square
x	radial
y (SYJ17)	azimuthal
y (SJB20)	in y-direction
z	vertical
0 (subscript)	protoplanetary disk mid-plane at $z = 0$
0, $1/2$ (superscript)	index of zeroth, first half time step

Table B.3: Constants

Constant	Meaning	Value
G	gravitational constant	6.674×10^{-8} g^{-1} cm^3 s^{-2}
k_B	Boltzmann constant	1.381×10^{-16} erg K^{-1}
$L_\odot$	Solar luminosity	3.839×10^{33} erg s^{-1}
m_H	hydrogen mass	1.674×10^{-24} g
M_Ceres	mass of Ceres	9.3×10^{23} g
$M_\oplus$	mass of Earth	5.972×10^{27} g
$M_\odot$	Solar mass	1.989×10^{33} g
R	ideal gas constant	8.314×10^{7} erg g^{-1} K^{-1}
σ	Stefan-Boltzmann constant	5.670×10^{5} erg cm^2 s^1 K^4

Eidesstattliche Versicherung

Hiermit versichere ich an Eides statt, die vorliegende Dissertationsschrift selbst verfasst und keine anderen als die angegebenen Hilfsmittel und Quellen benutzt zu haben.
Die eingereichte schriftliche Fassung entspricht der auf dem elektronischen Speichermedium.
Die Dissertation wurde in der vorgelegten oder einer ähnlichen Form nicht schon einmal in einem früheren Promotionsverfahren angenommen oder als ungenügend beurteilt.

Hamburg, den 01.10.2020

Urs Schäfer

Astronomy and Astrophysics
Editor in Chief: T. Forveille

T. Forveille
Astronomy & Astrophysics
Observatoire de Paris
61, avenue de l'Observatoire
75014 Paris, France

Tel.: 33 0(1) 43 29 05 41
Fax: 33 0(1) 43 29 05 57
e-mail: aanda.paris@obspm.fr
Web: http://www.aanda.org

merging
Annales d'Astrophysique
Arkiv for Astronomi
Bulletin of the Astronomical Institutes of the Netherlands
Bulletin Astronomique
Journal des Observateurs
Zeitschrift fur Astrophysik
Bulletin of the Astronomical Institutes of Czechoslovakia

Paris, April 28, 2020

Reprint Permission

Material:
Article by Schäfer, U., Yang,C.-C., & Johansen, A., A&A, 597:A69, 2017.
Article by Schäfer, U., Johansen, A., & Banerjee, R., A&A, 635:A190, 2020.

To be used in:
PhD thesis, University of Hamburg

Permission granted to:
Urs Schäfer
stnv005@hs.uni-hamburg.de

I hold copyright on the material referred to above, and hereby grant permission for its use as requested herewith.

The article should be reproduced as a whole in a coherent fashion fully consistent with the version published in A&A.

Credit should be given as follows:
Credit: Author, A&A, vol, page, year, reproduced with permission © ESO.

Thierry Forveille
A&A Editor-in-Chief

Sponsored by Argentina, Armenia, Austria, Belgium, Bulgaria, Chile, Croatia, Czech Republic, Denmark, Estonia, Finland, France, Germany, Greece, Hungary, Italy, Lithuania, Netherlands, Norway, Poland, Portugal, Slovak Republic, Spain, Sweden, and Switzerland.
Produced and distributed by EDP Sciences for ESO.

Astronomy and Astrophysics
Editor in Chief: T. Forveille

T. Forveille
Astronomy & Astrophysics
Observatoire de Paris
61, avenue de l'Observatoire
75014 Paris, France

Tel.: 33 0(1) 43 29 05 41
Fax: 33 0(1) 43 29 05 57
e-mail: aanda.paris@obspm.fr
Web: http://www.aanda.org

merging
Annales d'Astrophysique
Arkiv for Astronomi
Bulletin of the Astronomical Institutes of the Netherlands
Bulletin Astronomique
Journal des Observateurs
Zeitschrift fur Astrophysik
Bulletin of the Astronomical Institutes of Czechoslovakia

Paris, 20 August 2020

Reprint Permission

Material:
- Figure 6 of Drążkowska et al. 2016, A&A, 594:A105
- Figure 9 of Yang et al. 2017, A&A, 606:A80
- Figure 11 of Schoonenberg et al. 2018, A&A, 620:A134
-Figure 6 of Delbo et al. 2019, A&A, 624:A69

To be used in:
PhD thesis, University of Hamburg

Permission granted to:
Urs Schäfer
Hamburg Observatory at the University of Hamburg, Germany
stnv005@hs.uni-hamburg.de

I hold copyright on the material referred to above, and hereby grant permission for its use as requested herewith. The credit should be given as follows:
Credit: Author, A&A, vol, page, year, reproduced with permission © ESO.

Thierry Forveille
A&A Editor-in-Chief

Sponsored by Argentina, Armenia, Austria, Belgium, Bulgaria, Chile, Croatia, Czech Republic, Denmark, Estonia, Finland, France, Germany, Greece, Hungary, Italy, Lithuania, Netherlands, Norway, Poland, Portugal, Slovak Republic, Spain, Sweden, and Switzerland.
Produced and distributed by EDP Sciences for ESO.